

Static and Dynamic Delta E Effect in Magnetostrictive  
Materials with Application to Electrically-Tunable Vibration  
Control Devices

Dissertation

Presented in Partial Fulfillment of the Requirements for the Degree  
Doctor of Philosophy in the Graduate School of The Ohio State  
University

By

Justin Jon Scheidler, B.S.

Graduate Program in Mechanical Engineering

The Ohio State University

2015

Dissertation Committee:

Professor Marcelo Dapino, Advisor

Professor Giorgio Rizzoni

Professor Krishnaswamy Srinivasan

Professor Junmin Wang

© Copyright by  
Justin Jon Scheidler  
2015

## Abstract

Magnetostrictive materials transfer energy between the magnetic and mechanical domains as they magnetize in response to applied stresses and deform in response to applied magnetic fields. The deformation that arises from this coupling directly causes the material's effective elastic moduli to depend on stress and magnetic field. This phenomenon, known as the  $\Delta E$  effect, can be electrically modulated using electromagnets. Devices having an electrically-tunable stiffness can be developed by harnessing this effect. Such devices have broad application to the field of vibration control, particularly in instances where the vibration source or operating regime change over time. Although the static  $\Delta E$  effect has been extensively measured in many man-made magnetostrictive materials, such as Galfenol (FeGa) and Terfenol-D (TbDyFe), this tunability has been seldom applied to the development of vibration control devices. Real-time tuning of the elastic moduli (i.e., the dynamic  $\Delta E$  effect) has not been studied. Further, the effects of dynamic stress on the constitutive behavior of magnetostrictive materials are largely unknown, despite their critical importance to the modeling and design of many magnetostrictive systems, including dynamic sensors, energy harvesters, vibration dampers, and stiffness tuning devices. This work analytically, numerically, and experimentally explores the effects of dynamic stress on magnetostrictive materials and the use of the static and dynamic  $\Delta E$  effect in the development of novel vibration control devices.

Measurements of the quasi-static elastic response of Galfenol reveal that the Young's modulus and  $\Delta E$  effect are stiffer and smaller, respectively, for small amplitude applied stresses than for large amplitude applied stresses. The  $\Delta E$  effect of solid and laminated samples is found to be equal, despite the laminated sample's 17 % lower modulus under saturated conditions. The static  $\Delta E$  effect in Galfenol-based composite beams that are applied as adaptive vibration absorbers is studied by constructing nonlinear, dynamic models of their vibratory response. The absorber's resonant frequencies are shown to be controllable below an input power threshold via changes in the bias magnetic field. Resonant frequency tunability increases with the Galfenol element's volume fraction and offset from the bending axis.

Mechanically-induced magnetic diffusion in linear and nonlinear cylindrical ferromagnets is investigated. Analytical time and frequency domain solutions of linear diffusion are derived for the first time. The solutions are non-dimensionalized and used to define a skin depth and cut-off frequency, which can be used for design purposes. This diffusion causes the material's effective magnetoelastic coupling coefficient and elastic modulus to be complex-valued and frequency dependent. The effects of material property variations on the nonlinear diffusion response are studied numerically. A novel characterization of Galfenol's constitutive response to dynamic stress is presented along with a detailed experimental methodology that ensures the accuracy of the measurements. Solid and laminated Galfenol rods exhibit cut-off frequencies of 44 to 105 Hz and about 1 kHz, respectively. The mechanical loss factor of the solid rod reaches 0.13 due to eddy current-induced damping.

The dynamic  $\Delta E$  effect is studied using a magnetostrictive transducer designed for high speed stiffness switching. Electromechanical modeling of the transducer

shows that the rise time to stiffness control inputs can be on the order of 0.1 ms. Terfenol-D is found to outperform Galfenol by providing a slightly faster rise time, significantly higher magnetic diffusion cut-off frequency, and larger elastic modulus tunability. Young's modulus changes up to 21.9 GPa and 500 Hz, modulus switching up to 12.3 GPa and 100 Hz, and a rise time below 1 ms are measured. The transducer is applied in a computational study of switched stiffness vibration control of a simple mechanical system. Using a modified control law, control-induced damping equivalent to a viscous damping ratio of about 0.15 is demonstrated.

To my wife and parents  
*who pushed me to reach for the stars*

## Acknowledgments

I am deeply indebted to my advisor, Prof. Marcelo Dapino, for his exceptional technical guidance and strong commitment to my professional development. He has been a great role model; I know that the qualities he has instilled in me, particularly a dedication to perfection in technical communication, will benefit me throughout my career. I want to thank my committee members, Prof. Giorgio Rizzoni, Prof. Krishnaswamy Srinivasan, and Prof. Junmin Wang, for their time and careful review of my research. Their comments strengthened my research in many ways.

I am very grateful to Vivake Asnani of NASA Glenn Research Center for his excellent technical direction and the extensive time that he spent on my behalf. He went above and beyond to broaden my skill set and provide a remarkable internship at Glenn. His practical advice and intuitive logic will be remembered throughout my future endeavors.

My colleagues in the Smart Materials and Structures Laboratory have helped make graduate school an enjoyable and memorable experience. I am grateful to Zhangxian Deng for many interesting and beneficial discussions. Working alongside Paul Wolcott, Sheng Dong, Ryan Hahnen, John Larson, Adam Hehr, Josh Pritchard, and Mark Riggs helped with my technical development and provided relaxing breaks from my studies.

I give special thanks to my family for their love and encouragement. My parents' continual push to live up to my abilities has been instrumental in achieving my dreams. My wife's patience and support throughout graduate school and her commitment to my happiness will never be forgotten.

I would also like to acknowledge my funding sources, which afforded me the freedom to pursue my research interests. This work was supported by the NASA Aeronautics Scholarship Program (grant # NNX14AE24H) and a Graduate Automotive Technology Education (GATE) Fellowship from the U.S. DOE GATE Center of Excellence, DE FG2605NT42616, at The Ohio State University. Additional support was provided by NASA's Revolutionary Vertical Lift Technology (RVLT) Project, the NASA Aeronautics Research Mission Directorate Seedling Fund, and the member organizations of the Smart Vehicle Concepts Center ([www.SmartVehicleCenter.org](http://www.SmartVehicleCenter.org)), a National Science Foundation Industry/University Cooperative Research Center.



## Vita

May 8, 1988 .....	Born - Akron, OH, USA
June, 2011 .....	B.S., Mechanical Engineering, Magna Cum Laude, With Honors in Engineering, With Honors Research Distinction in Mechanical Engineering, The Ohio State University, Columbus, OH
2010-2015 .....	NASA Aeronautics Scholarship Pro- gram Scholar, DOE Graduate Automotive Technol- ogy Education Fellow, The Ohio State University, Columbus, OH

## Publications

### Journal Publications

J.J. Scheidler, V.M. Asnani, and M.J. Dapino, “Design and testing of a dynamically-tuned magnetostrictive spring with electrically-controlled stiffness,” *Smart Materials and Structures*, in review.

Z. Deng, J.J. Scheidler, V.M. Asnani, and M.J. Dapino, “Major and minor stress-strain loops in textured polycrystalline  $\text{Fe}_{81.6}\text{Ga}_{18.4}$  Galfenol,” *Journal of Applied Physics*, in review.

J.J. Scheidler, V.M. Asnani, and M.J. Dapino, “Frequency-dependent, dynamic sensing properties of polycrystalline Galfenol ( $\text{Fe}_{81.6}\text{Ga}_{18.4}$ ), *Applied Physics Letters*, in review.

J.J. Scheidler and M.J. Dapino, “Mechanically-induced magnetic diffusion in cylindrical ferromagnetic materials, *Journal of Magnetism and Magnetic Materials*, in review.

S. Santapuri, J.J. Scheidler, and M.J. Dapino, “Dynamic nonlinear two-dimensional modeling framework for composite laminates with embedded magnetostrictive materials, *Composite Structures* 132, p. 737-745, 2015.

J.J. Scheidler, M.J. Dapino, and V.M. Asnani, “Dynamic characterization of Galfenol ( $\text{Fe}_{81.6}\text{Ga}_{18.4}$ ), NASA/TP-2015-218754, 2015.

H. Tari, J.J. Scheidler, and M.J. Dapino, “Robust solution procedure for the discrete energy-averaged model on the calculation of 3D hysteretic magnetization and magnetostriction of iron–gallium alloys, *Journal of Magnetism and Magnetic Materials*, Vol. 384, pp. 266–275, 2015.

J.J. Scheidler and M.J. Dapino, “Nonlinear dynamic modeling and resonance tuning of Galfenol vibration absorbers, *Smart Materials and Structures* Vol. 22, 085015, 2013.

### Conference Publications

J.J. Scheidler, V.M. Asnani, and M.J. Dapino, “Design and testing of a dynamically-tuned magnetostrictive spring with electrically-controlled stiffness, *Proc. SPIE* 9433, 94330F, April 1, 2015.

J.J. Scheidler, V.M. Asnani, Z. Deng, and M.J. Dapino, “Dynamic characterization of Galfenol, *Proc. SPIE* 9432, 94320J, April 1, 2015.

J.J. Scheidler and M.J. Dapino, “Stiffness tuning of FeGa structures manufactured by ultrasonic additive manufacturing, *Proc. SPIE* 9059, 905907, March 10, 2014.

J.J. Scheidler and M.J. Dapino, “Nonlinear dynamic model for magnetically-tunable Galfenol vibration absorbers, *Proc. SPIE* 8690, 869002, March 29, 2013.

S.J. Dias, J. Scheidler, S.G. Taylor, K. Farinholt, and G. Park, “Structural Health Monitoring of Wind Turbine Blades Under Fatigue Loads, *Conf. Proc. of the Society for Experimental Mechanics Series*, Vol. 2, pp. 227-245, 2012.

## Fields of Study

Major Field: Mechanical Engineering

Studies in:

- Smart materials and structures
- Mechanical vibrations
- Electromagnetism
- Nonlinear dynamics

# Table of Contents

	Page
Abstract . . . . .	ii
Dedication . . . . .	v
Acknowledgments . . . . .	vi
Vita . . . . .	viii
List of Tables . . . . .	xiv
List of Figures . . . . .	xvi
1. Introduction . . . . .	1
1.1 Overview and Motivation . . . . .	1
1.2 Background . . . . .	3
1.2.1 Electromagnetism . . . . .	3
1.2.2 Magnetostrictive materials . . . . .	11
1.2.3 Magnetostrictive transducers . . . . .	31
1.2.4 Autoresonant control . . . . .	32
1.3 Literature Review . . . . .	35
1.3.1 Magnetic diffusion . . . . .	35
1.3.2 Delta E effect . . . . .	35
1.3.3 Dynamic behavior of Terfenol-D and Galfenol . . . . .	39
1.3.4 Magnetostrictive tunable stiffness devices . . . . .	40
1.4 Research Objectives and Outline . . . . .	41
2. Static Stiffness Change . . . . .	44
2.1 Quasi-Static Elastic Response of Galfenol . . . . .	44
2.1.1 Experimental design and setup . . . . .	45

2.1.2	Results and discussion . . . . .	47
2.1.3	Concluding remarks . . . . .	56
2.2	Galfenol Vibration Absorbers . . . . .	60
2.2.1	Lumped parameter modeling . . . . .	62
2.2.2	Distributed parameter modeling . . . . .	85
3.	Dynamic Stress Effects in Magnetostrictive Materials . . . . .	107
3.1	Mechanically-Induced Magnetic Diffusion . . . . .	108
3.1.1	Linear constitutive regimes . . . . .	108
3.1.2	Nonlinear constitutive regimes . . . . .	126
3.2	Dynamic Characterization of Galfenol . . . . .	141
3.2.1	Specimen design . . . . .	142
3.2.2	Sensor selection and uncertainty analysis . . . . .	152
3.2.3	Experimental setup and methods . . . . .	154
3.2.4	Data processing methods . . . . .	163
3.2.5	Dynamic sensing measurements . . . . .	173
3.2.6	Concluding remarks . . . . .	191
4.	Dynamic Stiffness Change . . . . .	195
4.1	Magnetostrictive Variable-Stiffness Spring . . . . .	195
4.1.1	Modeling and design . . . . .	196
4.1.2	Experimental setup . . . . .	205
4.1.3	Dynamic tuning . . . . .	208
4.1.4	Concluding remarks . . . . .	212
4.2	Case Study: Switched Stiffness Vibration Control . . . . .	214
4.2.1	Model development . . . . .	214
4.2.2	Results and discussion . . . . .	218
4.2.3	Concluding remarks . . . . .	222
5.	Conclusions and Future Work . . . . .	225
5.1	Research Summary . . . . .	226
5.2	Contributions and Findings . . . . .	232
5.3	Future Work . . . . .	236
	Appendices . . . . .	239
A.	Improved Discrete Energy-Averaged Model for Terfenol-D . . . . .	239

B.	Galfenol Vibration Absorbers: Distributed Parameter Modeling . . . . .	245
B.1	Stiffness and damping matrices . . . . .	245
B.2	Analytical response of the passive beam . . . . .	248
C.	Dynamic Characterization of Galfenol: Uncertainty and Calibration . . .	250
C.1	Uncertainty Analysis . . . . .	250
C.2	Calibration Methods . . . . .	261
C.3	Experimental Setup and Methods . . . . .	271
C.3.1	Wiring . . . . .	271
C.3.2	Magnetic field control . . . . .	271
C.3.3	Sensor reset . . . . .	274
C.4	Data Processing Methods . . . . .	276
C.4.1	Amplitude calibration . . . . .	276
C.4.2	Filtering . . . . .	279
C.4.3	Evaluation of reversibility in the constitutive response . . .	281
C.5	Procedure . . . . .	282
	Bibliography . . . . .	289

## List of Tables

Table	Page
1.1 Energies of the magnetic domain orientations in the DEAM . . . . .	23
1.2 A comparison of measured $\Delta E$ effects for a variety of magnetostrictive materials, calculated using Eq. (1.16). . . . .	38
2.1 Optimized model parameters for the DEA model. . . . .	48
2.2 Average RMS error for approximating the average elastic modulus through the thickness and along the length of the Galfenol element. .	69
2.3 Model parameters. . . . .	73
2.4 Autoresonant tracking of the passive beam's resonant frequency: relative numerical errors. . . . .	99
2.5 Percent difference between measured and calculated resonant frequencies of the UAM Galfenol/Al 6061 beam. . . . .	101
3.1 Modeling parameters common to all nonlinear magnetic diffusion simulations. . . . .	131
3.2 Geometric specifications for specimens from ASTM standards. . . . .	143
3.3 Model parameters used for the solution of the mechanically-induced magnetic diffusion problem. . . . .	150
3.4 Estimated uncertainty in the measured quantities. . . . .	153
3.5 Linear, least-squares regression of the phase responses of the conditioning electronics – phase offsets and relative time delays. . . . .	169

4.1	Approximate Young's moduli (in units of GPa) of the Terfenol-D rod inside the prototype Varispring at the maximum and minimum current for a bias stress of -5.90 MPa and different sinusoidal current frequencies and stress amplitudes. . . . .	211
4.2	Approximate Young's moduli (in units of GPa) of the Terfenol-D rod inside the prototype Varispring at the high and low current states for a bias stress of -5.90 MPa and different square wave current frequencies and stress amplitudes. . . . .	213
4.3	Model parameters for switched stiffness vibration control modeling. .	221
A.1	Model parameters for the improved DEA model for Terfenol-D. . . .	244
C.1	ASTM and JIS recommendations for distance measurements. . . . .	251
C.2	ASTM recommendations for force sensors. . . . .	251
C.3	Uncertainties of the force sensors. . . . .	253
C.4	ASTM and ISO recommendations for temperature sensors and constant temperature testing. . . . .	254
C.5	ASTM and ISO recommendations for strain sensors. . . . .	255
C.6	Uncertainty of measured variables used to calculate the strain uncertainty. . . . .	258
C.7	Temperature measurement of boiling water and ice water baths after calibration; tabulated values are an average of measurements obtained on two days. . . . .	267
C.8	Matrix of testing conditions for actuation, quasi-static sensing, and dynamic sensing experiments. . . . .	287



## List of Figures

Figure	Page
1.1 Eddy currents (a) as modeled by the classical eddy current loss and (b) in a multi-domain ferromagnetic material. . . . .	11
1.2 Schematic depiction of magnetoelastic coupling in a planar magnetostrictive material with positive magnetostriction. . . . .	14
1.3 Measured quasi-static constitutive behavior of $\text{Fe}_{81.6}\text{Ga}_{18.4}$ . . . . .	17
1.4 The $\Delta E$ effect. . . . .	19
1.5 (a) jump phenomenon and (b) simple phase-controlled system. . . . .	33
2.1 Comparison of the experimental and modeled quasi-static sensing responses of the solid $\text{Fe}_{81.6}\text{Ga}_{18.4}$ rod. . . . .	48
2.2 Comparison of the actuation responses of the solid Galfenol rod measured directly (solid black lines) and obtained from the sensing responses. . . . .	49
2.3 Young's modulus of the solid $\text{Fe}_{81.6}\text{Ga}_{18.4}$ rod (from major loops). . . . .	50
2.4 (a) Strain versus stress quasi-static minor loops of the solid $\text{Fe}_{81.6}\text{Ga}_{18.4}$ rod and (b) comparison of the major and minor loop responses. . . . .	52
2.5 (a) Young's modulus of the solid $\text{Fe}_{81.6}\text{Ga}_{18.4}$ rod (from minor loops) and (b) comparison of the modulus from the major and the minor loop responses. . . . .	53
2.6 Young's modulus of the solid $\text{Fe}_{81.6}\text{Ga}_{18.4}$ rod from constant field (a) major loops and (b) minor loops. . . . .	54

2.7	Comparison of the experimental and modeled quasi-static sensing responses of the solid $\text{Fe}_{81.6}\text{Ga}_{18.4}$ rod. . . . .	55
2.8	(a) variation in magnetic field and (b) relative magnetic permeability of the solid $\text{Fe}_{81.6}\text{Ga}_{18.4}$ rod under constant current. . . . .	56
2.9	Young's modulus of the solid $\text{Fe}_{81.6}\text{Ga}_{18.4}$ rod (from major loops) under constant current. . . . .	57
2.10	(a) strain versus stress quasi-static minor loops of the solid $\text{Fe}_{81.6}\text{Ga}_{18.4}$ rod under constant current. . . . .	58
2.11	(a) Young's modulus of the solid $\text{Fe}_{81.6}\text{Ga}_{18.4}$ rod under constant current and (b) comparison of the modulus from major and minor loops. . . . .	59
2.12	(a) strain and (b) Young's modulus major loops of the laminated $\text{Fe}_{81.6}\text{Ga}_{18.4}$ rod under constant current. . . . .	59
2.13	Very high power UAM machine installed in the Center for Ultrasonic Additive Manufacturing. . . . .	61
2.14	Al 3003 composite manufactured by UAM containing an embedded 0.05 x 1.27 cm Galfenol sheet. . . . .	61
2.15	Average elastic modulus through the thickness of a Galfenol element located at the neutral axis with $H_{\text{bias}} = 2$ kA/m (calculated using the DEA model). . . . .	65
2.16	Average elastic modulus of a Galfenol element located at the C-F beam's neutral axis. . . . .	68
2.17	Solution procedure to approximate a single, potentially hysteretic frequency response. . . . .	70
2.18	Hysteretic frequency response ( $\bar{w}/U_2$ ) of the C-F Galfenol-Al composite. . . . .	71
2.19	Normalized resonant frequency of the C-F composite as a function of the operating conditions for Galfenol volume fractions of (a) 10 %, (b) 28 %, (c) 46 %, (d) 64 %, (e) 82 %, and (f) 100 %. . . . .	74

2.20	Normalized resonant frequency of the C-C composite as a function of the operating conditions for Galfenol volume fractions of (a) 10 %, (b) 28 %, (c) 46 %, (d) 64 %, (e) 82 %, and (f) 100 %.	75
2.21	Effect of Galfenol volume fraction on the maximum tunability of the vibration absorber's resonance.	76
2.22	Normalized resonant frequency of the C-F composite as a function of the operating conditions for Galfenol embedded at the (a) reference or minimum, (b) 33 %, (c) 66 %, and (d) 100 % or maximum locations (top views shown, $\xi_G = 0.1$ ).	77
2.23	Normalized resonant frequency of the C-C composite as a function of the operating conditions for Galfenol embedded at the (a) reference or minimum, (b) 33 %, (c) 66 %, and (d) 100 % or maximum locations (top views shown, $\xi_G = 0.1$ ).	78
2.24	Effect of Galfenol's vertical location in the composite on the maximum tunability of the vibration absorber's resonance.	79
2.25	Schematic of the base-excited magnetostrictive composite beam and nodes used for finite difference discretization.	86
2.26	Galfenol/Al 6061 composite beam and schematic of the beam's cross section.	86
2.27	Schematic and free body diagram of the 1-D static composite subjected to an applied magnetic field with boundary conditions: (a) free-free, and (b) fixed-fixed.	92
2.28	Simulink block diagram for the vibration of the FeGa composite beam; autoresonant feedback shown by red, dotted arrows.	95
2.29	Example analytical amplitude versus phase response of the passive beam.	96
2.30	Calculated frequency response of the displacement transmissibility of the passive beam compared to the analytical response (B.20).	97
2.31	Tracking of the passive beam's 1st resonant frequency using autoresonant feedback control.	98

2.32	(a) Experimental setup for the model validation, and (b) experimental and simulated mode shapes of the UAM Galfenol/Al 6061 composite for the 1st and 3rd modes. . . . .	100
2.33	Normalized resonant frequency of the 3rd bending vibration mode of the clamped-clamped UAM composite. . . . .	103
2.34	Maximum resonant frequency tunability of the Galfenol/Al 6061 beam as a function of Galfenol volume fraction. . . . .	104
3.1	Non-dimensionalized time domain response to sinusoidal forcing for positive $d^*\hat{T}$ , (a) non-dimensionalized dynamic field $\bar{H}(r/R, t)$ at different radial locations for $R/\delta^M = q = 1$ and (b) non-dimensionalized, effective dynamic field $\bar{H}_{\text{eff}}(t)$ for different $R/\delta^M = q$ . . . . .	119
3.2	Spatial distribution of the steady-state, non-dimensionalized dynamic field for different $R/\delta^M = q$ . . . . .	121
3.3	Non-dimensionalized frequency response of (a) the dynamic field – magnitude (top) and phase (bottom) – and (b) the dynamic magnetic flux density magnitude. . . . .	122
3.4	Real and imaginary parts of the eddy current factor for mechanically-induced magnetic diffusion. . . . .	124
3.5	Discretization of the cylindrical ferromagnet. . . . .	128
3.6	Nonlinear magnetic diffusion solution procedure. . . . .	130
3.7	Validation of the numerical method: spatial distribution of the steady-state, non-dimensionalized dynamic field. . . . .	132
3.8	Validation of the numerical method: non-dimensionalized frequency response of the dynamic field. . . . .	133
3.9	Validation of the numerical method: non-dimensionalized frequency response of the effective (average) internal dynamic field. . . . .	134
3.10	Comparison of the proposed procedure and MATLAB's <i>fminunc</i> . . . . .	135

3.11	Comparison of a nonlinear diffusion response at the rod's axis calculated with and without iterations on $k$ ; $g = 40$ , $\omega = 0.25\omega_c$ , and $ T  = 2$ MPa. . . . .	136
3.12	Convergence of the nonlinear magnetic diffusion response to the linear, analytical diffusion response. . . . .	137
3.13	Magnetic permeability of Galfenol ( $\text{Fe}_{81.6}\text{Ga}_{18.4}$ ) about the selected bias point for different stress amplitudes. . . . .	138
3.14	Time domain, nonlinear magnetic diffusion response of Galfenol for different stress amplitudes. . . . .	139
3.15	Frequency domain, nonlinear magnetic diffusion response of Galfenol for different stress amplitudes. . . . .	140
3.16	Magnetic circuit used to generate a uniform magnetic state in the gauge region of the specimen, while allowing for independent mechanical excitation. . . . .	144
3.17	COMSOL Multiphysics simulation of the 3D magnetic response of the magnetic circuit . . . . .	145
3.18	Relations between the 1st transverse bending natural frequency and compressive stress . . . . .	148
3.19	Mechanically-induced magnetic diffusion for the Galfenol specimen: (a) temporal response and (b) normalized minimum magnetic field . . . .	149
3.20	Dimensions and tolerances of the highly-textured, $< 100 >$ oriented, polycrystalline Galfenol ( $\text{Fe}_{81.6}\text{Ga}_{18.4}$ ) rods . . . . .	151
3.21	MTS 831.50 load frame with experiment installed. . . . .	156
3.22	Detail of the (a) quasi-static and (b) dynamic experiments. . . . .	157
3.23	Schematic of the load path and mechanical model for inertial force error cases 1 and 2. . . . .	158
3.24	Measurement error in the force applied to the specimen due to the inertial force of fixturing . . . . .	159

3.25	Wheatstone quarter bridge strain measurement circuit considering electromagnetic noise $V_{\text{noise}}$ (leadwire resistance neglected). . . . .	160
3.26	Error in the strain measurement due to electromagnetic noise: the effects of (a) true strain magnitude and (b) normalized noise voltage; $F_G = 2.155$ . . . . .	160
3.27	Electromagnetic noise voltage induced in two strain gauges and their leadwires in response to a 3 MPa amplitude, 1 kHz axial stress . . . .	161
3.28	(a) weaving pattern for strain gauge leadwires to reduce electromagnetic noise and (b) wiring of a strain gauge pair to simultaneously cancel bending strains and electromagnetic noise . . . . .	162
3.29	(a) measured electromagnetic noise in the strain measurement for the solid Galfenol specimen and worst-case loading and (b) amplitude of the magnetic flux density response . . . . .	163
3.30	Experimental setup for measuring the phase response of the conditioning electronics for strain, load cell, load washer, and flux density signals.	165
3.31	Block diagram of the magnetic flux density channel during phase response measurement. . . . .	166
3.32	Phase response of the strain, static force, dynamic force, and magnetic flux density conditioning electronics (the phase offset in the dynamic force and flux density channels was removed for visualization purposes); (a) full response and (b) detail. . . . .	168
3.33	Method used to calculate the dynamic material properties. . . . .	172
3.34	Major loop dynamic sensing response of the solid Galfenol rod under a bias current of 0.30 A . . . . .	176
3.35	Major loop dynamic sensing response of the solid Galfenol rod for a bias current of 0.80 A . . . . .	177
3.36	Minor loop dynamic sensing response of the solid Galfenol rod for a bias current of 0.30 A . . . . .	178

3.37	Major loop dynamic sensing response of the solid Galfenol rod for a bias magnetic field of 2.46 kA/m . . . . .	181
3.38	Minor loop dynamic sensing response of the solid Galfenol rod for a bias magnetic field of 2.46 kA/m . . . . .	182
3.39	Major loop dynamic sensing response of the laminated Galfenol rod for a bias current of 0.30 A . . . . .	185
3.40	Minor loop dynamic sensing response of the laminated Galfenol rod for a bias current of 0.30 A . . . . .	186
3.41	(a) dynamic piezomagnetic coefficient and (b) dynamic Young's modulus of the solid and laminated $\text{Fe}_{81.6}\text{Ga}_{18.4}$ rods measured at constant current ( $T_{\text{bias}} = -9.93$ MPa, $I_{\text{bias}} = 0.3$ A) and constant field ( $T_{\text{bias}} = -7.96$ MPa, $H_{\text{bias}} = 2.46$ kA/m), (top) lossless component and (bottom) loss factor; dashed line denotes the expected trend (not measured data); dotted line denotes the linear fit: $\eta_E = 0.6262 \times 10^{-3}f + 0.0398$ . . . . .	188
3.42	Energy densities of the minor hysteresis loops of the solid and laminated $\text{Fe}_{81.6}\text{Ga}_{18.4}$ rods under constant current. . . . .	190
4.1	Rise time to reach $H_{\text{soft}}$ from $H = 0$ in response to a 250 V step voltage input. . . . .	200
4.2	Mechanically-induced magnetic diffusion cut-off frequency of 6.3 mm diameter solid Terfenol-D, solid Galfenol, and laminated Galfenol rods. . . . .	201
4.3	Effect of internal mass on the dynamic stiffness of the magnetostrictive rod. . . . .	203
4.4	(a) CAD model of the prototype Varispring and (b) manufactured Varispring. . . . .	204
4.5	Experimental setup (the compression spring used to improve the force control during dynamic stiffness tuning tests is not shown). . . . .	207
4.6	Force control performance during dynamic stiffness tuning tests when using the soft compression spring. . . . .	207
4.7	Quasi-static Young's modulus of the laminated Terfenol-D rod. . . . .	208

4.8	Strain response of the Terfenol-D rod inside the prototype Varispring to a (a) 100 Hz and (b) 500 Hz sinusoidal current and a 25 Hz, 2.00 MPa amplitude stress with -5.90 MPa bias. . . . .	210
4.9	Current control performance during testing of the dynamic $\Delta E$ effect. . . . .	211
4.10	Strain response of the Terfenol-D rod inside the prototype Varispring to a (a) 1 Hz and (b) 100 Hz square wave current and a 25 Hz, 4.00 MPa amplitude stress with -5.90 MPa bias. . . . .	212
4.11	Mechanical system used to investigate switched stiffness vibration control. . . . .	215
4.12	Mechanical resonance induced by switched stiffness vibration control due to the uncontrolled magnetostrictive force; model parameters given in Table 4.3, $H = 0_{-0}^{+35}$ kA/m. . . . .	220
4.13	Tuning conditions of the magnetostrictive Varispring needed to realize switched stiffness vibration control. . . . .	221
4.14	Stress and magnetic field dependence of the Young's modulus of a Terfenol-D rod and electromechanical coupling coefficient of a Terfenol-D-based Varispring. . . . .	222
4.15	Enhanced decay of damped, free vibration using switched stiffness vibration control. . . . .	223
A.1	Unphysical kinks in the magnetostriction response of Terfenol-D calculated using Evans and Dapino's original DEA model [61]; plot reproduced from [34]. . . . .	240
A.2	Crystal structure of a Terfenol-D rod. . . . .	241
A.3	Comparison of the improved DEA model for Terfenol-D with magnetostriction measurements. . . . .	243
C.1	Uncertainty in the (a) force and (b) stress calculations . . . . .	254
C.2	Uncertainty in the strain calculation. . . . .	258



C.3	Uncertainty in (a) the Hall chip's sensitivity and (b) the magnetic field calculation . . . . .	260
C.4	Uncertainty in the magnetic flux density. . . . .	261
C.5	Experimental setup for the calibration of the linear power amplifier. .	262
C.6	Calibration of the linear power amplifier: (a) voltage monitor, (b) current monitor. . . . .	263
C.7	Experimental setup for the calibration of the Kistler load washer and charge amplifier (schematic not to scale). . . . .	264
C.8	Calibration of the Kistler load washer and charge amplifier for a 10 Hz force . . . . .	265
C.9	Experimental setup for the thermocouple calibration. . . . .	266
C.10	Calibration of the thermocouple. . . . .	266
C.11	Experimental setup for the strain calibration. . . . .	267
C.12	Calibration of the strain measurement system. . . . .	268
C.13	Experimental setup for the Hall effect sensor calibration (sensors not to scale); the Hall chip supply voltage was 5.000 V. . . . .	268
C.14	30 point calibration of the Hall effect sensor. . . . .	269
C.15	Experimental setup for the calibration of the magnetic flux density sensing coil and fluxmeter; the magnetic circuit shown in Figs. 3.16 and 3.17 was used to magnetize the Ni 200 rod. . . . .	270
C.16	Calibration of the magnetic flux density measurement system. . . . .	270
C.17	Wiring schematic for all of the measurement channels. . . . .	272
C.18	Schematic of the magnetic field control system, which was independent of the measurement system and thus only included the signal conditioning depicted here. . . . .	273

C.19 Signal flow diagram 1 of 2. . . . .	277
C.20 Signal flow diagram 2 of 2. . . . .	278
C.21 (a) DFT of the unfiltered actuation response of the solid Galfenol rod for a mean bias stress of -10.23 MPa, (b) comparison of the filtered (red) and unfiltered (black) magnetostriction responses at -10.23 MPa.	280
C.22 (a) DFT of the unfiltered sensing response of the solid Galfenol rod for a mean bias current of 0.60 A, (b) comparison of the filtered (red) and unfiltered (black) flux density responses at 0.50, 0.60, and 0.70 A. . .	281
C.23 (a) DFT of the unfiltered sensing response of the solid Galfenol rod for a mean bias field of 3.88 kA/m, (b) comparison of the filtered (red) and unfiltered (black) flux density responses at 2.41 and 3.88 kA/m. .	282

# Chapter 1: Introduction

## 1.1 Overview and Motivation

Noise and vibration are undesirable side effects of many power generating and power transmitting systems, worsened by high performance designs and efficiency-motivated reductions in mass. For example, severe vibration is generated in helicopter transmissions due to the varying stiffness of the gear mesh, leading to significant cabin noise (up to 120 dB) and pilot fatigue [107]. In automotive applications, the internal combustion engine and transmission act as vibration sources that vary, over a broad frequency range, with changes in the engine's rpm, leading to audible and physical discomfort for passengers [66]. When vibration cannot be reduced through direct design modifications (e.g., by introducing additional damping or shifting natural frequencies away from operating conditions), vibration control systems, namely absorbers and isolators, are often utilized. Conventional control systems perform well, but must be designed for a specific vibration source and operating regime. Through changes in their stiffness or damping properties, adaptive (smart) vibration absorbers and isolators (AVAs and AVIs) can tune their response in conjunction with changes to the vibrating system. AVAs and AVIs therefore form robust vibration control systems. Additionally, vibration control via carefully-timed stiffness switching between

high and low stiffness states can provide a simple yet powerful means of vibration attenuation [40, 117].

A variety of smart materials, including piezoelectric [4], magnetorheological [103], shape memory [124], and magnetostrictive [69] materials, have been used to provide compact, solid-state forms of elastic modulus change. This research considers magnetostrictive materials for reasons discussed in Section 1.2.2. Quasi-static stiffness tuning of magnetostrictive materials has been an active field of research since the early 1900s; the effect has garnered more attention since the 1970s due to the discovery of significant elastic modulus tunability in man-made magnetostrictive materials. A large body of experimental work in this field has established the modulus tunability of many man-made magnetostrictive alloys along with the influence of the bias conditions (stress and magnetic field). However, this tunability has been seldom applied to the development of vibration control devices. Further, in practice, the tunable stiffness device is subjected to dynamic stress, for which the constitutive behavior of magnetostrictive materials has rarely been studied or applied. Also, dynamic, or real-time, stiffness tuning of magnetostrictive materials is an undiscovered field. This dissertation advances the state-of-the-art by analytically, numerically, and experimentally investigating the effects of dynamic stress on magnetostrictive materials and by utilizing both static and dynamic elastic modulus changes in the development of novel vibration control devices.

The subsequent section discusses important background information, including an introduction to electromagnetism, magnetostrictive materials, magnetostrictive transducers, and autoresonant control. After, a literature review of key topics is presented, followed by the research objectives and an outline of the contained research.

## 1.2 Background

### 1.2.1 Electromagnetism

This section provides an introduction to (a) the physical mechanisms underlying electromagnetism and the magnetization process, (b) Maxwell’s equations, (c) eddy currents and magnetic diffusion, and (d) energy dissipation in ferromagnetic materials.

A magnetic field  $\mathbf{H}$  is generated by the motion of electrical charges. Current flowing in a conductor creates magnetic fields that do not depend on the material properties of the surrounding medium. These fields encircle the current in a plane perpendicular to the current direction. At the atomic scale, imbalanced spin and orbital motion of electrons act as sources of additional magnetic fields. Due to their inherent nature and to differentiate them from fields due to conventional electric currents, these atomic-scale fields are together denoted as magnetic moments  $\mathbf{m}$  rather than a magnetic field. Magnetic moments can be envisioned as atomic-scale magnets that are able to rotate, but have a fixed magnitude for a given element at a given temperature.<sup>1</sup> The vector sum of magnetic moments per unit volume of a material is defined as the magnetization  $\mathbf{M}$ . The magnetic flux density  $\mathbf{B}$  is a measure of the total strength of the magnetic field at a point in space, namely a linear combination of the external magnetic field and the magnetization,

$$\mathbf{B} = \mu_0 (\mathbf{H} + \mathbf{M}), \quad (1.1)$$

where  $\mu_0$  is the magnetic permeability of free space (a constant). The magnetic flux density is visualized as field lines whose density in a plane normal to the line direction

<sup>1</sup>Analogous to electric dipoles, magnetic moments are also referred to as magnetic dipoles, with the understanding that magnetic “charges” always appear in opposing pairs (i.e., isolated magnetic charges do not exist).

is proportional to the field's strength. Its direction at a point in space is that in which a miniature compass needle would point.

Imbalanced spin and orbital motion occurs in the outer electron shell of most elements. However, when these elements exist in solids, neighboring atoms share electrons in a manner that completely or mostly eliminates the imbalance of individual atoms. Consequently, most materials contain magnetic moments with negligible or very small magnitudes. However, some elements (namely the rare earths, actinides, and transition metals [58]) exhibit imbalance in an inner electron shell that has little or no participation in bonding. Thus, the magnetic moment of these elements persists in solids containing them.

In ferromagnetic materials, magnetic moments are ordered as a collection of magnetic domains to minimize the collective energy of the moments. In each domain, magnetic moments are aligned in the same direction. The region between neighboring magnetic domains in which magnetic moments transition from the orientation of one domain to that of the other domain is called a magnetic domain wall. In a macroscopically-demagnetized ferromagnetic material, magnetic domains are arranged such that the vector sum of all of the magnetic moments is zero (i.e.,  $\mathbf{M} = 0$ ).<sup>2</sup> In the presence of an external magnetic field  $\mathbf{H}$ , magnetic moments rotate toward the direction of the field. In this way, domain walls translate as domains oriented closest to the applied field grow at the expense of domains oriented far from the field direction. When a material is magnetized such that all  $n$  of its moments are oriented parallel to each other, the material is in a state of complete magnetic saturation and has a magnetization of  $\mathbf{M}_0 = n\mathbf{m}$ . However, above 0 K, magnetic moments precess

<sup>2</sup>This condition can be satisfied by many different domain configurations; thus, there is not a unique demagnetized state for a given material.

about a nominal direction due to thermal activation; this reduces the magnetization of each domain. Consequently, when all  $n$  moments are nominally parallel (i.e., when the material consists of a single domain), the material is said to be technically saturated with a magnetization of  $\mathbf{M}_s$ .  $\mathbf{M}_s = \mathbf{M}_0$  at 0 K, but  $\mathbf{M}_s$  decays to 0 at the Curie temperature.

The process by which a material is magnetized by an external magnetic field primarily depends on the magnitude of the external field energy relative to the anisotropy energy, which promotes the alignment of magnetic moments along certain preferred directions. Anisotropy energy encompasses (a) magnetocrystalline anisotropy, which is intrinsic and depends on the symmetry of the crystal structure, (b) induced anisotropy, which is extrinsic and controlled by material processing, (c) shape anisotropy, which is extrinsic and depends on the size and shape of the material, and (d) stress-induced anisotropy, which is extrinsic and governed by a material's magnetostriction and the external stress. Consequently, the magnetization represents a constitutive response of a material and depends on the external field and external stress,  $\mathbf{M} = \mathbf{M}(\mathbf{H}, \mathbf{T})$ . Typically, the constitutive relation Eq. (1.1) is rewritten as a function of only  $\mathbf{H}$  as

$$\mathbf{B} = \mu_0 (\mathbf{H} + \mathbf{M}) = \mu_0 \left( 1 + \frac{\mathbf{M}}{\mathbf{H}} \right) \mathbf{H} = \mu_0 (1 + \chi) \mathbf{H} = \mu_0 \mu_r \mathbf{H} = \mu \mathbf{H}, \quad (1.2)$$

where the magnetic susceptibility  $\chi$ , relative magnetic permeability  $\mu_r$ , and magnetic permeability  $\mu$  are material properties. In ferromagnetic materials, these properties are nonlinear functions of  $\mathbf{H}$  and  $\mathbf{T}$ .

An in-depth discussion of magnetic domains and the magnetization process can be found in [99, 26, 89].

## Electromagnetic field equations

Maxwell's equations are a set of 4 equations that govern electromagnetic fields in free space and in matter. The physical meaning of each equation is listed below.

- **Gauss's law for electric fields:** Electric charges, both free charges and those bound to atoms, produce electrostatic fields that diverge from positive charges and converge upon negative charges. The divergence of this electric field  $\mathbf{E}$  is zero everywhere except at locations where charge is present.
- **Gauss's law for magnetic fields:** Since isolated positive and negative magnetic "charges" do not exist, there is no source of magnetic flux density nor is there a sink for it. Thus, magnetic flux lines must form closed loops.
- **Faraday's law of induction:** A time-varying magnetic flux density produces an encircling electric field in a plane perpendicular to the direction of the magnetic flux density. The direction of this induced electric field is such that the magnetic flux that it produces always opposes the existing change in magnetic flux.
- **Ampère-Maxwell law:** Free electric current<sup>3</sup>  $\mathbf{J}_{\text{free}}$  and a time-varying electric displacement (electric flux density)  $\mathbf{D}$  produce an encircling magnetic field in a plane perpendicular to the direction of the electric flux density.

<sup>3</sup>Free electric current refers to the motion of electrons that are not bound to an atom, i.e., they exist in the unfilled, outer electron orbit of metallic elements and are free to move throughout the material [92]. This is also referred to as the conduction current.



In matter, Maxwell's equations are written in differential form as

$$\nabla \cdot \mathbf{D} = \rho_{\text{free}}, \quad (1.3)$$

$$\nabla \cdot \mathbf{B} = 0, \quad (1.4)$$

$$\nabla \times \mathbf{E} = -\frac{\partial \mathbf{B}}{\partial t}, \quad (1.5)$$

$$\nabla \times \mathbf{H} = \mathbf{J}_{\text{free}} + \frac{\partial \mathbf{D}}{\partial t}, \quad (1.6)$$

where  $\rho_{\text{free}}$  is the free electric charge density,  $\mathbf{D} = \epsilon_0 \mathbf{E} + \mathbf{P}$ , and  $\mathbf{P}$  is the electric polarization, which is the electrical analog of  $\mathbf{M}$ .

A great introduction to Maxwell's equations can be found in [70], whereas a more detailed discussion is presented in [92].

### Magnetic diffusion

According to Faraday's Law Eq. (1.5), circulating electric fields are generated around a time-varying magnetic flux. Due to the finite resistivity of magnetic materials, these electric fields cause internal eddy currents, which alter magnetic fields propagating through the material [92]. The effect of eddy currents on magnetic fields inside electrically-conducting media is known as magnetic diffusion. The PDE governing magnetic diffusion is derived from Eqs. (1.4) to (1.6) using  $\mathbf{J}_{\text{free}} = \sigma \mathbf{E}$  (where  $\sigma$  is the electrical conductivity) after assuming that  $\partial \mathbf{D} / \partial t$  is negligible,<sup>4</sup> which is valid at frequencies sufficiently below the characteristic frequency of the magnetic system ( $> 1$  MHz [79]),

$$\nabla (\nabla \cdot \mathbf{H}) - \nabla^2 \mathbf{H} = -\sigma \frac{\partial \mathbf{B}}{\partial t}. \quad (1.7)$$

<sup>4</sup>This is equivalent to assuming that the displacement current density  $\epsilon_0 \partial \mathbf{E} / \partial t$  and electric polarization current density  $\partial \mathbf{P} / \partial t$  are negligible.

Diffusion of dynamic magnetic fields into electrically-conducting media (field-induced magnetic diffusion) is a classical problem in electromagnetics that has received significant attention since the late 1800s [92, 102, 144]. A common application in which this effect occurs is when conducting cylindrical rods are excited by axial, dynamic magnetic fields at their surface ( $H_{\text{ext}} = H_0 \exp(j\omega t)$ ). In this case, the internal magnetic field, which is only a function of the cylinder's radial coordinate  $r$ , is given in [58] as

$$H(r, t) = H_0 \frac{J_0(\sqrt{-1}\gamma' r)}{J_0(\sqrt{-1}\gamma' R)} \exp(j\omega t), \quad (1.8)$$

where  $\omega$  is the excitation frequency,  $J_0(\cdot)$  is the Bessel function of order zero,  $R$  is the cylinder's radius, and  $\gamma'$  is the inverse of the penetration (skin) depth,

$$\gamma' = \sqrt{\omega \mu \sigma}. \quad (1.9)$$

Eq. (1.8) reveals that the internal magnetic field decays toward the axis of the rod, shielding the rod's core from the applied field. In cylinders, magnetic diffusion is thus also referred to as the skin effect, because magnetic flux changes are constrained to occur near the surface (i.e., in the “skin”) of the cylinder. The cut-off frequency  $\omega_c$  quantifies the frequency at which the penetration of magnetic flux into the cylinder becomes “incomplete”, which is defined as when  $\gamma' R = 1$  [58],

$$\omega_c = \frac{1}{\sqrt{\mu \sigma R^2}}. \quad (1.10)$$

Although field-induced magnetic diffusion is a classical problem, the influence of magnetoelasticity and static stress on the effect has been investigated only more recently [100, 98, 119]. Hilgert et al. [80] studied the effect of frequency-dependent eddy currents on the magnetostriction of electrical steel, which causes noise in electromagnetic devices. Rasilo et al. [119] modeled this effect under different static stresses.

Dynamic *mechanical* inputs result in a diffusion of *static* magnetic fields into electrically-conducting ferromagnets, particularly ones that exhibit strong magnetoelastic coupling, such as magnetostrictive materials and ferromagnetic shape memory alloys. Mechanically-induced magnetic diffusion is critically important for applications in which these materials operate under dynamic mechanical loading, including dynamic sensors, energy harvesters, vibration dampers, and stiffness tuning devices. However, only a few studies on this effect have been reported, as discussed in Section 1.3.1.

### **Energy dissipation in ferromagnetic materials**

In ferromagnetic materials, purely reversible changes in the material’s state only occur for small magnetic field or stress increments [89]. Both domain wall motion and domain rotation can be irreversible.

Energy is dissipated via magnetic hysteresis, which is approximately frequency independent up to the characteristic frequency of the magnetic system ( $> 1$  MHz [79]) [26], and eddy currents, which are frequency dependent.

Magnetic hysteresis is caused by magnetocrystalline anisotropy and material imperfections. Magnetocrystalline anisotropy leads to discontinuous and irreversible rotation of magnetic moments within individual domains as moments jump from one energy well to another; this mechanism appears to play the primary role in damping of giant magnetostrictive materials [79]. The motion of magnetic domain walls is hindered when they reach imperfections, which include (a) dislocations in the crystal structure (e.g., due to cold working), (b) grain boundaries, (c) non-magnetic impurity elements (e.g., carbon in steel) and precipitates, and (d) voids [89, 25]. When domain walls become unpinned from these defects, very short (about  $1 \times 10^{-9}$  s)

and very intense eddy current pulses occur locally around the wall [25], dissipating energy through Joule heating. Applied magnetic fields cannot alter the dynamics of these domain wall jumps due to their extremely brief duration. Thus, it is clear that magnetic hysteresis occurs at the microscopic scale.

Even in the absence of magnetocrystalline anisotropy and material defects, internal eddy currents are generated as a material’s magnetic flux varies (as discussed in Section 1.2.1), which dissipate energy via Joule heating. In the simplest case – a homogeneous, single domain material undergoing sinusoidal changes in its uniaxial magnetic flux density – the time-varying eddy current distribution, schematically shown in Fig. 1.1a, can be derived from Maxwell’s equations (with or without considering magnetic diffusion). The energy loss associated with these macroscopic-scale eddy currents is called the classical eddy current loss and scales linearly with frequency [25]. However, flux changes result from the motion of domain walls; thus, eddy currents are actually concentrated in the vicinity of the walls as shown in Fig. 1.1b, rather than in the bulk. Accordingly, observed frequency-dependent losses are always larger than that predicted by the classical model [73].

An accurate prediction of the true eddy current loss would require knowledge of the very complex spatial and temporal dependence of the eddy current density. Consequently, the excess energy loss not quantified by the classical model is commonly approximated using the excess eddy current loss, a phenomenological expression based on measurements that scales with the square root of frequency [25]. The excess loss can be considerably larger than the classical loss when the specimen is composed of large, widely-spaced domain walls. However, when domains are small and walls are closely spaced, the eddy currents from adjacent moving walls tend to cancel, as

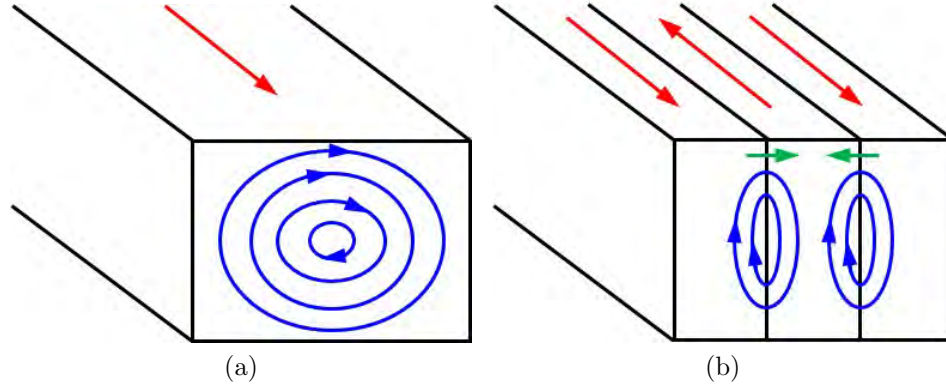


Figure 1.1: Eddy currents (a) as modeled by the classical eddy current loss and (b) in a multi-domain ferromagnetic material; eddy currents (blue), magnetization of a domain (red), and domain wall motion (green); images adapted from [73].

depicted in Fig. 1.1b; in this case, the measured eddy current loss will closely follow the classical prediction.

Due to the magnetomechanical coupling in ferromagnetic materials, the application of stress causes energy to be dissipated through magnetic hysteresis and eddy currents. In particular, the damping associated with stress-induced displacement of domain walls is the primary source of mechanical energy loss [51]. The mechanical damping observed in ferromagnetic materials can therefore significantly exceed that which results from conventional viscoelastic damping.

### 1.2.2 Magnetostrictive materials

This section introduces magnetostrictive materials, including their suitability for vibration control relative to other smart materials, their variable elastic moduli, and constitutive modeling.

As discussed in Section 1.2.1, appreciable magnetism occurs in solids containing elements that exhibit imbalanced spin and orbital motion of electrons located in inner electron shells. In most of these imbalanced elements, the imbalance also causes the atom to have a nonspherical electron charge cloud. In magnetostrictive materials, the direction of the magnetic moment is coupled to the orientation of the nonspherical electron cloud. Thus, magnetostrictive materials display magnetoelastic coupling and can transduce energy between magnetic and mechanical states. Accordingly, magnetic moment rotation is accompanied by a change in magnetization and a change in elastic strain, which is known as magnetostriction ( $\lambda$ ). The Joule (direct or actuation) effect denotes the magnetostriction that results from the application of a magnetic field. The Villari (inverse or sensing) effect, which can be harnessed for sensing, energy harvesting, and vibration attenuation [56, 146, 149, 27, 54], denotes the change in magnetization caused by the application of mechanical stress. This coupling is often described by the linear piezomagnetic equations, which can be written in incremental form as

$$\Delta B = \mu^T \Delta H + d^* \Delta T, \quad (1.11)$$

$$\Delta S = d \Delta H + s^H \Delta T, \quad (1.12)$$

where  $\Delta B$ ,  $\Delta H$ ,  $\Delta S$ , and  $\Delta T$  are the incremental magnetic flux density, magnetic field, strain, and stress,  $\mu^T$  is the magnetic permeability at constant stress,  $s^H$  is the compliance at constant field, and  $d^*$  and  $d$  are piezomagnetic coupling coefficients.

Natural magnetic materials (e.g., nickel, iron, and cobalt) exhibit magnetoelastic effects, but their weak coupling provides very little value. The magnetostriction in iron and nickel is 20 and  $-40 \times 10^{-6}$ , respectively [89]. Interest in magnetostrictive

materials was renewed with the discovery of giant magnetostrictive materials: man-made alloys of rare earth elements having magnetostrictions on the order of  $10^2$  to  $10^3$ . The two most widely used of these are Terfenol-D (an alloy of terbium, dysprosium, and iron) and Galfenol (an alloy of iron and gallium). Owing to their large magnetoelastic strains (magnetostrictions), both materials provide a sizable variation in their elastic moduli, as discussed in the following subsection. This effect forms the foundation for stiffness tuning using magnetostrictive materials.

The incorporation of smart materials into control systems can potentially revolutionize semi-active and active vibration control design. The optimal smart material for a specific vibration control system depends upon the operating conditions in service and the performance requirements. For the design of a dynamic, stiffness-tuning transducer, a high bandwidth and high stiffness change are essential. These characteristics are representative of the following material classes: magnetostrictive, piezoelectric, and magnetic shape memory (MSM). MSM materials have a very low blocking stress ( $\approx 3$  MPa) and require very high strength magnetic fields (up to 575 kA/m) to realize stiffness changes [122]. Terfenol-D and Galfenol outperform MSM materials in this regard by providing blocking stresses of 42 and 19 MPa and stiffness tuning fields of 56 and 10 kA/m, respectively [63, 96, 47]. Compared to piezoelectrics, magnetostrictive materials offer some key advantages. Piezoelectrics are susceptible to depolling at elevated temperatures, which irreversibly deactivates the material. Additionally, the performance of piezoelectrics degrades over time. Conversely, magnetoelastic coupling is an inherent material property that is fully present when the temperature is below the material's Curie temperature. Irreversible changes usually

only result if melting occurs. Magnetostrictive materials can also survive millions of actuation cycles without adverse effects [115, 114].

Regarding a stiffness tuning device, the primary differences between Terfenol-D and Galfenol are their magnetostrictions, magnetic permeability, and mechanical strength. Terfenol-D offers magnetostrictions up to  $1600 \times 10^{-6}$ , but has a low relative magnetic permeability of 1.5 to 10 and a tensile strength of only 28 MPa [123, 85]. Terfenol-D's low strength restricts its use to 1D applications. On the other hand, Galfenol provides magnetostrictions of about  $350 \times 10^{-6}$ , but has a high relative magnetic permeability up to 650 and a steel-like tensile strength of 500 MPa [53, 18, 95, 93]. Galfenol is capable of withstanding tension, compression, shear, and impact loadings, allowing it to operate in 3D, load-bearing applications. Galfenol can also be conventionally machined to simplify its integration into passive systems.

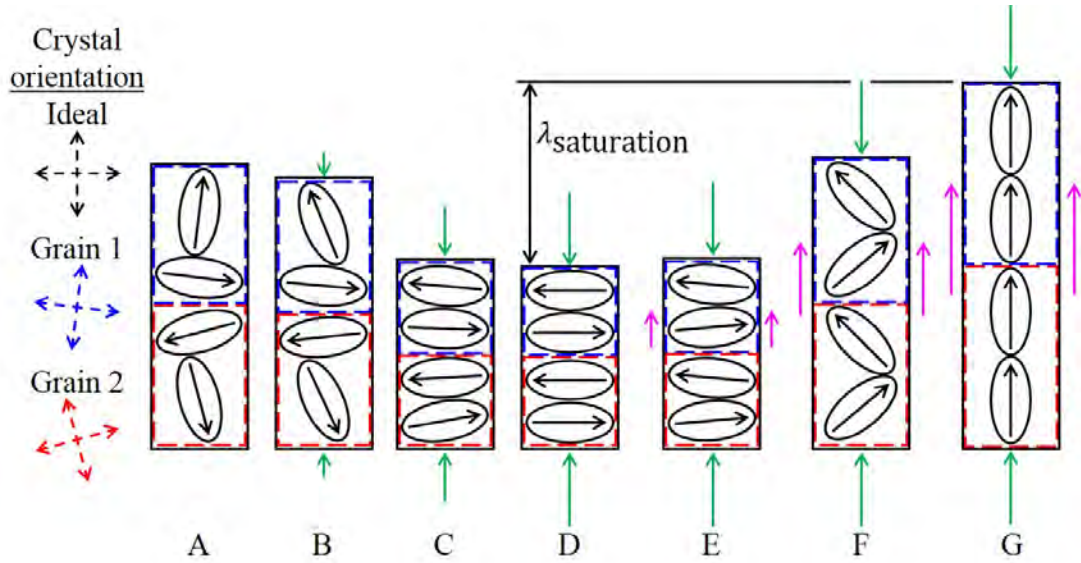


Figure 1.2: Schematic depiction of magnetoelastic coupling in a planar magnetostrictive material with positive magnetostriction.



Magnetoelastic coupling is depicted schematically in Fig. 1.2 for a planar magnetostrictive material that is composed of two crystals/grains and exhibits a magnetocrystalline anisotropy that favors domain alignment along two mutually orthogonal directions. For simplicity, the nonspherical electron cloud and magnetic moment orientation are represented by an ellipse and arrow, respectively. Due to the magnetoelastic coupling, the arrow is rigidly connected to the ellipse.<sup>5</sup> The ideal crystal orientation of each grain is coincident with the symmetry axes of the rectangular specimen. In practice, crystals are often slightly misaligned from the ideal orientation, as shown by the orientations of grains 1 and 2. In the unloaded state (A), magnetic domains align along the easy crystallographic directions (directions of minimum magnetocrystalline anisotropy energy) such that the magnetization of the specimen is minimized. Application of a small compressive stress (B) reorients domains away from the compression axis and towards a plane perpendicular to said axis; this reorientation continues as the compression increases to a large magnitude (C), at which point the domains jump to approximately the easy directions closest to the perpendicular plane. Under a very large compression (D), all domains have rotated into the perpendicular plane (complete mechanical saturation); however, the specimen's magnetization remains zero throughout (B) to (D). Application of a small field (E) reorients domains toward the field direction and away from an antiparallel direction. Rotation towards the field direction continues as the field is increased (F). At very large fields (G), the magnetocrystalline and stress-induced anisotropies are overcome and all domains align along the field direction (complete magnetic saturation). The

<sup>5</sup>In Fig. 1.2, a magnetostrictive material with positive magnetostriction is shown; thus, the arrow is oriented along the ellipse's major axis. A material exhibiting negative magnetostriction can be represented by an ellipse with an arrow oriented along its minor axis.

difference in strain from (D) to (G) is only caused by a 90 degree rotation of all of the magnetic moments. This strain denotes the maximum magnetoelastic response of the material; consequently, the strain is known as the saturation magnetostriction  $\lambda_{\text{saturation}}$  (or  $\lambda_{\text{sat}}$ ).

The elastic constants of magnetostrictive materials can be defined as

$$\mathbf{C}^{\mathbf{X}}(\mathbf{X}, \mathbf{T}) = \left. \frac{\partial \mathbf{S}}{\partial \mathbf{T}} \right|_{\mathbf{X}}, \quad (1.13)$$

where the partial derivatives can be evaluated at constant magnetization ( $\mathbf{X} = \mathbf{M}$ ), constant magnetic flux density ( $\mathbf{X} = \mathbf{B}$ ), or constant magnetic field ( $\mathbf{X} = \mathbf{H}$ ). Elastic constants specified as  $\mathbf{C}^{\mathbf{M}}$  were not found in the literature, because the magnetization cannot be directly measured, but must be inferred from measurements of  $\mathbf{B}$  and  $\mathbf{H}$ . Both Terfenol-D and Galfenol have cubic crystal symmetry, and can therefore be described mechanically by 3 independent elastic constants ( $c_{11}$ ,  $c_{12}$ , and  $c_{44}$ ).

The constitutive behavior of magnetostrictive materials is anisotropic, hysteretic, and nonlinear (see Fig. 1.3). The energy required to overcome material imperfections causes hysteresis (see the preceding subsection). Nonlinearity primarily results from magnetic saturation and anisotropy. As explained above, one form of anisotropy is the existence of easy directions, along which the material can be magnetized the easiest. The other main source is that the magnetostriction along certain directions is much larger than that along other directions. For example, the magnetostriction of Terfenol-D along the  $\langle 100 \rangle$  directions ( $\lambda_{100}$ )  $\approx 90 \times 10^{-6}$ , while along the  $\langle 111 \rangle$  directions ( $\lambda_{111}$ ) – its easy directions – it is  $\approx 1600 \times 10^{-6}$ . The easy directions in Galfenol are the  $\langle 100 \rangle$  family of directions.

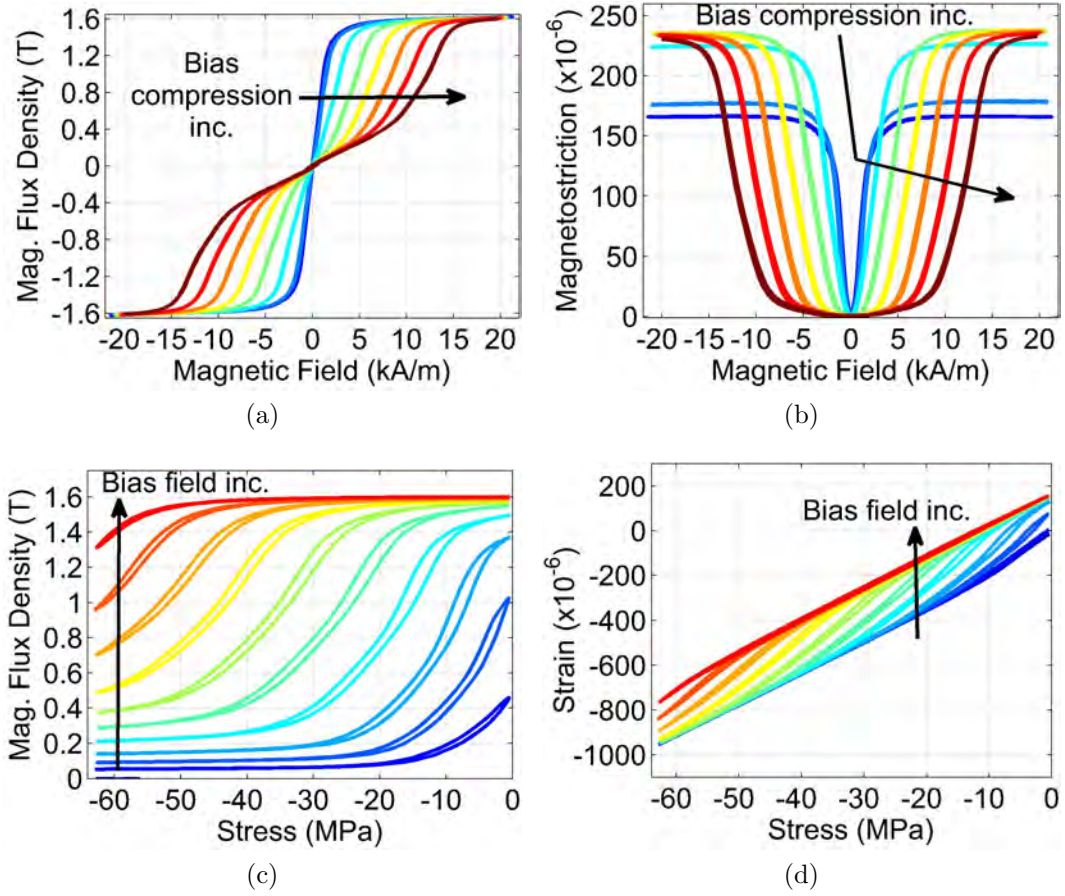


Figure 1.3: Measured quasi-static constitutive behavior of Fe<sub>81.6</sub>Ga<sub>18.4</sub> – (a),(b) axial actuation response at different constant compressive stresses, (c),(d) axial sensing response at different constant magnetic fields.

### Variable elastic moduli

In general, the only mechanism for a change in the elastic moduli of magnetostrictive materials is the rotation of magnetic moments [47], which causes magnetostriction (magnetoelastic strain). The total strain is a superposition of the elastic and magnetoelastic strains; thus, moment rotation causes an apparent reduction in the material's elastic moduli from their purely-elastic (magnetically-saturated) values

$\mathbf{C}_s$ . There are, however, a variety of conditions that lead to the rotation of moments, and thus a modulus change, including a change in magnetic boundary conditions, a change in AC magnetic field or stress amplitude (change in excitation), and a change in DC magnetic field or stress (change in operating point). The last condition is often referred to as the  $\Delta E$  effect (Fig. 1.4).

Constant field and constant induction denote the free and fixed magnetic boundary conditions, respectively. Thus, the Young's moduli  $E^B$  and  $E^H$  define the stiffest and softest elastic states of the material for a given excitation and operating point. Maintaining either condition requires a control system.  $E^B$  and  $E^H$  are related by the magnetomechanical coupling coefficient,  $k = k(\mathbf{H}, \mathbf{T})$ , which defines the fraction of magnetic or elastic energy that can be converted back and forth during the transduction process,

$$E^B = \frac{E^H}{1 - k^2}. \quad (1.14)$$

The difference between  $E^B$  and  $E^H$  increases as  $k$  increases. However, materials with high  $k$  have low magnetic permeabilities, making them difficult to magnetize [96]. Results by Calkins et al. [29] show that the efficiency of the transduction process increases as the AC field magnitude increases, thereby increasing the difference between  $E^B$  and  $E^H$ . Thus, for a given operating point or  $\Delta E$  effect, changes in the AC field magnitude will vary the elastic moduli [69]. The change in elastic modulus due to a change in magnetic boundary conditions is typically small compared to the  $\Delta E$  effect. Therefore, the  $\Delta E$  effect is the focus of the majority of work in the field.

At moderate to low AC stress amplitudes, reductions in the stress amplitude lead to a stiffening of the material, which reduces the  $\Delta E$  effect. The cause of this effect has yet to be identified, but is presently attributed to a lack of energy to rotate

magnetic moments away from energy wells [95, 96]. In Terfenol-D, this effect can be significant due to the material's large hysteresis, yet still smaller than the  $\Delta E$  effect [108, 29]. Although not measured in the literature, this effect is expected to be much smaller in Galfenol, as its hysteresis is comparatively small.

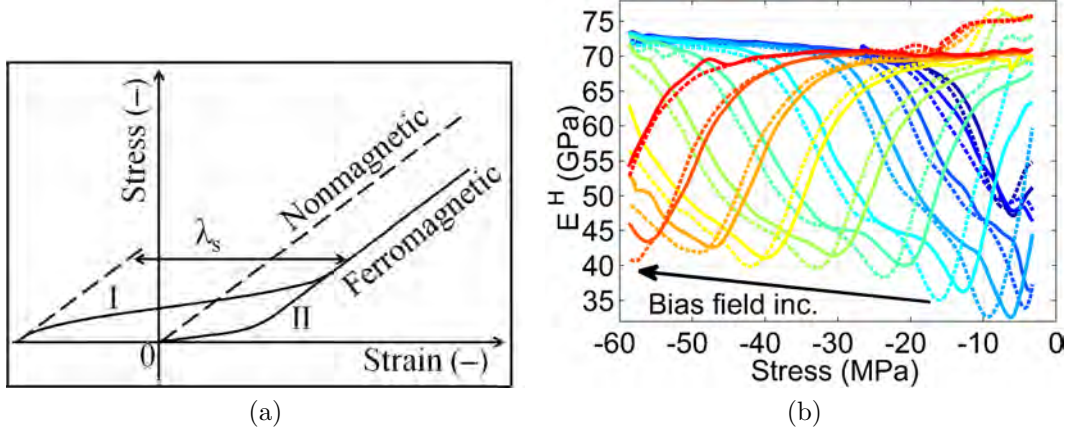


Figure 1.4: The  $\Delta E$  effect: (a) stress versus strain for (I) initially fully magnetized and (II) initially demagnetized ferromagnetic materials with positive maximum magnetostriction  $\lambda_s$ , (b) measured Young's modulus of  $\text{Fe}_{81.6}\text{Ga}_{18.4}$  in the [100] direction at multiple bias magnetic fields for a 1D, quasi-static stress input.

As the inputs to a magnetostrictive material, stresses and magnetic fields directly control the energy landscape that governs magnetic moment orientation. In the presence of deep energy wells, magnetic moment reorientation is hindered, limiting magnetostriction and maintaining a stiff elastic state. When shallow energy wells are present, even small perturbations in stress or magnetic field can cause magnetic moments to jump from one energy well to another. The material is elastically softened as magnetostriction can readily occur. Thus, the  $\Delta E$  effect is the primary source of stiffness tuning in magnetostrictive materials. The  $\Delta E$  effect is mathematically

defined as the difference in elastic modulus between two states, usually normalized by one of the moduli. No less than 7 different definitions have been used in the literature.

The conventional definition is

$$\Delta E = \frac{E_s - E_a}{E_a}, \quad (1.15)$$

where  $E_s$  is the modulus in the stiff (magnetically-saturated) condition, and  $E_a$  is the modulus in a demagnetized state [36, 39, 97]. When the applied field magnitude is limited (i.e., magnetic saturation cannot be reached), the following definition has been used,

$$\Delta E_{H_2H_1} = \frac{E_{H_2} - E_{H_1}}{E_{H_2}}, \quad (1.16)$$

where  $E_{H_1} = E(H_1) \geq E_{H_2} = E(H_2)$  [95, 96]. The most general and robust definition is

$$\Delta E(H, T) = \frac{E_s - E(T, H)}{E_s}, \quad (1.17)$$

where the effect is defined as a function of stress and magnetic field [47]. This definition has two key benefits: (a) it avoids the use of  $E_a$ , which is not the minimum modulus and is ambiguous, because its value depends on stress and there is not a unique demagnetized state [101], and (b) it normalizes with respect to the saturated modulus, which is a constant.  $\Delta E$  effects calculated using Eq. (1.17) are bounded between 0 and 100 %. Consequently, results from the proposed research will be presented using Eq. (1.17). Due to insufficient information provided in many references, Eq. (1.16) must be used to compare the  $\Delta E$  effects from across the literature.

Analytical expressions for the  $\Delta E$  effect Eq. (1.15) have been derived for ferromagnetic materials with  $\langle 100 \rangle$  easy magnetization directions (e.g., iron, Galfenol) and

$\langle 111 \rangle$  easy directions (e.g., nickel, Terfenol-D) [24, 26, 105],

$$\Delta E_{\langle 100 \rangle} = \frac{3}{20\pi} \frac{(\mu_i - 1) \lambda_{100}^2 E_s}{M_s^2}, \quad \Delta E_{\langle 111 \rangle} = \frac{\mu_i \lambda_{111}^2 E_s}{5\pi M_s^2} \left[ \frac{5c_{44}}{c_{11} - c_{12} + 3c_{44}} \right]^2, \quad (1.18)$$

where  $\mu_i$  is the initial relative magnetic permeability (i.e., at the demagnetized state), and  $M_s$  is the saturation magnetization. Eq. (1.18) shows that the effect depends on the square of the magnetostriction, the square of the saturation magnetization, and the ease with which the material is magnetized, which is measured by the initial magnetic susceptibility  $\chi_i = (\mu_i - 1)/4\pi$ . A directly-proportional dependence on the purely-elastic (magnetically-saturated) modulus  $E_s$  is intuitive, because in stiff materials, the magnetoelastic strain constitutes a larger fraction of the total strain.

### Constitutive modeling

Due to the diversity of active effects and the nonlinearities that magnetostrictive materials exhibit, modeling their behavior for arbitrary stress and magnetic field inputs is challenging. A wide range of models have been proposed. At one extreme, a phenomenological approach fits a curve or surface to the measurement data, which provides efficiency but ignores the underlying physics. At the other extreme, micromagnetic models consider all known energies and are very accurate. Macroscopic models use an intermediate approach by relating the macroscopic response of the material to simplified descriptions of the microscopic behavior. Macroscopic models therefore strike a balance between efficiency, accuracy, and predictive capability. The classical macroscopic models are the Preisach model [116], the Globus model [72], the Jiles-Atherton model [88], and the Stoner-Wohlfarth model [142]. Liorzou et al. [104] compares these models in detail.

Armstrong [3] proposed an incremental model for magnetoelastic hysteresis, which calculates the 3D bulk magnetization and magnetostriction as the expected values (via energy-weighted averaging) of a collection of non-interacting magnetic moments. The probability density function is a Boltzmann distribution, where minimum energy orientations are more probable. The Armstrong model [3], which considers eight fixed magnetic domain orientations, is only accurate when the input magnetic field or stress is aligned with an easy crystal direction. Atulasimha et al. [20] improved accuracy, at a significant computational cost, by considering 98 fixed orientations. Evans and Dapino [60] maintained a high level of accuracy while greatly reducing computational expense by considering the 6 (for Galfenol) or 8 (for Terfenol-D) directions that minimized the stress- and magnetic field-dependent enthalpy. Evans and Dapino [61] proposed a discrete energy-averaged (DEA) model, which appreciably improved efficiency with a minimal reduction in accuracy (relative to [60]) by separately minimizing the free energy defined locally about each easy crystallographic direction. For a more in depth review of the available constitutive models, refer to [63].

The efficiency improvements provided by the DEA model are crucial for the modeling of magnetostrictive systems, for which a large number of constitutive model executions are typically required at each time step. The DEA model is therefore used throughout this dissertation due to its unique combination of high accuracy and very high computational efficiency. The DEA model has been successfully used for the modeling of Galfenol-based systems of varying dimensionality [33, 137, 62, 154]. Section 1.2.2 summarizes this model and its improvements.



## Discrete energy-averaged constitutive models

Evans and Dapino’s DEA model [61] describes Galfenol as a collection of 6 non-interacting, mesoscopic magnetic domains that rotate in response to the inputs – the magnetic field vector  $\mathbf{H} = [H_1, H_2, H_3]^T$  and stress tensor  $\mathbf{T} = [T_1, T_2, T_3, T_4, T_5, T_6]^T$ , which is written in contracted vector notation<sup>6</sup>. The 6 directions  $\mathbf{m}^k$  are calculated by minimizing an energy function that is locally-defined about each of the 6 easy crystallographic directions, subject to the constraint  $\|\mathbf{m}^k\| = 1$ . The total free energy  $G^k$  of a magnetic moment in the vicinity of the  $k^{th}$  easy direction  $\mathbf{c}^k$  incorporates the local magnetocrystalline (anisotropy), magnetomechanical coupling (stress-induced anisotropy), and magnetic field (Zeeman) energies, which are given in Table 1.1, where the variables are defined in following two paragraphs.

Table 1.1: Energies of the magnetic domain orientations in the DEAM

Anisotropy	Magnetomechanical Coupling	Magnetic Field
$\frac{1}{2}K \left  \mathbf{m}^k - \mathbf{c}^k \right ^2 + K_0$	$-\frac{k}{\lambda} \cdot \mathbf{T}$	$-\mu_0 M_s \mathbf{m}^k \cdot \mathbf{H}$

The anisotropy energy constant  $K$  is the locally-defined analog of the fourth order crystalline anisotropy constant  $K_1$ , which is used to globally-define the anisotropy energy of magnetic materials with cubic symmetry. Mudivarthi et al. [109] has shown that the magnetomechanical coupling energy is equivalent to the sum of magnetoelastic, elastic, and mechanical work energies if  $K_1$  includes both intrinsic and

<sup>6</sup> $T_1 = T_{11}, T_2 = T_{22}, T_3 = T_{33}, T_4 = T_{12} = T_{21}, T_5 = T_{23} = T_{32},$  and  $T_6 = T_{13} = T_{31}$

magnetostriction-induced components. This condition is true for the majority of experimentally measured  $K_1$  (or  $K$ ), including those used in this dissertation.

The minimization procedure applied to Evans and Dapino's formulation requires as many matrix inversions as the number of easy directions. To reduce the number of matrix inversions to one, Chakrabarti [32] slightly modified the anisotropy energy. Accordingly, the Gibbs free energy can be written in matrix notation as

$$G = \frac{1}{2} \mathbf{m}^k \cdot \overline{\mathbf{K}} \mathbf{m}^k - \mathbf{b}^k \cdot \mathbf{m}^k + \frac{1}{2} K + K_0, \quad (1.19)$$

where  $K$  and  $K_0$  are anisotropy energy constants;  $\mathbf{m}^k = [m_1^k, m_2^k, m_3^k]^T$  is the magnetization direction having unit magnitude;  $k$  takes values  $\pm 1, \dots, \pm \frac{r}{2}$ ; and  $r$  is the number of easy crystallographic directions (the  $\langle 100 \rangle$  family of six directions for Galfenol). The magnetic stiffness matrix  $\overline{\mathbf{K}}$  and magnetic force vector  $\mathbf{b}^k$  are given by

$$\overline{\mathbf{K}} = K \mathbf{I} - 3 \begin{bmatrix} \lambda_{100} T_1 & \lambda_{111} T_4 & \lambda_{111} T_6 \\ \lambda_{111} T_4 & \lambda_{100} T_2 & \lambda_{111} T_5 \\ \lambda_{111} T_6 & \lambda_{111} T_5 & \lambda_{100} T_3 \end{bmatrix} \quad (1.20)$$

and

$$\mathbf{b}^k = K \mathbf{c}^k + \mu_0 M_s \mathbf{H}, \quad (1.21)$$

respectively, where  $\mathbf{I}$  is the  $3 \times 3$  identity matrix;  $\lambda_{100}$  and  $\lambda_{111}$  are magnetostriction constants;  $\mu_0$  and  $M_s$  are, respectively, the permeability of free space and saturation magnetization.

The macroscopic 3D magnetostriction  $\lambda$  and magnetization  $\mathbf{M}$  are defined as weighted sums of the response due to the  $r$  minimum energy directions,

$$\lambda = \sum_{k=\pm 1}^{\pm r/2} \xi_{an}^k \overline{\lambda}^k, \quad (1.22)$$

$$\mathbf{M} = M_s \sum_{k=\pm 1}^{\pm r/2} \xi_{an}^k \mathbf{m}^k, \quad (1.23)$$

where  $\xi_{an}^k$  and  $\bar{\boldsymbol{\lambda}}^k$  denote, respectively, the bulk anhysteretic volume fraction and the magnetostriction tensor written in vector notation for the  $k^{th}$  domain. Letting  $\Omega$  be a smoothing factor, the former is calculated as a Boltzman-type, energy-weighted average as

$$\xi_{an}^k = \exp \left( -\frac{G}{\Omega} \right) \sum_{j=\pm 1}^{\pm r/2} \exp \left( \frac{G}{\Omega} \right), \quad (1.24)$$

and the magnetostriction in tensor notation is given as

$$\begin{aligned} \bar{\lambda}_{ii}^k &= \frac{3}{2} \lambda_{100} m_i^k{}^2, & i, j = 1, 2, 3. \\ \bar{\lambda}_{ij}^k &= 3 \lambda_{111} m_i^k m_j^k, & i \neq j \end{aligned} \quad (1.25)$$

The strain tensor  $\mathbf{S}$  is given by the sum of the elastic and magnetoelastic strains,

$$\mathbf{S} = \mathbf{sT} + \sum_{k=1}^r \xi_{an}^k \bar{\boldsymbol{\lambda}}^k, \quad (1.26)$$

where  $\mathbf{s}$  is the compliance tensor.

*Calculation of  $\mathbf{m}^k$  (approximate solution)*

The application of an external magnetic field or stress changes the energy surface in the vicinity of each easy crystallographic direction, which may shift the  $k^{th}$  minimum energy direction away from the  $k^{th}$  easy direction. Thus, the unit magnitude, minimum energy directions  $\mathbf{m}$  are not known a priori for each easy direction, and must be calculated by minimizing the local free energies Eq. (1.19) before evaluating the volume fractions Eq. (1.24). Evans and Dapino[61] found an explicit solution that

approximately minimizes the energies Eq. (1.19), by formulating the constrained minimization as the following inhomogeneous eigenvalue problem through the application of the Lagrange multipliers method,

$$(\overline{\mathbf{K}} - \gamma \mathbf{I}) \mathbf{m}^k = \mathbf{b}, \quad (1.27a)$$

$$\mathbf{m}^k \cdot \mathbf{m}^k = 1, \quad (1.27b)$$

where  $\gamma$  is the unknown Lagrange multiplier corresponding to the  $k^{th}$  minimum energy direction, and  $\mathbf{I}$  is the  $3 \times 3$  identity matrix. In the absence of an explicit, analytical solution to the foregoing system of equations, Evans and Dapino [61] relaxed the normalization constraint through the approximation  $\mathbf{m} \cdot \mathbf{m} \approx \mathbf{c} \cdot \mathbf{m} = 1$  for each easy direction. As a result, the following explicit, approximate solution was reported:

$$\mathbf{m}^k \approx [\overline{\mathbf{K}}]^{-1} \left[ \mathbf{b} + \left( \frac{1 - \mathbf{c} \cdot [\overline{\mathbf{K}}]^{-1} \mathbf{b}}{\mathbf{c} \cdot [\overline{\mathbf{K}}]^{-1} \mathbf{c}} \right) \mathbf{c} \right]. \quad (1.28)$$

#### *Magnetomechanical hysteresis*

Hysteresis is implemented in an incremental form based upon an evolution equation for the volume fractions [61],

$$\Delta \xi^k(i) = (1 - c) \Delta \xi_{irr}^k(i) + c \Delta \xi_{an}^k(i), \quad (1.29)$$

where  $i$  is the increment index,  $c$  is a dimensionless constant quantifying the reversible processes during domain wall motion, and finally the change in the irreversible volume fractions for 3D stress and field inputs is defined as

$$\begin{aligned}
\Delta \xi_{irr}^k(i) = & \frac{\zeta}{k_p} (\xi_{an}^k(i) - \xi_{irr}^k(i-1)) \left[ \mu_0 M_s \sum_{p=1}^3 |\Delta H_p(i)| \right. \\
& \left. + (3/2) \lambda_{100} \sum_{p=1}^3 |\Delta T_p(i)| + 3 \lambda_{111} \sum_{q=4}^6 |\Delta T_q(i)| \right], \tag{1.30}
\end{aligned}$$

where  $\zeta$  is a binary number for avoiding a nonphysical negative susceptibility, and  $k_p$  is a pinning site density constant that characterizes the energy loss associated with domain wall rotation. Note that this hysteresis model is not self-starting, because the initial irreversible volume fractions are undefined. However, it is common practice to assume that  $\xi_{irr}(0) = 0$ .

#### *Calculation of $\mathbf{m}^k$ (exact solution)*

Linearization of the normalization constraint about each easy direction results in an explicit approximate solution, whose error is minimal since moments that have rotated far from the easy axes are more energetic, and thus less probable. Nonetheless, the approximate magnetization directions may significantly violate the unity norm constraint for large inputs. Post-normalization of the directions was proposed by Chakrabarti and Dapino [33], but the resulting directions can still deviate from the true energy minima for generic 3D inputs. Additionally, this solution procedure is prone to singularities, which could burden the computation, especially when the method is integrated into system-level models. The utility of such system-level models for use by non-experts is hampered if the model does not incorporate a black-box constitutive model that is valid for all inputs.

With the objective of developing a robust solution procedure for the DEA model that avoids singularities, Tari et al. [145] developed an analytical solution that exactly solves the constrained energy minimization. Additionally, Tari et al. [145] reformulated the DEA model based on the average of hysteretic data, as opposed to anhysteretic data, which would require additional measurements for parameter optimization and validation. As such, they employed the averaged hysteretic volume fractions, i.e.  $\bar{\xi}_{hys}$ , which correspond to the median curves obtained from averaging the hysteretic measurement data. Thus, every occurrence of  $\xi_{an}$  in the aforementioned equations is replaced by  $\bar{\xi}_{hys}$ . Tari et al. [145] also reformulated the magnetoelastic energy. Evans and Dapino[61] used the tensor-valued magnetostriction Eq. (1.25) given by Engdahl [58]. Instead, the more thorough formulation of Kittel [99] is used, which has a constant term not present in [58]. Kittel's expressions are given in tensor notation as

$$\begin{aligned}\frac{k}{\bar{\lambda}_{ii}} &= \frac{3}{2}\lambda_{100}(m_i^k)^2 - \frac{\overbrace{c_{12}}^{\triangleq c_0}}{c_{11} + 2c_{12}}, \\ \frac{k}{\bar{\lambda}_{ij}} &= 3\lambda_{111} m_i^k m_j^k, \quad i \neq j,\end{aligned}\tag{1.31}$$

where  $i, j = 1, 2, 3$ , and  $c_{11}$  and  $c_{12}$  are two of the three independent elastic moduli for crystals with cubic symmetry. Relative to Engdahl's equation used in the prior work, employment of Eq. (1.31) provides a better fit of the model to experimental data for the sensing case, as seen in [145].

Before deriving the exact solution procedure, Tari et al. [145] simplified the Gibbs free energy Eq. (1.19) as

$$\overset{k}{G} = \frac{1}{2} \overset{k}{\mathbf{m}} \cdot \mathbf{K} \overset{k}{\mathbf{m}} - \overset{k}{\mathbf{b}} \cdot \overset{k}{\mathbf{m}} + \overset{k}{K}_0 = \frac{1}{2} (\overset{k}{\gamma} - \overset{k}{\mathbf{b}} \cdot \overset{k}{\mathbf{m}}) + \overset{k}{K}_0, \quad (1.32)$$

where the simplified magnetic stiffness matrix is,

$$\mathbf{K} = -3 \begin{bmatrix} \lambda_{100} T_1 & \lambda_{111} T_4 & \lambda_{111} T_6 \\ \lambda_{111} T_4 & \lambda_{100} T_2 & \lambda_{111} T_5 \\ \lambda_{111} T_6 & \lambda_{111} T_5 & \lambda_{100} T_3 \end{bmatrix}. \quad (1.33)$$

The energy minimization problem becomes

$$(\mathbf{K} - \overset{k}{\gamma} \mathbf{I}) \overset{k}{\mathbf{m}} = \overset{k}{\mathbf{b}}, \quad (1.34a)$$

$$\overset{k}{\mathbf{m}} \cdot \overset{k}{\mathbf{m}} = 1. \quad (1.34b)$$

The exact solution is given as

$$\overset{k}{\mathbf{m}} = \mathbf{Q} (\mathbf{\Lambda} - \overset{k}{\gamma} \mathbf{I})^{-1} \mathbf{Q}^T \overset{k}{\mathbf{b}}, \quad (1.35)$$

where  $\mathbf{Q}$  is an orthogonal matrix containing the eigenvectors of  $\mathbf{K}$ ,  $\mathbf{\Lambda}$  is a diagonal matrix composed of the corresponding eigenvalues, i.e.  $\lambda_{1-3}$ , of  $\mathbf{K}$ , and  $\overset{k}{\gamma}$  is the given by the solution of a sixth order polynomial,

$$\begin{aligned} & \overset{k}{\gamma}^6 + 2(\bar{\lambda}_2 + \bar{\lambda}_3) \overset{k}{\gamma}^5 + (\bar{\lambda}_2^2 + 4\bar{\lambda}_2\bar{\lambda}_3 + \bar{\lambda}_3^2 - \bar{Q}_1 \\ & - \bar{Q}_2 - \bar{Q}_3) \overset{k}{\gamma}^4 + 2(\bar{\lambda}_2^2\bar{\lambda}_3 + \bar{\lambda}_2\bar{\lambda}_3^2 - \bar{\lambda}_2\bar{Q}_1 \\ & - \bar{\lambda}_3\bar{Q}_1 - \bar{\lambda}_3\bar{Q}_2 - \bar{\lambda}_2\bar{Q}_3) \overset{k}{\gamma}^3 + (\bar{\lambda}_2^2\bar{\lambda}_3^2 - \bar{\lambda}_2^2\bar{Q}_1 \\ & - 4\bar{\lambda}_2\bar{\lambda}_3\bar{Q}_1 - \bar{\lambda}_3^2\bar{Q}_1 - \bar{\lambda}_3^2\bar{Q}_2 - \bar{\lambda}_2^2\bar{Q}_3) \overset{k}{\gamma}^2 \\ & - 2\bar{\lambda}_2\bar{\lambda}_3\bar{Q}_1 (\bar{\lambda}_2 + \bar{\lambda}_3) \overset{k}{\gamma} - \bar{\lambda}_2^2\bar{\lambda}_3^2\bar{Q}_1 = 0, \end{aligned} \quad (1.36)$$

where  $\overset{k}{\gamma} = \lambda_1 - \gamma$ ,  $\bar{\lambda}_2 = \lambda_2 - \lambda_1$ ,  $\bar{\lambda}_3 = \lambda_3 - \lambda_1$ , and  $[\sqrt{\bar{Q}_1}, \sqrt{\bar{Q}_2}, \sqrt{\bar{Q}_3}]^T = \mathbf{Q}^T \overset{k}{\mathbf{b}}$ .

Eq. (1.36) can have up to six solutions. After eliminating complex solutions and solutions oriented sufficiently far from the corresponding easy direction, Tari et al. [145]

used the solution that minimizes most the Gibbs free energy. Simplification of the exact solution procedure for lower dimensional applications, parameter optimization, and validation of the model are presented in [145].

#### *Application of the DEA model to Terfenol-D*

When the original formulation of the DEA model is applied to Terfenol-D, unphysical kinks in the magnetization and magnetostriction responses appear and Terfenol-D's slow approach to saturation is absent [34]. Chakrabarti and Dapino [34] solved these problems by (a) adding an orientation-dependent global anisotropy energy to the existing local anisotropy energy and (b) redefining the constant smoothing factor  $\Omega$  as a function of field and stress. The latter modification makes the DEA model implicit, thereby increasing the model's computational expense by about 20 % due to need for convergence iterations [34]. Further, the redefined smoothing factor adds complexity to the hysteresis model and prevents the derivation of an analytical material Jacobian. Nevertheless, Chakrabarti and Dapino's model is very accurate, as evidenced by its mean modeling error of about 3 % [34].

Appendix A proposes a new approach to eliminate the aforementioned problems. The new approach, which is based on a simple coordinate transformation, retains the explicit nature and hysteresis model of the original formulation of the DEA model. Thus, the new approach is a faster alternative to the current art that provides an analytical material Jacobian.



### 1.2.3 Magnetostrictive transducers

This section briefly discusses magnetostrictive transducers, which are used for material characterization. Magnetostrictive transducers can also be implemented as actuators, sensors, and variable-stiffness devices, among other applications.

The simplest magnetostrictive transducer is a magnetostrictive rod surrounded by an electromagnet, which is required to generate variable magnetic fields. To reduce the current needed to produce a given field, a magnetically-permeable path connecting the ends of the rod is necessary. For material characterization or optimizing performance, magnetic and mechanical biasing mechanisms are vital. A magnetic bias is easily generated using a permanent magnet or DC current to the electromagnet. In Terfenol-D and Galfenol, compressive mechanical preloads are used to maximize the magnetostriction potential, while preventing unloading during high signal operation, which can damage brittle Terfenol-D specimens. For 1D transducers, the conventional method for creating the preload is to place a spring in parallel with the rod and series with the output shaft [95, 43, 41, 29]. Since the constitutive responses of both materials vary significantly with bias stress, the spring must be carefully designed to minimize changes in the bias force over the deflection range of the transducer. Consequently, softening Belleville springs are commonly used and operated at near max deflection, where their stiffness is very small. A consequence of larger compressive preloads is the need for larger magnetic fields, and thus larger electromagnets and more powerful amplifiers.

The performance of Terfenol-D degrades as temperature increases [95]. As a result, high performance transducers often require active cooling of the drive electronics or magnetostrictive specimen. Compressed air and water cooling have been used [95, 96].

This constraint is less severe for Galfenol, which exhibits limited variation in its active properties from -20 to 80 °C [94].

The vast majority of researchers measure the force, strain, magnetic field, and magnetic flux density using load cells, strain gauges, Hall effect sensors, and integrations of the voltage induced in sensing coils, respectively.

#### **1.2.4 Autoresonant control**

This section introduces autoresonant control, which is a technique for reaching and maintaining a resonant state of a dynamic system. In this dissertation, autoresonant control is used as a numerical technique to vastly decrease the computation time of parametric studies.

Autoresonant feedback control was born from the study of vibro-impact systems, which are designed to operate near resonance [23]. Conventionally, the frequency of the excitation is controlled and a resonant state is reached by exciting the system at the resonant frequency. In high quality factor (Q-factor) systems (i.e., lightly damped systems), resonance is very sensitive to changes in the system's parameters and inputs, and occurs at the boundary of stability for some linear systems and for frequency-controlled excitation of nonlinear systems; consequently, very fine control of the excitation frequency is needed to actively track resonance and avoid the jump phenomenon (Fig. 1.5a) that results from the stability issue.

An alternative to frequency-controlled excitation is phase-controlled excitation. After providing the system with an arbitrary initial condition, phase-controlled excitation achieves self-sustained vibration by feeding the actuator that drives the system with a phase-shifted and amplified signal of the system's vibration. Stability

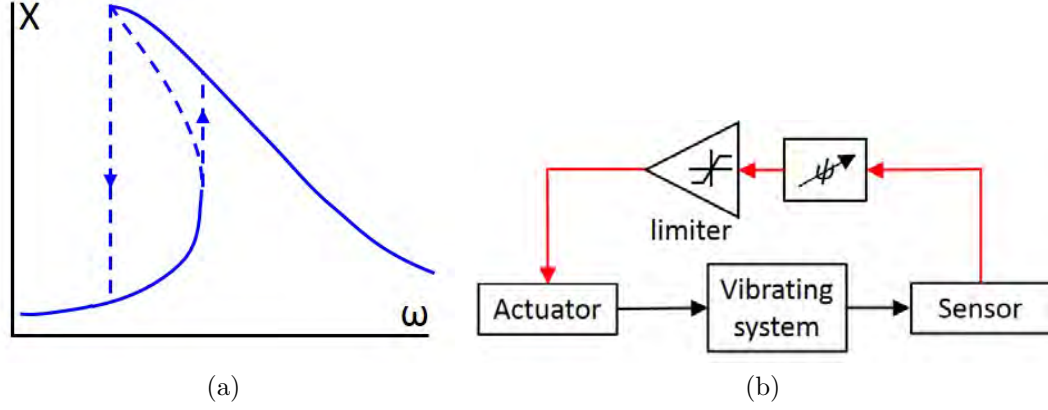


Figure 1.5: (a) jump phenomenon observed during frequency-controlled excitation of a nonlinear system and (b) simple phase-controlled system (phase-controlling feedback shown by the red arrows); images adapted from [140].

is maintained by limiting the magnitude of the feedback signal. Amplitude versus phase curves govern the vibration of phase-controlled systems, with frequency acting as a dependent variable. Sokolov and Babitsky [140] detailed the characteristics of single- and two-degree-of-freedom autoresonant systems, showing the flatness and single-valuedness of the amplitude versus phase curves that govern phase-controlled systems. As such, jump phenomenon is eliminated for most systems and fine control of the phase is unnecessary.

When the phase shift  $\phi$  is made to coincide with the phase that maximizes the amplitude-phase curve ( $\phi^*$ ), the system becomes autoresonant and maintains a resonant state under changes in the system's natural frequency [140], which result from

changes in the system's parameters or the operating conditions. Stability of the resonant state is again achieved by limiting the magnitude of the feedback signal<sup>7</sup>. The amplitude of the resonant vibration is controlled by varying the limitation level.

The autoresonant phase shift  $\phi^*$  is in general a function of the level of damping. For the case of hysteretic material damping, the energy dissipation per vibration cycle (damping capacity) is independent of the frequency of vibration. Consequently, the resonant frequency is equal to the undamped natural frequency and is independent of the magnitude of damping [52]. This is the ideal case for realizing autoresonant control, because, for a linear system, the resonance of each mode will occur when the excitation is in phase with vibratory velocity. If sufficient modal separation exists and the forcing is independent of frequency, then  $\phi^*$  is approximately  $-\frac{\pi}{2}$  or  $-\frac{3\pi}{2}$  for all modes and any level of damping. The damping capacity for viscoelastic material damping and linear viscous damping depends on frequency; these models of damping can be respectively used to describe the mechanical damping (as done in Section 2.2.2) and eddy current damping (i.e., frequency-dependent magnetic hysteresis) that occur in magnetostrictive materials. As a result, the resonant frequency (and therefore  $\phi^*$ ) will depend on the level of damping.

Autoresonant feedback control has been utilized in various applications, but primarily for ultrasonically-assisted machining [151]. Recently, Twiefel [148] numerically applied autoresonant feedback control to efficiently conduct parametric studies on the mode shape of a piezoelectric beam. In Section 2.2.2, autoresonant feedback control is used as a numerical technique to significantly reduce the computational expense of

<sup>7</sup>This is true except for systems with amplitude-phase curves that tend to infinity at resonance or nonlinear systems that have a negative restoring force for large displacements [140]

parametric studies by automatically tracking the resonance of a Galfenol composite beam under prescribed changes in the bias condition and excitation magnitude.

### **1.3 Literature Review**

This section summarizes the previous work completed in the characterization and dynamic modeling of magnetostrictive materials and transducers in relation to stiffness tuning.

#### **1.3.1 Magnetic diffusion**

The effects of 1D mechanically-induced magnetic diffusion have been briefly studied numerically [121, 42, 49]. Notably, Sarawate and Dapino [121] investigated the magnetic field in a Ni–Mn–Ga rod and illustrated the dependence of the field’s time domain response on radial coordinate and strain frequency for a small range of parameters. 1D mechanically-induced magnetic diffusion has been analytically treated in the context of magnetostrictive energy harvesters by Davino et al. [50], who derived an expression for average harvested power, and by Zhao and Lord [160], who derived an expression for the effective internal magnetic field. However, the spatial and frequency dependence of the internal magnetic field or magnetic flux density have not been derived. Further, a skin depth and cut-off frequency for this effect are absent from the literature.

#### **1.3.2 Delta E effect**

A number of methods have been used to measure the elastic moduli of magnetostrictive materials, including strain-stress, acoustic, electroacoustic, and lumped parameter modeling techniques.

The most common method is calculating the slope of strain responses to 1D, quasi-static stresses having small ( $\approx 10$  MPa or less) or large ( $\approx 20$  MPa or more) amplitude, referred to as minor or major hysteresis loops, respectively. Reported measurements include the minor loop [96] and major loop [108, 96] responses of Terfenol-D and the major loop responses of Galfenol [143, 157, 97, 22, 19, 21, 156, 47, 120]. Minor loop strain versus stress responses of Galfenol have not been reported. Major and minor loops can be measured at constant current to the electromagnet or at constant magnetic field. The former is easy to realize, but incorporates the response of the magnetic circuit in the measured response, while the latter requires feedback control, but provides a direct measure of the constitutive response. This method benefits from having a well defined and controllable stress input and from its low frequency excitation, for which magnetic diffusion is negligible. One drawback is the noise-amplifying differentiation required to calculate the moduli. This drawback has been mitigated by calculating slopes from polynomial fits of data subsets [156, 47, 120], in one case preceded by a moving average technique [154].

Other researchers have used acoustic techniques like ultrasonic velocity measurements [36, 39] and resonant ultrasound spectroscopy [37, 113], which are capable of measuring all 3 independent elastic constants from a single specimen. However, Clark et al. [36] noted a 17 % difference between elastic moduli measured using ultrasonic velocity measurements and static stress-strain curves. Furthermore, incorporating the effects of AC and DC stresses is challenging.

The Young's modulus of magnetostrictive materials can also be calculated from the electrical response of the solenoid used to magnetically excite the material [123, 30, 41, 29, 43]. This technique is known as the dynamic method, because it provides

a measure of the material’s behavior under dynamic operating conditions. Specifically, the modulus is calculated from electrical impedance and admittance frequency responses with the aid of a transducer model that couples electroacoustics theory with linear constitutive equations and a single-degree-of-freedom mechanical model. A variety of important material properties can be calculated from relatively simple measurements. As noted by Savage et al. [123], a problem of this method is the presence of flux leakage (i.e., magnetic flux passing through the drive coil, but not the sample), which is especially important for Terfenol-D due to its low magnetic permeability. Use of the voltage induced in a sensing coil instead of the voltage drop across the drive coil has been found to overcome this issue [123, 30]. The primary problem with this method is its reliance on the accuracy of the 1D, linear transducer model. The presence of losses (i.e., hysteresis, eddy currents, viscoelasticity) or spurious mechanical resonances of transducer parts can cause inaccuracies. Further, the linearity assumption is only valid for low signal operation (see Fig. 1.3).

Kellogg and Flatau [95] directly calculated the stiffness and elastic modulus of a Terfenol-D rod from displacement transmissibility frequency responses using the analytical response of a two-degree-of-freedom, base-excited mechanical model. Similar to the dynamic method, this technique relies on a linearity assumption, but still has value for some cases.

An exhaustive summary of the  $\Delta E$  effect measured in Terfenol-D and Galfenol is presented in Table 1.2, along with select measurements of other magnetostrictive materials. Clearly, the conventional and natural materials have limited usefulness for stiffness tuning. The performance of Metglas is attractive, but the material is manufactured in micron-thick sheets. Although bulk geometries can be made by

Table 1.2: A comparison of measured  $\Delta E$  effects for a variety of magnetostrictive materials, calculated using Eq. (1.16).

Material Class	Material	$ \Delta E $ , %
Conventional	Ni	19.1 [83], 21.0 [36]
	W steel	0.7 [83]
	Fe-rich Ni steel	0.5 [83]
	Ni-rich Ni steel	25.2 [83]
Metglas	Fe <sub>40</sub> Ni <sub>38</sub> Mo <sub>4</sub> B <sub>18</sub>	38.6 [2]
	Fe <sub>78</sub> Si <sub>9</sub> B <sub>13</sub>	180 [2]
Other rare-earth	Tb <sub>1</sub> Fe <sub>2</sub>	88.1 [36]
	Tb <sub>0.67</sub> Dy <sub>0.33</sub>	480 [38]
Terfenol-D	Tb <sub>0.3</sub> Dy <sub>0.7</sub> Fe <sub>1.93</sub>	100 [108]
	Tb <sub>0.3</sub> Dy <sub>0.7</sub> Fe <sub>1.95</sub>	266 [95], 414 [96]
	Tb <sub>0.3</sub> Dy <sub>0.7</sub> Fe <sub>2</sub>	144 [123], 161 [39]
Galfenol	Fe <sub>84</sub> Ga <sub>16</sub>	117 [47]
	Fe <sub>81.6</sub> Ga <sub>18.4</sub>	270 [156], 90 [156], 60.9 [120]
	Fe <sub>81</sub> Ga <sub>19</sub>	168 [47], 104 [97], 40 [22]
	Fe <sub>75.3</sub> Ga <sub>24.7</sub>	8 [22]

laminating many sheets, the structural integrity of these forms under compression is unclear. The  $\Delta E$  effect of TbDy only reaches the order of magnitude in Table 1.2 at cryogenic temperatures, where its magnetostriction is significantly larger than near room temperature [69]. Thus, Galfenol and Terfenol-D are the materials of interest. The  $\Delta E$  effect for specific alloys can be seen to vary significantly. The primary cause is a difference in the conditions under which the moduli were reported, however variations in the material's texture, material processing conditions, magnetic permeability, and saturation magnetostriction can contribute. This also illustrates a drawback of the  $\Delta E$  effect definition Eq. (1.16) used in the table.



### 1.3.3 Dynamic behavior of Terfenol-D and Galfenol

The design of magnetostrictive transducers that can dynamically tune their stiffness requires knowledge of the magnetostrictive material's constitutive behavior under dynamic operating conditions. This knowledge is also critically important for the validation of rate-dependent constitutive models [153]. The Young's modulus, coupling coefficient, and damping ratio of Galfenol rods have been calculated from electrical responses to controlled dynamic currents [147]; however, this electrically-controlled method relies on a linear piezomagnetic model relating electrical and mechanical domains. Besides the potential inaccuracy of linear models, this method cannot quantify the frequency dependence of material properties. Weng et al. [155] measured the magnetization of a Galfenol rod subjected to dynamic stress. However, only one bias condition and frequencies up to 10 Hz were considered. Ishimoto et al. [86] measured the damping capacity of Galfenol under dynamic stress, but the forcing frequency was limited to 10 Hz. Walker [152] measured flux density versus dynamic stress minor loops at a single bias point for forcing frequencies of 10 to 1000 Hz. As frequency increased, hysteresis was nearly constant, while sensitivity decayed monotonically. Strain responses were not presented and the force magnitude was limited to 3 MPa due to experimental limitations. These references also neglected their sensor signals' phase misalignment versus frequency, which significantly increases the uncertainty of energy loss calculations. No other measurements of Terfenol-D's or Galfenol's constitutive behavior in response to dynamic forces were found.

### 1.3.4 Magnetostrictive tunable stiffness devices

Ashour and Nayfeh [4] and Duan and Or [57] developed active and semi-active vibration absorbers using Terfenol-D and Terfenol-D/epoxy composite actuators, respectively. Neither author used the stiffness tuning property of Terfenol-D, but rather its actuation capability. Flatau et al. [69] and Pagliarulo et al. [112] harnessed the tunable stiffness of Terfenol-D rods to create semi-active AVAs whose axial resonant frequencies could be quasi-statically decreased by 30 and 13 %, respectively. Due to the use of Terfenol-D, these devices were relatively large to accommodate the rod geometry and a sizeable electromagnet. Hiller et al. [81] and Bryant et al. [28] used Terfenol-D actuators as active vibration isolators, demonstrating 50 and 82 % attenuations, respectively, of the disturbance vibration amplitude at low frequencies (10 to 70 Hz).

Many researchers have proposed models for magnetostrictive transducers (e.g., [138, 46, 44, 35, 62, 27]). Contributions to this field are primarily due to improvements to constitutive models. Others have modeled the dynamic behavior of beams containing Galfenol sheets or Terfenol-D particles, with focuses on dynamic actuation for positioning [136, 137] or for active vibration control [161]. The  $\Delta E$  effect and stiffness tuning were rarely mentioned in this body of work. AVAs based on magnetostrictive composites have not been studied.

Dapino et al. [45] modeled the shift in the 1st axial resonant frequency of a Terfenol-D rod due to changes in the bias magnetic field. The resonant frequencies were calculated from Fast Fourier Transformations of time domain impact responses at constant magnetic fields. The time domain model is based on a distributed parameter model of the rod's axial vibration, where the magnetostriction takes the form of

an internally-applied force. The model was shown to be only qualitatively accurate, due in part to the use of a phenomenological magnetostriction model and a constant elastic modulus of the rod.

Jin et al. [90] calculated the 1st axial resonant frequency of a Terfenol-D transducer as a function of magnetic field, stress, and temperature by coupling a distributed parameter axial vibration model with a 3D, nonlinear constitutive model, which was derived from Taylor series expansions of thermodynamic relations for strain, entropy, and magnetic field. The calculated resonant frequencies agreed qualitatively with measurements of a Metglas alloy.

Fukada et al. [71] presented a simple model for a novel method of semi-active stiffness control that accomplishes tuning by connecting the electromagnet surrounding a magnetostrictive rod to inductive loads of different positive and negative inductance. This is analogous to the use of negative capacitive loads to change the electrical boundary condition, and thus mechanical stiffness, of piezoelectric materials [111]. Although a linear constitutive model with constant material properties was used, limited yet promising modeling results show that stiffening on the order of 100 % as well as negative stiffness are possible.

## **1.4 Research Objectives and Outline**

The literature review shows the availability of a significant body of work regarding the measurement of quasi-static stiffness changes in magnetostrictive materials. However, the elastic response of Galfenol to small amplitude quasi-static stresses has not been reported. A select number of models and vibration control devices that

consider or utilize this effect for quasi-static tuning have also been presented. Although, Galfenol-based tunable stiffness devices have not been investigated, despite Galfenol’s unique mechanical robustness. Also, a critical aspect of magnetostrictive variable stiffness devices (as well as energy harvesters and dynamic sensors) – the constitutive behavior under dynamic stresses – has been largely neglected. Further, dynamic stiffness tuning of magnetostrictive materials is an undiscovered field, in spite of its importance and potential contribution to vibration control. Hence, the objectives of this research are to

- study the stiffness tuning response of Galfenol-based adaptive vibration absorbers through the development and application of nonlinear dynamic models that describe their mechanical vibration response,
- investigate the effect of dynamic stress on the constitutive behavior of and magnetic diffusion in ferromagnetic materials,
- experimentally characterize Galfenol’s response to dynamic, compressive stress, including the frequency dependence of its sensitivity and Young’s modulus,
- and model, design, test, and apply a magnetostrictive device that can electrically switch its stiffness at high speeds (up to 1 kHz).

The structure of this dissertation follows the objectives in order. Chapter 2 considers static stiffness changes in Galfenol. First, the minor loop strain response of the most common Galfenol alloy,  $\text{Fe}_{81.6}\text{Ga}_{18.4}$ , to quasi-static compressive stress is measured; from these measurements, Galfenol’s Young’s modulus is calculated and then studied to ascertain its variation with respect to stress and the applied bias magnetic field. Second, the stiffness tuning response of Galfenol beam adaptive vibration

absorbers is investigated using lumped parameter and distributed parameter models that are derived by incorporating Galfenol's nonlinear, stress- and magnetic field-dependent Young's modulus into classical mechanical vibration equations. Chapter 3 focuses on stress-induced dynamic effects in magnetostrictive materials. First, linear and nonlinear mechanically-induced magnetic diffusion in cylindrical ferromagnets is studied by deriving analytical and numerical solutions, respectively, of Maxwell's equations. Second, precise measurements of Galfenol's response to dynamic, compressive stress are presented along with a novel experimental design, wherein a detailed discussion of specimen design, sensor selection, uncertainty analysis, calibration, error sources, and data processing methods is included. Chapter 4 investigates the dynamic tuning of stiffness in magnetostrictive materials. First, a magnetostrictive device that can dynamically vary its stiffness is modeled, designed, and tested. Second, a case study is reported to illustrate the use of a dynamically-tunable magnetostrictive spring for switched stiffness vibration control of a single-degree-of-freedom mechanical system. Finally, Chapter 5 summarizes the research and discusses its contributions to the state-of-the-art. This chapter also identifies future work that can build upon the research contained herein.

## Chapter 2: Static Stiffness Change

In this chapter, the dependence of Galfenol’s minor loop elastic modulus on bias stress and bias magnetic field is measured. This understanding is then applied to the modeling of adaptive vibration absorbers composed of Galfenol-based metal-matrix composite beams.

### 2.1 Quasi-Static Elastic Response of Galfenol

As discussed in Section 1.3.2, the existing body of experimental work provides a thorough understanding of the major loop mechanical response of Galfenol alloys, particularly the effect of stoichiometry on the response. However, strain versus stress minor loops and a comprehensive comparison of constant current and constant field bias conditions have not been reported. Further, the elastic response of laminated Galfenol specimens, which are necessary for high frequency operation, is absent from the literature.

In this section, major and minor strain versus stress and Young’s modulus responses of a solid, research grade,  $\langle 100 \rangle$  oriented, polycrystalline  $\text{Fe}_{81.6}\text{Ga}_{18.4}$  rod are reported for constant current and constant field conditions. For comparison, major loop, constant current responses of a laminated specimen are also presented.

Major and minor loops were obtained for 1 Hz, 31.4 MPa and 4 Hz, 2.88 MPa amplitude sinusoidal stresses, respectively. Constant currents up to 1 A and constant fields up to 13.8 kA/m were considered, because this Galfenol alloy is most sensitive to stress for bias fields below 10 kA/m [154]. Evans and Dapino’s DEA constitutive model [60, 61] (summarized in Section 1.2.2) was fit to the experimental data to facilitate the use of the presented measurements for the design, optimization, and control of Galfenol-based systems. The model exhibits errors of 1.22 % and 1.02 % relative to constant current and constant field measurements, respectively, using the reported optimized model parameters.

The research in this section was conducted in collaboration with Zhangxian Deng, who lead the modeling work and helped analyze the data.

### **2.1.1 Experimental design and setup**

Solid and laminated cylindrical specimens were cut from a single  $\langle 100 \rangle$  oriented, polycrystalline  $\text{Fe}_{81.6}\text{Ga}_{18.4}$  bulk rod, which was grown by ETREMA Products, Inc. as discussed in Section 3.2.1. Each rod had a diameter of 6.35 mm (0.25 in) and a length of 76.2 mm (3 in). The laminates of the laminated rod were 0.84 mm (0.033 in) thick. The magnetic bias was applied by the symmetric electromagnetic transducer shown in Figs. 3.16 and 3.22(a), which generates a uniform magnetic state in the gauge region of the specimen while allowing for independent mechanical excitation. This transducer has been successfully used in previous research [154]. The electromagnets were driven by an AE Techron LVC5050 linear amplifier operated in controlled current mode. Axial stress was applied by a MTS 831.50 dynamic load frame operated in force

control mode using a MTS 793 FlexTest GT controller. Axial force was measured with an Interface 1010ACK-500-B load cell.

The magnetic flux density was measured using a Lake Shore 480 fluxmeter and custom pick-up coil, which was located in the center of the gauge region. The bias magnetic field was measured at the surface of the rods using an Allegro A1321LUA Hall chip. A dSPACE DS1103 board programmed for PI control was used to maintain a constant magnetic field throughout the stress cycle. The magnetic field was typically held within  $\pm 0.0125$  kA/m and  $\pm 0.004$  kA/m of the bias field for major and minor loops, respectively [129]. Comparatively, quasi-static constant field experiments by Wun-Fogle et al. [156] exhibited magnetic field variations of  $\pm 0.079$  kA/m (typical) to  $\pm 0.79$  kA/m (maximum). Bias current variation during constant current testing was typically less than 0.03 mA [129]. Axial strain was quantified by averaging the strain measured by a pair of Vishay Micro-Measurements EA-06-250BF-350/L strain gauges oriented along the axis of the rod and installed on opposite sides of the rod.

The sensors were calibrated as described in Appendix C.2, except for the pick-up coil, which was calibrated by measuring the static magnetic field generated between the poles of a large electromagnet using the pick-up coil and a calibrated Hall effect sensor. An uncertainty analysis of each measured quantity is detailed in Appendix C.1. Measurement signals were phase aligned in post processing by correcting for the phase response of the conditioning electronics, as explained in the **Phase calibration** subsection of Section 3.2.4.

The testing procedure included the application of a bias field (or current) followed by the bias force, after which 1 Hz, 31.4 MPa amplitude (for major loops) or 4 Hz, 2.88 MPa amplitude (for minor loops) sinusoidal compressive stress was applied until



a steady-state response was observed. Responses were recorded for constant currents of 0 to 1 A in 0.1 A increments and constant fields of 0.73, 1.42, 2.41, 3.88, 5.50, 7.17, 8.84, 10.51, 12.19, and 13.76 kA/m (the fields generated by each bias current under zero force). Minor loops were measured for nominal bias stresses of -41.6 MPa to -5.7 MPa in 7.2 MPa steps, where negative values denote compression.

## 2.1.2 Results and discussion

The DEA model was separately optimized to the constant field and constant current major loop responses of the solid Galfenol rod as discussed in [154]. The modeling error  $E_r$  was quantified as

$$E_r = \frac{1}{2N} \left( \frac{\|B_m - B_d\|}{\text{range}(B_d)} + \frac{\|S_m - S_d\|}{\text{range}(S_d)} \right), \quad (2.1)$$

where  $N$  is the number of data points in a single loop,  $B$  is the magnetic flux density,  $S$  is the strain, and the subscripts m and d denote modeled and measured quantities, respectively [32, 154].

### Solid rod: major strain versus stress loops under constant field

A comparison of the experimental and simulated strain versus stress responses of the solid Galfenol rod is given in Fig. 2.1. To enhance the optimization of the model and further illustrate the fit, flux density versus stress responses are also considered. There is extremely close agreement between the model and the data, with an average modeling error of 1.02 %. The optimized model parameters, shown in Table 2.1, closely fit results from the literature [143, 156, 65].

Galfenol exhibits a very high degree of kinematic reversibility (i.e., the order of application of stress and magnetic field does not matter) [65, 154]. To provide

Table 2.1: Optimized model parameters for the DEA model.

$K$ , kJ/m <sup>3</sup>	$K_0$ , kJ/m <sup>3</sup>	$\lambda_{100}$ , $\times 10^{-6}$	$\lambda_{111}$ , $\times 10^{-6}$	$\mu_0 M_s$ , T
18.78	0.03	157.93	N/A	1.58
$\Omega$ , J	$k_p$ , J	$c$	$E_s$ , GPa	
1024.50	381.78	0.82	72.04	

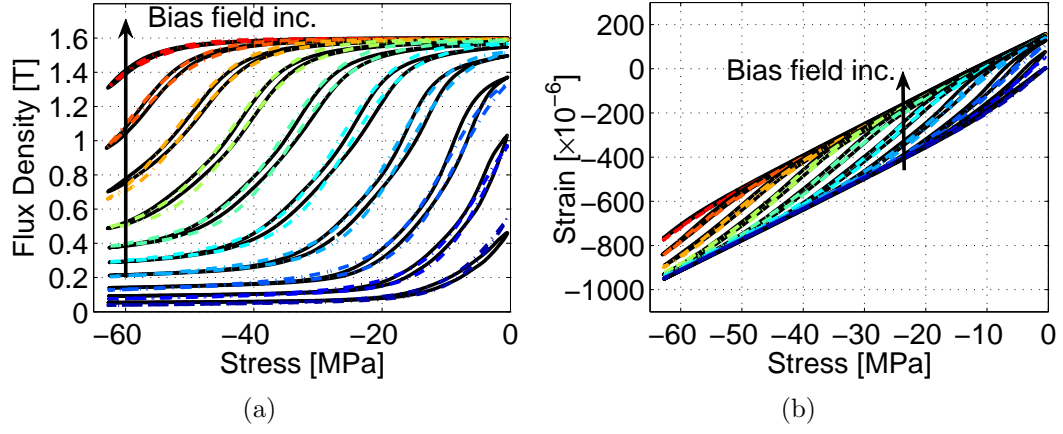


Figure 2.1: Comparison of the experimental (solid) and modeled (dashed) sensing responses of the solid  $\text{Fe}_{81.6}\text{Ga}_{18.4}$  rod to 1 Hz sinusoidal compression for constant magnetic fields of 0.73, 1.42, 2.41, 3.88, 5.50, 7.17, 8.84, 10.51, 12.19, and 13.76 kA/m: (a) magnetic flux density versus stress and (b) strain versus stress.

confidence in the experimental setup, reversibility was evaluated by measuring the actuation response of the solid rod in addition to its sensing response [129]. As seen in Fig. 2.2, the actuation points obtained from sensing curves almost mirror the directly measured actuation curves, which is consistent with reversibility measurements in prior work [65, 154].

The macroscopic strain consists of elastic deformation, which varies linearly with stress, and magnetostriction, which depends on the relative magnitude of magnetic,

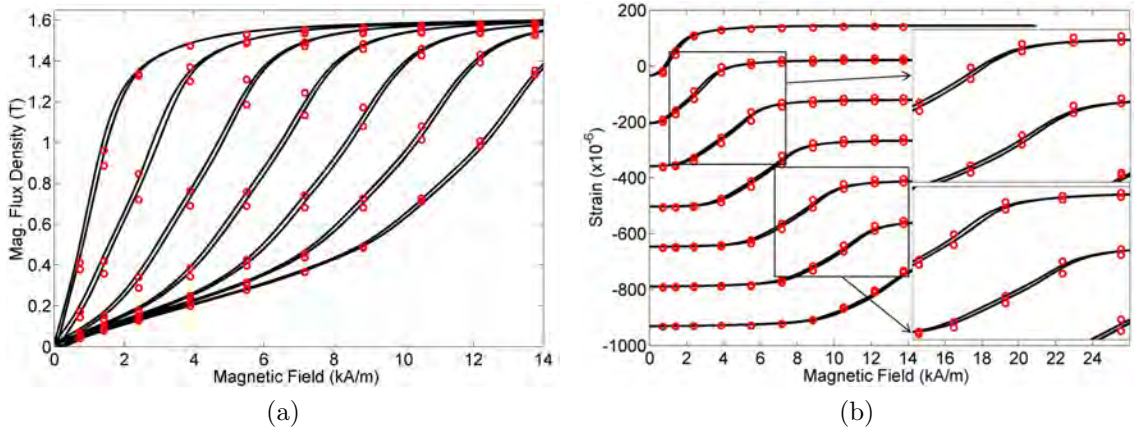


Figure 2.2: Comparison of the actuation responses of the solid Galfenol rod measured directly (solid black lines) and obtained from the sensing responses at constant field (red circles): (a) flux density versus field and (b) strain versus field.

mechanical, and magnetomechanical coupling energies. There are two saturation regions in which magnetostriction does not occur: (a) magnetic field-induced saturation, when the magnetic field energy dominates the total free energy and causes alignment of magnetic domains along the rod's axis, and (b) stress-induced saturation, when the magnetomechanical coupling energy dominates and moments are forced to lie in the basal plane. The burst region, where elastic deformation and magnetostriction occur simultaneously, denotes a transition between the two saturation states. In the burst region, the free energy terms have similar magnitude and magnetic domains are free to rotate. As the bias field increases, the location of the burst region shifts to larger compressive stress, because a larger mechanical energy is required to balance the increased magnetic energy.

The Young's modulus of the solid rod at constant field (Fig. 2.3) was calculated as the inverse of the slope of the measured strain versus stress responses. To mitigate

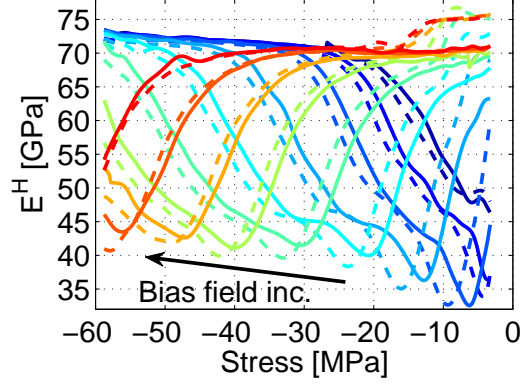


Figure 2.3: Young's modulus of the solid  $\text{Fe}_{81.6}\text{Ga}_{18.4}$  rod (from major loops) for a bias stress of -31.9 MPa and constant bias fields of 0.73, 1.42, 2.41, 3.88, 5.50, 7.17, 8.84, 10.51, 12.19, and 13.76 kA/m; color changes from blue to red as the bias field increases; decreasing stress (dashed) and increasing stress (solid).

the noise amplification from numerical differentiation, small sections of each curve were fit by 4th order polynomials, which were analytically differentiated to calculate the slope at the center of each section [154, 120, 47, 156]. A 75 % overlap of adjacent sections was used to smoothen the modulus curves. As seen in Fig. 2.3, the modulus for a given constant field is stress dependent. The location of the minimum modulus follows the center of the burst region, shifting to larger compression as the bias field is increased. The magnitude of the minimum modulus increases with increasing bias field, as observed and explained by Datta et al. [47]. The minimum Young's modulus is about 32.53 GPa and occurs at 2.41 kA/m and -6.25 MPa. According to Eq. (1.17), this corresponds to a  $\Delta E$  effect of 54.84 %.

For each constant field, there are two modulus curves: one corresponding to the loading half of the compression cycle and one to the unloading half. This hysteresis in the modulus is due to magnetic hysteresis, which is discussed in the **Energy dissipation in ferromagnetic materials** subsection of Section 1.2.1. The elastic modulus

tends to increase above the saturation value after the stress changes direction, particularly near zero stress. The cause was not investigated, although it is thought to result from having a stress reversal point before complete magnetic saturation. Noise prevented the calculation of material properties near reversal points in Ref. [120]. However, noise is not believed to be the cause here.

### **Solid rod: minor strain versus stress loops under constant field**

Fig. 2.4(a) shows the minor loop, strain versus stress responses of the solid Galfenol rod under constant field. Distinct saturation and burst regions are observed depending on the bias stress and field. A comparison of select major and minor loop responses under constant field is depicted in Fig. 2.4(b). As expected, the minor loops lie within the major loops. It is emphasized that the minor loop testing was conducted at 4 Hz for consistency with similar work on Terfenol-D [96] and Galfenol [154]; however, preliminary testing revealed that the minor loop responses for 0.1 Hz and 4 Hz sinusoidal compression were equal to within experiment error. In the burst region, the Galfenol rod is noticeably stiffer for small amplitude loading than for major loop loading. The same trend was observed in Terfenol-D by Kellogg and Flatau [96], who attributed the decrease to constrained magnetic moment rotation.

The Young's modulus of minor strain versus stress loops – shown in Fig. 2.5(a) for constant field testing of the solid rod – was calculated via linear regression. Fig. 2.5(b) gives a comparison of the modulus of select major and minor loop responses. As noted earlier, the modulus of minor loops is consistently larger than that of major loops in the burst region. The minimum modulus of the minor loop responses is 44.74 GPa, corresponding to a  $\Delta E$  effect of 37.90 %, when field and stress are 2.41 kA/m and -5.77 MPa, respectively.

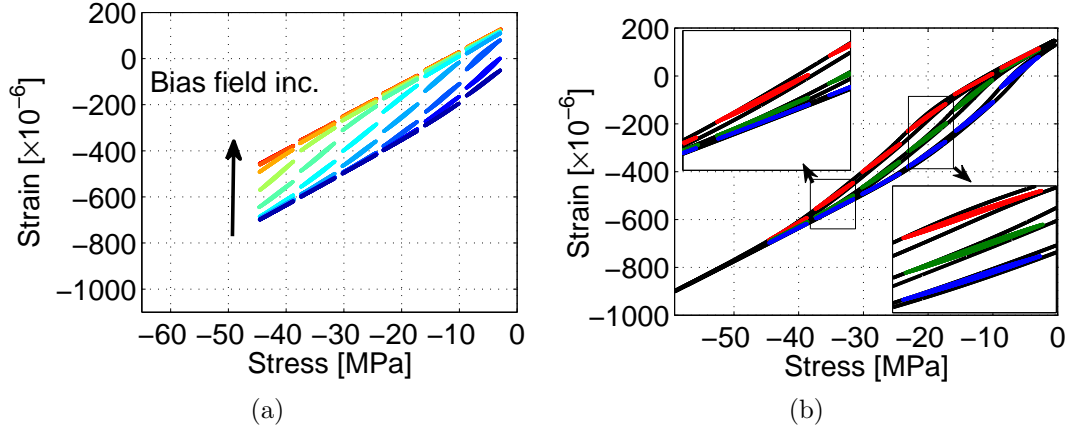


Figure 2.4: (a) Strain versus stress minor loops of the solid Fe<sub>81.6</sub>Ga<sub>18.4</sub> rod to 4 Hz sinusoidal compression for constant fields of 0.73, 1.42, 2.41, 3.88, 5.50, 7.17, 8.84, 10.51, 12.19, and 13.76 kA/m and nominal bias stresses of -5.73 to -41.6 MPa in 7.2 MPa steps and (b) comparison of the major and minor loop responses of the solid rod for constant field of 2.41, 3.88, and 5.50 kA/m.

Fig. 2.6(a) depicts the Young's modulus response of Galfenol to an applied field for different bias stresses. The Young's modulus first decreases to a minimum with increasing field, then increases toward the saturation modulus thereafter. The minimum modulus shifts to a larger magnetic field as the compressive stress increases. The minimum modulus, and thus maximum  $\Delta E$  effect, is achieved when the bias stress is small. The same trend is observed in existing measurements of Terfenol-D [96]. The Young's modulus from minor loops (Fig. 2.6(b)) also exhibits a minimum as field increases; however, the minimum moduli are larger than those of the major loop responses, because magnetostrictive materials are sensitive to the amplitude of the applied cyclic stress [96, 108].

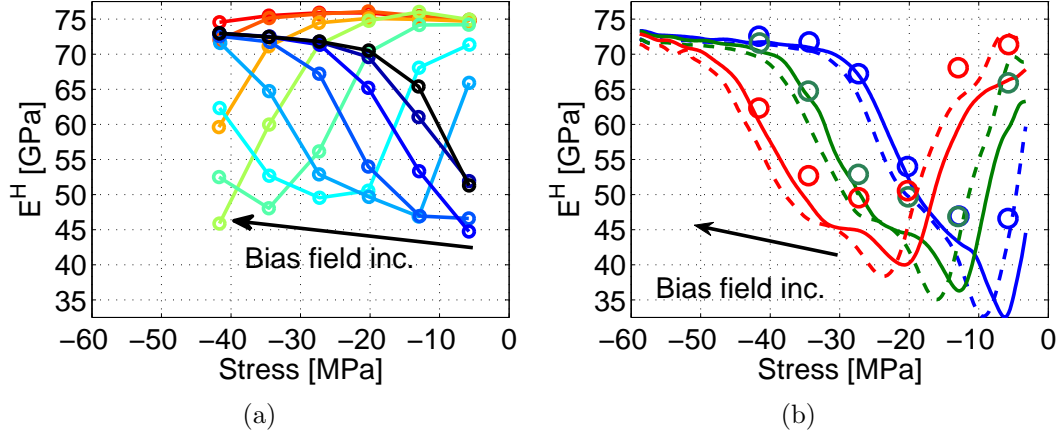


Figure 2.5: (a) Young's modulus of the solid  $\text{Fe}_{81.6}\text{Ga}_{18.4}$  rod (from minor loops) for constant fields of 0.73, 1.42, 2.41, 3.88, 5.50, 7.17, 8.84, 10.51, 12.19, and 13.76 kA/m and nominal bias stresses of -5.73 to -41.6 MPa in 7.2 MPa steps and (b) comparison of the modulus from the major (lines) and the minor (circles) loop responses for constant fields of 2.41, 3.88, and 5.50 kA/m.

### Solid rod: major strain versus stress loops under constant current

Practical Galfenol-based devices, such as force sensors and energy harvesters, will typically lack active magnetic field control. Thus, strain versus stress responses under constant current to the electromagnets were also measured. The major loop, constant current sensing response of the solid Galfenol rod is depicted in Fig. 2.7 along with optimized simulations, which exhibit an average modeling error of 1.22 %. Comparing constant field major loops (Fig. 2.1) to constant current major loops (Fig. 2.7) shows that the latter has a flatter slope in the burst region. This results from the stress-dependent field that occurs under constant current (see Fig. 2.8(a)) due to Galfenol's stress- and field-dependent magnetic permeability, which is shown in Fig. 2.8(b). The changes in magnetic field cause magnetostriction, which partially compensates for

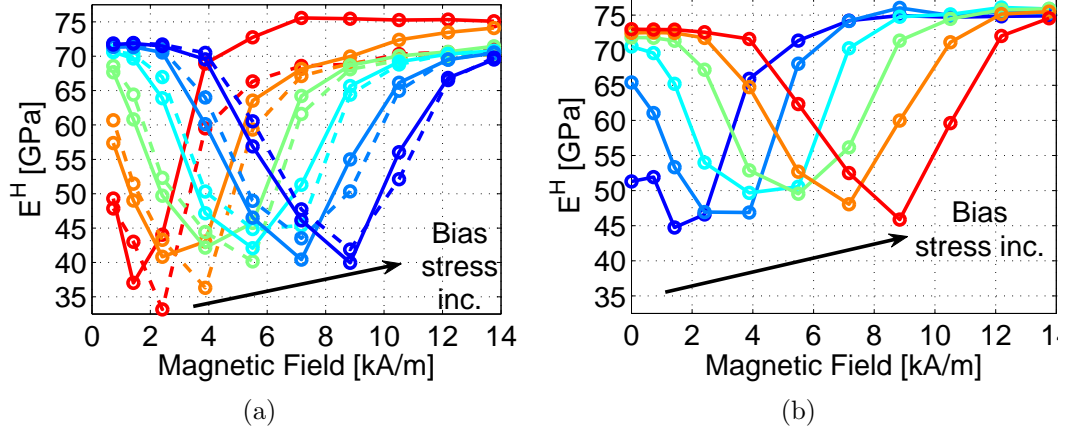


Figure 2.6: Young's modulus of the solid  $\text{Fe}_{81.6}\text{Ga}_{18.4}$  rod from constant field (a) major loops (dashed: decreasing stress; solid: increasing stress) and (b) minor loops; bias stresses are from -5.73 to -41.6 MPa in 7.2 MPa steps.

the passive elastic deformation, thus leading to smaller changes in strain for a given change in stress.

Fig. 2.9 presents the Young's modulus of the solid rod at constant current, which was calculated using the same method as used for Fig. 2.3. The minimum modulus of 43.94 GPa occurs at a 0.2 A bias current and a -3.34 MPa stress. The associated  $\Delta E$  effect of 39.01 % is considerably smaller than the effect under constant field. The minimum modulus increases as the bias current increases, similar to the effect of increasing the bias field. The hysteresis observed in the constant current modulus responses is slightly larger than in the constant field responses.

### Solid rod: minor strain versus stress loops under constant current

Fig. 2.10(a) depicts the minor loop, strain versus stress responses of the solid Galfenol rod under constant current. A comparison of select major and minor loop



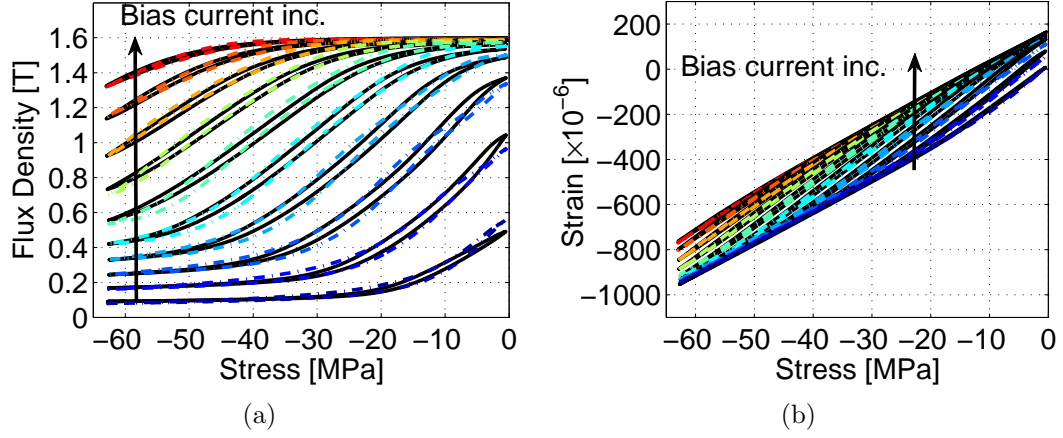


Figure 2.7: Comparison of the experimental (solid) and modeled (dashed) sensing responses of the solid  $\text{Fe}_{81.6}\text{Ga}_{18.4}$  rod to 1 Hz sinusoidal compression: (a) flux density versus stress and (b) strain versus stress. Bias current values are from 0 A to 1 A in 0.1 A steps.

responses under constant current is depicted in Fig. 2.10(b). Minor loops are again circumscribed by their corresponding major loops.

The minor loop Young's modulus of the solid Galfenol rod under constant current, which is calculated using linear regression, is shown in Fig. 2.11(a). Fig. 2.11(b) compares select major and minor loop modulus responses. As observed for constant field conditions, the constant current minor loop responses are stiffer than their corresponding major loop responses. The minimum modulus for this case is 52.26 GPa at 0 A bias current and -5.76 MPa bias stress, providing a  $\Delta E$  effect of 27.46 %.

#### **Laminated rod: major strain versus stress loops under constant current**

To relate the quasi-static performance of laminated Galfenol rods with that of solid Galfenol rods, major loop strain versus stress responses of a laminated  $\text{Fe}_{81.6}\text{Ga}_{18.4}$  rod were measured under constant current for the same conditions as used for the

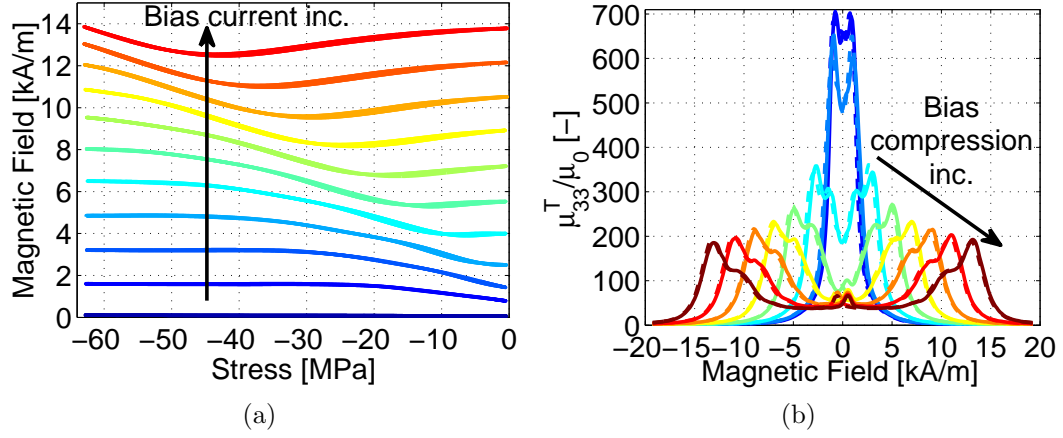


Figure 2.8: (a) variation in magnetic field for constant currents of 0 A to 1 A in increments of 0.1 A and (b) relative magnetic permeability of the solid  $\text{Fe}_{81.6}\text{Ga}_{18.4}$  rod for constant stresses of 0, -1.62, -10.3, -20.5, -30.7, -40.9, -51.2, and -61.5 MPa.

solid rod. The measurements are shown in Fig. 2.12 along with the Young's modulus response, which was calculated as explained in the **Solid rod: major strain versus stress loops under constant field** subsection of Section 2.1.2. Relative to the solid rod, the laminated rod has a considerably lower saturation modulus of 59.54 GPa, which is primarily due to the presence of adhesive layers that have a modulus of only 0.86 GPa. The observed trends are consistent with the behavior of the solid rod. The minimum modulus is 36.31 GPa, which occurs at 0.5 A bias current and -3.25 MPa stress. Interestingly, the corresponding  $\Delta E$  effect of 39.02 % is equal, within experimental error, to that of the solid rod under the same conditions.

### 2.1.3 Concluding remarks

In this section, major strain versus stress responses of solid rods of research grade,  $\langle 100 \rangle$  oriented, textured polycrystalline  $\text{Fe}_{81.6}\text{Ga}_{18.4}$  were measured under constant magnetic fields from 0.73 kA/m to 13.76 kA/m and under constant currents from 0 A

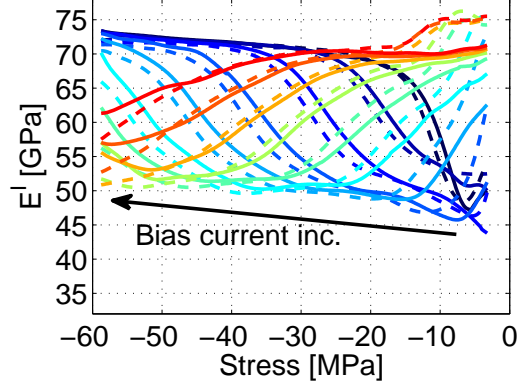


Figure 2.9: Young's modulus of the solid  $\text{Fe}_{81.6}\text{Ga}_{18.4}$  rod (from major loops) versus stress for constant currents of 0 A to 1 A with 0.1 A steps; decreasing stress (dashed) and increasing stress (solid).

to 1 A. The mechanical loading consisted of a 1 Hz stress ranging from -63.3 MPa to -0.5 MPa. The minimum major loop modulus under constant field and constant current is 32.53 GPa and 43.94 GPa, respectively, corresponding to  $\Delta E$  effects of 54.84 % and 39.01 %, respectively. The DEA model was optimized to the constant field and constant current elastic responses. The modeling results show a close agreement with the data, exhibiting average modeling errors of 1.02 % and 1.22 % for constant field and constant current conditions, respectively. Minor loop mechanical excitations were also applied by superimposing a 4.0 Hz, 2.88 MPa amplitude sinusoidal stress on bias stresses ranging from -41.6 MPa to -5.7 MPa. In general, the minor loop responses are flatter than their circumscribing major loop responses. The minimum minor loop modulus under constant field and constant current is 44.74 GPa and 52.26 GPa, respectively, corresponding to  $\Delta E$  effects of 37.90 % and 27.46 %, respectively. A laminated Galfenol sample, cut from the same bulk rod as the solid rod, was tested under the same constant current conditions. Due to the soft adhesive layer between

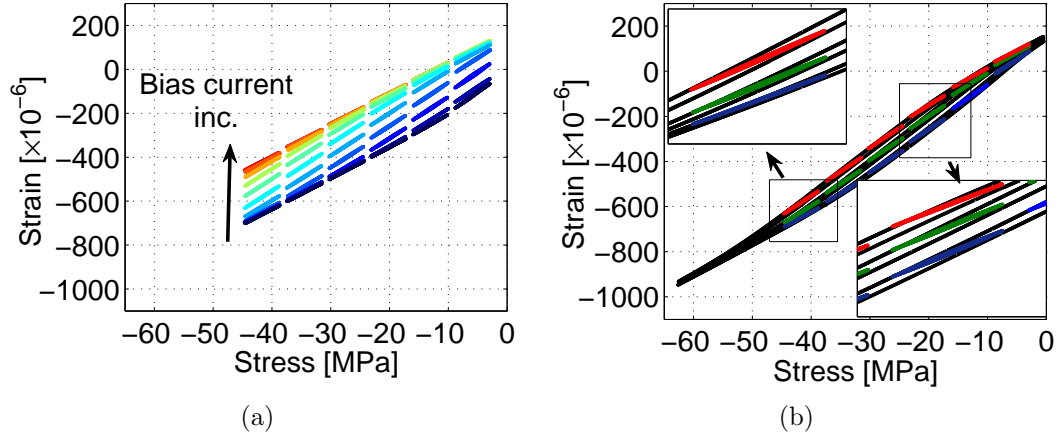


Figure 2.10: (a) strain versus stress minor loops of the solid  $\text{Fe}_{81.6}\text{Ga}_{18.4}$  rod for constant currents of 0 A to 1 A in increments of 0.1 A and nominal bias stresses of -5.7 MPa to -41.6 MPa with 7.2 MPa steps and (b) comparison of the major and minor loop responses of the solid rod for constant currents of 0.2, 0.3, and 0.4 A.

laminates, the saturation modulus of the laminated sample is 59.54 GPa, which is 82.65 % of the solid rod's saturation modulus. The minimum major loop modulus of the laminated rod is 36.31 GPa, corresponding to a 39.02 %  $\Delta E$  effect.

In all cases, the minimum modulus occurs at larger compressive stress as the bias field or current increases. The  $\Delta E$  effect associated with minor loops is consistently lower than that associated with major loops, regardless of the magnetic bias condition. The hysteresis of constant field responses is smaller than that of constant current responses; this may result from the field control system providing energy to the magnetic circuit.

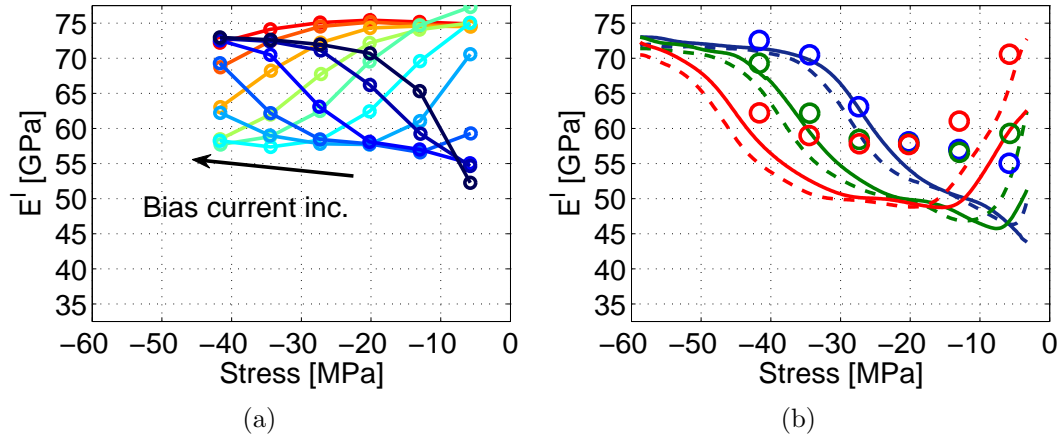


Figure 2.11: (a) Young's modulus of the solid  $\text{Fe}_{81.6}\text{Ga}_{18.4}$  rod for constant currents of 0 A to 1 A in 0.1 A steps and nominal bias stresses of -5.7 MPa to -41.6 MPa with 7.2 MPa steps and (b) comparison of the modulus from major (lines) and minor (circles) loops for constant currents of 0.2, 0.3, and 0.4 A.

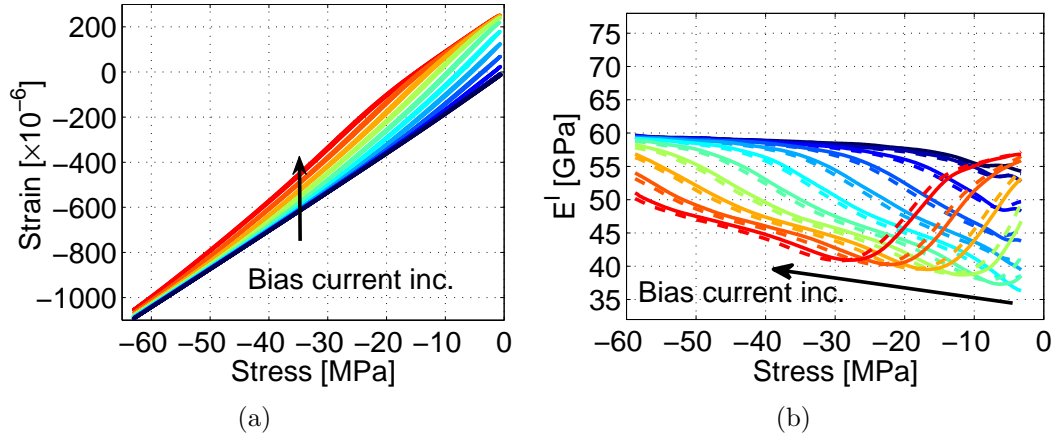


Figure 2.12: (a) strain and (b) Young's modulus major loops of the laminated  $\text{Fe}_{81.6}\text{Ga}_{18.4}$  rod for constant currents of 0 A to 1 A in 0.1 A steps; decreasing stress (dashed) and increasing stress (solid).

## 2.2 Galfenol Vibration Absorbers

Vibration absorbers are a common solution when undesirable vibration or transmitted forces cannot be reduced through direct design modifications (e.g., by introducing additional damping or shifting resonant frequencies away from operating conditions). While conventional absorbers must be designed for a specific operating condition and vibrating structure, adaptive vibration absorbers (AVAs) can tune their response in conjunction with changes in operating conditions.

Recent advancements in manufacturing technology have enabled the development of composites containing active materials. By harnessing Galfenol's robustness and its electrically-tunable elastic modulus, load-bearing composites that provide a controllable stiffness can be realized. One enabling technology is ultrasonic additive manufacturing (UAM), a metal layering technique for creating multimaterial composites containing seamlessly-embedded smart materials. UAM is a low temperature rapid prototyping process based on solid-state welding of metal foils to themselves or to a metallic substrate [135]. In UAM, a sonotrode applies transverse ultrasonic vibration ( $>20$  kHz) to the tape-substrate pair creating a scrubbing action that shears asperities and disperses surface contaminants and oxides. The resulting nascent surfaces metallurgically bond under an applied normal force. A 9 kW UAM machine and a schematic of the ultrasonic weld head are shown in Fig. 2.13. Metallic tapes are welded additively to form bulk 3D geometries, which may include complex internal channels created through periodic machining.

The manufacture of layered structures by UAM is computer controlled and automatic. A tape feed mechanism supplies the metal foils to the weld head and cuts them at the beginning and end of each pass. Embedding smart materials is presently

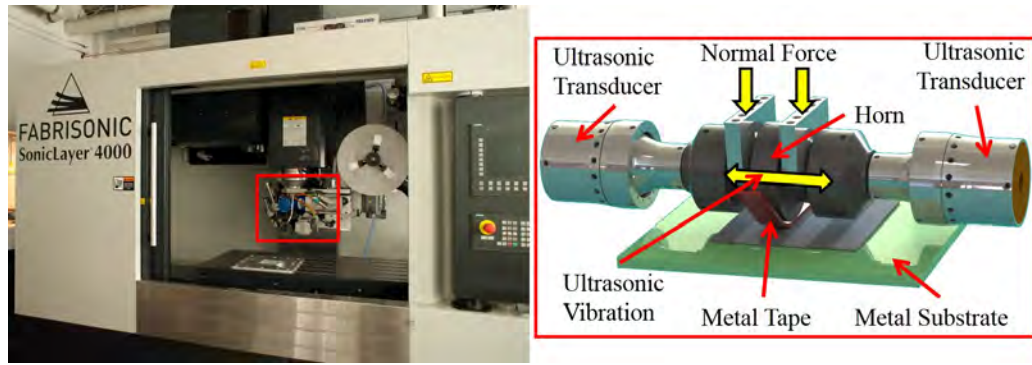


Figure 2.13: Very high power UAM machine installed in the Center for Ultrasonic Additive Manufacturing at The Ohio State University, and schematic of the ultrasonic system (motion during welding shown by arrows).

done by combining this automatic process for layering of the matrix along with manual placement of the smart materials. Galfenol is best embedded as sheet stock or wires. Depending on the thickness of the Galfenol features relative to the typical foil thickness (0.15 mm, or 0.006 in), grooves are machined in the matrix to partially bury the material under the surface of the build. This is done via the built-in CNC mill or laser etching system. A Galfenol/Al 3003 composite manufactured via UAM is shown in Fig. 2.14.

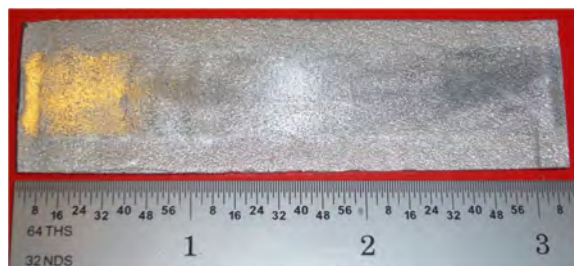


Figure 2.14: Al 3003 composite manufactured by UAM containing an embedded 0.05 x 1.27 cm Galfenol sheet.

In this section, a metal-matrix composite beam, like that shown in Fig. 2.14, containing an embedded sheet of Galfenol is considered as an AVA. The objective of this section is to assess the controllability of the composite’s resonance through bias field tuning of the elastic modulus. The magnitude of the change in the composite’s resonant frequency provides a measure of the tunability of the AVA, and therefore its ability to absorb the vibration of a host structure that exhibits variable operating conditions or dynamic characteristics. Tuning of the composite’s resonant frequency is studied by calculating the nonlinear, bending vibration of the composite at different forcing frequencies. In the first subsection, the composite is modeled as a single-degree-of-freedom mechanical system, whereas in the second subsection, a 1D distributed parameter model is used. A Galfenol/aluminum composite beam, manufactured via UAM, is used to validate the distributed parameter model.

### **2.2.1 Lumped parameter modeling**

In this section, the nonlinear, bending vibration of the aforementioned composite beam is modeled to quantify changes in the composite’s frequency response due to variations in the excitation power amplitude and the bias magnetic field. To improve computational efficiency, the composite is approximated as a simple mass-spring-damper system, where the spring behaves nonlinearly due to Galfenol’s stress- and magnetic field-dependent elastic modulus. Accuracy is retained by (i) incorporating a fully-coupled, nonlinear constitutive model of Galfenol accurate for arbitrary stress and magnetic field (the DEA model), (ii) considering the variation in Galfenol’s elastic modulus along the length of the composite, and (iii) including the asymmetric tension-compression behavior of Galfenol. Two boundary conditions, clamped-free (C-F) and



clamped-clamped (C-C), are considered. To optimize the composite geometry for resonance tuning, a parametric study is presented to determine the effect of Galfenol volume fraction and of the location of Galfenol elements within the composite.

### Model development

The frequency domain response of the composite's vibration is desired to quantify the tunability of the composite's resonance. However, an eigenvalue problem cannot be formulated, because the stiffness nonlinearity is state dependent. Consequently, the frequency response must be approximated by calculating the steady-state vibration of the composite in the time domain and extracting the vibration amplitudes at discrete excitation frequencies. The number of time domain responses required to approximate the frequency responses for the parametric studies is  $\mathcal{O}(10^4)$ , because (i) about 30 discrete frequencies are needed for smoothness of the frequency responses, (ii) both forward and reverse frequency sweeps are required, (iii) a wide range of operating conditions (excitation power amplitude and bias magnetic field) must be considered, and (iv) the independent parameter (Galfenol volume fraction or location) must be varied. As such, the system must be simplified for computational efficiency. To preserve the complex constitutive behavior, the composite is approximated as a single lumped mass with an equivalent bending stiffness and constant damping.

#### *Bending Vibration Model*

Following the standard application of Newton's 2nd law, the governing ODE for the composite beam represented as a single-degree-of-freedom resonator is,

$$m\ddot{w} + c\dot{w} + k_{\text{eq}}(H_{\text{bias}}, T)\bar{w} = m\omega^2 U_2 e^{i\omega t}, \quad (2.2)$$

where  $\bar{w}$  is defined as the relative displacement between the mass and base, and harmonic base excitation with amplitude  $U_2$  and frequency  $\omega$  is used,

$$\bar{w} = \bar{w}_1 - \bar{w}_2 = \bar{w}_1 - U_2 e^{i\omega t}. \quad (2.3)$$

In Eq. (2.2), the spring is nonlinear due to the dependence of Galfenol's elastic modulus on the bias magnetic field ( $H_{\text{bias}}$ ) and bending stress ( $T$ ). The damping ratio,

$$\xi = \frac{c}{2m\omega_n} = \frac{c}{2m} \sqrt{\frac{m}{k_{\text{eq}}}}, \quad (2.4)$$

was held constant for all simulations. Using results from Meirovitch [106], the equivalent spring constants for a C-F beam subject to a tip load and a C-C beam subject to midspan load are,

$$k_{\text{eq}}^{\text{CF}}(H_{\text{bias}}, T) = \frac{3E_{\text{eq}}(H_{\text{bias}}, T)I(H_{\text{bias}}, T)}{L^3} \quad (2.5)$$

and

$$k_{\text{eq}}^{\text{CC}}(H_{\text{bias}}, T) = \frac{192E_{\text{eq}}(H_{\text{bias}}, T)I(H_{\text{bias}}, T)}{L^3}, \quad (2.6)$$

respectively, where  $L$  is the length of the beam. As such,  $\bar{w}$  represents the tip deflection of the C-F beam and the midspan deflection of the C-C beam. The equivalent elastic modulus of the composite  $E_{\text{eq}}$  is calculated as a function of the matrix and average Galfenol elastic moduli ( $E_{\text{M}}$  and  $E_{\text{G}}$ ) and volume fractions ( $\xi_{\text{M}}$  and  $\xi_{\text{G}}$ ) using the rule of mixtures [141],

$$E_{\text{eq}}(H_{\text{bias}}, T) = E_{\text{G}}(H_{\text{bias}}, T)\xi_{\text{G}} + E_{\text{M}}\xi_{\text{M}}. \quad (2.7)$$

The area moment of inertia  $I$  is calculated in the standard manner after first homogenizing the composite by scaling the Galfenol width ( $W_{\text{G}}$ ) to yield an equivalent section of matrix material,

$$W_{\text{Geq}} = \frac{E_{\text{G}}(H_{\text{bias}}, T)}{E_{\text{M}}} W_{\text{G}}. \quad (2.8)$$

The magnetic field is assumed homogeneous throughout the composite. Considering the stress variation in the beam and the asymmetry in the material's tension-compression behavior, an average elastic modulus for the Galfenol element is calculated. As seen in Figs. 2.1(a) and 2.3, respectively, the magnetic flux in Galfenol and its elastic modulus vary almost exclusively in the compressive stress regime. Thus, even for Galfenol located at the neutral axis, the symmetric (zero average) bending stress will yield an asymmetric elastic modulus distribution through the Galfenol thickness. This asymmetric distribution will change as the stress magnitude varies, leading to a non-constant average elastic modulus through the Galfenol element's thickness. An example of this variation in elastic modulus is shown in Fig. 2.15 as a function of the maximum bending stress in a Galfenol beam.

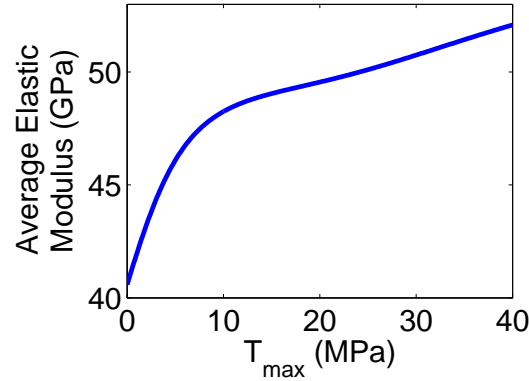


Figure 2.15: Average elastic modulus through the thickness of a Galfenol element located at the neutral axis with  $H_{\text{bias}} = 2$  kA/m (calculated using the DEA model).

Galfenol's elastic modulus varies along the length of the beam due to the position-dependent stress in the Galfenol element. As such, this variation is incorporated in the single-degree-of-freedom model of the composite by using an average value of the

stress in the element. As will be discussed in Section 2.2.1, the stress acting on the Galfenol element is calculated from its strain using a numerical inversion of the DEA model. Thus, an average value of the strain is required.

The strain in the Galfenol element at a distance  $y$  from the neutral axis is calculated from mechanics of materials as,

$$S = -y \frac{\partial^2 w}{\partial x^2}, \quad (2.9)$$

where  $w(x)$  is the transverse deflection of the beam along its length. This strain is evaluated at each time step by assuming that the instantaneous beam deflection is due to a virtual, static force  $F$  at the tip (for the C-F beam) or the midspan (for the C-C beam). Under these conditions, the elastic curves of the C-F and C-C beams are,

$$w^{\text{CF}}(x) = \frac{1}{2E_{\text{eq}}I} \left( FLx^2 - \frac{1}{3}Fx^3 \right) \quad (2.10)$$

and

$$w^{\text{CC}}(x) = \begin{cases} (4E_{\text{eq}}I)^{-1} \left( -\frac{1}{3}Fx^3 + \frac{1}{4}FLx^2 \right) & 0 \leq x \leq \frac{L}{2} \\ (4E_{\text{eq}}I)^{-1} \left( \frac{1}{3}Fx^3 - \frac{3}{4}FLx^2 + \frac{1}{2}FL^2x - \frac{1}{12}FL^3 \right) & \frac{L}{2} \leq x \leq L \end{cases}, \quad (2.11)$$

respectively. The average curvature of the C-F beam is,

$$\left( \frac{\partial^2 w}{\partial x^2} \right)_{\text{avg}}^{\text{CF}} = \frac{FL}{2E_{\text{eq}}I}. \quad (2.12)$$

Setting  $x = L$  in Eq. (2.10) to relate the calculated tip deflection  $\bar{w}^{\text{CF}}$  to the virtual tip force and using Eq. (2.12), the strain in the Galfenol element Eq. (2.9) for the C-F beam can be rewritten as,

$$S^{\text{CF}} = -\frac{3\bar{w}^{\text{CF}}y}{2L^2}. \quad (2.13)$$

For the C-C beam, the average curvature is zero. Despite this, the average elastic modulus of the Galfenol element will still vary even if it is also located at the beam's

neutral axis. For the C-C beam, the average curvature over the middle half and over the outer quarters of the beam,

$$\left(\frac{\partial^2 w}{\partial x^2}\right)_{\text{avg1}}^{\text{CC}} = \frac{-FL}{16E_{\text{eq}}I} \quad (2.14)$$

and

$$\left(\frac{\partial^2 w}{\partial x^2}\right)_{\text{avg2}}^{\text{CC}} = \frac{FL}{16E_{\text{eq}}I}, \quad (2.15)$$

respectively, are both used. Setting  $x = L/2$  in Eq. (2.11) to relate the calculated midspan deflection  $\bar{w}^{\text{CC}}$  to the virtual midspan force and using Eqs. (2.14) and (2.15), the strain in the Galfenol element Eq. (2.9) over these sections of the C-C beam can be rewritten as,

$$S_1^{\text{CC}} = \frac{12\bar{w}^{\text{CC}}y}{L^2} \quad (2.16)$$

and

$$S_2^{\text{CC}} = -\frac{12\bar{w}^{\text{CC}}y}{L^2}. \quad (2.17)$$

In summary, the change in Galfenol's elastic modulus along the length of the beam is incorporated into the proposed model using a single average strain Eq. (2.13) for the C-F beam and two average strains Eqs. (2.16) and (2.17) for the C-C beam.

The variation in Galfenol's elastic modulus through the element's thickness is considered by averaging the elastic moduli that are calculated at 2, 4, 6, 8, and 10 equally-spaced locations through the thickness. The number of locations necessary for an accurate approximation was determined through a short parametric study. The independent variables in the study were the bias magnetic field (values of 0, 2, and 4 kA/m) and the location of the Galfenol element (at the neutral axis, 75 % of the element above the neutral axis, and 75 % of the element below the neutral axis). For each case, the force applied to the beams was varied such that the maximum

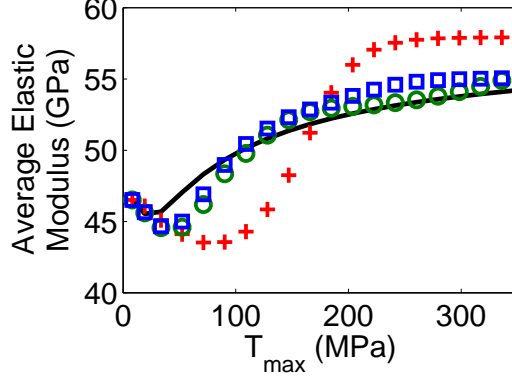


Figure 2.16: Average elastic modulus of a Galfenol element located at the C-F beam’s neutral axis calculated from 2 (+), 6 (○), and 10 (□) locations through the element’s thickness compared to the true average (—) ( $H_{\text{bias}} = 4$  kA/m; 4 and 8 location averages not shown for clarity).

stress in the Galfenol element varied between 0 and 350 MPa. A uniform grid of points was applied to the Galfenol element (100 points through its thickness and 100 points along its length). At each grid point, the strain was calculated using Eq. (2.9). The true average elastic modulus in the Galfenol element was taken as the average over this 100 x 100 grid. An example comparison between the true average and the approximated averages is shown in Fig. 2.16. For each case, the RMS error was calculated relative to the true average. The average RMS error over all of the test cases is tabulated in Table 2.2 for each approximation.

Note that the approximations for the C-C beam average twice as many elastic moduli as for the C-F beam, because two average strains (and therefore two elastic moduli) are needed to describe the elastic modulus variation along the C-C beam’s length. Considering accuracy and computational efficiency of the composite vibration model, 6 and 4 averages through the Galfenol element’s thickness were used for the C-F and C-C beams, respectively.

Table 2.2: Average RMS error for approximating the average elastic modulus through the thickness and along the length of the Galfenol element using 2, 4, 6, 8, and 10 equally-spaced locations through its thickness.

Number of Locations	Average RMS Error (GPa)	
	C-F Beam	C-C Beam
2	4.06	2.41
4	2.40	1.70
6	1.80	1.49
8	1.80	1.54
10	1.82	1.62

### Nonlinear solution procedure

The solution procedure is graphically depicted in Fig. 2.17. The inner loop approximates the nonlinear time domain response of the composite beam through linearization of the nonlinear ODE Eq. (2.2) by updating the equivalent stiffness for each time step. The DEA model is used to update Galfenol's elastic modulus, which requires knowledge of the stress and magnetic field in the Galfenol element. The magnetic field is a known input. However, due to the bi-directional coupling present in the Galfenol element, direct calculation of the stress from the beam's deflection is not possible. Instead, stress must be calculated from the bias magnetic field and strain in the Galfenol element by numerically inverting the DEA model. In this paper, the inversion is performed using the quasi-Newton SR1 algorithm [33]. Therefore, for each time increment, the strain, stress, and elastic modulus must be calculated at each of the 6 and 8 averaging locations for the C-F and C-C beams, respectively. Each cycle of the excitation is divided into 50 differential time steps to maintain accuracy and

smoothness. Solutions are obtained for 15 cycles of the base excitation, which was determined a posteriori to ensure that steady state was reached.

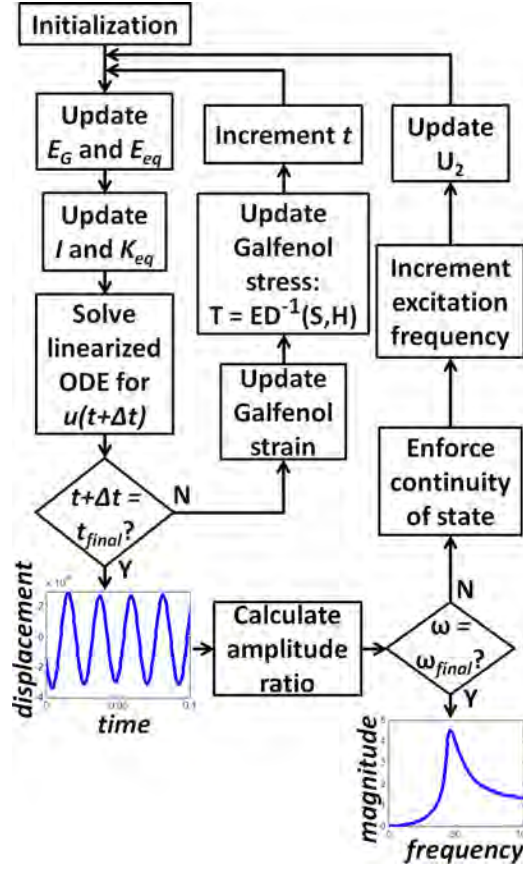


Figure 2.17: Solution procedure to approximate a single, potentially hysteretic frequency response.

The outer loop approximates the frequency response of the composite's nonlinear vibration. The amplitude ratio is calculated as the steady-state tip or midspan displacement divided by the excitation amplitude. Forward and reverse excitation frequency sweeps are necessary due to the nonlinearities in the system, which may



result in multiple, stable periodic orbits of composite vibration for a single set of operating conditions. When this occurs, it is seen in the frequency response as hysteresis in the steady-state vibration of the system. This also explains the need for enforcing continuity of state (i.e., equating the initial state of the next time domain response with the final state of the current response) at the beginning of each time domain simulation.

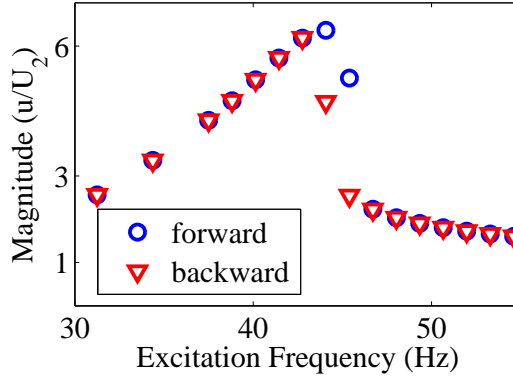


Figure 2.18: Hysteretic frequency response of the C-F Galfenol-Al composite,  $H_{\text{bias}} = 1 \text{ kA/m}$ ,  $|P| = 0.0119 \text{ J}$ , and  $\xi_G = 0.82$ .

A hysteretic frequency response obtained using the proposed model is shown in Fig. 2.18. Throughout each frequency sweep, the input power amplitude  $|P| = |Fv|$  is held constant by defining the excitation amplitude as,

$$U_2 = \sqrt{\frac{|P|}{m\omega^3}}, \quad (2.18)$$

which can be derived from Eqs. (2.2) and (2.3). This is a more physically accurate operating condition than that used in [125]. This numerical simulation is equivalent to a forward and reverse stepped sine experiment that includes the first vibration mode.

## Model results

The entire range of composite behavior is described by the excitation magnitude and the bias magnetic field. Thus, a complete characterization of the stiffness tuning behavior, and therefore resonant frequency tuning behavior, is obtained by considering a range of input power amplitudes ( $1 \times 10^{-3}$  to  $1 \times 10^4$  J) that leads to Galfenol stresses between 50 and -50 MPa and bias magnetic fields (0 to 13 kA/m) capable of magnetically saturating the Galfenol element over this stress range. The 1D strain response of Galfenol is symmetric with respect to magnetic field. Therefore, negative bias magnetic fields do not need to be considered. To accurately approximate the resonant frequency for each case, both the forward and reverse frequency sweeps were curve fit with cubic splines. The resonant frequency was taken as the frequency at which the maximum amplitude ratio occurs in the interpolated data. The resonant frequency of vibration for every combination of input power amplitude and bias magnetic field was obtained in this manner. The resulting frequencies were normalized with respect to the maximum frequency to show the percent changes in resonant frequency from the saturated (stiff) case. For a given geometry of the composite, the percent change in resonant frequency is calculated according to

$$\Delta\omega_r = \left| \frac{\omega_{r,\min}}{\omega_{r,\max}} - \frac{\omega_{r,\max}}{\omega_{r,\max}} \right| = \left| \frac{\omega_{r,\min}}{\omega_{r,\max}} - 1 \right|. \quad (2.19)$$

In order to determine the geometry that maximizes the stiffness tunability of the composite, Galfenol volume fraction and its offset from the horizontal midplane of the composite's cross section were varied. Surface plots of the normalized resonant frequency were generated for each case, and are presented as a top view of the surface

Table 2.3: Model parameters.

FeGa				Matrix (Al)	Composite				
$M_s$ (T)	$\lambda_{100}$ ( $\times 10^{-6}$ )	$K^k$ (kJ/m <sup>3</sup> )	$\Omega$ (J/m <sup>3</sup> )	$E$ (GPa)	$\xi$	$L$ (cm)	$m$ (kg)	width (cm)	thickness (cm)
1.3787	157	$2.71 \times 10^4$	776.73	68.9	0.1	2.54	0.058	1.65	0.0762

in Figs. 2.19, 2.20, 2.22, and 2.23. Results are presented for the model parameters given in Table 2.3; the material properties for Galfenol were obtained through a least-squares optimization routine using the anhyseretic DEA model and experimental measurements of a highly-textured, polycrystalline Fe<sub>81.6</sub>Ga<sub>18.4</sub> Galfenol rod [154].

For the parametric study of Galfenol volume fraction, the Galfenol element was located at the horizontal midplane of the composite's cross section, while its volume fraction was varied between 10 % and 100 % (i.e., the limiting case of no surrounding matrix). A surface plot of the composite's normalized resonant frequency is shown for each case in Figs. 2.19 and 2.20 for the C-F and C-C beams, respectively. The surface plots for negative bias magnetic fields are simply reflections about the  $H_{\text{bias}} = 0$  line of those shown in Figs. 2.19 and 2.20. The maximum resonant frequency tunability as a function of the volume fraction is summarized in Fig. 2.21.

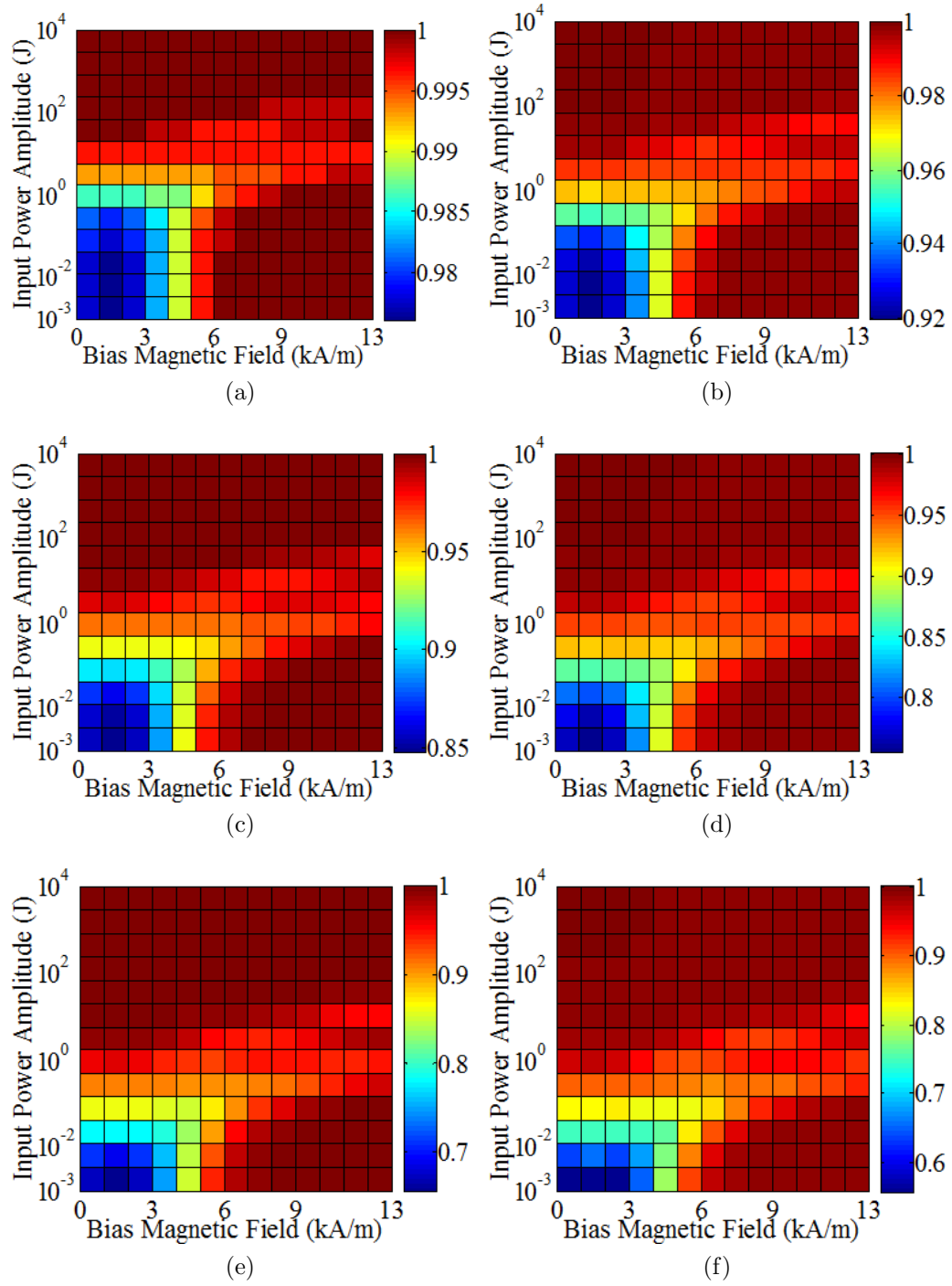


Figure 2.19: Normalized resonant frequency of the C-F composite as a function of the operating conditions for Galfenol volume fractions of (a) 10 %, (b) 28 %, (c) 46 %, (d) 64 %, (e) 82 %, and (f) 100 % (top views shown, Galfenol embedded at the neutral axis). Resonant frequencies normalized with respect to the saturated (stiff) case.

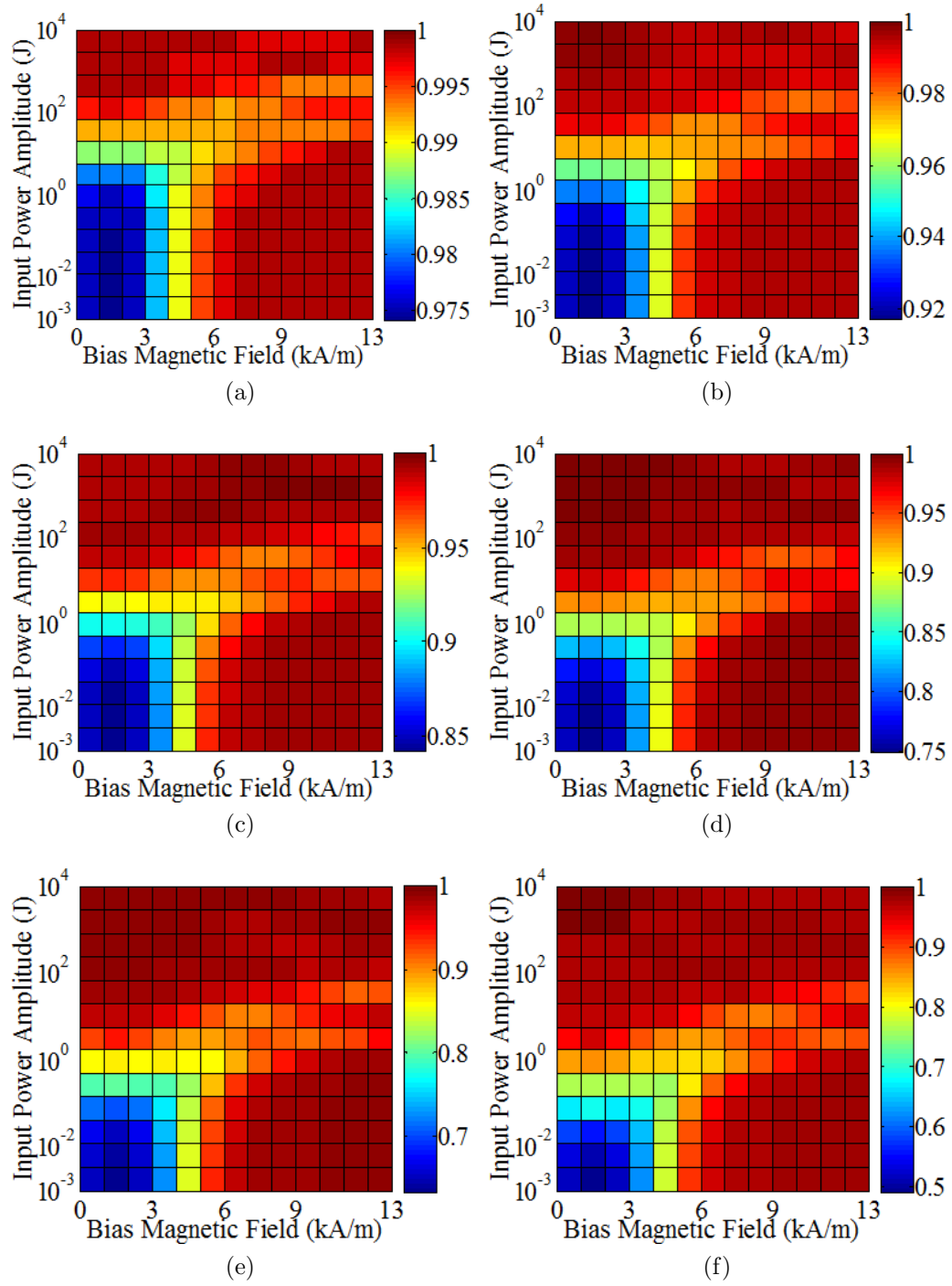


Figure 2.20: Normalized resonant frequency of the C-C composite as a function of the operating conditions for Galfenol volume fractions of (a) 10 %, (b) 28 %, (c) 46 %, (d) 64 %, (e) 82 %, and (f) 100 % (top views shown, Galfenol embedded at the neutral axis).

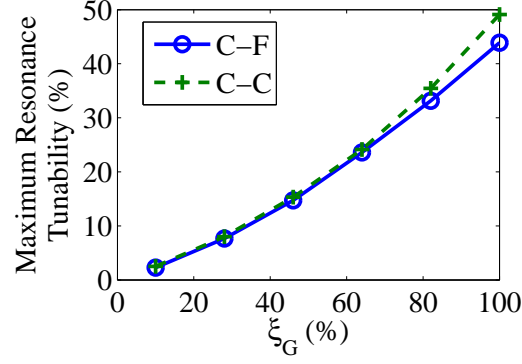


Figure 2.21: Effect of Galfenol volume fraction on the maximum tunability of the vibration absorber's resonance for the C-F and C-C boundary conditions (Galfenol embedded at the neutral axis).

The parametric study of Galfenol's location was conducted by holding the volume fraction of Galfenol constant at 10 %, while varying Galfenol's location vertically in the composite's cross section. Four different cases were modeled: (i) the reference case – Galfenol midplane coincident with the composite midplane, (ii) Galfenol midplane shifted upward 33 % of the limiting value (iv), (iii) Galfenol midplane shifted upward 66 % of the limiting value (iv), and (iv) the limiting case – top surface of Galfenol coincident with the top surface of the composite. A surface plot of the composite's normalized resonant frequency is shown for each case in Figs. 2.22 and 2.23 for the C-F and C-C beams, respectively. The maximum resonant frequency tunability as a function of Galfenol's offset from the composite midplane is summarized in Fig. 2.24.

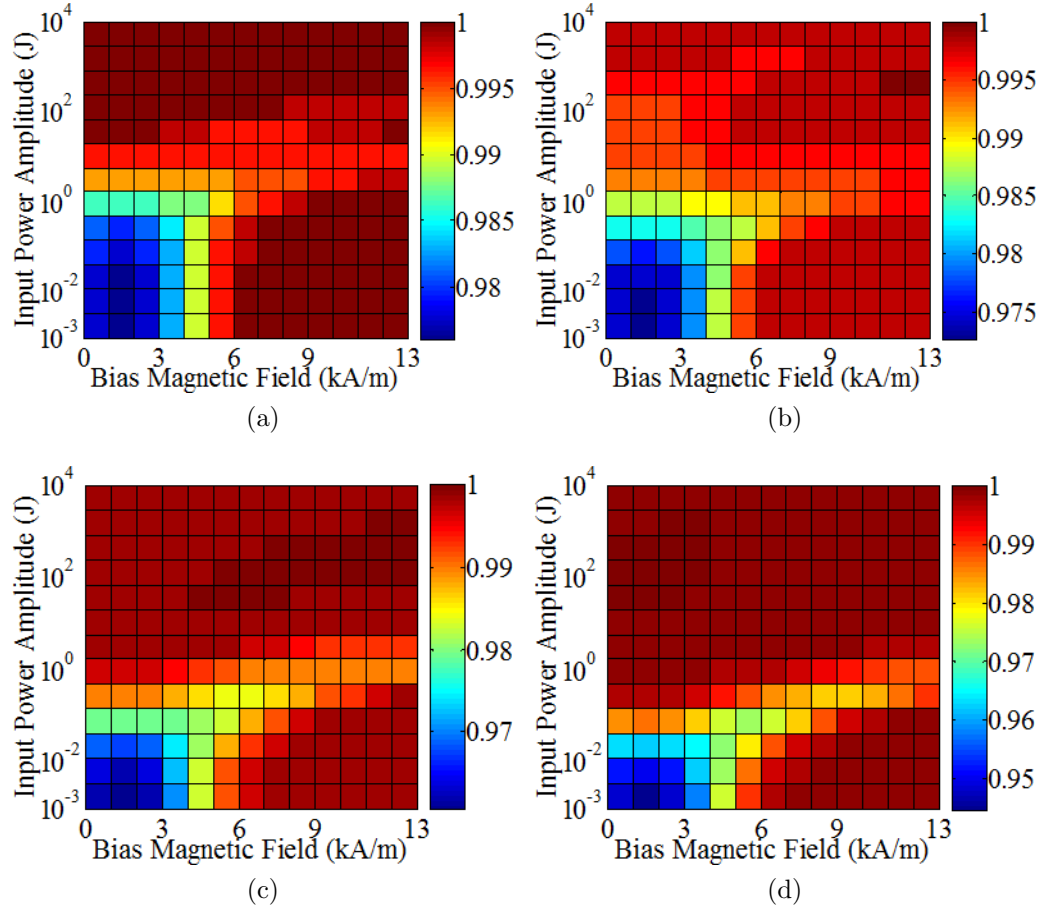


Figure 2.22: Normalized resonant frequency of the C-F composite as a function of the operating conditions for Galfenol embedded at the (a) reference or minimum, (b) 33 %, (c) 66 %, and (d) 100 % or maximum locations (top views shown,  $\xi_G = 0.1$ ).

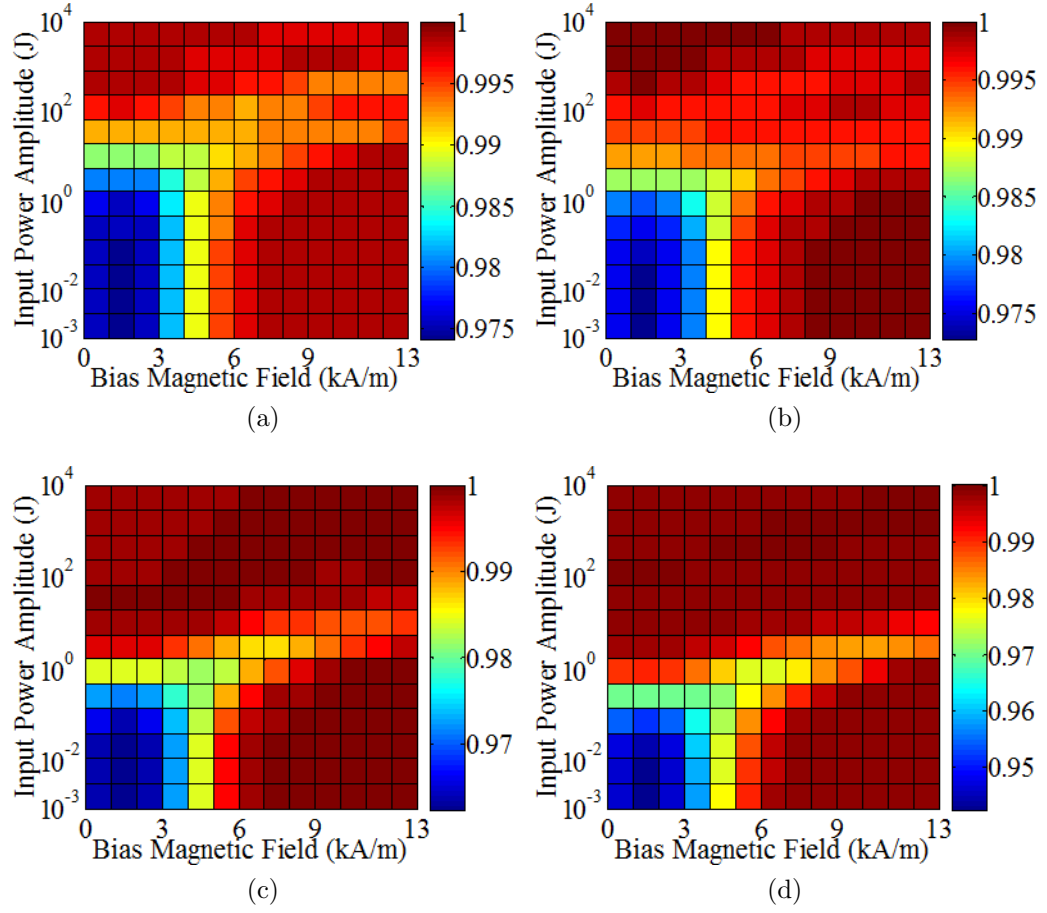


Figure 2.23: Normalized resonant frequency of the C-C composite as a function of the operating conditions for Galfenol embedded at the (a) reference or minimum, (b) 33 %, (c) 66 %, and (d) 100 % or maximum locations (top views shown,  $\xi_G = 0.1$ ).



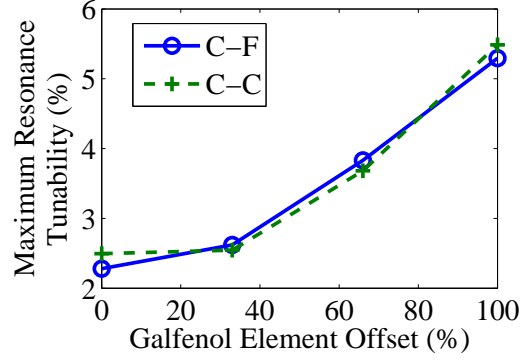


Figure 2.24: Effect of Galfenol's vertical location in the composite on the maximum tunability of the vibration absorber's resonance for the C-F and C-C boundary conditions ( $\xi_G = 0.1$ ).

## Discussion

For a given input power amplitude, semi-active control of the vibration absorber's resonant frequency is accomplished by modulating the composite's resonance between its minimum and maximum frequencies through changes in the bias magnetic field. The results show that nearly uniform controllability occurs below a threshold of the input power amplitude (i.e., about  $5 \times 10^{-1}$  J for the C-F boundary conditions,  $\xi_G = 0.1$ , and Galfenol located at the neutral axis). The maximum tunability of the vibration absorber's resonant frequency also occurs in this region, and can be achieved with relatively weak magnetic fields of 8 kA/m or less.

Above the threshold of the input power amplitude, the composite's capacity for resonance tuning decreases, and eventually the composite's resonant frequency becomes uncontrollable. Despite this, some controllability exists over a wide range (about 3 to 5 orders of magnitude) of the power amplitude of the excitation. The

decrease in controllability is attributed to the increased stress on the Galfenol element as the power amplitude increases. Galfenol becomes magnetically saturated when subjected to sufficiently large compressive stresses, causing the elastic modulus to saturate (see Fig. 2.3). Thus, the expression,

$$\lim_{|T| \rightarrow \infty} E_G(t) = E_G^{\text{sat}} \approx 58 \text{ GPa}, \quad (2.20)$$

holds for 1D Galfenol elements. This tendency toward a constant elastic modulus is slowed by increasing the bias magnetic field to counteract increases in the stress amplitude. This explains why the location of the minimum resonant frequency in Figs. 2.19 and 2.20 shifts to higher magnetic fields as the input power amplitude increases above the threshold value.

From the above reasoning, it can be postulated that the effect of the input power amplitude will depend upon the composite geometry. The power amplitude threshold will be lower for more compliant composites, and vice versa. This is supported by the results of the parametric studies. As seen in Figs. 2.19 and 2.20, the threshold decreases as Galfenol volume fraction increases, because the aluminum matrix is replaced with a softer material. Similarly in Figs. 2.22 and 2.23, the threshold decreases as Galfenol is shifted away from the neutral axis due to a decrease in the composite's area moment of inertia and an increased bending stress on the Galfenol element. Thus, while the results are obtained for the single set of composite parameters given in Table 2.3, the topology of the resonant frequency surfaces for arbitrary composite geometries will be equivalent to those presented in this paper, but scaled along the input power axis.

When the input power is small, the Galfenol element behaves nearly linearly, because the bending stress has a small variation. Under this condition, the percent

change in the resonant frequency due to a change in the bias magnetic field is maximized for a given geometry of the composite,

$$\Delta\omega_{r,\max} \approx \left| \sqrt{\frac{E_{\text{eq,min}} I(E_{\text{eq,min}})}{E_{\text{eq,max}} I(E_{\text{eq,max}})}} - 1 \right|, \quad (2.21)$$

where  $I(E_{\text{eq,min}})$  and  $I(E_{\text{eq,max}})$  are the area moments of inertia when the equivalent Young's modulus of the composite is at its minimum and maximum value, respectively. The area moment of inertia of the composite varies with the Galfenol volume fraction and Young's modulus of the Galfenol element, because the Galfenol element is scaled according to Eq. (2.8) to yield an equivalent section of matrix material. Accordingly, the area moment of inertia of the composite decreases as the volume fraction increases and as the Young's modulus of Galfenol decreases from its saturated value. The observed tunability in the resonant frequency is therefore due to a combination of the change in Galfenol's Young's modulus and the change in the composite's area moment of inertia. The maximum resonant frequency tunability peaks when the Galfenol volume fraction is 100 %. For this case, if the constitutive response of the Galfenol element is assumed linear and uniform, Eq. (2.21) approximately becomes

$$\Delta\omega_{r,\max} \approx \left| \sqrt{\frac{(28.5 \times 10^9) (2.47 \times 10^{-13})}{(58.0 \times 10^9) (5.12 \times 10^{-13})}} - 1 \right| = 51.3 \%, \quad (2.22)$$

which is close to the observed maximum resonant frequency tunability of 49 %. The resonant frequency tunability due to only the maximum change in Galfenol's Young's modulus would be about 30 %.

The magnitude of the resonant frequency tunability and the effect of the bias magnetic field on the surfaces will be altered if the Galfenol properties given in Table 2.3 are modified. The material anisotropy constants  $K^k$ , and saturation magnetization  $M_s$  have a minimal effect on Galfenol's elastic modulus behavior. However, the smoothing factor  $\Omega$  (which accounts for material imperfections) and the magnetostriction constant  $\lambda_{100}$  directly control the  $\Delta E$  effect. Referring to Fig. 1.4, the smoothness of the transition between the two linear elastic branches is controlled by  $\Omega$ , while  $\lambda_{100}$  controls the width of the transition. As such, the  $\Delta E$  effect is enhanced as the magnetostriction constant increases and as the amount of material imperfections ( $\Omega$ ) decreases. Only small improvements over the  $\Omega$  value of 776.73 used in this paper can be expected, as evidenced by the reported values of  $\Omega$  for Galfenol in the literature (500 to 2100 [61, 19, 32]). A  $\lambda_{100}$  value of  $157 \times 10^{-6}$  is used in this paper, yielding  $E_0 = 28.6$  GPa. From Eq. (1.16) with  $E_{H2} = E(H = 0, T = 0)$ , this results in  $\Delta E_{\max} \approx 100$  %. If the maximum  $\lambda_{100}$  value for polycrystalline Galfenol –  $187 \times 10^{-6}$  [93] – is instead used, then  $E_0 = 23.5$  GPa and  $\Delta E_{\max} \approx 150$  %. Therefore, the resonant frequency tunability results presented in this paper are relatively conservative estimations of the true potential of Galfenol-based active composites.

The effect of the boundary conditions on the resonant frequency surfaces is small for both parametric studies. The thresholds of the input power amplitude are lower for the C-F boundary condition due to the composite's increased compliance as discussed above. As seen in Figs. 2.21 and 2.24, the boundary condition has an insignificant effect on the maximum resonant frequency tunability in all cases. For the C-C beam, as the magnetic field increases a compressive blocking stress develops to constrain the Galfenol element and prevent magnetostriction along the axis of the beam. It

is well known that this will result in an effective softening of the beam with respect to transverse vibration, and will thus contribute to the resonant frequency tuning response of the vibration absorber. This effect is not included in the proposed model and should be investigated in future studies.

### **Concluding remarks**

This section investigated the semi-active control of a magnetically-tunable vibration absorber's resonant frequency. The vibration absorber that was considered is an aluminum-matrix composite containing Galfenol. For computational reasons, the composite was modeled as a single-degree-of-freedom system. The complex constitutive behavior was included by using a fully-nonlinear, anhyseretic model of Galfenol from the literature. Despite the one dimensional simplification, the variation in Galfenol's elastic modulus along the length and through the thickness of the Galfenol element was retained by considering the stress distribution throughout the element and the asymmetric tension-compression behavior of Galfenol. Two boundary conditions – cantilevered and clamped-clamped – were imposed on the composite. Resonant frequency tunability of the absorber was investigated by computing its frequency response to harmonic base excitation as a function of the operating conditions – input power amplitude and bias magnetic field. Parametric studies were presented to characterize the effect on resonant frequency tunability of Galfenol volume fraction and Galfenol's location within the composite.

Results and conclusions from the study are summarized as follows:

- Nearly uniform controllability of the vibration absorber’s resonant frequency is possible below a threshold of the input power amplitude. The resonant frequency is modulated between its minimum and maximum value using weak magnetic fields of 0 to 8 kA/m. As the input power amplitude increases above the threshold, the controllability decreases and stronger magnetic fields are required to realize the control.
- The observed resonant frequency tunability results from changes in Galfenol’s Young’s modulus and the composite’s area moment of inertia.
- The boundary condition imposed on the composite was found to have a minimal effect on its resonant frequency tuning behavior. However, the model does not include the effect of axial loading, which is well known to affect the resonant frequency of transverse vibration in beams.
- When the Galfenol element is located at the neutral axis, the maximum resonant frequency tunability varies between 2.5 and 49 % as Galfenol volume fraction increases from 10 to 100 %.
- When Galfenol volume fraction is fixed at 10 %, the maximum resonant frequency tunability varies between 2.5 and 5.5 % as the Galfenol element is offset from the composite’s midplane.
- It was reasoned that the resonant frequency tuning results presented in this section are conservative estimates of the true potential of Galfenol-based vibration absorbers, and can be applied to systems with differences in composite geometry and certain Galfenol material properties.

### 2.2.2 Distributed parameter modeling

The objective of this section is to characterize and model Galfenol composite beams operating as AVAs that are subjected to axial loads and operate at an arbitrary mode of the beam. In this section, the characterization is performed by calculating the beam's resonant frequency as a function of (a) mode number, (b) base acceleration magnitude, (c) bias magnetic field, and (d) Galfenol volume fraction. For nonlinear systems that do not permit the formulation of an eigenvalue problem, the conventional approach for calculating resonant frequencies is to approximate the nonlinear frequency response using a large number of time domain simulations. This approach, which is computationally intensive, especially for multi-degree-of-freedom systems, was used in Section 2.2.1. In the model contained in this section, resonant frequencies of the continuous beam are calculated from time domain responses by incorporating autoresonant feedback control, which was introduced in Section 1.2.4. The continuous, nonlinear bending vibration of the composite beams is modeled using Euler-Bernoulli beam theory. The effects of axial force on the beam, viscoelastic material damping, and beam non-uniformity are included. The distributed parameter model is spatially discretized using the finite difference method. The resulting state-space system is then implemented in Simulink and solved using the Runge-Kutta-Fehlberg method. The model is validated by comparing numerical frequency domain responses to analytical responses, which are derived for the case of a passive beam. Further validation is presented by comparing calculated and measured resonant frequencies and mode shapes of a UAM composite beam containing Galfenol.

## Model development

The system of interest is a metal-matrix composite beam composed of a single matrix material and a single sheet of Galfenol. The system and finite difference nodes are shown in Fig. 2.25. The beam's cross section and an example Galfenol/Al 6061 composite manufactured using UAM are shown in Fig. 2.26.

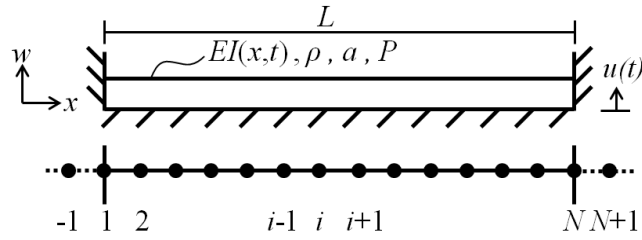


Figure 2.25: Schematic of the base-excited magnetostrictive composite beam and nodes used for finite difference discretization.

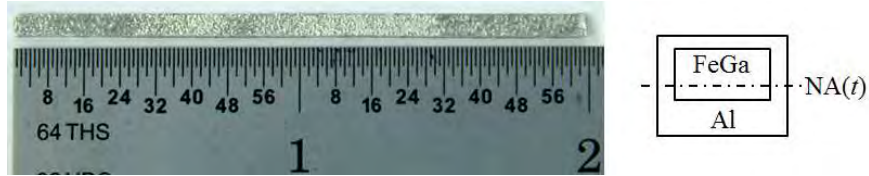


Figure 2.26: Galfenol/Al 6061 composite beam manufactured using UAM and schematic of the beam's cross section; Galfenol and composite dimensions (thickness x width) are 0.51 x 1.02 and 1.02 x 1.91 mm, respectively.

To investigate the effect of an axial force on the dynamic behavior of this composite, clamped-clamped (C-C) boundary conditions are considered. In order to characterize the beam's suitability for use as an AVA, a distributed parameter model of



the beam's transverse vibration is presented. To incorporate the nonlinearity resulting from Galfenol's stress- and magnetic field-dependent elastic modulus, the non-uniformity of the beam along its length is fully retained. The non-uniformity through the thickness is approximated as in Section 2.2.1. AVAs are implemented by coupling them to a host structure exhibiting undesirable vibration. As such, the response of the beam to base excitation is modeled.

Material damping in the composite is modeled as viscoelastic, which is frequency dependent. This model was selected over hysteretic damping, which is frequency independent, because it is well known that ferromagnetic materials exhibit frequency-dependent hysteresis due to eddy currents, which occur even for stress application in the absence of AC magnetic fields. In this paper, the Kelvin-Voigt model for viscoelastic material damping is adopted. This damping model was successfully used (in a simplified form) for the modeling of Galfenol unimorphs by Shu et al. [137]. The following assumptions are used to develop the proposed model detailed in the subsequent subsections:

- Euler-Bernoulli beam theory (i.e., small deflections and negligible shear deformation)
- Mass per unit length of the beam  $\rho A$  and Kelvin-Voigt damping constant  $a$  are constant and uniform
- Bias magnetic field  $H$  is uniform
- The uniform axial force  $P$  is calculated from a static analysis of the 1-D composite

*Beam vibration model*

In this subsection, a state-space system is derived by discretizing the PDE governing transverse vibration of the composite beam. The axial force is then derived, after which the flexural rigidity is presented in the context of unidirectional composites. From Meirovitch [106], the governing equation for the transverse vibration of the Euler-Bernoulli beam considered above is

$$\rho A \ddot{w}(x, t) + [EI(x, t) (a \dot{w}_{xx}(x, t) + w_{xx}(x, t))]_{xx} - P(t) w_{xx}(x, t) = f(x, t), \quad (2.23)$$

where  $P$  is the uniform axial force,  $f$  denotes the applied distributed force,  $\rho$  and  $A$  are the density and cross-sectional area, respectively,  $EI$  represents the flexural rigidity,  $a$  is a viscoelastic parameter for the Kelvin-Voigt damping model,  $w$  is the transverse deflection of the beam, and  $w_x$  and  $\dot{w}$  denote partial derivatives of  $w$  with respect to  $x$  and  $t$ , respectively;  $EI$  is state-dependent and non-uniformity. For base excitation, the total deflection is written as

$$w(x, t) = \bar{w}(x, t) + u(t), \quad (2.24)$$

where  $\bar{w}(x, t)$  is the beam's displacement relative to the base and  $u$  is the base displacement. Insertion of Eq. (2.24) into Eq. (2.23) and neglecting the applied force gives

$$\rho A \ddot{\bar{w}}(x, t) + [EI(x, t) (a \dot{\bar{w}}_{xx}(x, t) + \bar{w}_{xx}(x, t))]_{xx} - P(t) \bar{w}_{xx}(x, t) = -\rho A \ddot{u}(t). \quad (2.25)$$

Thus, in terms of the relative displacement  $\bar{w}(x, t)$ , the base-excited system can be viewed as a beam with static boundary conditions subject to an equivalent force,

$$f_{\text{eq}}(t) = -\rho A \ddot{u}(t). \quad (2.26)$$

After expanding the differentiation, (2.25) can be written as

$$\rho A \ddot{\bar{w}}(x, t) + F^C(\dot{x}, t) + F^K(x, t) = f_{\text{eq}}(t), \quad (2.27)$$

where the damping force  $F^C$  is

$$F^C(\dot{x}, t) = a (EI_{xx}\dot{w}_{xx} + 2EI_x\dot{w}_{xxx} + EI\dot{w}_{xxxx}), \quad (2.28)$$

and the flexural force  $F^K$  is

$$F^K(x, t) = EI_{xx}\bar{w}_{xx} + 2EI_x\bar{w}_{xxx} + EI\bar{w}_{xxxx} - P\bar{w}_{xx}. \quad (2.29)$$

The governing PDE given by Eqs. (2.27) to (2.29) does not admit an eigenvalue problem nor a closed-form solution due to the beam's spatial and temporal non-uniformity, which results from the magnetic field- and stress-dependent elastic properties of the Galfenol component. Consequently, the PDE is solved approximately by (i) discretizing the beam (Fig. 2.25), (ii) using the finite difference method to approximate spatial derivatives and express the discretized system in state-space form, and (iii) using the explicit Runge-Kutta-Fehlberg method (MATLAB's *ode45*) to solve the state-space system iteratively.

Following discretization, the continuous PDE Eq. (2.27) becomes a system of discrete PDEs in terms of the unknown nodal displacements  $\bar{w}_i$  and their derivatives, where  $i = 2, \dots, N - 1$  since the boundary conditions provide  $\bar{w}_1 = \bar{w}_N = \bar{w}_{x_1} = \bar{w}_{x_N} = 0$ . Of the standard finite difference methods (backward, central, and forward), the central difference method provides the best accuracy [82]; however, it may be undefined at or near boundaries due to its dependence on fictitious nodes  $i = -1, -2, \dots$  or  $i = N + 1, N + 2, \dots$

Using the 2nd order central difference method [82] to approximate the spatial partial derivatives, Eqs. (2.28) and (2.29) can be written at the  $i^{th}$  node as

$$F_i^C(t) \approx a\Delta x^{-4} (A_i\dot{w}_{i+2} + B_i\dot{w}_{i+1} + C_i\dot{w}_i + D_i\dot{w}_{i-1} + G_i\dot{w}_{i-2}), \quad (2.30)$$

and

$$\begin{aligned}
F_i^K(t) &\approx \Delta x^{-4} (A_i \bar{w}_{i+2} + (B_i - \bar{P}) \bar{w}_{i+1} + (C_i + 2\bar{P}) \bar{w}_i + (D_i - \bar{P}) \bar{w}_{i-1} + G_i \bar{w}_{i-2}) \\
&= \Delta x^{-4} (A_i \bar{w}_{i+2} + \bar{B}_i \bar{w}_{i+1} + \bar{C}_i \bar{w}_i + \bar{D}_i \bar{w}_{i-1} + G_i \bar{w}_{i-2}),
\end{aligned} \tag{2.31}$$

where

$$\begin{aligned}
\bar{P} &= \Delta x^2 P \\
A_i &= EI_i + \frac{1}{2}(EI_{i+1} - EI_{i-1}) \\
B_i &= -6EI_i + 2EI_{i-1} \\
C_i &= -2EI_{i+1} + 10EI_i - 2EI_{i-1} \\
D_i &= -6EI_i + 2EI_{i+1} \\
G_i &= EI_i - \frac{1}{2}(EI_{i+1} - EI_{i-1}).
\end{aligned} \tag{2.32}$$

Evaluation of Eqs. (2.30) and (2.31) at nodes  $i = 2$  and  $i = N - 1$  therefore depends on the fictitious nodes  $\bar{w}_{-1}$  and  $\bar{w}_{N+1}$ , respectively. However, by approximating the boundary condition on the slope of the beam using the 2nd order central difference method, the following relations can be derived:

$$\bar{w}_{-1} \approx \bar{w}_2, \quad \bar{w}_{N+1} \approx \bar{w}_{N-1}. \tag{2.33}$$

Using the relations Eq. (2.33), the 2nd order central difference approximation of the damping force  $F_i^C$  and flexural force  $F_i^K$  can be evaluated at all interior nodes.

Since the approximate damping and flexural forces depend only on the nodal velocities and displacements, respectively, the set of  $(N - 2)$  discrete PDEs approximating Eqs. (2.27) to (2.29) can be written in a form resembling a standard multi-degree-of-freedom system,

$$[M] \{\ddot{\bar{w}}\} + [C] \{\dot{\bar{w}}\} + [K] \{\bar{w}\} = \{f_{\text{eq}}\}, \tag{2.34}$$

where  $n$  denotes the order of the error in the approximation of the damping and flexural forces. When the beam is free from an added mass, the global mass matrix

$[M]$  is

$$[M] = \rho A [I], \quad (2.35)$$

where  $[I]$  is the identity matrix. Added masses can be incorporated by increasing  $\rho A$  at nodes over which the mass is located. For this case,  $[M]$  remains diagonal. The 2nd order accurate damping and stiffness matrices ( $[\overset{2}{C}]$  and  $[\overset{2}{K}]$ ) are pentadiagonal matrices, as detailed in Appendix B.1. If increased accuracy is necessary,  $[\overset{4}{C}]$  and  $[\overset{4}{K}]$  may be derived using the 4th order central difference method, as shown in Appendix B.1. For this case, the damping and stiffness matrices are heptadiagonal. Consequently, the system matrices can be considered sparse when a reasonable number of nodes is used. By defining the state vector  $W$  as the nodal displacements and velocities, the state-space representation of Eq. (2.34) can be written as

$$\dot{W} = \begin{bmatrix} [0] & [I] \\ -[M]^{-1}[K] & -[M]^{-1}[\overset{2}{C}] \end{bmatrix} \begin{Bmatrix} \{\bar{w}\} \\ \{\dot{w}\} \end{Bmatrix} + \begin{Bmatrix} \{0\} \\ [M]^{-1}\{f_{eq}\} \end{Bmatrix}. \quad (2.36)$$

The state-space system is implemented and solved in Simulink to utilize an available solver and to improve computational efficiency by precompiling the model.

#### *Calculation of the axial force $P$*

The application of a magnetic field to the composite generates magnetostriction  $\lambda$  in the Galfenol element that is counteracted by the matrix and by a compressive force due to the fixed boundary conditions. To derive an expression for the axial force that develops in the composite, static analysis of a free-free composite subjected to a magnetic field is first considered (Fig. 2.27(a)).

Assuming that a uniform shear stress acts between Galfenol and the surrounding matrix, free body diagrams of the matrix and Galfenol constituents are given in Fig. 2.27(a). Further assuming that there is no slip at the interfaces, the displacement

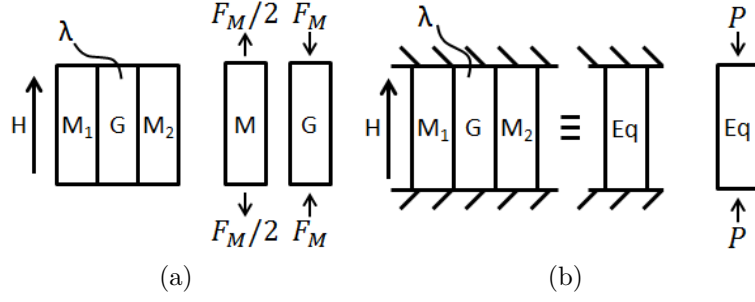


Figure 2.27: Schematic and free body diagram of the 1-D static composite subjected to an applied magnetic field with boundary conditions: (a) free-free, and (b) fixed-fixed.

compatibility between the layers can be expressed as

$$\begin{aligned}\delta_{F-F} &= \delta_G = \delta_{M_1} = \delta_{M_2} \\ &= \frac{-F_M L}{A_G E_G} + \lambda L = \frac{(F_M/2)L}{A_M E_M},\end{aligned}\tag{2.37}$$

where  $\delta_{F-F}$ ,  $\delta_G$ , and  $\delta_{M_1}$  are the displacements of the free-free composite, the Galfenol section, and one of the matrix sections;  $E_M$  and  $E_G$  are the elastic moduli of the matrix and Galfenol, respectively; and  $A_M$  and  $A_G$  are the cross-sectional areas of one of the matrix sections and the Galfenol section, respectively. Rearranging Eq. (2.37) one gets the total force on the Galfenol section applied by the matrix,

$$F_M = \frac{2\lambda(A_M E_M)(A_G E_G)}{A_G E_G + 2A_M E_M}.\tag{2.38}$$

Insertion of Eq. (2.38) in Eq. (2.37) gives the free-free deflection,

$$\delta_{F-F} = \delta_G = \lambda \left(1 - \frac{2A_M E_M}{A_G E_G + 2A_M E_M}\right) L = \lambda_{\text{eff}} L,\tag{2.39}$$

where  $\lambda_{\text{eff}}$  is the effective magnetostriction of the composite. The effective magnetostriction is consistent with the cases of no matrix ( $A_M = 0$ ) and no Galfenol

( $A_G = 0$ ), for which the magnetostriction in the composite is  $\lambda$  and 0, respectively. Now consider a static, fixed-fixed composite and its homogeneous equivalent (Fig. 2.27(b)). By writing a compatibility equation for the equivalent beam, the axial force on the composite can be written as

$$P = -\lambda_{\text{eff}} A_{\text{eq}} E_{\text{eq}}, \quad (2.40)$$

where the parameters of the equivalent beam are found by considering the matrix and Galfenol as springs in parallel,

$$A_{\text{eq}} E_{\text{eq}} = A_G E_G + 2A_M E_M. \quad (2.41)$$

#### *Calculation of the flexural rigidity $EI_i$*

Solution of the state-space system Eq. (2.36) requires calculation of the flexural rigidity  $EI_i$  at each time step for all nodes. The composite's area moment of inertia  $I_i$  is a function of the cross-sectional geometry of an equivalent, homogeneous cross section of matrix material, which depends upon the elastic moduli of the matrix  $E_i^M$  and Galfenol  $E_i^G(x, t)$ . The elastic modulus  $E_i$  of a unidirectional composite is found using the rule of mixtures given by Agarwal et al. [1],

$$E_i(x, t) = E_i^M \xi^M + E_i^G(x, t) \xi^G, \quad (2.42)$$

where  $\xi^M$  and  $\xi^G$  denote the matrix and Galfenol volume fractions, respectively. Consequently, a constitutive model for Galfenol is needed to calculate the magnetic field- and stress-dependent flexural rigidity of the composite. As detailed in [126], before calculating the elastic modulus in the Galfenol element, the stress must be calculated using an inversion of the constitutive model, which has inputs of magnetic field and strain. In this paper, the strain in the beam is calculated using the exact

expression for an Euler-Bernoulli beam,

$$S = -y\bar{w}_{xx} (1 + \bar{w}_x^2)^{-3/2}. \quad (2.43)$$

The spatial derivatives in Eq. (2.43) are calculated at interior nodes  $i = 3, \dots, N - 2$  using the 4th order central difference method. The 2nd order backward, central, and forward difference methods are used for the remaining nodes.

This work utilizes the DEA model developed by Evans and Dapino [61] and discussed in Section 1.2.2.

#### *Autoresonant feedback control*

A Simulink block diagram of the dynamic beam model is shown in Fig. 2.28, where the red, dotted arrows denote the autoresonant feedback. Arbitrary, nonzero initial conditions can be used. Stability of the feedback control is ensured for most systems by limiting the magnitude of the feedback signal [140]. The amplitude of the resonant vibration is controlled by varying the limit. To consider the excitation magnitude's effect on the resonant frequency tunability of the beam, Section 2.2.1 varied the base excitation power. With autoresonant feedback, the in situ excitation power cannot be correctly limited. Thus, the base acceleration magnitude is limited in this model. As a result,  $f_{eq}$  approximately becomes a square wave.

The damping capacity for viscoelastic material damping depends on frequency [52]. As a result, the resonant frequency and autoresonant phase shift  $\phi^*$  will depend on the level of damping. In this section, the damping matrix  $[C]^n$  varies temporally due to the flexural rigidity's non-uniformity, which implies that  $\phi^*$  is time dependent. However, as shown in the following section, the composite beam is a high Q-factor (low damping) system, for which  $\omega_r \approx \omega_n$ . Thus, the time dependence is neglected.



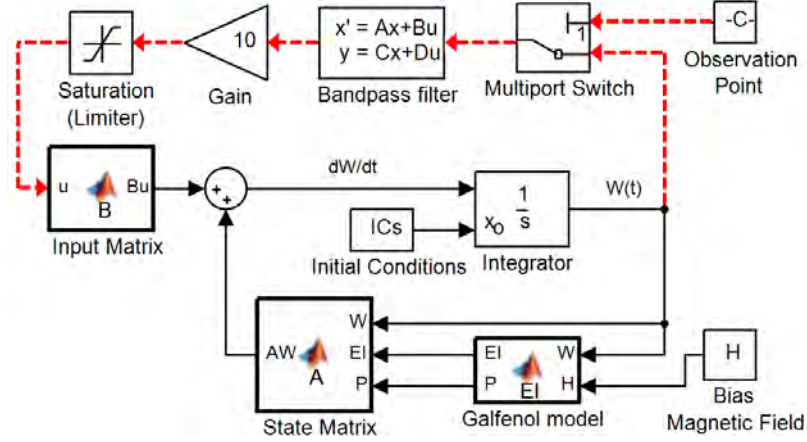


Figure 2.28: Simulink block diagram for the vibration of the FeGa composite beam; autoresonant feedback shown by red, dotted arrows.

For convenience, this section uses an autoresonant feedback control with phase shift  $\phi = \pm\pi/2$  (velocity feedback).

A multi-degree-of-freedom system has a set of amplitude versus phase relations, because the mass(es) on which the force is applied (loading point(s)) and on which the vibration is measured (the observation point(s)) can be selected arbitrarily and independently. For base excitation Eq. (2.26), the loading points are fixed. The observation point is selected by considering a passive, damped beam (i.e., uniform flexural rigidity and no axial force), for which the analytical frequency response of the displacement transmissibility ( $\bar{w}/u$ ) is given by Eqs. (B.19) and (B.20) in Appendix B.2. A representative amplitude versus phase response at 4 locations along the symmetric beam is shown in Fig. 2.29(a). The 3 peaks in the responses correspond to the 1st, 3rd, and 5th modes of vibration, because the base excitation Eq. (2.26) cannot excite asymmetric modes in a clamped-clamped (symmetric) beam. The amplitude versus phase curves are not single-valued and have maxima that deviate significantly from

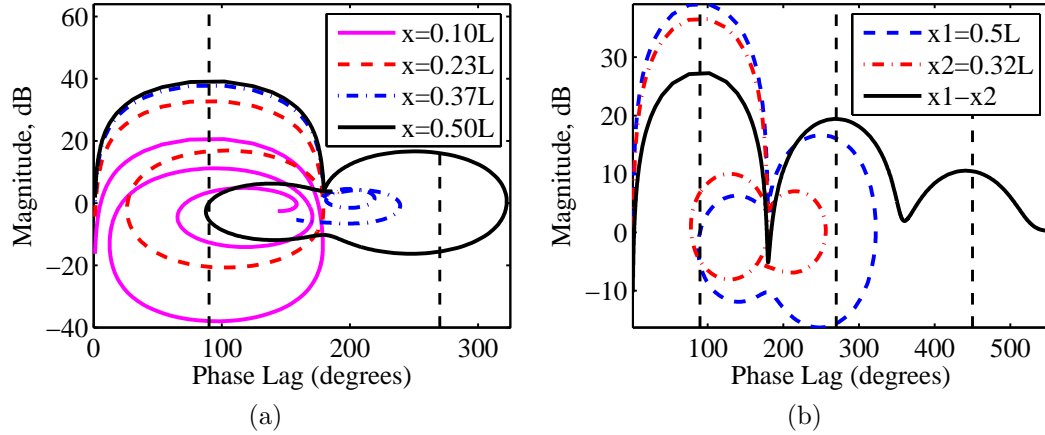


Figure 2.29: Example analytical amplitude versus phase response of the passive beam (a) at select locations along the beam, and (b) for the relative displacement transmissibility  $\tilde{w}/u = (\bar{w}(x = 0.5L) - \bar{w}(x = 0.32L))/u$ ; dashed vertical lines denote  $\phi = \pi/2, 3\pi/2, 5\pi/2$ ; 0 dB = 1 m/m.

the assumption  $\phi^* = \pm\pi/2$ . Sokolov and Babitsky [140] showed that antiresonant regimes (minima in Fig. 2.29(a)) are unstable under phase control. By observing the relative displacement between two points having opposite polarity for the 3rd and 5th modes, the amplitude versus phase curve has peaks at  $\phi \approx \pi/2, 3\pi/2, 5\pi/2$  (Fig. 2.29(b)). Consequently, the simplified autoresonant feedback implemented in this section (velocity feedback) provides an accurate calculation of the resonant frequencies, as detailed in Section 2.2.2. The remaining multi-valuedness is resolved by utilizing a bandpass filter which, when tuned properly, serves as a mode selector. This bandpass filter must be carefully designed for a given system based on mode separation and amplitude versus phase characteristic response.

## Model validation

Model validation is performed in two stages. First, the model is validated for a passive beam, for which an analytical solution is derived in Appendix B.2. Second, the model is validated for the clamped-clamped active beam by comparing measured and calculated mode shapes and resonant frequencies after calculating the Kelvin-Voigt damping constant  $a$ .

Validation of the model for a passive beam is performed by calculating the frequency response of the displacement transmissibility assuming  $a = 1 \times 10^{-6}$  s. The percent error between simulated and analytical responses is shown in Fig. 2.30, where two discretizations (h-refinement, increasing  $N$ ) and two orders of differentiation accuracy (p-refinement, increasing  $n$ ) are compared. The calculated response converges to the analytical using h- and p-refinement.

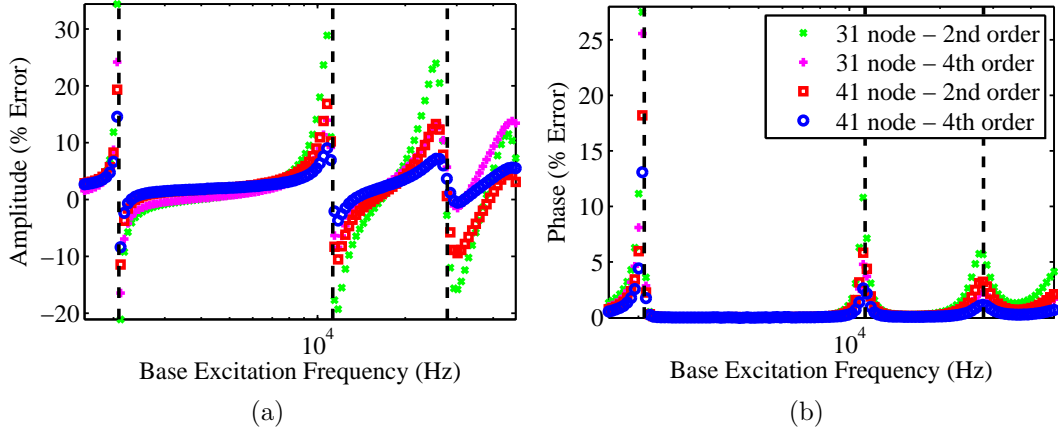


Figure 2.30: Calculated frequency response of the displacement transmissibility of the passive beam  $\tilde{w}/u = (w(x = 0.5L) - w(x = 0.32L))/u$  compared to the analytical response (B.20): percent errors in the (a) amplitude and (b) phase responses; dashed vertical lines denote 1st, 3rd, and 5th undamped resonant frequencies.

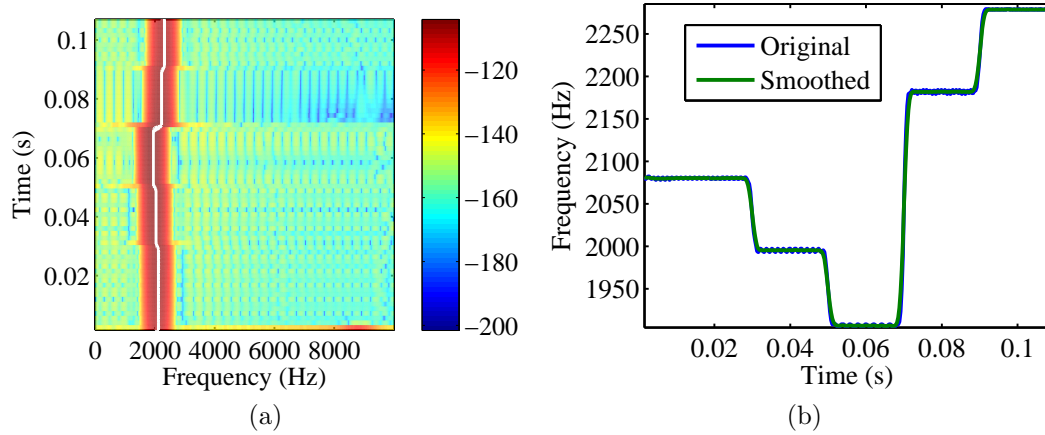


Figure 2.31: Tracking of the passive beam’s 1st resonant frequency using autoresonant feedback control: (a) spectrogram of the simulated relative displacement  $\tilde{w}$  and (b) dominant vibration frequency versus time (overlayed in (a) as a white line); EI decreased at 0.03 and 0.05 s, and increased at 0.07 and 0.09 s.

The autoresonant feedback control is validated by calculating the beam’s vibration while discretely varying  $EI$ , and therefore  $\omega_r$ . An example spectrogram of the time domain response and  $\omega_r(t)$  are given in Fig. 2.31. From an interpolated spectrogram, the resonant frequency is taken as the dominant frequency of vibration after the feedback control stabilizes. For each flexural rigidity, the analytical resonant frequencies of the 1st, 3rd, and 5th modes were calculated from Eq. (B.20) in Appendix B.2. Two metrics are used to characterize the resonant frequency tuning of the AVA (Galfenol beam): the absolute resonant frequencies and the shifts in resonant frequencies. The relative numerical error for the absolute and shift metrics are denoted by  $Er_A$  and  $Er_S$ , respectively. These errors are summarized in Table 2.4, where h- and p-refinement is compared. Modes 1 and 5 were distinguished using a bandpass filter. Thus, the error caused by the filter’s frequency-dependent phase is

included. For the passive beam, the autoresonant feedback control has a fast response time, results in vibration having a very stable frequency content, and is very accurate, with errors below 4 % for all but the 5th mode of one case.

Prior to validating the model for the active beam, the Kelvin-Voigt damping constant  $a$  was estimated from an impulse response of the clamped-clamped UAM composite that is shown in Fig. 2.26. The damping ratio  $\zeta_1$  was calculated as 0.00217 using the logarithmic decrement method, which is applicable due to the presence of significant mode separation [52]. From Eq. (B.13), the damping constant is calculated as  $a = (2\zeta_1)/\omega_1 = 3.56 \times 10^{-7}$ . Transverse vibration of the UAM beam was measured using a Polytec PSV-400 scanning laser vibrometer. A periodic chirp excitation was used, because it has a nearly constant acceleration magnitude over the chirp bandwidth. The experimental setup is shown in Fig. 2.32(a). Masses were glued to the beam at the antinodes of the 3rd mode to shift the 1st and 3rd resonant frequencies into the bandwidth of the shaker. The 5th mode could not be excited. In the model,

Table 2.4: Autoresonant tracking of the passive beam’s resonant frequency: relative numerical errors for the absolute resonant frequencies ( $Er_A$ ) and shifts in resonant frequencies ( $Er_S$ ).

	Mode 1		Mode 3		Mode 5	
	$Er_A$ (%)	$Er_S$ (%)	$Er_A$ (%)	$Er_S$ (%)	$Er_A$ (%)	$Er_S$ (%)
N=31, n=2	0.515	0.768	1.92	1.70	3.54	7.51
N=31, n=4	0.413	0.719	1.02	2.11	2.28	3.79
N=41, n=2	0.334	0.612	1.13	2.04	1.58	2.70
N=41, n=4	0.256	0.519	0.629	2.37	0.256	2.82

the masses were incorporated at nodes over which they were located by locally increasing  $\rho A$ , such that the total mass added to the beam remained constant under h-refinement.

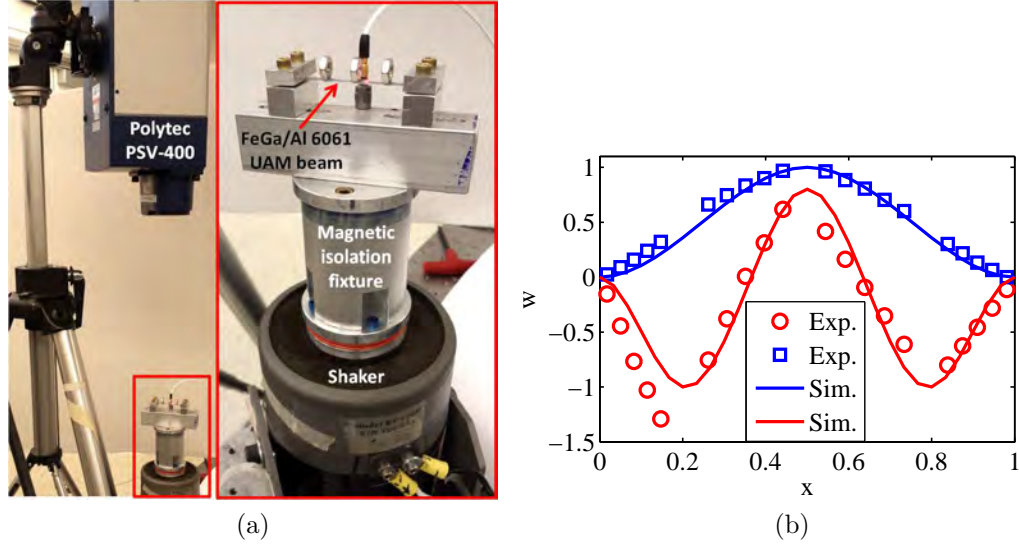


Figure 2.32: (a) Experimental setup for the model validation, and (b) experimental and simulated mode shapes of the UAM Galfenol/Al 6061 composite for the 1st and 3rd modes.

Fig. 2.32(b) compares the measured and simulated 1st and 3rd mode shapes for a base acceleration magnitude of about 2 g. Since only modes 1 and 3 were considered, a bandpass filter was not needed. The laser vibrometer measurements showed that torsional motion of the masses was small compared to the transverse deflection. Experimental and calculated resonant frequencies are compared in Table 2.5. Discrepancies between the two can be attributed to the presence and finite size of the masses, which cause a significant increase in the beam's rotary inertia and a constraint on its local curvature. These physics are not incorporated into the model. The effect

of the rotary inertia of the masses is more pronounced for the 1st mode, because displacements are an order of magnitude higher and the two outside masses rotate. Additional error may have been introduced from imperfect boundary conditions and placement of masses, and by assuming an autoresonant phase  $\phi^* = \pm\pi/2$ . However, considering the model's assumptions and the size of the masses relative to the beam, the accuracy is good overall.

Table 2.5: Percent difference between measured and calculated resonant frequencies of the UAM Galfenol/Al 6061 beam as a function of the number of nodes  $N$  and the order of accuracy  $n$  for the approximation of spatial derivatives; experimental resonant frequencies:  $\omega_{r1} = 502$  Hz,  $\omega_{r3} = 2300$  Hz;  $H = 0$  kA/m,  $|\ddot{u}| \approx 2$  g.

	Mode 1		Mode 3	
	$\omega_{r1}$ (Hz)	Percent Difference	$\omega_{r3}$ (Hz)	Percent Difference
N=31, n=2	594	18.3	2340	1.74
N=31, n=4	598	19.1	2360	2.61
N=41, n=2	597	18.9	2310	0.43
N=41, n=4	593	18.1	2320	0.87

## Results and discussion

To characterize the ability of the UAM Galfenol/Al 6061 beam to operate as an AVA, the resonant frequencies of the 1st and 3rd modes were calculated as a function of bias magnetic field (0–10 kA/m), base acceleration magnitude (0.5–20 g), and Galfenol volume fraction (10–100 %). Time domain responses were calculated using the Simulink model in Fig. 2.28, but without the bandpass filter. Resonant frequencies were calculated as detailed above after the autoresonant feedback control stabilized following a change in the inputs. For each Galfenol volume fraction, the

resonant frequencies were normalized by the maximum frequency to show the percent change that can be achieved by varying the bias magnetic field. This normalization is consistent with prior work [126, 47], but is different from that used to calculate the elastic modulus changes summarized in the introduction of Section 2.2. Results are presented as a series of surfaces (one for each Galfenol volume fraction) using the bias magnetic field and base acceleration limit as independent variables. The data are interpolated to smoothen the surfaces. A top view of the surfaces is shown in Fig. 2.33 for the 3rd mode. Results for the 1st mode are similar and are therefore not shown. For Galfenol volume fractions of 82 % and 100 %, the surfaces are less smooth, because the autoresonant feedback control had difficulty in reaching a steady state. This can be attributed to the large spatial and fast temporal variations in the composite's flexural rigidity that occur for these cases.

In all cases, the minimum resonant frequency occurs for small excitation magnitudes and weak magnetic fields, because the flexural rigidity is a minimum when stress and magnetic field are small. Weak excitations therefore allow for the greatest change in resonant frequency, because Galfenol can be easily tuned to its stiff (magnetically-saturated) state by applying stronger bias magnetic fields. As the base acceleration increases, the resulting higher stresses begin to saturate the Galfenol element. Consequently, the composite beam begins to lose its resonant frequency tunability as the Galfenol element behaves more like a passive material. These results are supported by the authors' previous work [126]. The range of acceleration magnitudes over which the beam's behavior transitions from active to nearly passive will depend on the beam's geometry, the mass loading, and the stiffness of the matrix



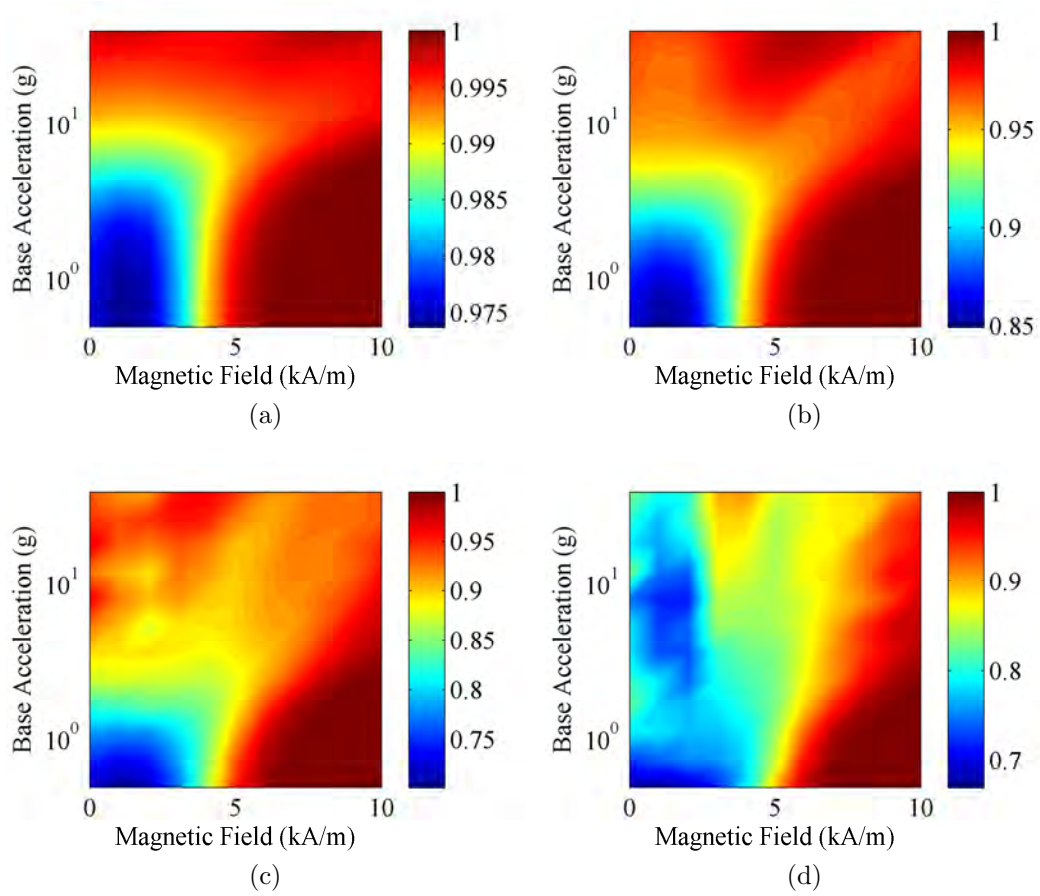


Figure 2.33: Normalized resonant frequency of the 3rd bending vibration mode of the clamped-clamped UAM composite as a function of the base acceleration limit and the bias magnetic field for Galfenol volume fractions of (a) 10 %, (b) 46 %, (c) 82 %, and (d) 100 %; results for 28 % and 64 % are not shown for brevity.

material. The effect of variations in Galfenol's elastic modulus on the composite's behavior will be more pronounced for composites with softer matrices (see Eq. (2.42)). Al 6061 is about 15 % to 130 % stiffer than Galfenol depending on stress and magnetic field. Thus, in Fig. 2.33, the transition shifts toward smaller accelerations as Galfenol volume fraction increases.

The compressive axial force on the beam that develops in response to applied magnetic fields tends to soften the beam and reduce its resonant frequencies. This counteracts the stiffening that occurs as the magnetic field tries to saturate the Galfenol element. This is seen in Fig. 2.33 as a broadening of the tunable region along the magnetic field axis. A broadening along the base acceleration axis was also found for high Galfenol volume fractions. This may be an artifact of the autoresonant feedback control caused by its difficulty in reaching a steady state as mentioned above. In future work, the autoresonant feedback control will be better tuned to more accurately investigate this behavior.

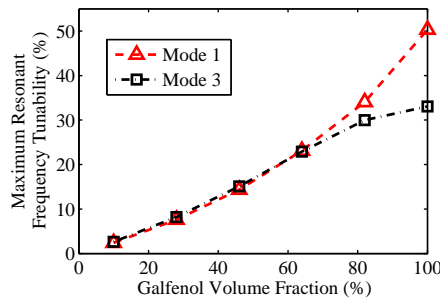


Figure 2.34: Maximum resonant frequency tunability of the Galfenol/Al 6061 beam as a function of Galfenol volume fraction.

A figure of merit for an AVA is its maximum change in resonant frequency. The dependence of this figure of merit on Galfenol volume fraction is detailed in Fig. 2.34 for the 1st and 3rd modes. The maximum tunability increases monotonically from 3 to 51 % as Galfenol volume fraction increases from 10 % to 100 %, respectively. The results for the 1st mode are very similar to those in Section 2.2.1, which used a single-degree-of-freedom model and neglected the axial force. Thus, the incorporation

of the axial force in this model appears to have only a small effect on the maximum tunability of the 1st resonant frequency. The maximum tunability of the 1st and 3rd resonant frequencies was found to be nearly equal except at high Galfenol volume fractions. Thus, with regard to this figure of merit, the performance of the Galfenol beam as an AVA does not degrade when operated at higher modes.

### **Concluding remarks**

This section investigated the use of Galfenol composite beams as solid-state, adaptive vibration absorbers that operate at an arbitrary vibration mode. The manufacture of these structures by UAM was discussed. To characterize the stiffness tunability of the beams, a distributed parameter model of their transverse vibration was presented. The model adopts Euler-Bernoulli beam theory and incorporates Galfenol's nonlinear constitutive behavior, an axial force, viscoelastic material damping, and the beams' non-uniformity. The model was used to calculate the 1st and 3rd resonant frequencies of a FeGa/Al 6061 composite beam as a function of base acceleration, FeGa volume fraction, and bias magnetic field. Autoresonant feedback control was used as a numerical technique to maintain the resonant state under changes to the system. An extensive validation of the model was conducted using analytical responses and measurements of a FeGa/Al 6061 composite beam, which was manufactured using UAM. Additional measurements should be obtained in future work to quantify the model's performance at nonzero bias magnetic fields.

The conclusions from the study are summarized as follows:

- Autoresonant feedback control is an efficient numerical technique for the calculation of the resonant frequency of complex nonlinear systems that are subjected to changes in system parameters. For multi-degree-of-freedom systems, the performance of the control system is improved through careful selection of the vibration observation point(s) and careful tuning of the mode selector (bandpass filter).
- The composite's stiffness can be modulated between its soft and stiff states with weak bias magnetic fields of 10 kA/m or less.
- The maximum tunability of the beam's resonant frequency is possible when the base acceleration, and therefore stress in the Galfenol element, is small. A maximum tunability of 3 to 51 % was found for the UAM Galfenol/Al 6061 composites containing 10 % to 100 % Galfenol by volume, respectively.
- The axial force developed in the clamped-clamped composite due to the application of a bias magnetic field was found to have a minimal effect on the maximum resonant frequency tunability, but an appreciable effect on the range of parameters over which tuning can occur.
- With respect to the maximum resonant frequency tunability, the performance of the Galfenol beam as an adaptive vibration absorber does not degrade (for most cases) when it is operated at higher modes.
- The effect of variations in Galfenol's elastic modulus on the composite's resonant frequency will be more pronounced for composites having softer matrices.

## **Chapter 3: Dynamic Stress Effects in Magnetostrictive Materials**

This chapter investigates the effects of dynamic stress on the constitutive behavior of magnetostrictive materials. In the first section, the effect of mechanically-induced eddy currents on the internal magnetic field and magnetic flux density of cylindrical ferromagnets is studied. This effect, which is known as mechanically-induced magnetic diffusion, is first considered in linear constitutive regimes by analytically solving Maxwell's equations. To investigate the effect of constitutive nonlinearities on the diffusion response, Maxwell's equations are then solved numerically. In the second section, precise measurements of Galfenol's strain and magnetic flux density responses to dynamic, compressive stress are presented along with a novel experimental design, wherein a detailed discussion of specimen design, sensor selection, uncertainty analysis, calibration, error sources, and data processing methods is included. From these measurements, the frequency dependence of dynamic material properties and energy loss components is presented.

## 3.1 Mechanically-Induced Magnetic Diffusion

### 3.1.1 Linear constitutive regimes

In this section, an analytical model of the radial dependence of mechanically-induced magnetic diffusion in cylindrical ferromagnets is presented. Analytical time and frequency domain solutions are derived. The solutions are non-dimensionalized and then used to investigate the spatial and frequency dependence of the internal magnetic field and magnetic flux. Unlike the analytical and numerical solutions referenced in Section 1.2.1, these analytical solutions provide design criteria, reveal the relative importance of each material property, and provide expressions for skin depth and cut-off frequency. For nonlinear operating regimes, the derived solutions can be used to assess whether lamination of the ferromagnet is necessary.

#### Model development

The magnetic diffusion equation for ferromagnets is derived from Maxwell's equations and the assumption that displacement currents are negligible,

$$-\nabla(\nabla \cdot \mathbf{H}) + \nabla^2 \mathbf{H} = \sigma \mathbf{B}_t = \sigma \mu_0 (\mathbf{H} + \mathbf{M})_t, \quad (3.1)$$

where the subscript  $t$  denotes partial differentiation with respect to time,  $\sigma$  represents the electrical conductivity,  $\mu_0$  is the magnetic permeability of free space, and  $\mathbf{H}$ ,  $\mathbf{B}$ , and  $\mathbf{M}$  are the magnetic field strength, magnetic flux density, and magnetization vectors, respectively, which each depend on time  $t$  and position. In magnetostrictive materials,  $\mathbf{M}$  depends on the stress vector  $\mathbf{T}$  such that Eq. (3.1) becomes

$$-\nabla(\nabla \cdot \mathbf{H}) + \nabla^2 \mathbf{H} - \sigma([\mu] \mathbf{H})_t = \sigma([d^*] \mathbf{T})_t, \quad (3.2)$$

where  $[\mu]$  and  $[d^*]$  denote the magnetic field- and stress-dependent magnetic permeability and piezomagnetic coefficient tensors, respectively. In ferromagnetic shape memory alloys,  $\mathbf{M}$  depends on the strain vector  $\mathbf{S}$  such that Eq. (3.1) becomes

$$-\nabla(\nabla \cdot \mathbf{H}) + \nabla^2 \mathbf{H} - \sigma([\mu] \mathbf{H})_t = \sigma(\mu_0 [e] \mathbf{S})_t, \quad (3.3)$$

where  $[e]$  represents the magnetic field- and strain-dependent coupling coefficient tensor.

For biased operation and sufficiently low amplitude excitation, the constitutive tensors  $[\mu]$ ,  $[d^*]$ , and  $[e]$  can be assumed constant. If a cylindrical magnetostrictive material or ferromagnetic shape memory alloy is operated in a transducer having a closed magnetic circuit of low reluctance, demagnetizing fields can be neglected and the circuit can be represented as an infinitely long rod subjected to an axial magnetic field  $H_{\text{ext}}$  at its surface and an axial, distributed force on its ends. Due to the inhomogeneous internal magnetic field, the rod's stiffness, and therefore the applied stress, will be radially dependent [100]. However, to permit an analytical solution, the stress is assumed uniform throughout the rod. Stress uniformity along the axial direction is valid for forcing frequencies sufficiently below mechanical resonance of the rod. Due to this assumption, the rod's mechanical inertia and damping are ignored.

Under the aforementioned assumptions, Eqs. (3.2) and (3.3) simplify to

$$H_{rr}(r, t) + H_r(r, t)/r - \sigma\mu H_t(r, t) = \sigma d^* T_t(t), \quad (3.4)$$

and

$$H_{rr}(r, t) + H_r(r, t)/r - \sigma\mu H_t(r, t) = \sigma\mu_0 e S_t(t), \quad (3.5)$$

respectively, where  $r$  is the radial coordinate, the subscript  $r$  denotes partial differentiation with respect to  $r$ , and  $\mu$ ,  $d^*$ , and  $e$  are the 33 components of the respective

tensors. Thus, the 1D magnetic diffusion problem for ferromagnetic shape memory alloys is identical to that for magnetostrictive materials if  $\mu_0 e$  and  $S(t)$  are substituted for  $d^*$  and  $T(t)$ , respectively. Consequently, it is sufficient to only solve Eq. (3.4), which resembles the 1D field-induced magnetic diffusion problem, but with a forcing term.

### 1D time- and frequency domain solutions

To solve Eq. (3.4), it is convenient to have zero boundary conditions. This is accomplished using the change of variables,  $\tilde{H}(r, t) = H(r, t) - H_{\text{ext}}$ , so that the initial boundary value problem is

$$\tilde{H}_{rr}(r, t) + \tilde{H}_r(r, t)/r - \sigma\mu\tilde{H}_t(r, t) = \sigma d^* T_t(t), \quad (3.6)$$

$$\tilde{H}(r, t = 0) = 0, \quad (3.7)$$

$$\tilde{H}(r = R, t) = 0, \quad (3.8)$$

$$\tilde{H}(r, t) \text{ finite}, \quad (3.9)$$

where  $r = R$  is the surface of the rod. Eqs. (3.6)–(3.9) can be written as an inhomogeneous Bessel equation of order zero using the change of variables,  $u = \sqrt{\mu\sigma}r$ ,

$$u^2 \tilde{H}_{uu}(u, t) + u \tilde{H}_u(u, t) - u^2 \tilde{H}_t(u, t) = \frac{d^*}{\mu} u^2 T_t(t), \quad (3.10)$$

$$\tilde{H}\left(\frac{u}{\sqrt{\mu\sigma}}, t = 0\right) = 0, \quad (3.11)$$

$$\tilde{H}(u = \sqrt{\mu\sigma}R, t) = 0, \quad (3.12)$$

$$\tilde{H}\left(\frac{u}{\sqrt{\mu\sigma}}, t\right) \text{ finite}, \quad (3.13)$$

where the subscript  $u$  indicates partial differentiation with respect to  $u$ .

The solution of Eqs. (3.10)–(3.13) is found using the method of eigenfunction expansions. After assuming that  $\tilde{H}(u, t) = D(t)U(u)$ , the eigenvalue problem can be



derived from the homogeneous form of Eq. (3.10) using the method of separation of variables,

$$u^2 U_{uu}(u) + u U_u(u) = k u^2 U(u), \quad (3.14)$$

$$U\left(\frac{u}{\sqrt{\mu\sigma}}\right) \text{ finite}, \quad (3.15)$$

$$U(\sqrt{\mu\sigma}R) = 0, \quad (3.16)$$

where the separation constant  $k$  must be negative (i.e.,  $k = -\lambda^2$ ) to avoid trivial solutions [5]. The solution of the eigenvalue problem Eqs. (3.14)–(3.16) is given by Asmar [5] as

$$U^n(u) = J_0\left(\frac{\alpha_0^n}{\sqrt{\mu\sigma}R}u\right), \quad (3.17)$$

corresponding to the eigenvalues

$$(\lambda^n)^2 = (\alpha_0^n / (\sqrt{\mu\sigma}R))^2, \quad (3.18)$$

where  $n = 1, 2, 3 \dots$  is an index,  $J_0$  is the Bessel function of order zero, and  $\alpha_0^n$  is the  $n^{\text{th}}$  positive zero of  $J_0$ . Using the method of eigenfunction expansions, the solution of Eq. (3.10) has the form

$$\tilde{H}(u, t) = \sum_{n=1}^{\infty} D^n(t) U^n(u) = \sum_{n=1}^{\infty} D^n(t) J_0\left(\frac{\alpha_0^n}{\sqrt{\mu\sigma}R}u\right). \quad (3.19)$$

Insertion of Eq. (3.19) into Eq. (3.10) followed by simplification using Eqs. (3.14) and (3.17) gives

$$\sum_{n=1}^{\infty} \left[ J_0\left(\frac{\alpha_0^n}{\sqrt{\mu\sigma}R}u\right) (D_t^n(t) + (\lambda^n)^2 D^n(t)) \right] = -\frac{d^* T_t(t)}{\mu}. \quad (3.20)$$

After multiplying both sides of Eq. (3.20) by  $u J_0(\alpha_0^s u / (\sqrt{\mu\sigma}R))$ , integrating with respect to  $u$  from 0 to  $\sqrt{\mu\sigma}R$ , interchanging the order of integration and summation,

and using the orthogonality of the Bessel functions [5], only the  $s^{\text{th}}$  term of the summation survives,

$$\frac{\mu\sigma R^2}{2} J_1^2(\alpha_0^s) (D_t^s(t) + (\lambda^s)^2 D^s(t)) = -\frac{d^*}{\mu} T_t(t) \int_0^{\sqrt{\mu\sigma}R} u J_0\left(\frac{\alpha_0^s}{\sqrt{\mu\sigma}R} u\right) du, \quad (3.21)$$

where  $J_1$  is the Bessel function of order 1. Evaluating the integral in Eq. (3.21) using the change of variables,  $k = \alpha_0^s u / (\sqrt{\mu\sigma}R)$ , and an integral identity of Bessel functions [5], one gets

$$D_t^s(t) + (\lambda^s)^2 D^s(t) = -\frac{2d^*}{\mu\alpha_0^s J_1(\alpha_0^s)} T_t(t), \quad (3.22)$$

$$D^s(0) = 0. \quad (3.23)$$

The initial condition Eq. (3.23) is derived by inserting Eq. (3.19) into Eq. (3.11) to get

$$\tilde{H}(r, t=0) = \sum_{s=1}^{\infty} D^s(0) J_0\left(\frac{\alpha_0^s}{R} r\right) = 0, \quad (3.24)$$

which is a 0<sup>th</sup> order Bessel series expansion of  $f(r) = 0$ , for which the expansion coefficients  $D^s(0)$  must all equal zero. For a harmonic stress,  $T(t) = \hat{T} \exp(j\omega t)$ , the solution of Eqs. (3.22)–(3.23) is

$$D^s(t) = \hat{T} M^s(\omega) \left( e^{j(\omega t + \phi^s(\omega))} - e^{j\phi^s(\omega)} e^{-(\lambda^s)^2 t} \right), \quad (3.25)$$

where the magnitude  $M^s(\omega)$  and phase  $\phi^s(\omega)$  of the modal frequency response  $\hat{D}^s(j\omega)$  are

$$M^s(\omega) = \left( \left( \hat{D}_{\text{Re}}^s(\omega) \right)^2 + \left( \hat{D}_{\text{Im}}^s(\omega) \right)^2 \right)^{1/2} \quad (3.26)$$

and

$$\phi^s(\omega) = \angle \left( \hat{D}_{\text{Re}}^s(\omega) + j \hat{D}_{\text{Im}}^s(\omega) \right), \quad (3.27)$$

where

$$\hat{D}_{\text{Re}}^s(\omega) = \frac{-2d^* (\mu\sigma\omega R^2)^2}{\mu\alpha_0^s J_1(\alpha_0^s) ((\alpha_0^s)^4 + (\mu\sigma\omega R^2)^2)}, \quad (3.28)$$

$$\hat{D}_{\text{Im}}^s(\omega) = \frac{-2d^* \alpha_0^s (\mu\sigma\omega R^2)}{\mu J_1(\alpha_0^s) ((\alpha_0^s)^4 + (\mu\sigma\omega R^2)^2)}. \quad (3.29)$$

The total time domain solution in the original coordinates is

$$H(r, t) = \sum_{s=1}^{\infty} \left[ D^s(t) J_0\left(\alpha_0^s \frac{r}{R}\right) \right] + H_{\text{ext}}, \quad (3.30)$$

where the real and imaginary part of Eq. (3.25) are retained for cosinusoidal and sinusoidal forcing, respectively. By inserting the steady-state part of Eq. (3.25) into Eq. (3.19), the frequency response of  $\tilde{H}(r, t)$  can be written as

$$G(r, j\omega) = \hat{T} \sqrt{G_{\text{Re}}^2 + G_{\text{Im}}^2} \exp(j\angle(G_{\text{Re}} + jG_{\text{Im}})), \quad (3.31)$$

where

$$G_{\text{Re}}(r, \omega) = \sum_{s=1}^{\infty} \left[ J_0\left(\alpha_0^s \frac{r}{R}\right) \hat{D}_{\text{Re}}^s(\omega) \right], \quad (3.32)$$

$$G_{\text{Im}}(r, \omega) = \sum_{s=1}^{\infty} \left[ J_0\left(\alpha_0^s \frac{r}{R}\right) \hat{D}_{\text{Im}}^s(\omega) \right]. \quad (3.33)$$

### Non-dimensionalization of the analytical solutions

The time domain solution is non-dimensionalized in two steps. First, the rod's radius is written in terms of a parameter  $q$  and penetration (skin) depth  $\delta$  as

$$\frac{R}{\delta} = q. \quad (3.34)$$

For field- and mechanically-induced diffusion, the skin depth can be generally defined as the depth from the surface at which the amplitude of the dynamic magnetic flux

$\tilde{B}$  has attenuated by an amount  $\psi$  relative to the amplitude at the surface. Using the linear piezomagnetic equation

$$\tilde{B}(r, t) = \mu \tilde{H}(r, t) + d^* T(t) \quad (3.35)$$

and boundary condition Eq. (3.8), the surface field is  $\tilde{B}(r = R, t) = d^* T(t)$ . Consequently, if  $R = \delta$  then

$$\left| \tilde{B}(r = 0, t) \right| = \psi \left| \tilde{B}(r = R, t) \right| = \psi d^* \hat{T}. \quad (3.36)$$

Evaluation of Eq. (3.36) using Eq. (3.35) and the steady-state response of Eq. (3.19) followed by simplification gives

$$\left| \sum_{s=1}^{\infty} \left[ \frac{(-2p^2/\alpha_0^s) + j(-2p\alpha_0^s)}{J_1(\alpha_0^s) ((\alpha_0^s)^4 + p^2)} \right] + 1 \right| = \psi, \quad (3.37)$$

where  $p = \mu\sigma\omega\delta^2$ . For field-induced diffusion of plane waves,  $\psi = \exp(-1)$  [92], whereas for field-induced diffusion in cylinders,  $\psi = (J_0(\sqrt{-1}))^{-1}$  [58]. By numerically solving Eq. (3.37) for the latter condition, one gets  $p \approx 4.3393$ . Thus, the skin depth for mechanically-induced diffusion in cylinders is

$$\delta^M \approx 2.0831 (\mu\sigma\omega)^{-1/2} = 2.0831 \delta^H, \quad (3.38)$$

where  $\delta^H$  is the skin depth for field-induced diffusion in cylinders, which is given in [58]. The condition  $\delta^M = \delta^H$  can be specified, but at the expense of having a different meaning (i.e., different  $\psi$ ) for the skin depth for the two types of diffusion. Thus,  $\delta^M$  as given by Eq. (3.38) is used in this section.

The second step used to non-dimensionalize the time domain solution is to non-dimensionalize the dynamic field such that the dynamic flux it would produce on its own is normalized by the magnitude of the dynamic flux produced by the stress alone.

Therefore, the non-dimensionalized dynamic field is

$$\bar{H}(r, t) = \frac{\mu}{|d^* \hat{T}|} \tilde{H}(r, t), \quad (3.39)$$

while the non-dimensionalized total field is  $\dot{H}(r, t) = \bar{H}(r, t) + H_{\text{ext}}$ .

To non-dimensionalize the frequency domain solution, the first step is to normalize the frequency by a cut-off frequency defined as the frequency for which  $\delta = R$  [58]. Using Eq. (3.38), the cut-off frequency for mechanically-induced diffusion is given as

$$\omega_c^M \approx (2.0831)^2 (\mu \sigma R^2)^{-1} = 4.3393 \omega_c^H, \quad (3.40)$$

where  $\omega_c^H$  is the cut-off frequency for field-induced diffusion in cylinders, which is given in [58]. Thus, by comparing Eq. (3.40) to Eqs. (3.34) and (3.38), it is found that the frequency can be scaled according to

$$\omega = q^2 \omega_c^M. \quad (3.41)$$

The second generalization step is the same as that used for the time domain solution (i.e., Eq. (3.39)).

The non-dimensionalized time domain solution is given as follows. After simplification, the use of Eqs. (3.34) and (3.38) in Eq. (3.39) gives

$$\bar{H}\left(\frac{r}{R}, t\right) = \sum_{s=1}^{\infty} \left[ J_0\left(\alpha_0^s \frac{r}{R}\right) \bar{M}^s(q) (W(t) - X(t)) \right], \quad (3.42)$$

where

$$W(t) = \exp(j(\omega t + \bar{\phi}^s(q))), \quad (3.43)$$

$$X(t) = \exp(j\bar{\phi}^s(q)) \exp\left(-\frac{(\alpha_0^s)^2 \omega}{4.3393 q^2} t\right). \quad (3.44)$$

As before, the real and imaginary parts of Eqs. (3.43) and (3.44) are retained for cosinusoidal and sinusoidal forcing, respectively. The magnitude  $\bar{M}^s(q)$  and phase  $\bar{\phi}^s(q)$  of  $\bar{D}^s(jq)$  are calculated analogous to Eqs. (3.26) and (3.27), where the real and imaginary parts of  $\bar{D}^s(jq)$  are, respectively,

$$\bar{D}_{\text{Re}}^s(q) = \frac{-2 \operatorname{sgn}(d^* \hat{T}) (4.3393q^2)^2}{\alpha_0^s J_1(\alpha_0^s) ((\alpha_0^s)^4 + (4.3393q^2)^2)} \quad (3.45)$$

and

$$\bar{D}_{\text{Im}}^s(q) = \frac{-2 \operatorname{sgn}(d^* \hat{T}) \alpha_0^s (4.3393q^2)}{J_1(\alpha_0^s) ((\alpha_0^s)^4 + (4.3393q^2)^2)}, \quad (3.46)$$

where  $\operatorname{sgn}()$  is the signum function. The steady-state magnitude of  $\bar{H}$ ,

$$\left| \bar{H}\left(\frac{r}{R}, t \rightarrow \infty\right) \right| = \sum_{s=1}^{\infty} \left[ J_0\left(\alpha_0^s \frac{r}{R}\right) \sqrt{(\bar{D}_{\text{Re}}^s)^2 + (\bar{D}_{\text{Im}}^s)^2} \right], \quad (3.47)$$

is only a function of  $r/R$  and  $q$ .

The frequency response of  $\bar{H}(r/R, t)$  is

$$\bar{G}\left(\frac{r}{R}, jq\right) = \frac{\mu}{|d^* \hat{T}|} G\left(r, j(q^2 \omega_c^M)\right) = \sqrt{\bar{G}_{\text{Re}}^2 + \bar{G}_{\text{Im}}^2} \exp(j \angle (\bar{G}_{\text{Re}} + j \bar{G}_{\text{Im}})), \quad (3.48)$$

where

$$\bar{G}_{\text{Re}}\left(\frac{r}{R}, q\right) = \sum_{s=1}^{\infty} \left[ J_0\left(\alpha_0^s \frac{r}{R}\right) \bar{D}_{\text{Re}}^s(q) \right], \quad (3.49)$$

$$\bar{G}_{\text{Im}}\left(\frac{r}{R}, q\right) = \sum_{s=1}^{\infty} \left[ J_0\left(\alpha_0^s \frac{r}{R}\right) \bar{D}_{\text{Im}}^s(q) \right]. \quad (3.50)$$

A non-dimensionalized magnetic flux density can be defined as the dynamic flux density normalized by its magnitude at the surface,

$$\bar{B}\left(\frac{r}{R}, t\right) = \frac{\tilde{B}(r, t)}{|d^* \hat{T}|}. \quad (3.51)$$

After inserting Eqs. (3.35) and (3.19) into Eq. (3.51) and simplifying, the frequency response of  $\bar{B}(r/R, t)$  can be expressed as

$$\bar{F}\left(\frac{r}{R}, jq\right) = \left(\bar{G}_{\text{Re}} + \text{sgn}\left(d^* \hat{T}\right)\right) + j \bar{G}_{\text{Im}}. \quad (3.52)$$

### Eddy current effects in 0D constitutive models

To incorporate the effects of mechanically-induced magnetic diffusion in 0D linear constitutive models, an effective internal magnetic field is first defined as the average field over the rod's cross section,

$$H_{\text{eff}}(t) = \frac{1}{\pi R^2} \int_A H(r, t) dA = \frac{2}{R^2} \int_0^R H(r, t) r dr, \quad (3.53)$$

where  $A$  is the cross-sectional area. Inserting Eq. (3.30) into Eq. (3.53), neglecting the transient part of Eq. (3.25), evaluating the integral as done in Eq. (3.21), and simplifying, one gets

$$H_{\text{eff}}(t) = 2 \sum_{s=1}^{\infty} \left[ \frac{\hat{D}^s(j\omega) J_1(\alpha_0^s)}{\alpha_0^s} \right] \hat{T} e^{j\omega t} + H_{\text{ext}} = \hat{H}_{\text{eff}} T(t) + H_{\text{ext}}. \quad (3.54)$$

Use of the effective field Eq. (3.54) in the 0D linear piezomagnetic equation  $B(t) = \mu^T H(t) + d^* T(t)$  results in

$$B(t) = \mu^T H_{\text{ext}} + \left(d^* + \mu^T \hat{H}_{\text{eff}}\right) T(t) = \mu^T H_{\text{ext}} + d^* \chi^M T(t). \quad (3.55)$$

$\chi^M = \chi_{\text{Re}}^M - j \chi_{\text{Im}}^M$  is the eddy current loss factor for mechanically-induced diffusion,

$$\chi_{\text{Re}}^M = 1 - 4 \sum_{s=1}^{\infty} \left[ \frac{(4.3393q^2)^2}{(\alpha_0^s)^2 ((\alpha_0^s)^4 + (4.3393q^2)^2)} \right], \quad (3.56)$$

$$\chi_{\text{Im}}^M = 4 \sum_{s=1}^{\infty} \left[ \frac{4.3393q^2}{(\alpha_0^s)^4 + (4.3393q^2)^2} \right], \quad (3.57)$$

where Eqs. (3.41) and (3.40) were used to simplify the expressions. Therefore, mechanically-induced magnetic diffusion effects can be represented in linear models

of magnetostrictive materials as a complex piezomagnetic coefficient (or, in general, as a complex magnetoelastic coupling coefficient in ferromagnetic materials),

$$d_c^* = d^* \chi^M = d^* (\chi_{\text{Re}}^M - j \chi_{\text{Im}}^M). \quad (3.58)$$

This is analogous to the representation of field-induced diffusion as a complex magnetic permeability [58]. The non-dimensionalized, effective dynamic field can now be written as

$$\bar{H}_{\text{eff}}(t) = \text{sgn}(d^* \hat{T}) ((\chi_{\text{Re}}^M - 1) - j \chi_{\text{Im}}^M) e^{j\omega t}. \quad (3.59)$$

If the effective field Eq. (3.54) is instead inserted into the 0D linear piezomagnetic equation  $S(t) = dH(t) + s^H T(t)$ , the following results,

$$\begin{aligned} S(t) &= dH_{\text{ext}} + (s^H + d\hat{H}_{\text{eff}}) T(t) = dH_{\text{ext}} + s^H \left( 1 + (\chi^M - 1) \frac{dd^*}{\mu^T s^H} \right) T(t) \\ &= dH_{\text{ext}} + s^H (1 + (\chi^M - 1) \kappa^2) T(t), \end{aligned} \quad (3.60)$$

where  $s^H$  is the compliance at constant field,  $d = d^{*T}$ , and  $\kappa$  is the magnetomechanical coupling factor. Thus, mechanically-induced magnetic diffusion also causes the ferromagnet's effective compliance (and elastic modulus,  $E^H = 1/s^H$ ) to be a complex function of the excitation frequency,

$$s_c^H = s^H (1 + (\chi^M - 1) \kappa^2). \quad (3.61)$$

## Results and discussion

The derived solutions involve infinite summations. For the cases considered in this section, 20 terms are sufficient to ensure convergence of the summations; to generate the following figures, summations were truncated at 500 terms. The general solutions given in the **Non-dimensionalization of the analytical solutions** and



**Eddy current effects in 0D constitutive models** subsections above are illustrated below; thus, the following figures and discussion are valid for all ferromagnetic materials when their behavior is sufficiently linear.

The non-dimensionalized time domain behavior of mechanically-induced diffusion is shown in Fig. 3.1 for positive  $d^*\hat{T}$ . If  $d^*\hat{T}$  is negative, the response is the negative of that shown in Fig. 3.1. The spatial dependence of  $\bar{H}(r/R, t)$  is depicted in Fig. 3.1(a) for  $R/\delta^M = q = 1$ . The transient response quickly decays, and the internal magnetic field becomes nearly sinusoidal in time. The amplitude and phase lag of the steady-state response increase while moving from the rod's surface to its axis. Fig. 3.1(b) shows the frequency dependence of the non-dimensionalized, effective dynamic field  $\bar{H}_{\text{eff}}(t)$  for varying  $q$ . As  $q$  increases, the amplitude and phase lag increase monotonically from 0 and  $\pi/2$  to 1 and  $\pi$ , respectively. The prior numerical solutions [121, 42] are consistent with these trends.

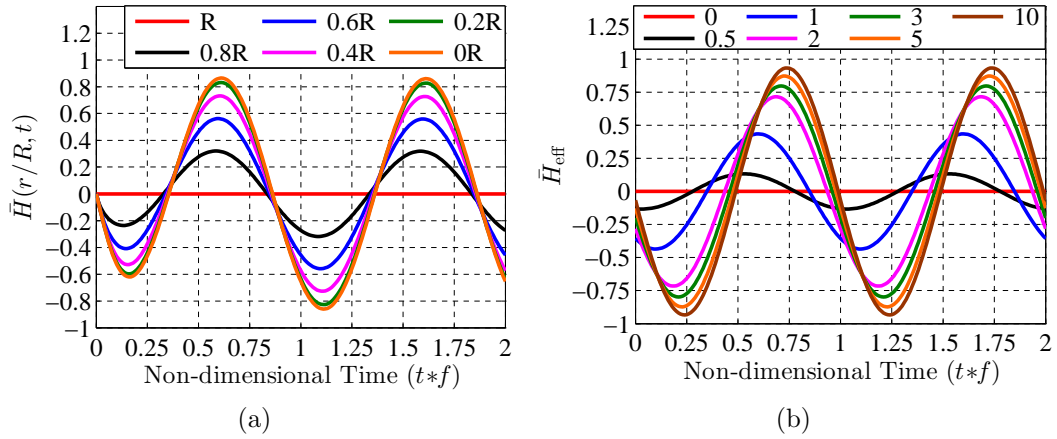


Figure 3.1: Non-dimensionalized time domain response to sinusoidal forcing for positive  $d^*\hat{T}$ , (a) non-dimensionalized dynamic field  $\bar{H}(r/R, t)$  at different radial locations for  $R/\delta^M = q = 1$  and (b) non-dimensionalized, effective dynamic field  $\bar{H}_{\text{eff}}(t)$  for different  $R/\delta^M = q$ .

Physically, as the magnitude of the non-dimensionalized dynamic field increases from 0 toward 1, the magnetic energy increases in magnitude and varies with time such that it opposes changes in the magnetoelastic coupling energy. This suppresses the rotation of magnetic domains, leading to a reduction in magnetic flux changes and a stiffening of the elastic behavior. When the non-dimensionalized dynamic field has a magnitude of 1 and lags behind the stress by  $\pi$  (or by 0 for a material with negative  $d^*$ ), changes in the magnetoelastic coupling energy are balanced by changes in the magnetic energy. As a result, there is no driving potential to rotate magnetic domains away from their bias positions. Therefore, the magnetic flux remains constant and the material behaves passively. This state forms the upper bound on mechanically-induced magnetic diffusion. From this state, increases in  $q$  will have no effect on the constitutive response at radial locations for which the upper bound has been reached.

Fig. 3.2 depicts the steady-state, spatial distribution of the magnitude of the non-dimensionalized dynamic field, which is only a function of  $R/\delta^M = q$ . In each case, the dynamic field is zero at the rod's surface due to the boundary condition Eq. (3.8). Thus, mechanically-induced magnetic domain rotation is unimpeded at the surface, where the dynamic magnetic flux attains its maximum value. When the radius is one skin depth (i.e.,  $q=1$ ), the magnitude of the non-dimensionalized dynamic field at the rod's axis is about 0.86. As  $q$  increases, magnetic diffusion becomes more severe and the magnitude of the internal dynamic field increases accordingly. Interestingly, for moderate to high  $q$ , the magnitude of the non-dimensionalized dynamic field exceeds 1. This is discussed after presenting the frequency domain responses.

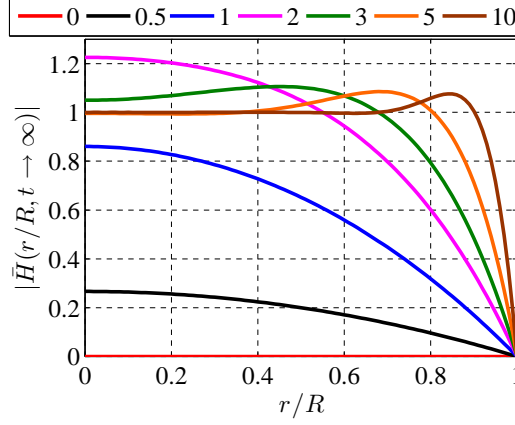


Figure 3.2: Spatial distribution of the steady-state, non-dimensionalized dynamic field for different  $R/\delta^M=q$ .

The non-dimensionalized frequency response of  $\bar{H}(r/R, t)$  at different radial locations is presented in Fig. 3.3(a). For  $\omega/\omega_c$  less than about 1, the magnitude response increases monotonically with frequency and with decreasing  $r$ . In this regime,  $|\bar{G}(r/R, jq)| \propto f^{1.0}$ . With further increases in frequency, the magnitude overshoots 1, peaks, then decreases to 1 and becomes independent of frequency. The peak magnitude decreases and is successively shifted to higher frequencies as one moves closer to the rod's surface. The normalized, frequency-independent field magnitude is 1 at all locations. A  $-\pi/2$  phase shift occurs as frequency increases. The response toward the surface leads that at the axis, particularly after the magnitude response at the axis peaks.

To explain the frequency response in Fig. 3.3(a), recall that diffusion-produced fields are in phase with the eddy currents (Ampère's law), which are induced in proportion to  $-B_t(t)$  (Faraday-Lenz law). Consequently,  $\tilde{H}(r, t) \propto -B_t(r, t)$ . At low frequency, the internal magnetic field is nearly constant and  $-B_t(r, t) \approx -d^*T_t(t)$ ;

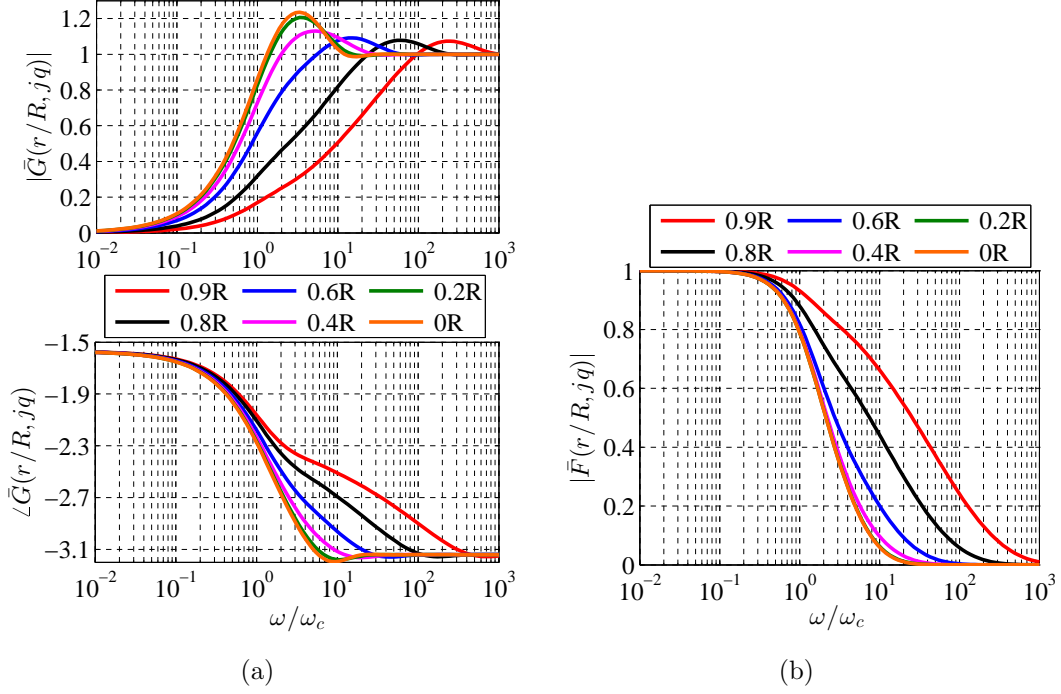


Figure 3.3: Non-dimensionalized frequency response of (a) the dynamic field  $\tilde{H}(r, t)$  – magnitude (top) and phase (bottom) – and (b) the dynamic magnetic flux density magnitude as functions of  $\omega/\omega_c = q^2$  at different radial locations.

thus, the internal field is in phase with  $-d^*T_t(t)$ , which lags  $\pi/2$  behind  $T(t)$ . As frequency increases, the magnitude of the internal field increases along with the proportion of  $-B_t(r, t)$  caused by the field. As a result,  $B(r, t)$  phase shifts toward  $\tilde{H}(r, t)$  and lags behind  $T(t)$ . This in turn creates a lag in the eddy currents and  $\tilde{H}(r, t)$ . This behavior continues with increasing frequency until  $H(t)$  lags behind  $T(t)$  by  $\pi$ , at which point the magnitude of  $\tilde{H}(r, t)$  becomes frequency independent. The overshoot in the magnitude response of  $\tilde{H}(r/R, t)$  results from the non-180 degree phase misalignment between the dynamic field and stress; it does not imply that the dynamic field overcomes the applied stress and begins to drive the system. To illustrate this, the magnitude response of the non-dimensionalized dynamic flux is shown

in Fig. 3.3(b). At the cut-off frequency, the magnitude of the non-dimensionalized dynamic flux is  $0.789 \approx (J_0(\sqrt{-1}))^{-1}$  at the axis; thus, the derivation of the cut-off frequency in the **Non-dimensionalization of the analytical solutions** subsection is verified. Above the cut-off frequency, the magnitude decays monotonically to zero, first at the axis, then closer to the surface.

Given a maximum desired attenuation of the magnetic flux density, Fig. 3.3(b) can be used to define design criteria for applications in which cylindrical ferromagnetic materials are subjected to dynamic axial stress. Selecting 10% attenuation as an example, the forcing frequency should be kept below about 0.63 times the cut-off frequency. If this condition cannot be met, the cut-off frequency should be increased by altering the bias condition, changing the material, or decreasing the rod's radius. If this does not suffice, the material can be laminated to reduce the effect of eddy currents.

The real and imaginary parts of the eddy current factor for mechanically-induced magnetic diffusion are presented in Fig. 3.4. Since this plot is general, it can be used with Eq. (3.58) to directly calculate a complex magnetoelastic coupling coefficient for incorporating mechanically-induced magnetic diffusion effects in any ferromagnetic material.

## Concluding remarks

This section considered the radial dependence of magnetic diffusion in cylindrical ferromagnets that results from the application of a constant surface magnetic field with dynamic mechanical inputs; this effect, which is particularly pronounced in magnetoelastic materials, was termed mechanically-induced magnetic diffusion to distinguish it from the conventional magnetic field-induced magnetic diffusion. The PDE

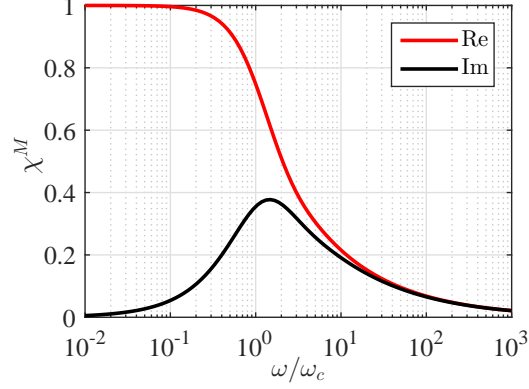


Figure 3.4: Real and imaginary parts of  $\chi^M$ , the eddy current factor for mechanically-induced magnetic diffusion, as a function of  $\omega/\omega_c = q^2$ .

governing radial diffusion was derived from the general magnetic diffusion equation by considering the symmetry of the problem and assuming linear constitutive behavior. Analytical time and frequency domain solutions were derived using the method of eigenfunction expansions. By non-dimensionalizing the dynamic magnetic field and deriving a penetration (skin) depth  $\delta^M$  and cut-off frequency  $\omega_c^M$  for mechanically-induced diffusion, the solutions were non-dimensionalized (i.e., made applicable to all ferromagnetic materials). The skin depth and cut-off frequency are

$$\delta^M \approx 2.0831 (\mu\sigma\omega)^{-1/2} = 2.0831\delta^H \quad (3.62)$$

and

$$\omega_c^M \approx 4.3393 (\mu\sigma R^2)^{-1} = 4.3393\omega_c^H, \quad (3.63)$$

respectively, where  $\delta^H$  and  $\omega_c^H$  are the skin depth and cut-off frequency for field-induced diffusion in cylinders, respectively. By defining an effective internal magnetic field as the average field over the cylindrical rod's cross section, it was shown that the effects of mechanically-induced diffusion can be incorporated in 0D constitutive

models through the use of a complex magnetoelastic coupling coefficient and complex mechanical compliance (or complex elastic modulus).

The non-dimensionalized solutions were plotted to illustrate the response of these materials to mechanically-induced diffusion. The spatial distribution of the magnitude of the non-dimensionalized dynamic field was given for a wide range of skin depths. For forcing frequencies below about 5 times the cut-off frequency (or equivalently, for rods with radii less than about 2.2 times the skin depth), the dynamic, internal magnetic field increases monotonically from zero at the rod's surface to a maximum at its axis. The internal field at the axis also phase lags behind the field closer to the surface. Up to about the cut-off frequency, the magnitude of the steady-state, dynamic field increases in proportion to  $f^{1.0}$ . As forcing frequency increases above that range, the magnitude overshoots its high frequency limit, peaks, then decreases to its high frequency limit, at which point the dynamic magnetic flux becomes zero and further increases in forcing frequency have no effect. The magnitude response of the dynamic magnetic flux was also presented. Given a maximum desired attenuation of the magnetic flux density, this magnitude response can be used to define design criteria for many applications, including dynamic sensors, energy harvesters, vibration dampers, and tunable stiffness devices. For example, for a maximum attenuation of 10 %, the forcing frequency should be kept below about 0.63 times the cut-off frequency. The normalized real and imaginary part of the eddy current factor were plotted as a function of the normalized forcing frequency. Given a material of known properties, the complex magnetoelastic coupling coefficient can be directly calculated from this plot.

### 3.1.2 Nonlinear constitutive regimes

In this section, nonlinear, mechanically-induced magnetic diffusion is investigated by numerically solving the PDE governing mechanically-induced diffusion in cylindrical ferromagnets for the case of nonlinear constitutive behavior. Non-uniformity of the applied stress along the cylindrical specimen's radial direction is also incorporated. First, the model and solution procedure are presented. Next, the procedure is validated for linear regimes by forcing the material properties to be constant and comparing the calculated responses to the analytical solution derived in Section 3.1.1. Then, the effect of nonlinear and time-varying material properties on the diffusion response is studied.

#### Model development

As noted in the **Model development** subsection of Section 3.1.1, mechanically-induced magnetic diffusion in magnetostrictive materials is governed by,

$$-\nabla(\nabla \cdot \mathbf{H}) + \nabla^2 \mathbf{H} - \sigma([\mu] \mathbf{H})_t = \sigma([d^*] \mathbf{T})_t. \quad (3.64)$$

Assuming a cylindrical geometry and neglecting demagnetizing fields, Eq. (3.64) simplifies to

$$H_{rr} + \frac{1}{r}H_r - \sigma(\mu H_t + \mu_t H) = \sigma(d^* T_t + d_t^* T), \quad (3.65)$$

$$H(r, t = 0) = H_{\text{ext}}, \quad (3.66)$$

$$H(r = R, t) = H_{\text{ext}}, \quad (3.67)$$

$$H(r, t) \text{ symmetric about } r = 0, \quad (3.68)$$

where the magnetic permeability  $\mu$ , piezomagnetic coupling coefficient  $d^*$ , magnetic field  $H$ , and stress  $T$  depend on the radial coordinate  $r$  and time  $t$ . The nonlinear



magnetic diffusion response  $H$  is found by numerically solving Eq. (3.65) for a given distributed force  $\bar{F}$  applied to the ends of the rod.

Eq. (3.65) is iteratively solved using the backward time central space (BTCS) finite difference method as done by Evans and Dapino [64], who numerically solved an equivalent equation. To apply this method, the rod is discretized into concentric sections of equal radial width, as shown in Fig. 3.5. Discretization nodes are located at the center of each section to facilitate the calculation of the stress applied to each section. By considering the sections as axial springs in parallel, the force  $F_i$  applied to section  $i$  is

$$F_i = \frac{k_i}{k_{\text{eq}}} F = \frac{A_i E_i}{L_i} \left( \sum \frac{A_i E_i}{L_i} \right)^{-1} F, \quad (3.69)$$

where  $F$  is the total applied force,  $k_{\text{eq}}$  is the equivalent axial stiffness of the discretized rod, and  $k_i$ ,  $A_i$ ,  $E_i$ , and  $L_i$  are the axial stiffness, cross-sectional area, Young's modulus, and length of section  $i$ . The stress  $T_i$  applied to section  $i$  is therefore

$$T_i = \frac{F_i}{A_i} = \frac{F_i E_i}{\sum A_i E_i}. \quad (3.70)$$

Since  $E_i$  varies due to the temporal and spatial dependence of the internal magnetic field,  $T_i$  is also a function of  $r$  and  $t$ .

Using the BTCS method, Eq. (3.65) becomes

$$\begin{aligned} \frac{1}{\Delta r^2} (H_{i+1}^{j+1} - 2H_i^{j+1} + H_{i-1}^{j+1}) + \frac{1}{2\Delta r} (H_{i+1}^{j+1} - H_{i-1}^{j+1}) - \frac{\sigma}{\Delta t} (\mu_i^{j+1} - \mu_i^j) H_i^{j+1} \\ - \frac{\sigma}{\Delta t} \mu_i^{j+1} (H_i^{j+1} - H_i^j) = \frac{\sigma}{\Delta t} (d_i^{j+1} - d_i^j) T_i^{j+1} + \frac{\sigma}{\Delta t} d_i^{j+1} (T_i^{j+1} - T_i^j), \end{aligned} \quad (3.71)$$

where  $\Delta r$  is the distance between neighboring nodes,  $\Delta t$  is the time increment between solution steps, the subscripts denote the spatial index, and the superscripts denote the temporal index. The accuracy of the BTCS method is on the order of  $(\Delta t, \Delta x^2)$ .

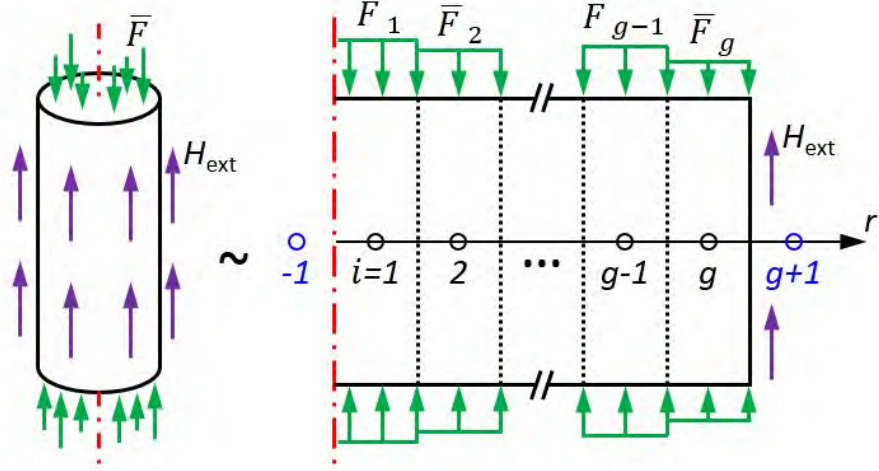


Figure 3.5: Discretization of the cylindrical ferromagnet; symmetry axis (red), distributed force (green), bias magnetic field at the surface (purple), discretization nodes (black circles), and fictitious nodes (blue circles).

Eq. (3.71) depends on the fictitious nodes  $i = -1$  and  $i = g + 1$  at nodes  $i = 1$  and  $i = g$ , respectively. This issue is resolved by applying the boundary conditions. As done in [100], the boundary condition Eq. (3.68) is written as a Taylor series expansion about  $r = 0$ ,

$$0 = \left. \frac{\partial H}{\partial r} \right|_{r=0} = \left. \frac{\partial H}{\partial r} \right|_{r=r_1} - \frac{\Delta r}{2} \left. \frac{\partial^2 H}{\partial r^2} \right|_{r=r_1} + \mathcal{O} \left( \left( \frac{\Delta r}{2} \right)^2 \right). \quad (3.72)$$

Similarly, the boundary condition Eq. (3.67) is written as a Taylor series expansion about  $r = R$ ,

$$H_{\text{ext}} = H_g + \frac{\Delta r}{2} \left. \frac{\partial H}{\partial r} \right|_{r=r_g} + \frac{1}{2} \left( \frac{\Delta r}{2} \right)^2 \left. \frac{\partial^2 H}{\partial r^2} \right|_{r=r_g} + \mathcal{O} \left( \left( \frac{\Delta r}{2} \right)^3 \right). \quad (3.73)$$

Approximation of the derivatives in Eqs. (3.72) and (3.73) using the 2nd order central difference method followed by simplification gives

$$H_{-1}^j \approx H_1^j \quad (3.74)$$

and

$$H_{g+1}^j \approx \frac{8}{3}H_{\text{ext}} - 2H_g^j + \frac{1}{3}H_{g-1}^j. \quad (3.75)$$

Together, Eqs. (3.71), (3.74), and (3.75) form a system of algebraic equations, from which the internal magnetic field at the next time step,  $\{H^{j+1}\}$ , can be easily calculated via a matrix inversion.

The time domain response of the internal magnetic field is solved iteratively according to the procedure shown in Fig. 3.6. A piece-wise linear procedure cannot be used, because the material properties at the next time step  $j + 1$  are required to calculate the solution at  $j + 1$ . To begin each time step, the solution at the next time step  $j + 1$  is estimated from the known, converged solution at the current time step  $j$  and previous step  $j - 1$  using linear extrapolation in time. Initially, the stress at  $j + 1$  is calculated from the known, applied force at  $j + 1$  and the elastic modulus at  $j$  using Eq. (3.70). Then, the elastic modulus at  $j + 1$  is calculated from the present estimate of the stress and magnetic field at  $j + 1$  using the constitutive model discussed in the **Discrete energy-averaged constitutive models** subsection of Section 1.2.2. This updated modulus at  $j + 1$  is used to update the stress at  $j + 1$ . Since the elastic modulus and stress are functions of each other, each is successively updated within a while loop until a convergence condition on the change in stress is met. The piezomagnetic coefficient and permeability at  $j + 1$  are then calculated from the converged stress at  $j + 1$  and the present estimate of the field at  $j + 1$  using the aforementioned constitutive model. Next, the estimate of the field at  $j + 1$  is updated using the BTCS method and boundary conditions. If a convergence condition on the change in the estimated field is not met, the modulus and stress at  $j + 1$  are again iteratively calculated using the new estimate, after which  $d$  and  $\mu$  at  $j + 1$  are updated, before once

again updating the estimated field. Once the field at  $j + 1$  has converged, the time index is incremented and the procedure repeats. If the field at  $j + 1$  stops converging and begins to diverge, iterations on  $k$  are stopped and the time index is incremented.

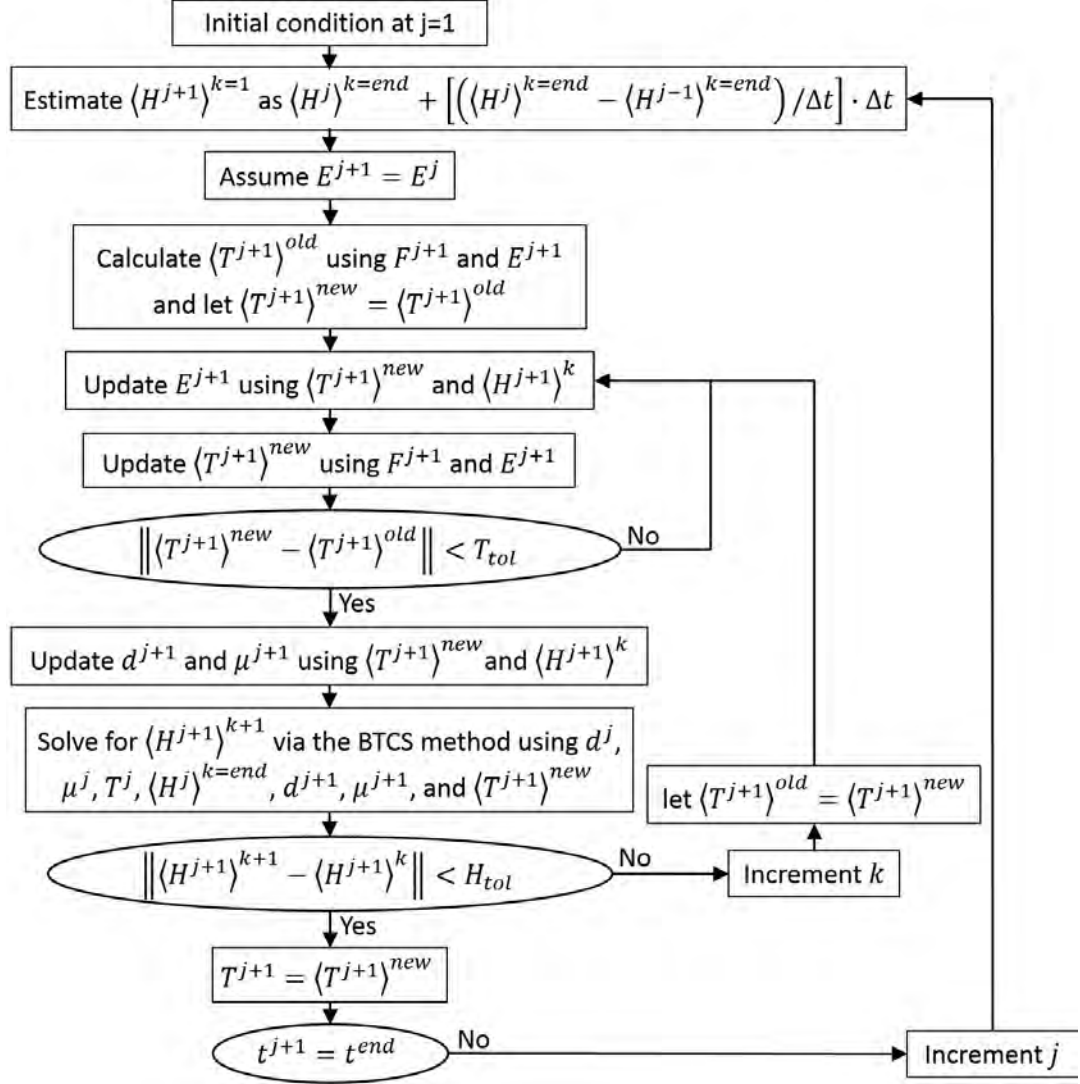


Figure 3.6: Solution procedure for calculating the nonlinear magnetic diffusion response of magnetostrictive materials.

## Validation for linear constitutive behavior

The numerical method is validated for the case of linear constitutive behavior by forcing the material properties to be constant and comparing the calculated responses to the analytical solution derived in Section 3.1.1. The model parameters common to all of the simulations in this section are given in Table 3.1. Additionally, 20 discretization nodes (i.e.,  $g = 20$ ) are used for the validation. Figs. 3.7 and 3.8 respectively show the spatial distribution and frequency response of the steady-state, non-dimensionalized dynamic field.

Table 3.1: Modeling parameters common to all nonlinear magnetic diffusion simulations.

$dt$ , s	$\sigma$ , $1/\Omega\mu\text{m}$	$R$ , mm	$T_{\text{bias}}$ , MPa	$H_{\text{ext}}$ , kA/m
$2\pi/(500\omega)$	2.15	3.2	-8	2.5

As seen in Figs. 3.7 and 3.8, the numerical method very accurately calculates the spatial and frequency dependence of linear mechanically-induced magnetic diffusion. In particular, Fig. 3.8(b) gives the numerical error ( $E_r = \text{numerical} - \text{analytical}$ ) for the frequency domain calculation. For the parameters used, the error does not exceed 1 % and is typically less than 0.5 % regardless of the radial location. The effective internal magnetic field was also calculated at each excitation frequency by averaging the magnetic field along the radial coordinate.<sup>8</sup> Fig. 3.9 depicts the frequency response of the non-dimensionalized, effective (average) internal dynamic field. The analytical

<sup>8</sup>Averaging along the radial coordinate is equivalent to integrating over the radial direction and dividing by the radius  $R$ .

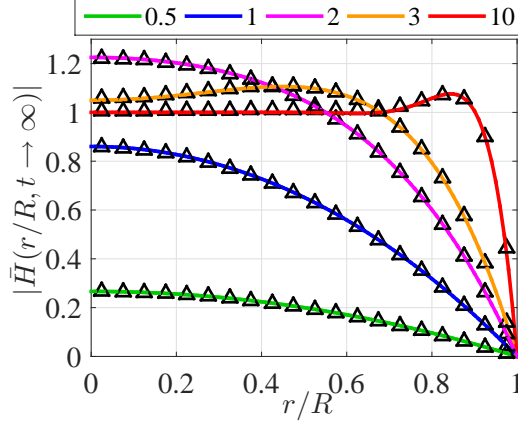


Figure 3.7: Validation of the numerical method: spatial distribution of the steady-state, non-dimensionalized dynamic field for different  $R/\delta^M=q$ ; analytical (solid) and numerical (triangles).

response is accurately quantified; however, the numerical error between  $\omega/\omega_c$  of 1 and 10 is considerably larger than that observed in the radially-dependent response, due in part to error propagation (see Section 3.2.2). The numerical error improves with the use of a finer spatial mesh, because the calculation of the average field at a given frequency converges to the true average of the numerical response.

Next, the effectiveness of the nonlinear solution procedure shown in Fig. 3.6 is assessed by comparing its numerical solution to that calculated using MATLAB's *fminunc* nonlinear minimization procedure. In quasi-linear and many nonlinear operating regimes, the two solutions are nearly identical (as observed for the case depicted in Fig. 3.10(a)), although the proposed procedure is markedly faster. However, in some cases, typically when the response is considerably nonlinear, neither solution procedure converges; in particular, both procedures diverge over approximately the same time spans, as shown in Fig. 3.10(b). When convergence is not achieved, the solution procedure is repeated without iterations on  $k$ ; as shown in Fig. 3.11, this

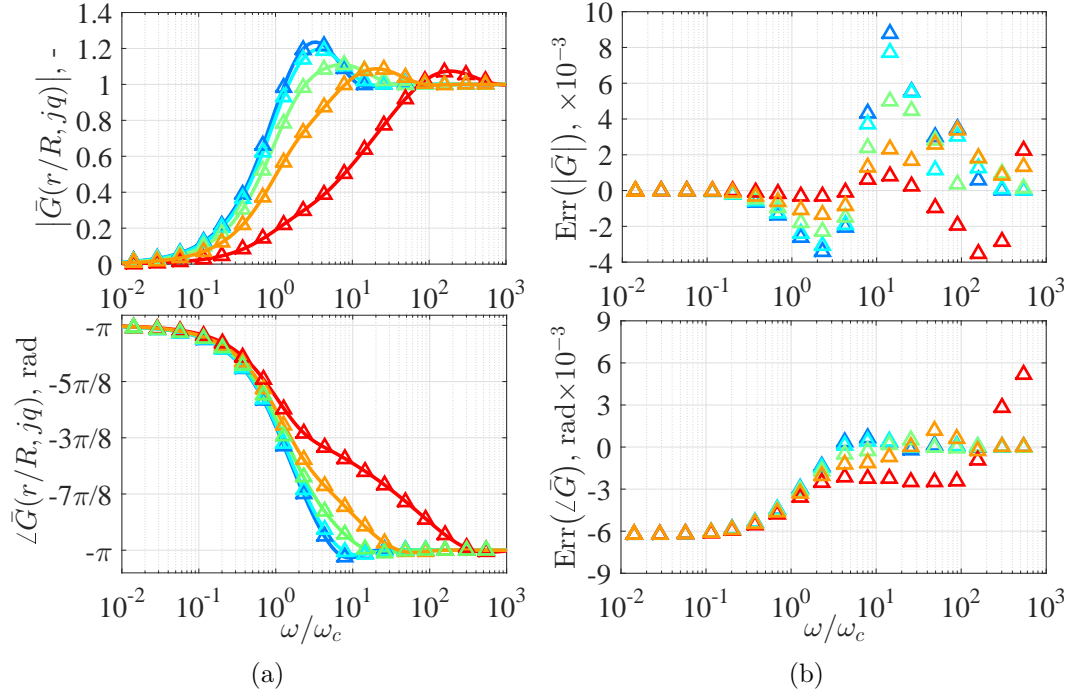


Figure 3.8: Validation of the numerical method: (a) non-dimensionalized frequency response of the dynamic field  $\tilde{H}(r, t)$  – magnitude (top) and phase (bottom) – as a function of  $\omega/\omega_c = q^2$  at different radial locations and (b) numerical error; analytical (solid) and numerical (triangles).

can provide a smooth, accurate solution in some cases. The following section only considers cases for which the proposed solution procedure provides a smooth solution. The development of a more robust solution procedure is tasked to future work.

## Results and Discussion

Using the validated model, the behavior of nonlinear, mechanically-induced magnetic diffusion in Galfenol is now studied. The effect of a time-varying piezomagnetic coefficient and permeability is first investigated for a prescribed sinusoidal variation in the properties. Variations of different amplitude that are in-phase and 180 degrees

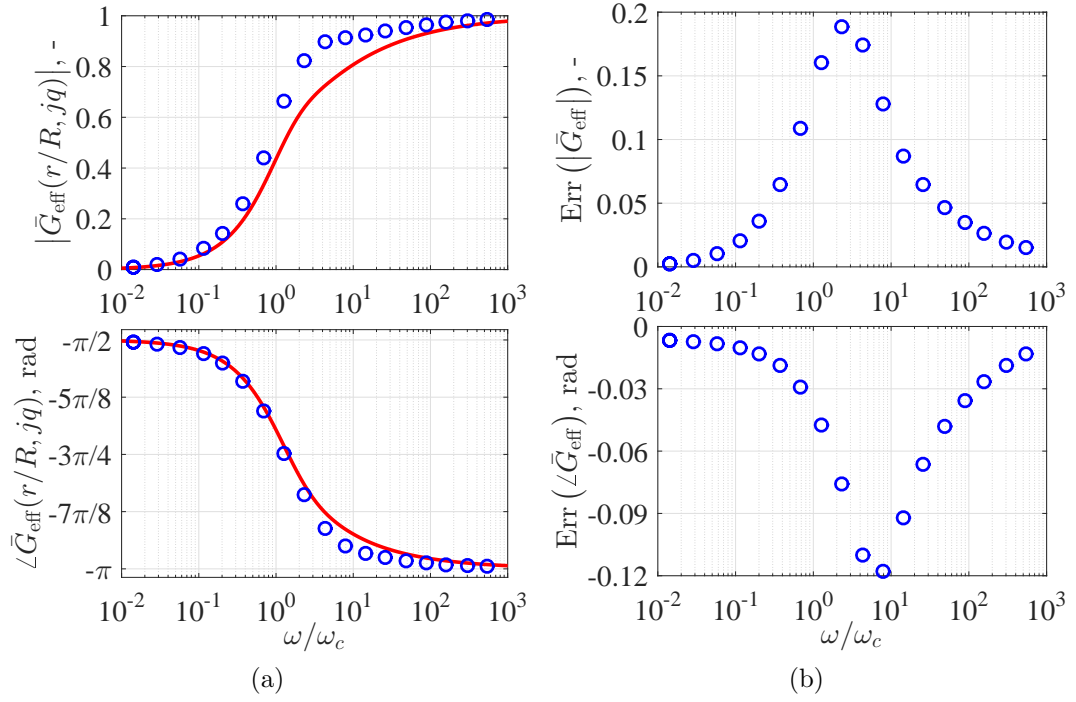


Figure 3.9: Validation of the numerical method: (a) non-dimensionalized frequency response of the effective (average) internal dynamic field – magnitude (top) and phase (bottom) – as a function of  $\omega/\omega_c = q^2$  and (b) numerical error; analytical (solid) and numerical (circles).

out-of-phase with the applied dynamic stress are considered. The results are shown in Figs. 3.12(a) and 3.12(b) for a low frequency stress having a small and moderate stress amplitude, respectively. There are three key observations. First, as the variation amplitude decreases, the nonlinear diffusion response converges to the linear, analytical response, as expected. Second, when the variation is out-of-phase with the dynamic stress, the parametric excitation caused by the variation adds to the stress excitation. Conversely, the parametric excitation caused by an in-phase variation counteracts the stress excitation and, for large variations, drives the response



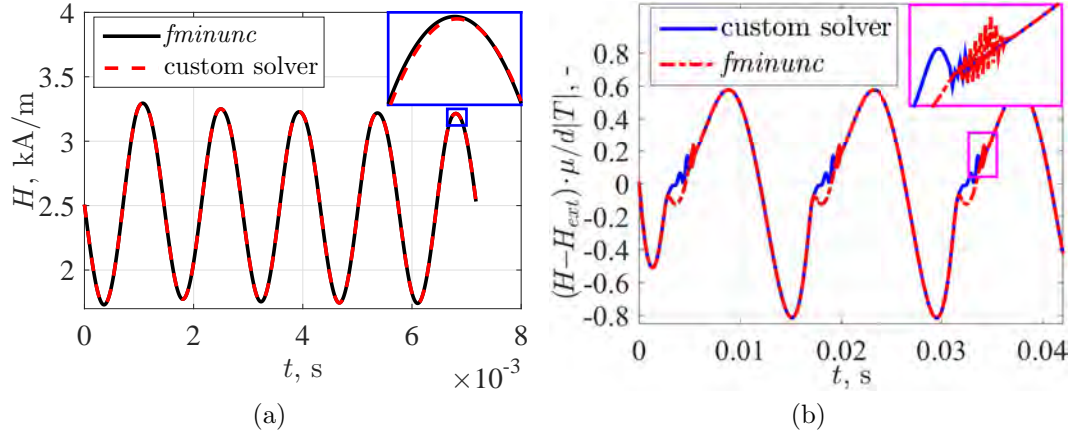


Figure 3.10: Comparison of a nonlinear diffusion response at the rod's axis calculated using the proposed solution procedure and MATLAB's *fminunc*: (a)  $g = 20$ ,  $\omega = 10\omega_c$ , and  $|T| = 4$  MPa and (b)  $g = 40$ ,  $\omega = \omega_c$ , and  $|T| = 2$  MPa.

out-of-phase from the linear, analytical response.<sup>9</sup> Third, at a low stress amplitude, the effect of out-of-phase and in-phase variations have a similar magnitude. However, at a moderate stress amplitude, in-phase variations have a considerably larger effect than out-of-phase.

Next, the full complexity of Galfenol's nonlinear diffusion response is investigated by calculating its time-varying material properties using the DEA model, as depicted in Fig. 3.6. The model parameters are given in Table 3.1. For the selected bias stress, the material operates within a small region that is adjacent to the point of maximum magnetoelastic coupling at the selected external (surface) field, which is a desirable operating point for many applications. However, this is expected to be a near worst-case operating point with regard to nonlinear magnetic diffusion, due

<sup>9</sup>This observation also holds for high forcing frequencies.

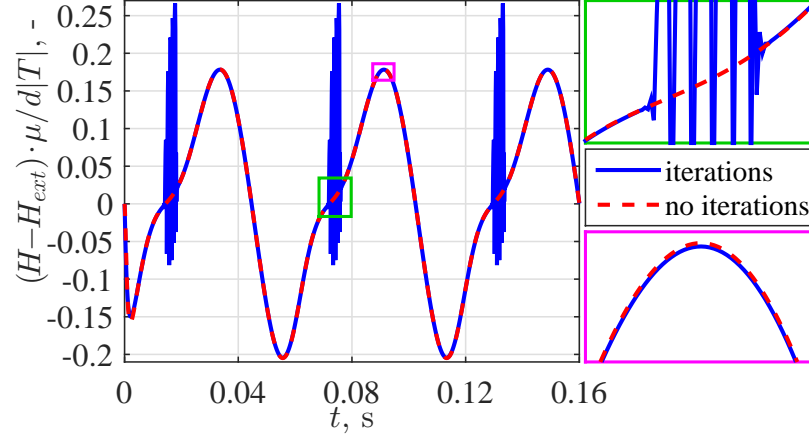


Figure 3.11: Comparison of a nonlinear diffusion response at the rod's axis calculated with and without iterations on  $k$ ;  $g = 40$ ,  $\omega = 0.25\omega_c$ , and  $|T| = 2$  MPa.

to the magnetic permeability's large magnitude and strong stress dependence at this point (see Fig. 3.13 and also refer to Fig. 2.8(b)).

Fig. 3.14 shows the temporal response of a Galfenol rod for low to moderate forcing frequencies and stress amplitudes. At low stress amplitudes, the nonlinear diffusion response resembles that of linear diffusion, i.e., the steady-state response is sinusoidal and symmetric about the surface field. As the stress amplitude increases, the non-dimensionalized internal field becomes asymmetric with respect to the surface field and its amplitude increases, particularly near the rod's axis. However, the mean field over one oscillation cycle is equal to  $H_{\text{ext}}$  in every case. At the selected bias, nonlinearity becomes appreciable at a stress amplitude of about 1.5 MPa.

The frequency response of a Galfenol rod at low to moderate stress amplitudes is depicted in Fig. 3.14, where the response is only reported at frequencies for which the numerical solution procedure converged. At low forcing frequencies, the magnitude of the internal field is small and the variation in material properties is nearly 180

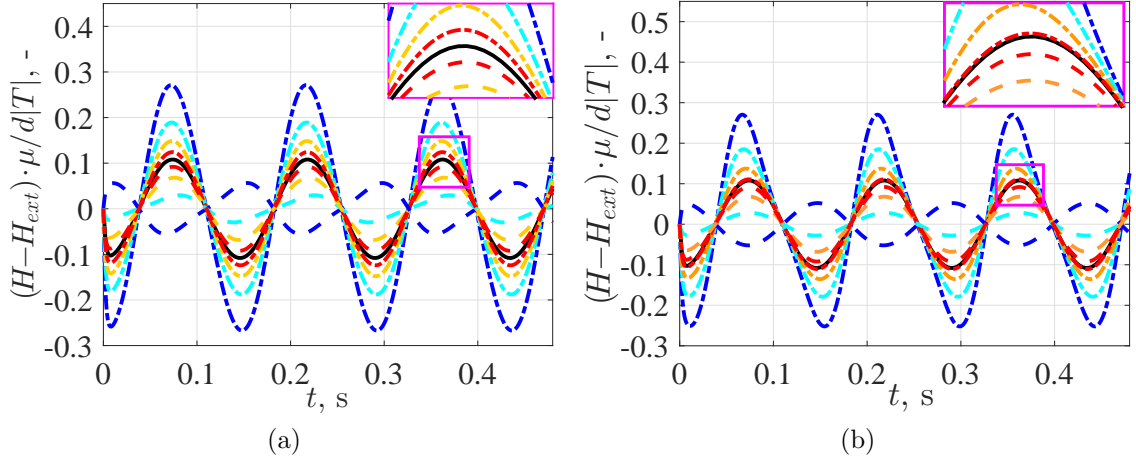


Figure 3.12: Convergence of the nonlinear magnetic diffusion response to the linear, analytical diffusion response (solid black) at the rod's axis for a uniform stress and a prescribed sinusoidal  $d^*$  and  $\mu$  of amplitude  $74.52 \cdot X$  nm/A and  $365.6\mu_0 \cdot X$ , respectively: (a)  $|T| = 0.5$  MPa,  $X = [0.01, 0.025, 0.05, 0.1]$  for out-of-phase (dashed-dotted) and in-phase (dashed) sinusoids and (b)  $|T| = 3$  MPa,  $X = [0.01, 0.1, 0.25, 0.5]$  for out-of-phase sinusoids (dashed-dotted) and  $X = [0.001, 0.0025, 0.005, 0.01]$  for in-phase sinusoids (dashed);  $g = 20$ ,  $\omega = 0.1\omega_c$ ,  $H_{\text{ext}} = 5$  kA/m, and  $T_{\text{bias}} = -40$  MPa; nonlinear curves are normalized using the stress amplitude and the bias  $d^*$  and  $\mu$ .

degrees out-of-phase with the dynamic stress. Thus, according to the observations of Fig. 3.12, diffusion is more pronounced for higher stress amplitudes due to a larger variation in material properties. Conversely, at high forcing frequencies, diffusion is generally less pronounced for higher stress amplitudes, because the magnitude of the internal field is large, which causes the material properties to vary almost in-phase with the dynamic stress. At a forcing frequency of about  $2\omega_c$ , the diffusion response is the same for different stress amplitudes. As seen in the inset of Fig. 3.15(a), the magnitude of the non-dimensionalized diffusion response does not reach 0.86 (i.e., the value of the linear response at the cut-off frequency) until about  $1.4\omega_c$ ; this suggests that the cut-off frequency of the nonlinear diffusion response at the chosen bias is

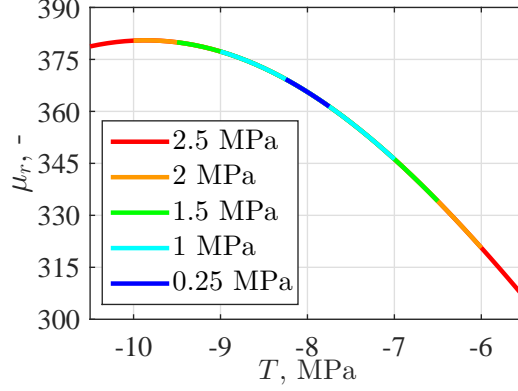


Figure 3.13: Magnetic permeability of Galfenol ( $\text{Fe}_{81.6}\text{Ga}_{18.4}$ ) about the selected bias point for different stress amplitudes, calculated using the DEA model after optimizing it to the measurements in Section 2.1.

about 1.4 times that of the linear response. At high frequency, the magnitude of the internal field is significantly larger than that of the linear response for all cases. The cause of this trend is unknown and requires further investigation.

### Concluding remarks

In this section, the behavior of nonlinear mechanically-induced magnetic diffusion was studied by numerically solving the PDE that governs radial diffusion in cylindrical ferromagnets. Radial non-uniformity of the applied stress was also considered. The PDE was solved using the backward time central space finite difference method along with equilibrium iterations. The numerical method was validated by comparing the linear, analytical solution from Section 3.1.1 to responses calculated for the case of constant material properties. The numerical error is below 1 % at every radial location. The effectiveness of the proposed numerical method was analyzed by comparing responses calculated using the proposed method and MATLAB's *fminunc*

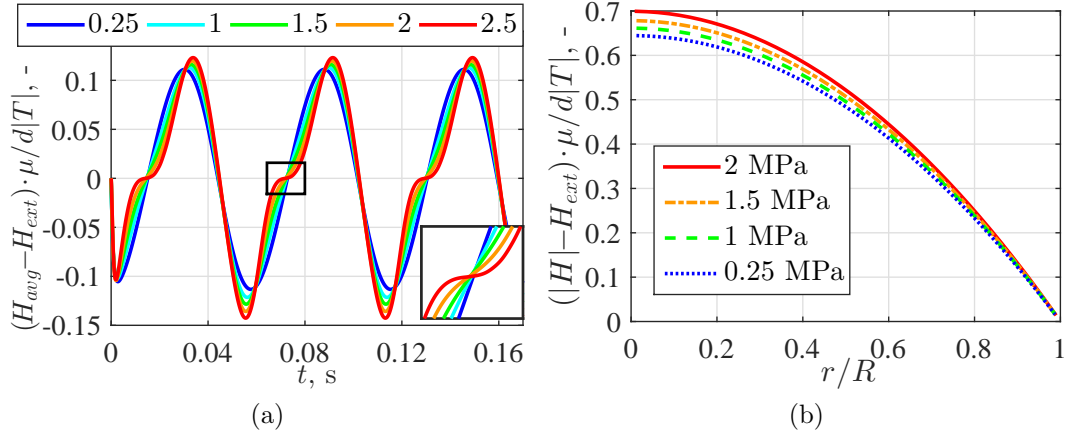


Figure 3.14: Time domain, nonlinear magnetic diffusion response of Galfenol for different stress amplitudes: (a) temporal response at the rod's axis ( $\omega = 0.25\omega_c$ ) and (b) spatial dependence of the field amplitude ( $\omega = \omega_c$ );  $g = 40$ .

function. When the response exhibits low to moderate nonlinearity, the methods produce nearly identical results. However, when nonlinearity is significant, both methods diverge. This prevented the computation and analysis of the diffusion response for large stress amplitudes and forcing frequencies.

The effect of time-varying material properties on the nonlinear diffusion response was first studied by prescribing a sinusoidal variation of the properties. When the variation is 180 degrees out-of-phase with the dynamic stress, the parametric excitation caused by the variation adds to the stress excitation, resulting in larger internal field magnitudes. Conversely, when the variation is in-phase with the dynamic stress, the parametric excitation counteracts the stress excitation; this reduces the internal field magnitude unless the variation is very large relative to the stress amplitude. Nonlinear diffusion in a Galfenol rod was investigated by using the DEA model to calculate the material properties. A bias stress and field were selected to provide

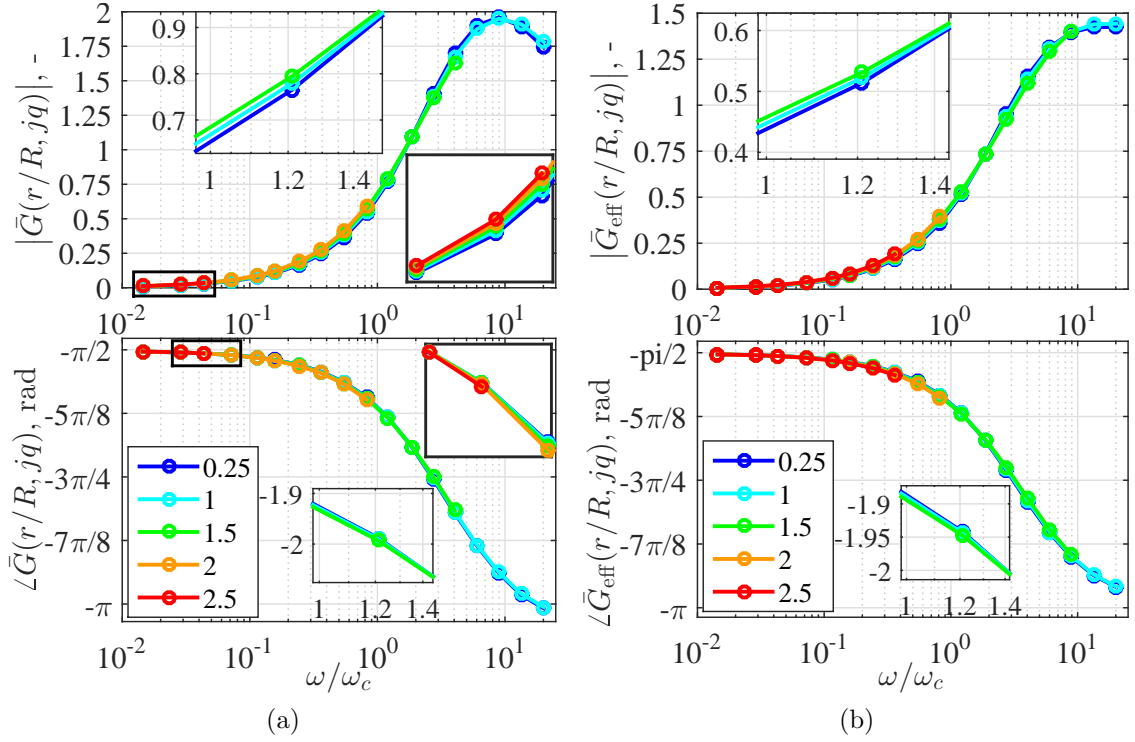


Figure 3.15: Frequency domain, nonlinear magnetic diffusion response of Galfenol for different stress amplitudes: (a) non-dimensionalized dynamic field at the rod's axis and (b) non-dimensionalized effective (average) dynamic field.

near worst-case diffusion. At this bias, nonlinearity in the diffusion response becomes appreciable at a stress amplitude of about 1.5 MPa. At forcing frequencies below about  $2\omega_c$ , diffusion is more pronounced for higher stress amplitudes, whereas at higher forcing frequencies, diffusion is generally less pronounced for higher stress amplitudes. Calculated frequency responses suggest that the diffusion cut-off frequency of the nonlinear response at the selected bias is about 1.4 times that of the linear response. At high frequency, the magnitude of the calculated internal field is significantly larger than that of the linear response. Further study is needed to ascertain the cause of this behavior. It is expected that the diffusion response will exhibit less

nonlinearity at bias points for which the magnetic permeability has a smaller magnitude and a weaker dependence on stress; in this case, the linear, analytical solution should be valid for larger stress amplitudes.

### 3.2 Dynamic Characterization of Galfenol

This section provides a complete record of a precise characterization of Galfenol's ( $\text{Fe}_{81.6}\text{Ga}_{18.4}$ ) magnetic and mechanical responses to dynamic compressive stresses up to 31 MPa and 1 kHz. The objective is to measure the 1D, dynamic sensing response of the material and to quantify from the response, the frequency dependence of the material properties for 1D sensing. This was accomplished by controlling the axial, dynamic stress and static magnetic field over a specific region of a Galfenol rod, and measuring the axial strain and magnetic flux density. Auxiliary variables – drive voltage, drive current, and temperature – were also measured for reference.

At each forcing frequency, sensing-based material properties are calculated using a frequency domain method adapted from an ASTM standard. Solid and laminated Galfenol rods are considered. To verify the experimental setup with existing data and to evaluate the frequency-independent performance, quasi-static actuation [129] and sensing responses (Section 2.1) were also measured. First, the design of the experiment is discussed in detail. This is presented in the following sections: specimen design, sensor selection and uncertainty analysis, experimental setup and methods, and data processing methods. Then, the complete set of dynamic measurements is provided, along with a discussion of the observed trends. Calibration methods, testing procedures, and additional details of the experimental and data processing methods are reported in Appendix C.

### 3.2.1 Specimen design

A cylindrical specimen was selected, because it was the standard geometry manufactured by the material supplier and it allowed for the use of an existing magnetic transducer (magnetic circuit). The magnetic circuit generated uniform magnetic fields only over a central region of the rod, which is referred to as the gauge region. Thus, state variables were controlled and measurements were taken within the gauge region.

#### Recommendations from ASTM standards

To assist with specimen design, particularly with tolerancing, relevant ASTM standards were reviewed, and specimen specifications were recorded. A full list of the relevant ASTM standards is given in the references. Table 3.2 summarizes geometric specifications taken from standards for magnetic testing, compression testing, and dynamic testing. Additionally, specimens should be free from residual stresses [11]. The most stringent of the tolerancing specifications in Table 3.2 were supplied to the specimen's manufacturer, ETREMA Products, Inc, who attempted to meet these very tight tolerances. This table is presented to allow the tolerances of the manufactured specimens (given in the **Specimen geometry** subsection of Section 3.2.1) to be benchmarked against those of an ideal specimen.

To accurately control the magnetic state of the specimen over a gauge region, a magnetic circuit was used to generate magnetic flux and guide it uniformly into the specimen. When standard magnetic circuits are used for magnetic testing, the length and diameter specifications from [6] help to ensure magnetic uniformity in the specimen. In this experiment, both magnetic and mechanical excitations were needed. Thus, a custom magnetic circuit (Figs. 3.16 and 3.17) was used. As suggested in [6],



Table 3.2: Summary of geometric specifications for specimens from relevant ASTM standards.

Parameter	Specification	ASTM Standard
length ( $L$ )	$\geq 5$ in	A 314/A314M [6]
diameter ( $D$ )	$\geq 0.5$ in	A 314/A314M [6]
$L/D$ ratio	about 8 to 10 (for modulus of elasticity testing)	E9 [17]
diameter tolerance	$\pm 0.001$ in $\leq 1$ % or 0.002 in (whichever is less) $\pm 0.1$ % $\pm 0.010$ in $\pm 0.005$ in	E209 [12] E9 [17] E1875 [8], E1876 [9] A 314/A314M [6] D5992 [7]
surface roughness	ground smooth to $\leq 100$ $\mu\text{in}$ (RMS) machined smooth to $\leq 63$ $\mu\text{in}$ (avg.)	A 314/A314M [6] E9 [17], E209 [12]
parallelism of ends	$\leq 0.0005$ in/in $\leq 0.00025$ in $\leq 0.1$ %	E9 [17] E209 [12] E1875 [8], E1876 [9]
flatness of ends	$\leq 0.0005$ in/in	E9 [17]
perpendicularity of ends relative to sides	$\leq 0.05$ degrees $\leq 0.25$ degrees	E9 [17] E209 [12]

this circuit's flux return path was composed of silicon iron laminations (0.018 in thick) that were bolted together and operated up to a flux density (about 0.6 T) for which their magnetic permeability was below its maximum value. To minimize eddy currents in the flux return path, laminations were separated by electrically-insulating Kapton film (about 0.001 in thick). The circuit was symmetric and contained two electromagnets, which were nominally identical, to improve the uniformity of the magnetic state in the specimen. This magnetic circuit was successfully used in previous work by the authors [154, 53]. The use of this circuit constrained the diameter of the specimen to 0.25 in and its minimum length to 3 in (to allow for the specimen ends to be mechanically engaged); therefore, the length-to-diameter ratio specification suggested by ASTM E9 [17] was adhered to instead of the length and diameter specifications.

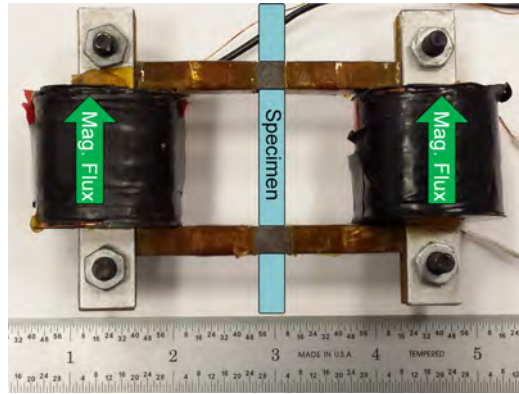


Figure 3.16: Magnetic circuit used to generate a uniform magnetic state in the gauge region of the specimen, while allowing for independent mechanical excitation.

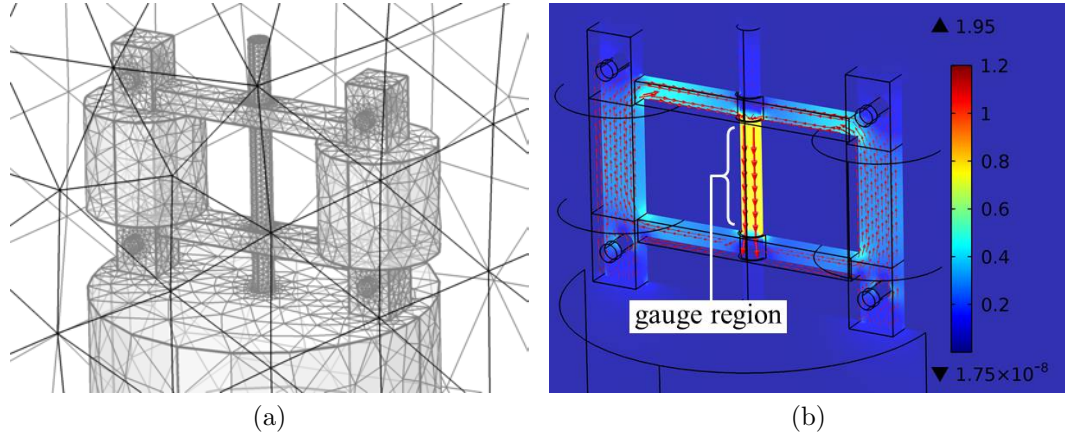


Figure 3.17: COMSOL Multiphysics simulation of the 3D magnetic response of the magnetic circuit: (a) meshed circuit, magnetic base/platen, and large air volume, (b) magnetic flux density vector (arrow length proportional to magnitude) and slice plot of its norm (in units of Tesla) in response to a 1 A electromagnet current; the relative magnetic permeability of the platen and Galfenol are 100, each coil is composed of 300 turns of 26 AWG wire, and the air gap between the Galfenol specimen and silicon iron was included; note the uniformity and axial orientation of the magnetic flux within the gauge region of the specimen.

## Buckling

Buckling of specimens subjected to quasi-static, compressive, axial loads occurs when the specimen's 1st natural frequency of transverse bending becomes zero. The critical buckling stress  $T_{\text{crit}}$  and load  $P_{\text{crit}}$  at which this occurs is given by [17],

$$T_{\text{crit}} = \frac{P_{\text{crit}}}{A} = C \frac{\pi^2 EI}{L^2 A}, \quad (3.76)$$

where  $E$  is the Young's modulus,  $I$  denotes the area moment of inertia about the centroid of the cross-section,  $L$  is the specimen's length,  $A$  denotes the specimen's cross-sectional area, and  $C$  is the end-fixity coefficient, which takes a value of 3.75 for the reported experiment (compression testing of flat-end specimens between flat, rigid anvils). Comparing Eq. (3.76) with Table 3.2 reveals a tradeoff between a

short sample (large critical buckling stress) and long sample ( $L/D$  ratio ideal for the measurement of elastic moduli). Considering this tradeoff and the constraints imposed by the magnetic circuit, a specimen length of 3 in was used.

If the loading is dynamic and perfectly compressive, buckling should not occur unless the compressive load exceeds the quasi-static buckling load. However, pure compression cannot be realized, and some amount of transverse excitation will always occur. Consequently, for dynamic compression, the excitation frequency should be well below the 1st natural frequency of transverse vibration of the specimen. To approximate this natural frequency of the cylindrical specimen, the transverse vibration of beams subjected to axial loads was considered. The mode shapes ( $W_n$ , eigenfunctions) are provided by [118],

$$W_n(x) = Z_1 (\cosh(s_1 x) + Z_2 \sinh(s_1 x) + Z_3 \cos(s_2 x) + Z_4 \sin(s_2 x)), \quad (3.77)$$

where

$$s_1^2, s_2^2 = \frac{P}{2EI} \pm \left( \left( \frac{P}{2EI} \right)^2 + \frac{\rho A \omega_n^2}{EI} \right)^{1/2}, \quad (3.78)$$

$x$  is the location along the beam's length,  $P$  is the applied axial force,  $\rho$  denotes the density,  $\omega_n$  are the circular natural frequencies of transverse vibration (eigenvalues) of the beam, and  $Z_i$  are constants that depend on the boundary conditions. Application of fixed-fixed boundary conditions to Eq. (3.77) gives the frequency equation

$$2s_1 s_2 (1 - \cos(s_2 L) \cosh(s_1 L)) + \sin(s_2 L) \sinh(s_1 L) (s_1^2 - s_2^2) = 0. \quad (3.79)$$

An analytical expression for  $\omega_n$  from Eqs. (3.78) and (3.79) could not be found. Thus, a numerical solution for  $\omega_1$  as a function of  $P$  was calculated. For comparison, an assumed relation between  $\omega_1$  and  $P$  was developed based on the analytical relation

for a pinned-pinned beam [118],

$$\omega_n = \frac{\pi^2}{L^2} \left( \frac{EI}{\rho A} \right)^{1/2} \left( n^4 - n^2 \frac{P}{P_{\text{crit}}} \right)^{1/2}, \quad (3.80)$$

and the known bounds of the curve – Eq. (3.76) and the 1st transverse bending natural frequency of a fixed-fixed beam for zero axial stress [118],

$$\omega_1 = (\beta L)_1^2 \left( \frac{EI}{\rho A L^4} \right)^{1/2}, \quad (\beta L)_1 = 4.730041. \quad (3.81)$$

The assumed relation has the form

$$\omega_1 = \left( Y - V \frac{P}{P_{\text{crit}}} \right)^{1/2}, \quad (3.82)$$

where application of the bounds gives

$$Y = V = (\beta L)_1^4 \left( \frac{EI}{\rho A L^4} \right). \quad (3.83)$$

To accurately compare the numerical and assumed relations, an end-fixity coefficient of 4 (perfectly fixed-fixed boundary conditions) was temporarily used to derive the assumed relation. The comparison in Fig. 3.18(a) shows a near perfect agreement; thus, the assumed relation with realistic boundary conditions (end-fixity coefficient of 3.75) could be used to analyze the Galfenol specimen. The assumed relation for the Galfenol specimen is plotted in Fig. 3.18(b) for the minimum and maximum values of Galfenol's Young's modulus. At the maximum applied compressive stress of 60 MPa, the specimen's 1st transverse bending natural frequency will approximately fall in the range 1950 to 2900 Hz. The maximum excitation frequency in this experiment (1000 Hz) was well outside this range, which suggested that buckling should not occur. Further, Galfenol exhibits low to moderate damping [159]. Consequently, any magnitude or phase distortion introduced in the results due to bending should

be minimal. However, it is acknowledged that resonant frequencies are system-level properties that depend on the effective mass loading during experimentation. A larger mass would result in greater reductions in the resonant frequencies.

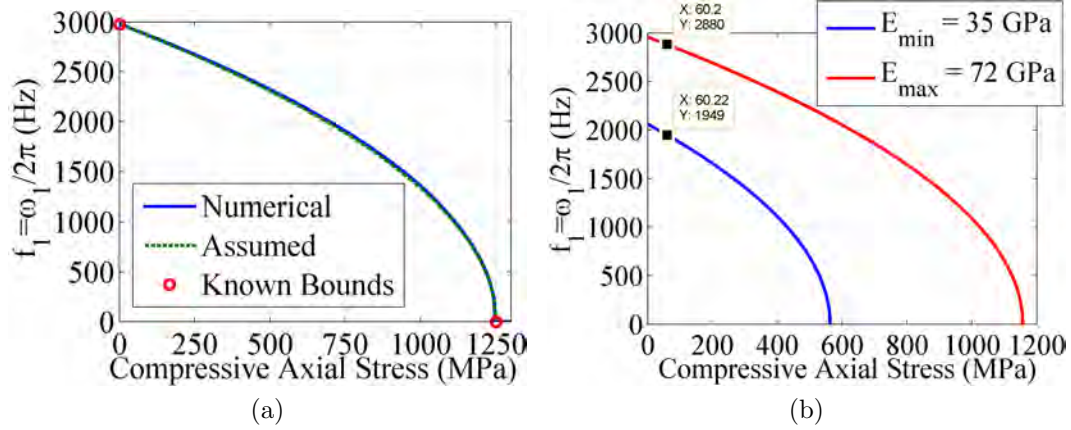


Figure 3.18: (a) comparison of the numerical and assumed relations between the 1st transverse bending natural frequency and compressive stress for perfectly fixed-fixed boundary conditions (end-fixity coefficient of 4), and (b) Assumed relation between the 1st transverse bending natural frequency and compressive stress for the Galfenol specimen with realistic boundary conditions (end-fixity coefficient of 3.75) and its minimum (35 GPa) and maximum (72 GPa) Young's modulus.

## Lamination

The goal of the material characterization was to measure Galfenol's response to dynamic, axial stresses and constant magnetic fields (applied at the surface). In magnetostrictive rods, dynamic, axial stresses produce a time-varying, axial magnetic flux in the material. According to the Faraday-Lenz law, this time-varying magnetic flux induces electric fields that circulate around the rod's axis. Due to the material's

finite resistivity, these electric fields drive circulating currents, which generate a time-varying, axial magnetic field that is superposed on the constant applied magnetic field (Fig. 3.19(a)). Consequently, the magnetic field is non-uniform along the radial direction of the rod (Fig. 3.19(b)), which prevents a well defined and accurate characterization. This effect has been termed mechanically-induced magnetic diffusion by the authors. Simplifying the problem by assuming constant Galfenol properties (valid in the “burst” region) allows for an analytical solution for this effect in solid rods (Fig. 3.19) [134]. Model parameters are given in Table 3.3. In Fig. 3.19(b), the minimum magnetic field is used to show a time-independent profile of the largest deviation of the internal field from the surface value at each point along the rod’s radius.

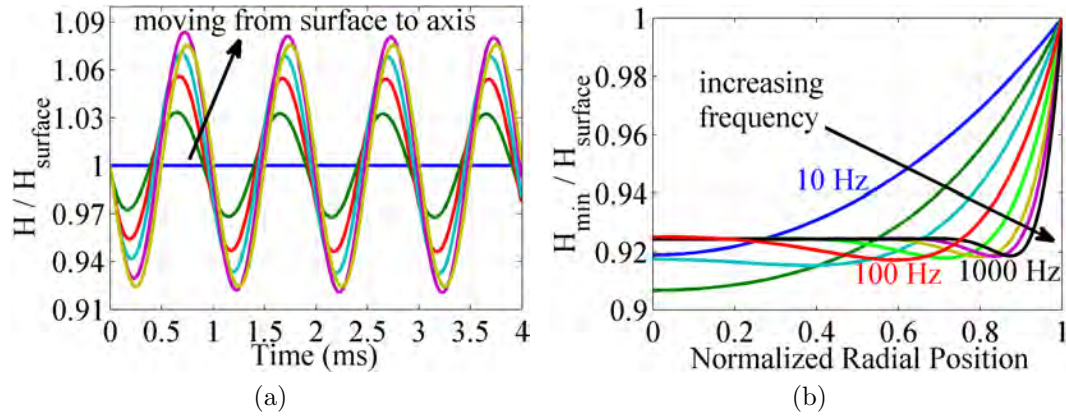


Figure 3.19: Mechanically-induced magnetic diffusion for the Galfenol specimen: (a) temporal response of the normalized magnetic field at varying locations along the radial direction for a 1000 Hz stress, and (b) normalized minimum magnetic field as a function of radial position (normalized by the radius) for varying stress frequencies.

Table 3.3: Model parameters used for the solution of the mechanically-induced magnetic diffusion problem.

Electrical Conductivity, S/m $5.96 \times 10^6$	Relative Magnetic Permeability 350	Piezomagnetic Coefficient, T/Pa $40 \times 10^{-9}$
Radius, mm 6.35	Bias Magnetic Field, kA/m 6	Stress Amplitude, MPa 5

The analytical solution shows that the magnitude of the time-varying magnetic field increases toward the rod’s axis and that the effect is more significant as the stress frequency increases. The conventional method for mitigating the effects of magnetic field-induced magnetic diffusion is to laminate the material, whereby the material is cut into thin laminates then bonded back together with an electrically-insulating adhesive. This constrains eddy currents to circulate within each laminate – a condition for which the analytical solution is invalid. In determining a laminate thickness, there is a tradeoff between minimizing eddy currents (thin laminates) and practical manufacturing limitations (thicker laminates). Thinner laminates also reduce the volume fraction of Galfenol for a given rod diameter. A laminate thickness of 0.033 in (26 % of the radius) was chosen to balance this tradeoff, with more weight placed on reducing eddy currents.

### Specimen geometry

The purchased alloy was  $\langle 100 \rangle$  oriented, polycrystalline  $\text{Fe}_{81.6}\text{Ga}_{18.4}$ . Although the specimen was polycrystalline, the manufacturer’s expertise allowed them to produce highly-textured polycrystals (misorientation angle of grains was very small),



whose performance can approach that of single crystalline material. Solid and laminated rods were cut from the same bulk rod, which was grown using the free standing zone melt method at about 25 mm/hr (a rate used to produce research-grade material). Specimens cut from the same bulk rod can still be expected to have some variation in their properties. The geometry of all specimens is depicted in Fig. 3.20, where the tolerances reflect the capabilities of the material supplier. The most stringent ASTM-recommended tolerance for surface finish, diameter variation, and parallelism could not be met. A tolerance for flatness of the rod's ends was not specified, because the supplier does not measure flatness. The laminated rod had 0.033 in thick laminates.

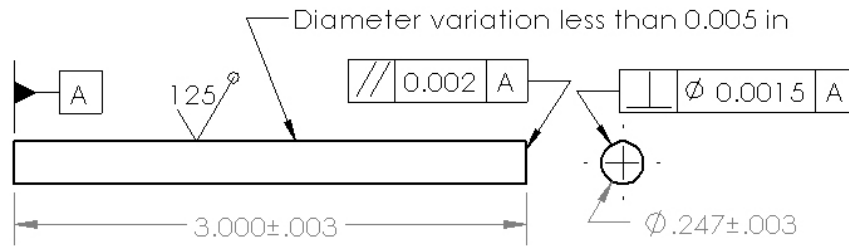


Figure 3.20: Dimensions and tolerances of the highly-textured,  $\langle 100 \rangle$  oriented, polycrystalline Galfenol ( $\text{Fe}_{81.6}\text{Ga}_{18.4}$ ) rods purchased from Etrema Products, Inc.; all specifications have units of in, except for the surface roughness, which is specified in units of  $\mu\text{in}$ .

### 3.2.2 Sensor selection and uncertainty analysis

When possible, the uncertainty of each calculated quantity  $u_R$  was quantified by the standard formula for the propagation of error given by [68],

$$u_R = \pm \left[ \sum_{i=1}^n \left( \frac{\partial R}{\partial x_i} u_{x_i} \right)^2 \right]^{1/2}, \quad (3.84)$$

where  $u_{x_i}$  is the uncertainty in the measured variable  $x_i$  and  $n$  denotes the number of variables on which the result  $R$  depends. Eq. (3.84) is valid when individual uncertainties  $u_{x_i}$  are small. Individual uncertainties were calculated as

$$u_{x_i} = (u_{0_i}^2 + u_{c_i}^2)^{1/2}, \quad (3.85)$$

where  $u_{0_i}$  is the interpolation error,

$$u_{0_i} = \pm \frac{1}{2}(\text{resolution}), \quad (3.86)$$

and  $u_{c_i}$  is the instrument error, which is a combination of elemental errors  $e_{k_i}$  (e.g., sensitivity and linearity errors),

$$u_{c_i} = \pm \left[ \sum_{k=1}^K (e_{k_i}^2) \right]^{1/2}. \quad (3.87)$$

For most sensors,  $u_{c_i}$ , and thus  $u_R$ , is a function of the magnitude of the measured quantity. This is illustrated in Appendix C.1, which details the uncertainty analysis for each measured quantity. Table 3.4 summarizes the estimated range of uncertainty for each measurement and compares it to the suggested maximum uncertainty from ASTM standards. In most cases, the expected uncertainty approximately met ASTM recommendations. The magnetic flux density uncertainty exceeded its recommendation due to a high range-dependent uncertainty, which resulted from having a low signal-to-range ratio of 15 %.

Table 3.4: Estimated uncertainty in the measured quantities.

Physical quantity	Measurement uncertainty, $\pm\%$ of span	ASTM-suggested uncertainty, $\pm\%$ of span
Distance	0.20	0.10–0.50
Area	0.41	1.0
Force	0.065–1.0 (static), 1.1–1.3 (dynamic)	1.0
Stress	0.065–1.1 (static), 1.1–1.3 (dynamic)	–
Temperature	$\pm 2.0^\circ\text{C}$	$\pm 1.0^\circ\text{C}$
Strain	0.21–0.46	0.10–1.0
Magnetic field strength	0.92–1.3	1.0
Magnetic flux density	1.4–1.9	1.0

The method, experimental setup, and results for the calibration of each sensor and the linear power amplifier are detailed in Appendix C.2. Most of the calibrations were conducted by comparing the device’s output to an absolute reference or the output of a calibrated sensor. However, the strain gauges were shunt calibrated, whereas the magnetic flux density sensing (pick-up) coil was calibrated by measuring the magnetic response of a 0.25 in diameter Ni 200 rod and comparing the resulting B-H loop to accurate measurements from the literature [139].

The instruments used in the experiment are as follows. A Kepko BOP 72-6M linear amplifier, operated in current control mode, was selected based on its availability. Static force was measured using an Interface 1010ACK-500-B fatigue rated load cell and MTS 493.21 signal conditioner. As discussed in Section 3.2.3, dynamic forces vibrate the specimen and fixtures, resulting in inertial forces that cause error

in measurements of the force applied to the specimen. To minimize this error, the dynamic force was measured with a Kistler 9001A piezoelectric load washer and Kistler 5010 charge amplifier, instead of the Interface load cell. A Type K thermocouple and Omega DRG-SC-TC signal conditioner were used to measure the temperature of the specimen. Strain measurements were obtained using Vishay Micro-Measurements EA-06-250BF-350/L strain gauges and a Vishay Micro-Measurements 2310 signal conditioner. An Allegro A1321LUA Hall chip was selected to measure the surface magnetic field, while a Lake Shore Model 480 fluxmeter and custom pick-up coil were used to measure the magnetic flux density.

### **3.2.3 Experimental setup and methods**

This section details the physical setup of the experiment and the reduction of inertial force error and strain gauge noise. A wiring diagram of the experiment, a discussion of the magnetic field control, and a discussion of the sensor reset process are contained in Appendices C.3.1, C.3.2, and C.3.3, respectively.

#### **Physical setup**

An MTS 831.50 dynamic load frame was used to excite the Galfenol specimen with quasi-static and dynamic axial forces up to -2000 N and 1 kHz (Fig. 3.21). Due to the high stiffness of the specimen, the load frame was operated in force control mode, instead of displacement control mode; this was realized using an MTS 793 FlexTest GT controller. A closer look at the test setups used for quasi-static and dynamic testing is provided in Fig. 3.22. Here, the thermocouple, Hall chip, sensing coil, and strain gauges can be seen installed on the Galfenol rod. Surrounding the rod is the electromagnetic circuit used to generate the magnetic field.

Fig. 3.22(a) focuses on the quasi-static test setup. The Interface load cell, shown at the bottom of the picture, was used to measure the force in the rod and to provide feedback to the controller. Above the load cell was an aluminum platen, which supported the Galfenol rod and the electromagnetic circuit that surrounded the rod. There was also a thin plate sitting on the platen, which had a through hole for centering the rod. Above the setup was the load frame piston with a steel platen that was used to engage the sample.

As discussed in the following section, the mass in-between the load cell and the sample (i.e., the platen, alignment plate, and the electromagnetic circuit) generated significant inertial forces that limited the accuracy of the load cell measurement at high frequency. As a result, the test setup was modified for dynamic testing to include an auxiliary force sensor. The physical setup is shown in Fig. 3.22(b). Here, a load washer was placed on top of the platen. A circular scribe mark on the platen was used to visually center the load washer. Then a small steel part, shaped like a puck, was used to connect the sample to the load washer. The puck had a pin on the bottom side for alignment with the load washer, and a circular scribe mark on the top for alignment with the sample.

### **Inertial force error reduction**

Any moving mass in-between the force transducer and sample will generate inertial force that corrupts the measurement. In the testing standard [15], it is recommended that the inertial force error be  $\leq 0.5$  % of the loading span. A lumped parameters model, as shown in Fig. 3.23, was used to estimate the error for the test setups used in this experiment. Here, case 1 corresponds to the quasi-static test setup, where force is measured with the load cell, and case 2 corresponds to the dynamic setup,



Figure 3.21: MTS 831.50 load frame with experiment installed.

where force is measured with the load washer. The sample and force transducers are modeled as springs, while the fixtures are modeled as masses.

The inertial force error is defined as the difference between the transducer force and the sample force, normalized by the loading span (the peak-to-peak dynamic force) of the sample force. Equations for the inertial force error associated with cases 1 and 2 are derived in Appendix C of [129] and can be expressed, respectively, as

$$|E_1| = \left| \frac{F_3 - F_2}{2|F_2|} \right| = \frac{m_3\omega^2}{2|k_3 - m_3\omega^2|} \quad (3.88)$$

and

$$|E_2| = \left| \frac{F_2 - F_1}{2|F_1|} \right| = \frac{1}{2} \left( 1 + \left| \frac{k_2(k_3 - m_3\omega^2)}{m_2\omega^2(m_3\omega^2 - (k_2 + k_3))} \right| \right)^{-1}, \quad (3.89)$$

where  $\omega$  is the circular frequency of the excitation force. In both cases, the error magnitude increases with the mass in-between the sample and force transducer. The errors for cases 1 and 2 are plotted in Fig. 3.24 versus frequency along with the

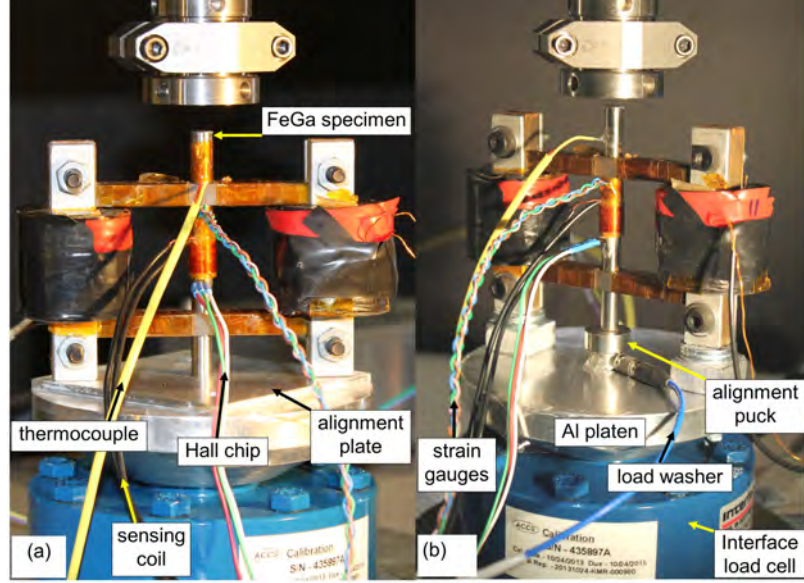


Figure 3.22: Detail of the (a) quasi-static and (b) dynamic experiments.

threshold specified in the ASTM standard. Accordingly, the forcing frequency for case 1 is limited to 213 Hz, while for case 2 the forcing frequency may be up to 1077 Hz before exceeding the error threshold. As noted in Section C.1, forces up to 100 Hz were measured using the Interface load cell, whereas forces above this cut-off were measured using the piezoelectric load washer. At 100 Hz, the error magnitude for case 1 is 0.11 % of the loading span. At 1000 Hz, the error magnitude for case 2 is 0.41 % of the loading span.

### Strain gauge noise reduction

As detailed in Section 3.1, a time-varying magnetic flux through a surface (e.g., the cross-section of the Galfenol rod) induces a circulating electric field along the boundary of the surface. This electric field creates noise voltages in the grid of the strain gauges that were attached to the rod's surface. Since the gauges used in this

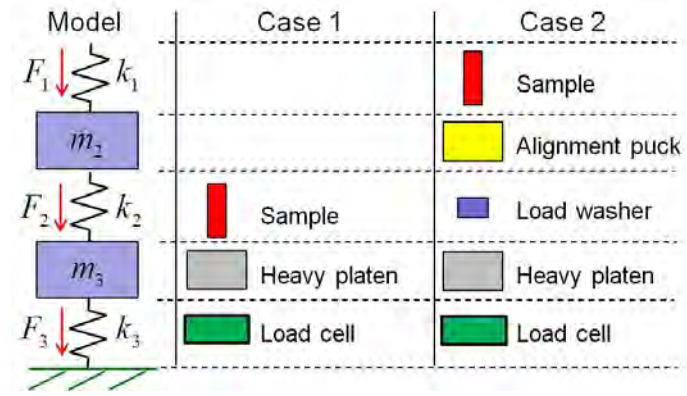


Figure 3.23: Schematic of the load path and mechanical model for inertial force error cases 1 and 2.

experiment were oriented to measure axial strain in the rod, the noise voltage was only generated in the narrow, horizontal links of the grid; thus, long and narrow strain gauge grids were ideal for minimizing electromagnetic noise. The electromagnetic noise can be directly measured at the strain gauge terminals after setting the bridge excitation to 0 V.

To investigate the effect of electromagnetic noise  $V_{\text{noise}}$  on a quarter bridge strain measurement, the circuit shown in Fig. 3.25 was analyzed in Appendix B of [129]. The normalized strain error due to the electromagnetic noise is

$$E_\epsilon = \frac{\epsilon_{\text{meas}} - \epsilon_{\text{true}}}{\epsilon_{\text{span}}} = \frac{V_r (F_G \epsilon_{\text{true}} + 2)}{F_G \epsilon_{\text{span}} (1 - V_r)}, \quad (3.90)$$

where  $\epsilon_{\text{meas}}$  is the measured strain,  $\epsilon_{\text{true}}$  is the true strain,  $\epsilon_{\text{span}}$  is the strain span ( $1350 \times 10^{-6}$  for this experiment),  $F_G$  is the gauge factor, and  $V_r$  is the normalized noise voltage,

$$V_r = \frac{V_{\text{noise}}}{V_{\text{ex}}}. \quad (3.91)$$



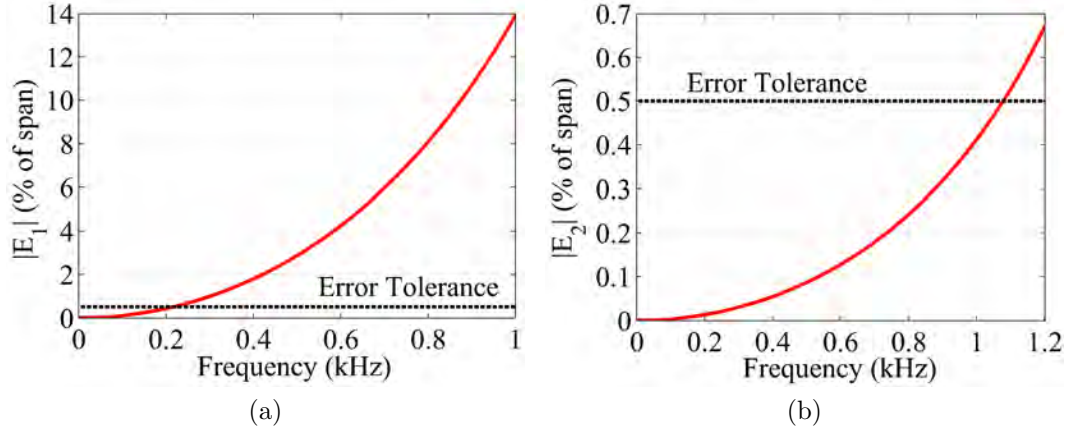


Figure 3.24: Measurement error in the force applied to the specimen due to the inertial force of fixturing: (a) case 1 and (b) case 2;  $k_{\text{LoadCell}} = 175 \times 10^6$  N/m,  $k_{\text{LoadWasher}} = 1 \times 10^9$  N/m,  $m_{\text{Puck}} = 0.025$  kg, and  $m_{\text{Platen}} = 0.965$  kg.

The strain error is plotted in Fig. 3.26. Clearly, the strain error is a very weak function of the true strain magnitude; however, the error increases significantly as a function of the normalized noise voltage. For a typical bridge excitation of 10 V, an electromagnetic noise voltage of 10 mV results in a strain error of about 100 %. Fig. 3.27 shows a direct measurement of the electromagnetic noise voltage during a 3 MPa amplitude, 1 kHz excitation of a Galfenol rod in a similar experiment, where no noise reduction techniques were utilized. The measured noise voltages correspond to strain errors of 200 % or larger. Thus, noise reduction techniques were required for accurate strain measurement, especially for high frequency, large amplitude forces.

Electromagnetic noise was reduced by (a) weaving leadwires in the pattern shown in Fig. 3.28(a), (b) routing leadwires as far away from the noise sources as possible and in a direction orthogonal to the rod's circumference and the perimeter of the laminates' cross section, and (c) wiring the two gauges in series such that the noise

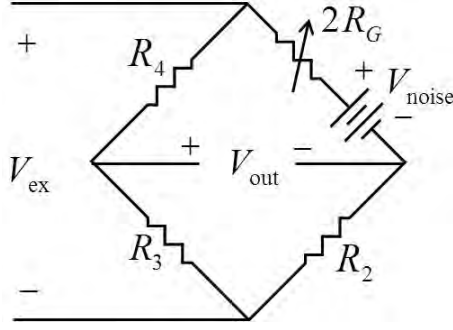


Figure 3.25: Wheatstone quarter bridge strain measurement circuit considering electromagnetic noise  $V_{\text{noise}}$  (leadwire resistance neglected).

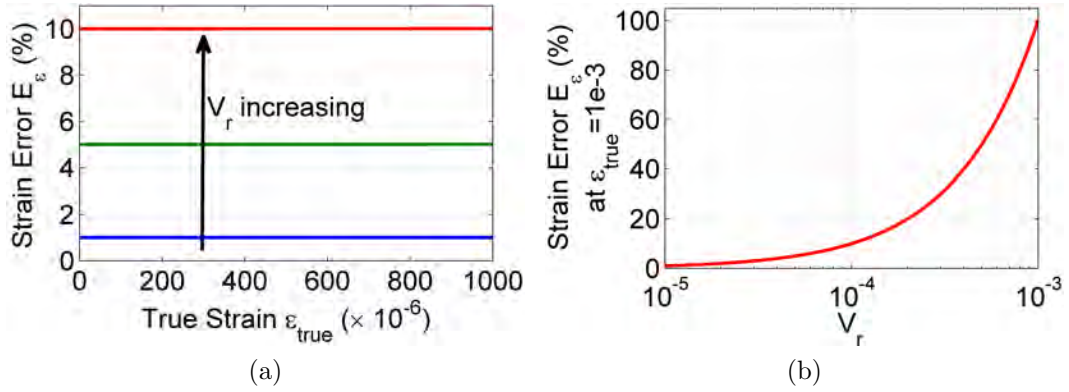


Figure 3.26: Error in the strain measurement due to electromagnetic noise: the effects of (a) true strain magnitude and (b) normalized noise voltage;  $F_G = 2.155$ .

induced in one cancels that induced in the other (Fig. 3.28(b)). Typically, strain is measured separately by two gauges located on opposite sides of the rod, and the average strain is reported [156]; this allows for the identification of bending-induced differences in the strains and, if necessary, the correction of the specimen's mount. Wiring two identical strain gauges in series (as shown in Fig. 3.28(b)) to form a Wheatstone quarter bridge causes the individually measured strains to be averaged,

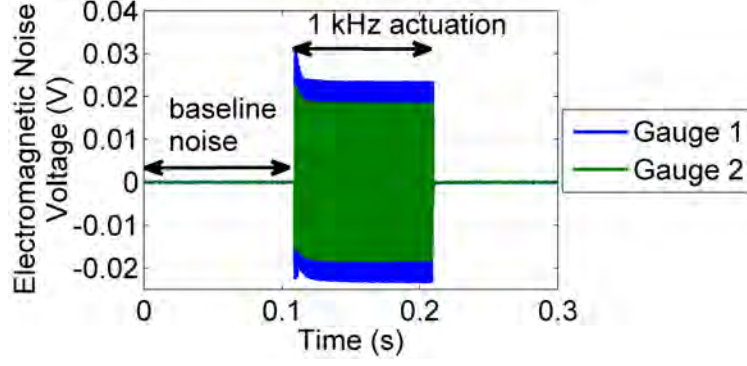


Figure 3.27: Electromagnetic noise voltage induced in two strain gauges and their leadwires in response to a 3 MPa amplitude, 1 kHz axial stress applied to a  $\text{Fe}_{81.6}\text{Ga}_{18.4}$  rod; strain gauges were oriented along the axis of the rod; no noise reduction techniques were used.

but it does not allow for an assessment of the specimen's mount. Although the ends of the specimen were ground to a tight tolerance (see the **Specimen geometry** subsection of Section 3.2.1) and the load frame is very stiff and well aligned, achieving even contact pressure between the platens and specimen necessitates the use of a spherical platen, especially when the specimen is stiff [17]. However, a lightweight spherical platen was not available. Thus, bending of the specimen is a point of uncertainty in this experiment.

To quantify the performance of the noise reduction techniques, the electromagnetic noise in the strain measurement was measured in situ by dynamically exciting the Galfenol specimen while measuring the strain with the strain bridge excitation voltage set to zero. The noise was measured for a constant current of 0.3 A applied to the electromagnets and an applied force of

$$F = 681 + 586\sin(2\pi ft) \text{ N.} \quad (3.92)$$

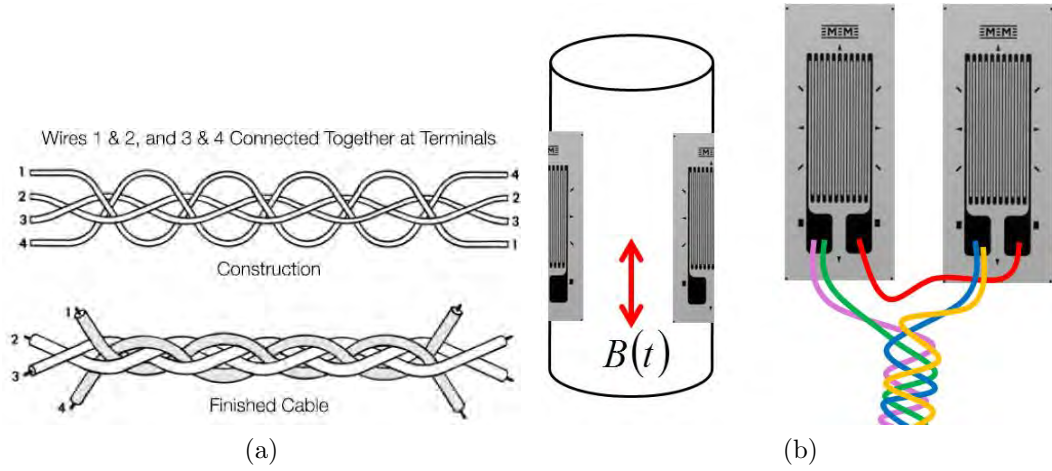


Figure 3.28: (a) weaving pattern for strain gauge leadwires to reduce electromagnetic noise induced in the wires [77] and (b) wiring of a strain gauge pair to simultaneously cancel bending strains and electromagnetic noise; gauges are bonded to opposite sides of the rod, but in otherwise identical locations and orientations.

At quasi-static frequencies, this loading caused the largest and steepest change in flux density (see Section 8.2.1 of [129]). Thus, this loading provided the worst-case scenario for electromagnetic noise throughout the forcing frequency range. The resulting electromagnetic noise for the solid Galfenol specimen over a range of forcing frequencies is shown in Fig. 3.29(a). The noise reduction techniques were very effective, as the electromagnetic noise peaks at about  $10 \times 10^{-6}$ , or 0.74 % of the strain span. As seen in Fig. 3.29(b), the amplitude of the magnetic flux density response decreased significantly with frequency, which was due to eddy currents in the solid Galfenol rod. This behavior helped to reduce the electromagnetic noise, because the induced voltage is directly related to the time derivative of the flux density. For the laminated Galfenol rod, the decay of the flux density amplitude was less severe, which likely led to slightly larger electromagnetic noise.

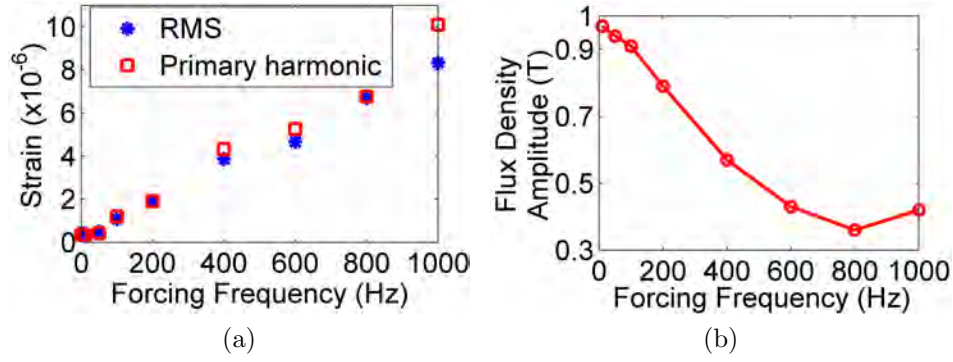


Figure 3.29: (a) measured electromagnetic noise in the strain measurement for the solid Galfenol specimen and worst-case loading under constant current to the electromagnets (the noise is quantified in terms of its RMS and the amplitude of its primary harmonic) and (b) amplitude of the magnetic flux density response at each frequency.

### 3.2.4 Data processing methods

This section includes the calibration of each measurement channel's phase response and the method used for calculating material properties. Calibration of each measurement channel's amplitude, filtering of the data, and the method for evaluating the level of reversibility in the constitutive response are discussed in Appendices C.4.1, C.3.2, and C.4.3, respectively.

#### Phase calibration

Each signal conditioner and corresponding anti-aliasing filter created a different phase shift, resulting in misalignment of the measured sensor signals. This misalignment created error in the size of the material characterization hysteresis loops. Typically, force and displacement signals are aligned by testing a sample that has near zero energy loss [7]. This technique could not be applied for this system, as the

mechanical and magnetic sensor signals needed to be mutually aligned. Instead, a new technique was used.

As shown in Fig. 3.30 and explained below, the sensors were removed and the sensor signals were simulated by manipulating a voltage signal produced by a function generator.

- Strain sensor: This sensor uses a strain bridge circuit, which produces a millivolt level signal in proportion to the applied strain. This was simulated using a voltage divider to attenuate the function generator signal while presenting the bridge resistance to the signal conditioner.
- Load cell: This sensor also uses a strain bridge circuit, producing a millivolt level signal proportional to the applied force. The same voltage divider circuit used for the strain sensor was used.
- Load washer: This sensor uses a piezoelectric crystal that generates charge in proportion to the applied stress. A capacitor was therefore placed in series with the function generator, so that the voltage signal was converted into a charge signal. Considering that  $\text{charge} = \text{capacitance} \times \text{voltage}$ , the capacitance was scaled to create a charge level similar to the sensor.
- Magnetic field sensor: This sensor produces a voltage proportional to the applied field. The function generator was used directly to represent this signal.
- Pick-up coil: This sensor produces a voltage proportional to  $-dB/dt$ , where  $B$  is the magnetic flux density. This implies a phase shift of  $\pi/2$  between the flux density and voltage signals. This phase shift was not simulated. However, the

fluxmeter is an integrator, and therefore introduced an additional  $\pi/2$  phase shift. Consequently, the total phase shift was implemented in post processing by multiplying the flux density signal by -1. Here, a voltage divider circuit was used to adjust the voltage level and match the resistance of the pick-up coil. Additionally, an isolation amplifier was placed in-between the function generator output and the voltage divider, because the fluxmeter requires a floating input to operate correctly.

The phase delay of each channel was measured with respect to the magnetic field sensor channel at multiple frequencies. During a test, the function generator signal was simultaneously sent to the magnetic field sensor channel and the channel under test. The output data was then acquired and saved.

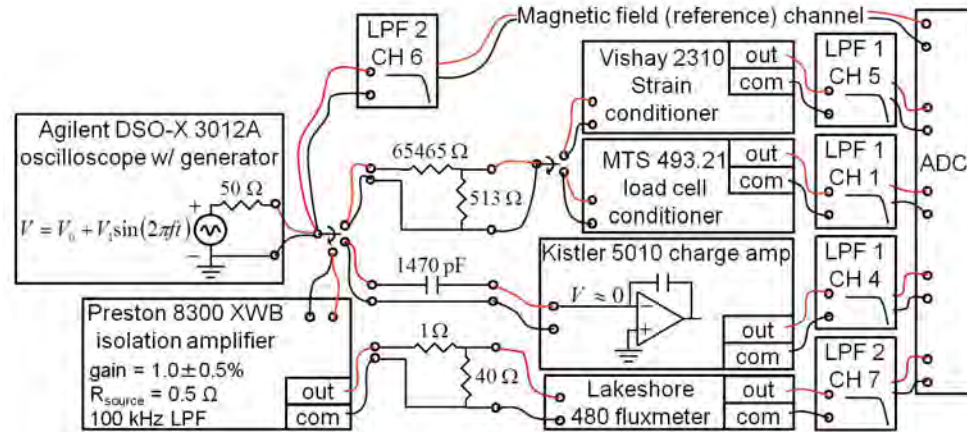


Figure 3.30: Experimental setup for measuring the phase response of the conditioning electronics for strain, load cell, load washer, and flux density signals.

Assuming that the electronics behave linearly, each channel in Fig. 3.30 can be represented as a block diagram, where each piece of equipment is described by a

transfer function  $G_i(s)$ . To illustrate how the phase response of each measurement channel was calculated, the magnetic flux density channel is considered (Fig. 3.31).

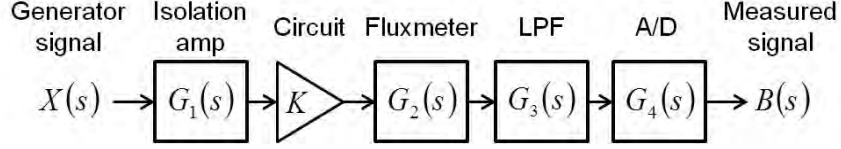


Figure 3.31: Block diagram of the magnetic flux density channel during phase response measurement.

For harmonic generator signals, the measured signal in Fig. 3.31 is

$$B(j\omega) = KG_4(j\omega)G_3(j\omega)G_2(j\omega)G_1(j\omega)X(j\omega). \quad (3.93)$$

By expressing each transfer function by its magnitude  $M_i(\omega)$  and phase  $\phi_i(\omega)$ , Eq. (29) becomes

$$B(j\omega) = M(\omega)\exp[j\phi(\omega)]X(j\omega), \quad (3.94)$$

where  $M(\omega)$  and  $\phi(\omega)$  are the magnitude and phase response, respectively, of the measurement channel in Fig. 3.31,

$$M(\omega) = KM_4(\omega)M_3(\omega)M_2(\omega)M_1(\omega) \quad (3.95)$$

and

$$\phi(\omega) = \phi_4(\omega) + \phi_3(\omega) + \phi_2(\omega) + \phi_1(\omega). \quad (3.96)$$

From Eq. (3.96), it is clear that the phase response of each measurement channel is simply a summation of the phase responses of the conditioning electronics. Further, the phase response of the magnetic flux density channel relative to the magnetic



field channel,  $\phi^{B/H}(\omega)$ , can be calculated by subtracting the phase responses of the isolation amplifier and magnetic field channel, i.e.,

$$\phi^{B/H}(\omega) = \phi^B(\omega) - \phi^H(\omega) = \phi(\omega) - \phi_1(\omega) - \phi^H(\omega). \quad (3.97)$$

By applying the time shift property of Laplace transforms to Eq. (3.94) followed by an inverse Laplace transform, the measured signal can be written in the time domain as

$$B(t) = M(\omega)X\left(t + \frac{\phi(\omega)}{\omega}\right)u\left(t + \frac{\phi(\omega)}{\omega}\right) = M(\omega)X(t - t_d)u(t - t_d), \quad (3.98)$$

where  $u(t)$  is the step function and  $t_d = -\phi(\omega)/\omega$  is the time delay imposed by the measurement system. If the flux density signal is phase referenced to the field signal, the time delay becomes the time delay of the flux density channel relative to the time delay of the field channel,

$$t_d \rightarrow -\frac{\phi^{B/H}(\omega)}{\omega} = -\frac{\phi^B(\omega) - \phi^H(\omega)}{\omega} = t_d^B - t_d^H = t_d^{B/H}. \quad (3.99)$$

Points on the phase response  $\phi^{B/H}(\omega)$  were measured by first generating a single tone sinusoid and extracting the phase of the measurement and field signals at the frequency of the sinusoid from discrete Fourier transforms (DFTs) of the two signals. Then the phase response of the isolation amplifier (measured independently) and field channel were subtracted according to Eq. (3.97). Finally, the relative time delay was calculated as the slope of a linear, least-squares regression of  $\phi^{B/H}(\omega)$ . The relative phase response and time delay of the other channels were measured in an analogous manner. This method assumes that the phase response of the A/D converter is equal for all channels.

Fig. 3.32 presents the measured phase response of each measurement channel (conditioner and corresponding low-pass filter) relative to the magnetic field channel,

which only includes scaling of the magnetic field sensor's signal and the common, low-pass filtering. Table 3.5 summarizes the linear, least-squares regression of each response. The dynamic force channel has a  $-\pi$  offset, because the charge amplifier contains an inverting op-amp. The flux density channel has a  $-\pi/2$  offset as discussed above. Unexpectedly, the relative time delay of the flux density channel is negative. Although the fluxmeter's manufacturer has not measured the fluxmeter's phase response, the instrument's designers suggested that the observed behavior may result from interactions between the inverting op-amp stage and other internal stages. Nonetheless, the absolute phase of the fluxmeter and flux density channel are always negative. For frequencies below about 100 Hz, the phase response of the charge amplifier becomes nonlinear due to discharge circuitry, which creates a high-pass filter effect. Consequently, only higher frequencies were used for linear regression.

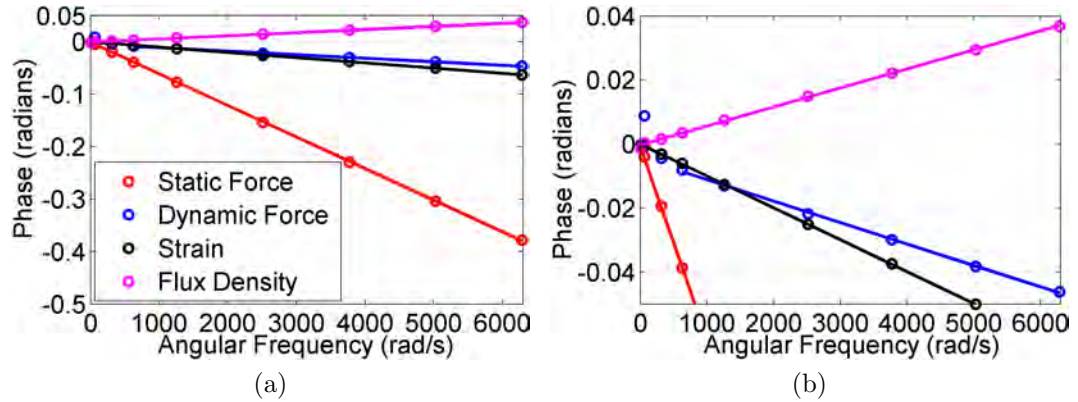


Figure 3.32: Phase response of the strain, static force, dynamic force, and magnetic flux density conditioning electronics (the phase offset in the dynamic force and flux density channels was removed for visualization purposes); (a) full response and (b) detail.

Table 3.5: Linear, least-squares regression of the phase responses of the conditioning electronics – phase offsets and relative time delays.

	Linear fit: $y = -mx + b$		Linear fit correlation, $R^2$
	$b$ , phase offset (rad)	$m$ , relative time delay (s)	
dynamic force	-3.146	$6.694 \times 10^{-6}$	0.9993
flux density	-1.571	$-5.950 \times 10^{-6}$	0.9990
static force	$-8.141 \times 10^{-4}$	$6.026 \times 10^{-5}$	1.0000
strain	$-4.159 \times 10^{-5}$	$9.965 \times 10^{-6}$	1.0000

### Calculation of material properties

The constitutive behavior of magnetostrictive materials can be represented by the piezomagnetic equations,

$$\mathbf{B} = [\mu]^T \mathbf{H} + [d^*]^H \mathbf{T}, \quad (3.100)$$

$$\mathbf{S} = [d]^T \mathbf{H} + [s]^H \mathbf{T}, \quad (3.101)$$

where  $\mathbf{B}$ ,  $\mathbf{H}$ ,  $\mathbf{S}$ , and  $\mathbf{T}$  are the magnetic flux density, magnetic field, strain, and stress vectors, respectively,  $[d]^T$  and  $[d^*]^H$  are piezomagnetic coefficient matrices,  $[s]^H$  is the compliance matrix,  $[\mu]^T$  is the magnetic permeability matrix, and the superscripts  $H$  and  $T$  denote measurement at constant magnetic field and constant stress, respectively. In this work, excitation was applied axially (typically denoted as the 3 direction) and outputs were measured along the axial direction. For these conditions, Eqs. (3.100) and (3.101) become

$$B_3 = \mu_{33}^T H_3 + d_{33}^{*H} T_3, \quad (3.102)$$

$$S_3 = d_{33}^T H_3 + s_{33}^H T_3. \quad (3.103)$$

The quasi-static material properties are derived from the slope of  $B_3$  versus  $H_3$  and  $S_3$  versus  $H_3$  curves measured at constant stress, as well as the slope of  $B_3$  versus  $T_3$  and  $S_3$  versus  $T_3$  curves measured at constant field. To simplify the notation of subsequent quantities, the 3 and 33 subscripts are dropped. To mitigate the noise amplification from numerical differentiation, small sections of each curve were fit by polynomials, which were analytically differentiated to calculate the slope at the center of each section [154, 120, 47, 156]. Fourth order polynomials were used in this work. A 75 % overlap of adjacent sections was used to ensure smooth material property curves. The Young's modulus  $E^H$  was calculated as the inverse of  $s^H$  [47]. Since constitutive responses were also measured at constant current to the electromagnets, the piezomagnetic coefficient and Young's modulus were also calculated at constant current:  $E^I$  and  $d^{*I}$ , respectively.

Under dynamic mechanical excitation, the sensing properties are complex and frequency dependent due to mechanically-induced magnetic diffusion (i.e., stress-induced eddy currents), as detailed in Section 3.1. Therefore, a frequency domain method adapted from [7] was used to calculate the dynamic material properties. First, the measured strain and stress signals ( $S$  and  $T$ , respectively) were transformed to the frequency domain ( $\tilde{S}$  and  $\tilde{T}$ , respectively) using DFTs. The complex, fundamental component (denoted by (1)) of each transformed signal,  $\tilde{S}(1)$  and  $\tilde{T}(1)$ , was then extracted. After, these fundamentals, which are linear, harmonic waveforms, were represented as phasors that differed in only magnitude and phase. The dynamic, complex elastic modulus was then calculated using a vector relationship,

$$\tilde{E} = \tilde{T}(1)/\tilde{S}(1). \quad (3.104)$$

The elastic component  $E$  of the dynamic modulus and the loss factor  $\eta_E$  were determined using the phase angle by which the stress leads the strain  $\delta_{T/S}$ ,

$$E = \operatorname{Re}(\tilde{E}) = \tilde{E} \cos(\delta_{T/S}) \quad (3.105)$$

and

$$\eta_E = \operatorname{Im}(\tilde{E}) / \operatorname{Re}(\tilde{E}) = \tan(\delta_{T/S}). \quad (3.106)$$

The phase angle  $\delta_{T/S}$  is simply the phase difference between the stress phasor and the strain phasor. Eqs. (3.104) to (3.106) are analogous to those presented in [7] for the calculation of the elastic component and loss factor of the dynamic stiffness. The calculation procedure is illustrated in Fig. 3.33. In an analogous manner, the lossless component  $d^*$  of the dynamic piezomagnetic coefficient  $\tilde{d}^*$  and the associated loss factor  $\eta_{d^*}$  were determined using the phase angle by which the stress leads the magnetic flux density  $\delta_{T/B}$ ,

$$d^* = \tilde{d}^* \cos(\delta_{T/B}) \quad (3.107)$$

and

$$\eta_{d^*} = \tan(\delta_{T/B}), \quad (3.108)$$

where

$$\tilde{d}^* = \tilde{B}(1) / \tilde{T}(1). \quad (3.109)$$

The use of this method is valid for the analysis of minor loop responses, because, for the applied excitation, the minor loop responses were nearly linear and the sensing properties were essentially constant at each forcing frequency. Loss factors are computed as shown in Eqs. (3.106) and (3.108). However, for a linear response, Eq. (3.106) is equivalent to the mechanical loss factor  $\eta_{\text{mech}}$  [150]

$$\eta_{\text{mech}} = \frac{W_{\text{d,mech}}/2\pi}{W_{\text{osc,mech}}} = \frac{(AL \cdot \oint T dS) / 2\pi}{AL \cdot \frac{1}{2} E |\tilde{S}_1|^2}, \quad (3.110)$$

where  $W_{\text{d,mech}}$  is the mechanical energy dissipated by the specimen per cycle,  $W_{\text{osc,mech}}$  is the steady-state oscillation energy stored by the specimen.  $W_{\text{osc,mech}}$  is taken as the stored mechanical energy at maximum deflection in a lossless, linear spring of stiffness  $AE/L$ , where  $A$  and  $L$  are the cross-sectional area and length of the rod, respectively [150].

Although this method neglects the harmonics of each signal, the areas of the hysteresis loops formed by the fundamentals and by the raw signals are equal [7]. Thus, the hysteresis (energy density) loss per cycle in the  $B$  versus  $T$  and  $S$  versus  $T$  responses –  $\bar{W}_{B-T}$  and  $\bar{W}_{S-T}$ , respectively – can be accurately calculated as

$$\bar{W}_{B-T} = \pi \tilde{T} \tilde{B} \sin(\delta_{T/B}) \quad (3.111)$$

and

$$\bar{W}_{S-T} = \pi \tilde{T} \tilde{S} \sin(\delta_{T/S}) . \quad (3.112)$$

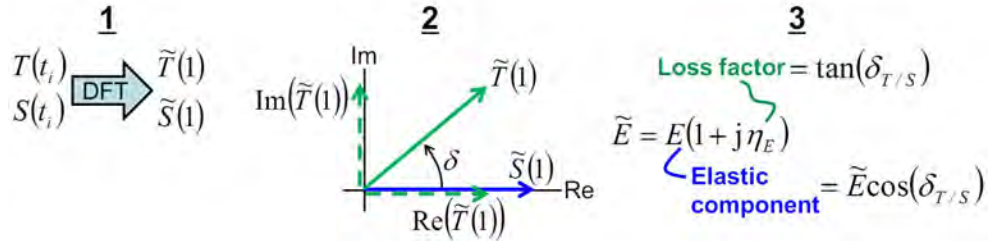


Figure 3.33: Frequency domain method used to calculate the dynamic material properties at each forcing frequency (adapted from [7]).

### 3.2.5 Dynamic sensing measurements

To verify the experimental setup with existing data and to evaluate the frequency-independent performance, quasi-static actuation and sensing responses were first measured. These measurements are reported in [129] and Section 2.1.

For the dynamic minor loops, the bias conditions were those for which the quasi-static magnetomechanical coupling of the solid rod was maximized (i.e., maximum sensitivity and minimum elastic modulus): 0.30 A and -9.93 MPa for constant current tests and 2.46 kA/m and -7.96 MPa for constant field tests (see Section 2.1 and [129]). Dynamic major loops were measured for a mechanical bias of -31.9 MPa (roughly the midpoint of the stress range) and the same magnetic biases as used for dynamic minor loops. To determine the effect of forcing frequency on positive and negative saturation, dynamic major loops were also measured for a 0.80 A bias. The stress amplitude for major and minor loops was 2.88 and 31.4 MPa, respectively. Measurements are shown for forcing frequencies of 4, 10, 50, 100, 200, 400, 600, 800, and 1000 (or 975) Hz. Appendix C.5 details the measurement procedure, whereas Table C.8 summarizes the loading conditions for each group of tests. Throughout testing, temperature increases above the 23 °C ambient were  $< 5$  °C.

#### **Solid Galfenol rod, constant current**

The major loop sensing responses at constant current are shown in Figs. 3.34 and 3.35 for bias currents of 0.30 and 0.80 A, respectively. The performance of the current control is shown by the current versus stress responses in Figs. 3.34(a) and 3.35(a). Two performance metrics – the maximum and standard deviation of the variation – were calculated at each forcing frequency and are presented in Figs. 3.34(b)

and 3.35(b). For both bias currents, current variation increases nearly linearly with frequency, but remains below 14 mA for all cases. The strain curves in Figs. 3.34(c) and 3.35(c) are successively shifted along the strain axis starting with the 10 Hz curve to more clearly visualize the behavior. At 4 Hz, there is an elbow in the strain response where the magnetostriction saturates and the elastic modulus reaches its stiff or saturated value. For stresses greater than the elbow stress, magnetostriction occurs and the effective elastic modulus of the material is reduced. As frequency increases, the elbow disappears and the region of softened behavior stiffens until it coincides with the saturated, purely-elastic regime. Evident in the flux density versus stress plots in Figs. 3.34(d) and 3.35(d), hysteresis increases and sensitivity to stress decreases with frequency. These trends imply that at high frequency, magnetic moment rotation is severely inhibited in the solid Galfenol rod. Although the stress amplitude was not large enough to reach both positive and negative saturation in the same test (i.e., to measure full hysteresis loops), these saturation states were separately reached in Figs. 3.34 and 3.35. The results separately show that the flux density magnitude at positive and negative saturation is frequency independent, which suggests that the limits of full hysteresis loops (i.e., the saturation states) are also frequency independent.

Minor loop responses are depicted in Fig. 3.36. The current variation and its metrics are given in Figs. 3.36(a) and 3.36(b), respectively. Current variation is very small at all frequencies. The mechanical and magnetic responses are shown in Figs. 3.36(c) and 3.36(d), respectively. Due to the low amplitude excitation and the bias condition, the response is nearly linear throughout the frequency range. An increase in hysteresis with frequency is clear in the strain versus stress and flux



density versus stress plots. Similar to the major loop responses, but to a much lesser extent, the active behavior (i.e., flux density changes and a softened elastic modulus) is suppressed as frequency increases. Material properties calculated from the minor loops are shown along with those for the laminated rod in Fig. 3.41 in the **Dynamic sensing properties and energy loss** subsection of this section.

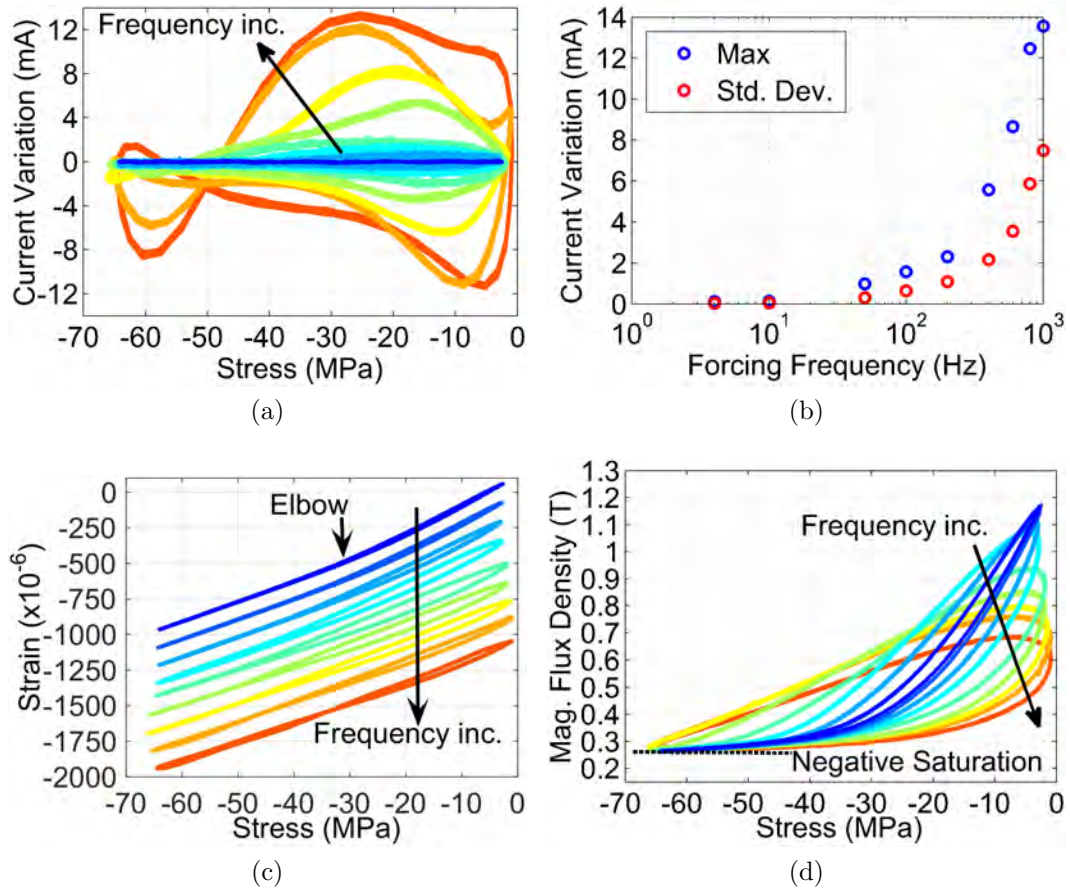


Figure 3.34: Major loop dynamic sensing response of the solid Galfenol rod for a bias current of 0.30 A, bias stress of -31.9 MPa, stress amplitude of 31.4 MPa, and forcing frequencies of 4, 10, 50, 100, 200, 400, 600, 800, and 1000 Hz: (a) variation in current about the current bias versus stress, (b) current variation metrics versus forcing frequency, (c) strain versus stress (successively shifted by  $-125 \times 10^{-6}$  for visualization purposes), and (d) flux density versus stress; color changes from blue to red as the frequency increases.

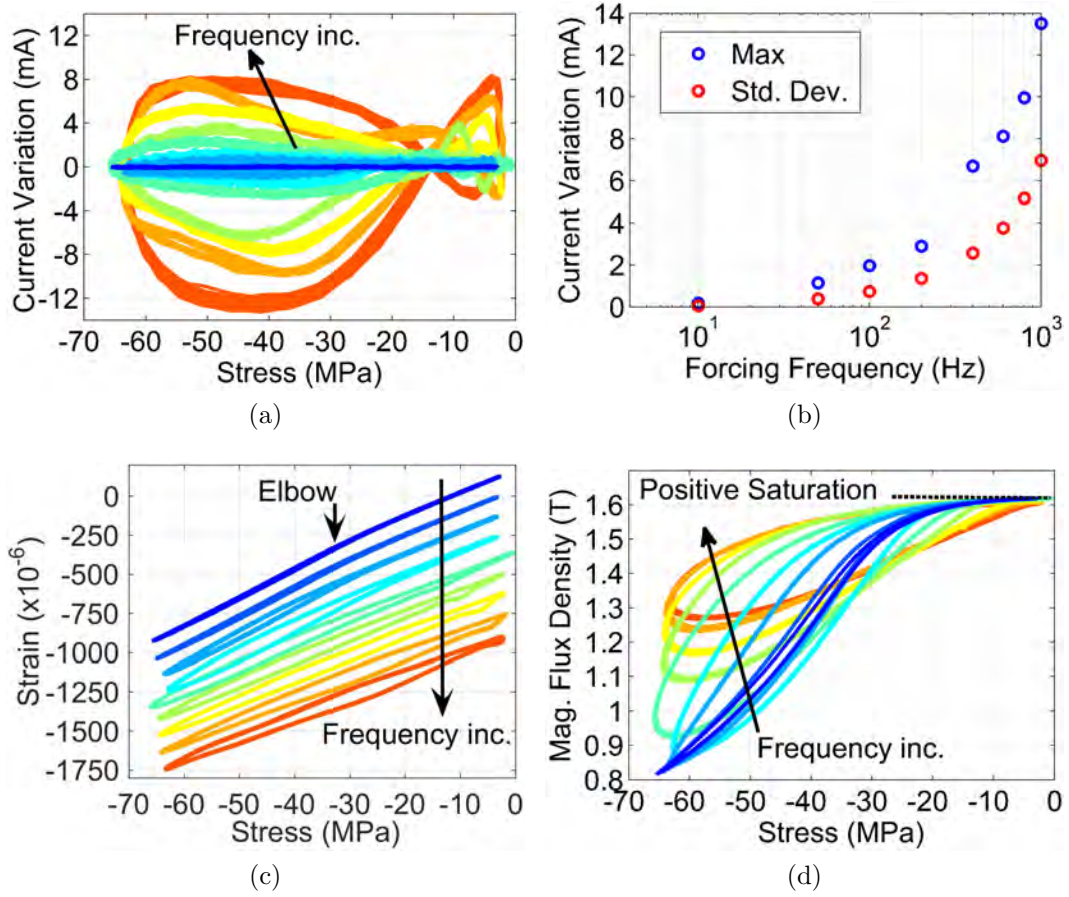


Figure 3.35: Major loop dynamic sensing response of the solid Galfenol rod for a bias current of 0.80 A, bias stress of -31.9 MPa, stress amplitude of 31.4 MPa, and forcing frequencies of 4, 10, 50, 100, 200, 400, 600, 800, and 1000 Hz: (a) variation in current about the current bias versus stress, (b) current variation metrics versus forcing frequency, (c) strain versus stress (successively shifted by  $-125 \times 10^{-6}$  for visualization purposes), and (d) flux density versus stress; color changes from blue to red as the frequency increases.

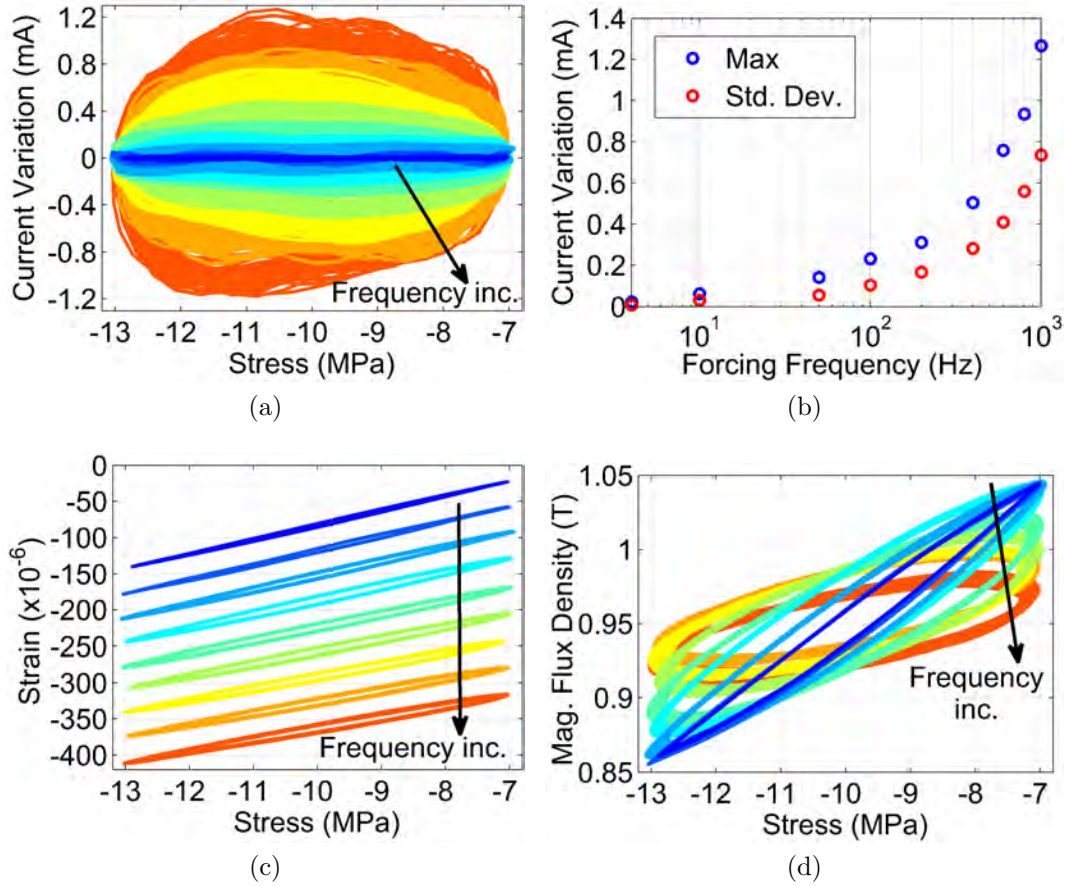


Figure 3.36: Minor loop dynamic sensing response of the solid Galfenol rod for a bias current of 0.30 A, bias stress of -9.93 MPa, stress amplitude of 2.88 MPa, and forcing frequencies of 4, 10, 50, 100, 200, 400, 600, 800, and 1000 Hz: (a) variation in current about the current bias versus stress, (b) current variation metrics versus forcing frequency, (c) strain versus stress (successively shifted by  $-35 \times 10^{-6}$  for visualization purposes), and (d) flux density versus stress; color changes from blue to red as the frequency increases.

### Solid Galfenol rod, constant field

Fig. 3.37 presents the dynamic, major loop sensing responses of the solid Galfenol rod at constant magnetic field. The variation in field about the bias field and the field control metrics are depicted in Figs. 3.37(a) and 3.37(b), respectively; the performance of the field controller significantly degrades as frequency increases. For comparison, the change in magnetic field during major loop constant current tests was about 2.4 kA/m at low frequency and 2.1 kA/m at high frequency. This suggests that the magnetic field controller has a limited impact above 100 to 200 Hz. For this reason, the dynamic sensing behavior of the laminated rod was only measured at constant current. Figs. 3.37(c) and 3.37(d) present the strain and flux density responses. Trends in these curves mirror those in the constant current responses.

Fig. 3.38 shows the dynamic, minor loop response at constant field. The effectiveness of the magnetic field controller is shown in Figs. 3.38(a) and 3.38(b). The absolute variation in the magnetic field is considerably lower than for dynamic, major loop tests. However, the change in magnetic field during dynamic, minor loop constant current tests was only about 0.9 kA/m, compared to a change of 2.1 kA/m for major loops. Thus, the maximum variation in the controlled field is about 50 % of the variation in the uncontrolled field. Since the minor loop response is nearly linear at each forcing frequency, the analytical solution of the mechanically-induced magnetic diffusion problem (Section 3.1.1) was used to estimate the effective (average) magnetic field inside the Galfenol rod at each forcing frequency. The results are depicted in Section 9.1.2 of [129]. The effective magnetic field exhibits more variation than observed in the surface magnetic field, particularly for frequencies below 400 Hz. The variation in the Mechanical and magnetic responses are given in Figs. 3.38(c) and

3.38(d). The slope of the flux density versus stress and strain versus stress responses decreases with frequency faster than at constant current due the combined effects of suppressed magnetic moment rotation and degraded constant field control. The dynamic modulus and piezomagnetic coefficient of the solid rod at constant field is depicted in Fig. 3.41.



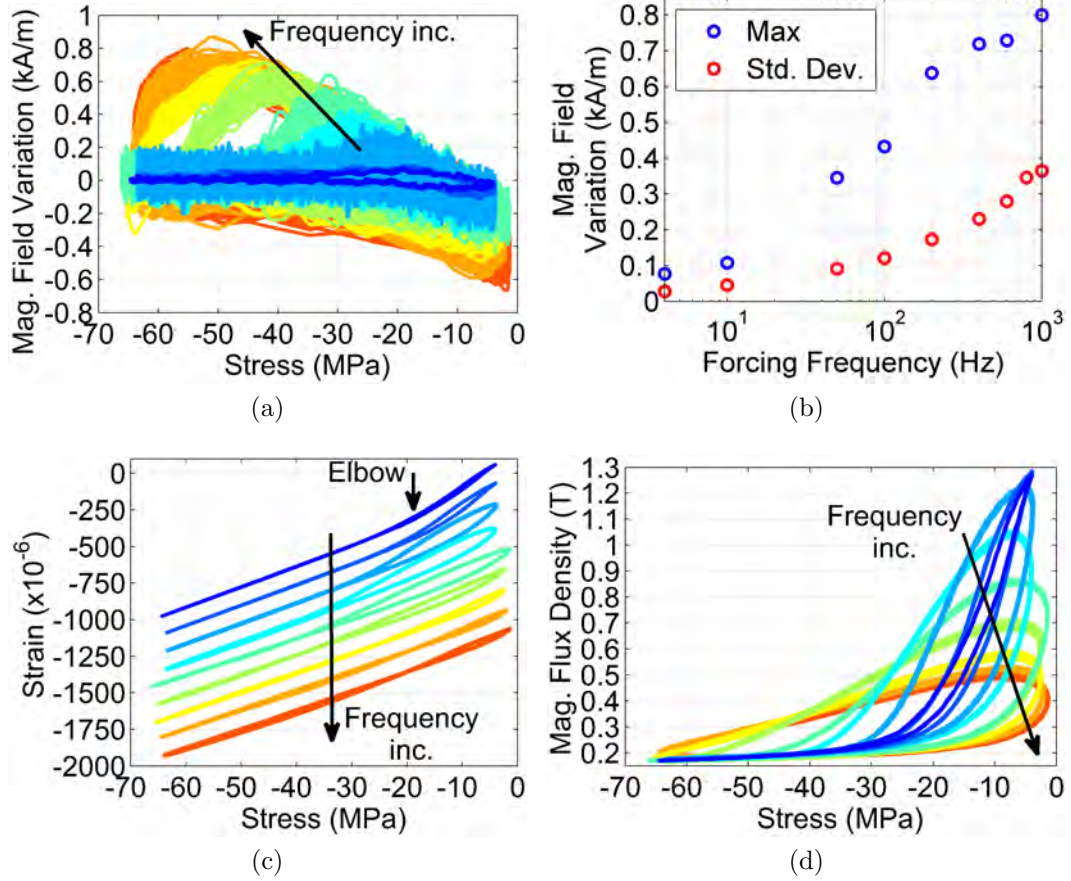


Figure 3.37: Major loop dynamic sensing response of the solid Galfenol rod for a bias magnetic field of 2.46 kA/m, bias stress of -31.9 MPa, stress amplitude of 31.4 MPa, and forcing frequencies of 4, 10, 50, 100, 200, 400, 600, 800, and 1000 Hz: (a) variation in field about the field bias versus stress, (b) field variation metrics versus forcing frequency, (c) strain versus stress (successively shifted by  $-125 \times 10^{-6}$  for visualization purposes), and (d) flux density versus stress; color changes from blue to red as the frequency increases.

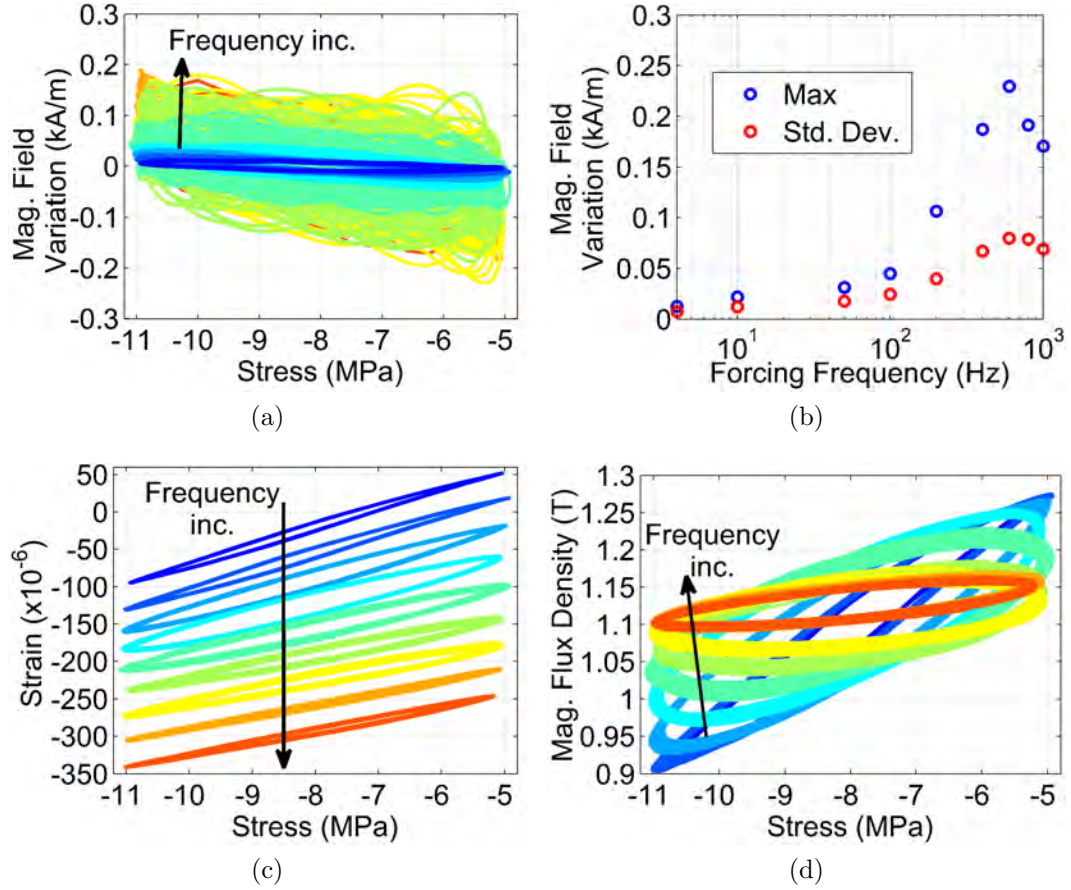


Figure 3.38: Minor loop dynamic sensing response of the solid Galfenol rod for a bias magnetic field of 2.46 kA/m, bias stress of -7.96 MPa, stress amplitude of 2.88 MPa, and forcing frequencies of 4, 10, 50, 100, 200, 400, 600, 800, and 1000 Hz: (a) variation in the surface field about the surface field bias versus stress, (b) surface field variation metrics versus forcing frequency, (c) strain versus stress (successively shifted by  $-35 \times 10^{-6}$  for visualization purposes), and (d) flux density versus stress; color changes from blue to red as the frequency increases.



### Laminated Galfenol rod, constant current

The dynamic sensing response of the laminated rod was only measured for constant current, because the measurements of the solid rod in the preceding subsection indicate that the magnetic field controller has a limited impact above 100 to 200 Hz.

Major and minor dynamic sensing responses of the laminated Galfenol rod are shown in Figs. 3.39 and 3.40, respectively. The magnetic and mechanical bias conditions were identical to the constant current testing of the solid rod. For visualization purposes, strain versus stress responses (Figs. 3.39(c) and 3.40(c)) and flux density versus stress responses (Figs. 3.39(d) and 3.40(d)) are successively shifted downward starting with the 10 Hz response. The variation in the current about the current bias is presented in Figs. 3.39(a) and 3.40(a), while the current control metrics are depicted in Figs. 3.39(b) and 3.40(b). Although slightly worse than for the solid rod, current control still performs well. Compared to the solid rod, hysteresis increases much slower with frequency and the quasi-static behavior extends to higher frequencies. These trends are consistent with an appreciable reduction in eddy currents. Differences in the quasi-static behavior of the solid and laminated rods can account for the remaining disparities in the dynamic responses; in particular, the change in flux density is considerably less for the laminated rod and the active behavior occurs over a different stress range.

At 400 Hz and above, the major loop strain versus stress responses exhibits repeatable, yet erratic oscillations within each forcing cycle. The magnitude of these oscillations seems too large to be an artifact of imperfect current control or electromagnetic strain noise. This may be a result of imperfect load control. However, this behavior is nearly absent from the flux density versus stress responses. The root

cause is currently unknown and further investigation is needed. Dynamic material properties were calculated from the minor loop responses and are shown in Fig. 3.41 along with the dynamic properties of the solid rod.

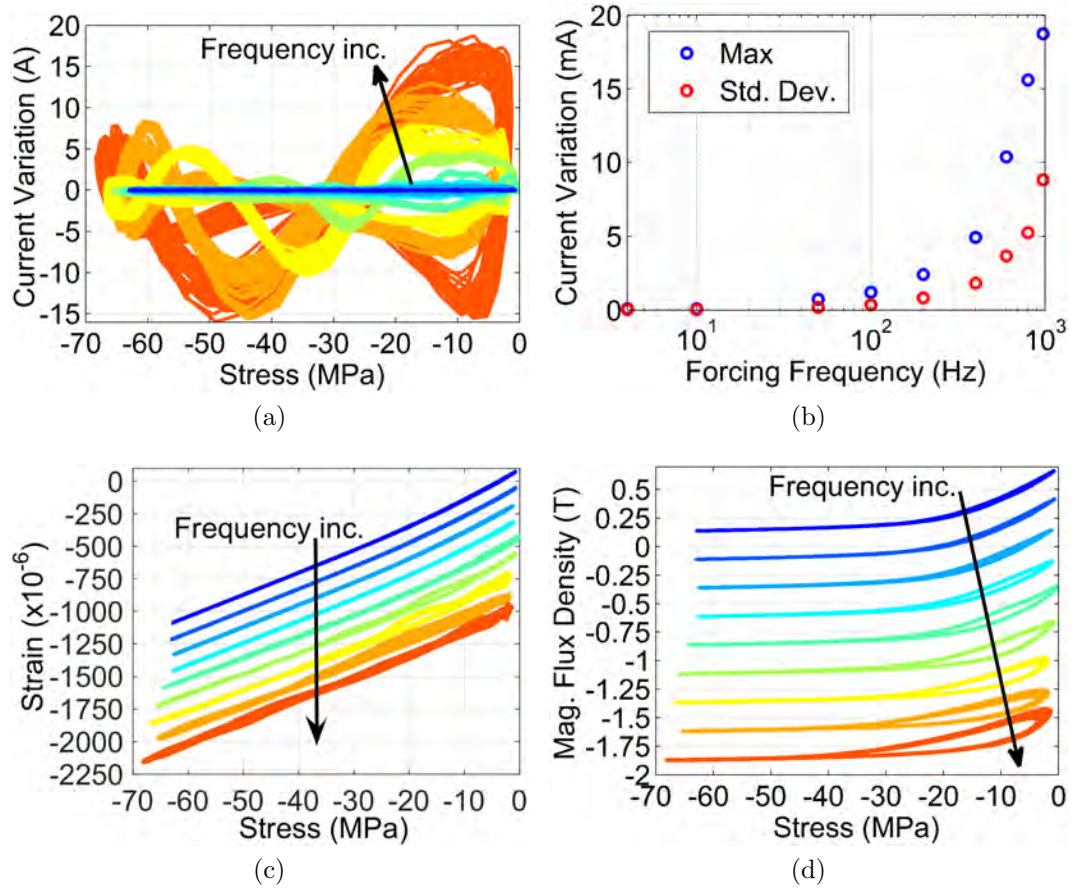


Figure 3.39: Major loop dynamic sensing response of the laminated Galfenol rod for a bias current of 0.30 A, bias stress of -31.9 MPa, stress amplitude of 31.4 MPa, and forcing frequencies of 4, 10, 50, 100, 200, 400, 600, 800, and 975 Hz: (a) variation in current about the current bias versus stress, (b) current variation metrics versus forcing frequency, (c) strain versus stress, and (d) flux density versus stress (strain and flux density responses are successively shifted by  $-125 \times 10^{-6}$  and -0.25 T, respectively, for visualization purposes); color changes from blue to red as the frequency increases.

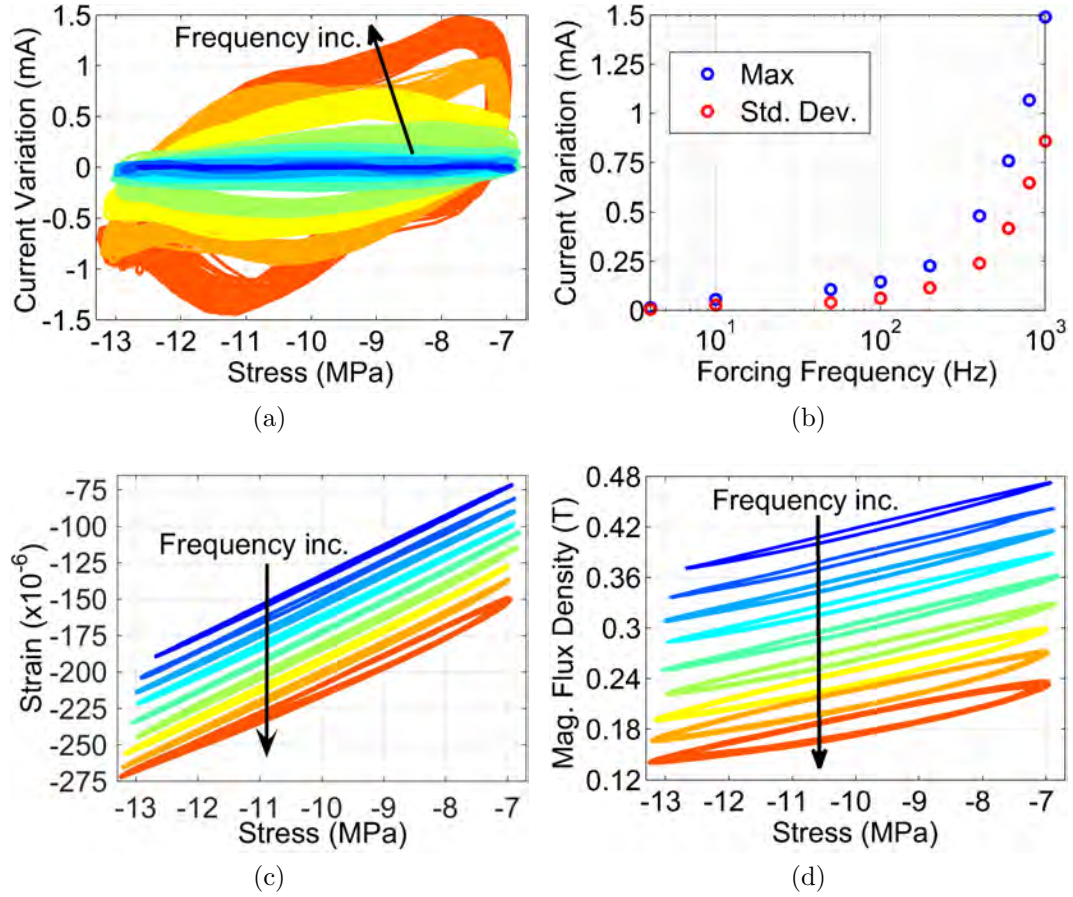


Figure 3.40: Minor loop dynamic sensing response of the laminated Galfenol rod for a bias current of 0.30 A, bias stress of -9.93 MPa, stress amplitude of 2.88 MPa, and forcing frequencies of 4, 10, 50, 100, 200, 400, 600, 800, and 1000 Hz: (a) variation in current about the current bias versus stress, (b) current variation metrics versus forcing frequency, (c) strain versus stress, and (d) flux density versus stress (strain and flux density responses are successively shifted by  $-10 \times 10^{-6}$  and -0.03 T, respectively, for visualization purposes); color changes from blue to red as the frequency increases.

## Dynamic sensing properties and energy loss

The frequency dependence of the dynamic sensing properties of the solid and laminated Galfenol rods is shown in Fig. 3.41, where the dashed line denotes the expected trend in the regime where field control was inadequate and data is not reported. At low frequency, there is a distinct difference between the sensing properties of the solid and laminated specimens. This was also observed in quasi-static actuation and sensing measurements [129]. Thus, the difference can be attributed to fundamental differences in the microstructure of the specimens. As shown in prior work [120, 154], the response of a solid rod under constant field is significantly more sensitive than that under constant current at low frequency. The solid rod exhibits a strong dependence on forcing frequency over the 0 to 1 kHz range due to eddy currents, which dampen domain wall motion, causing the piezomagnetic coefficient to decay toward 0 and the Young's modulus to monotonically approach its saturation value (72.1 GPa). This strong frequency dependence was expected because the theoretical mechanically-induced magnetic diffusion cut-off frequency [134] of the solid rod at the constant field and constant current bias points is about 69 Hz and 81 Hz, respectively; these estimates were calculated using an approximate electrical conductivity ( $\sigma = 2.15 \times 10^6$  S/m) [160] and magnetic permeabilities estimated from measurements (constant field:  $\mu \approx 370\mu_0$ , constant current:  $\mu \approx 310\mu_0$ ) [129, 55]. From Fig. 3.41(a), the experimental cut-offs are about 44 Hz and 105 Hz for constant field and constant current conditions, respectively. This behavior illustrates the need for frequency-dependent measurements and the inaccuracy, even for linear operating regimes, of dynamic properties [147] calculated via linear piezomagnetic models from experimental responses to electrical excitation.

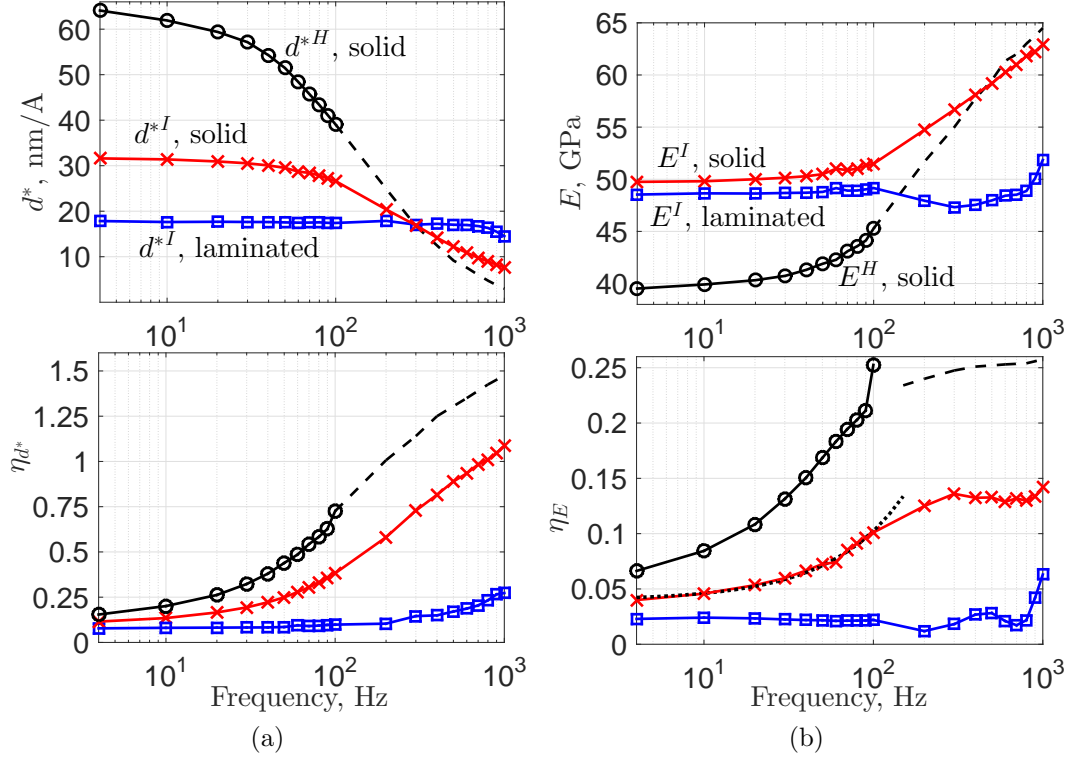


Figure 3.41: (a) dynamic piezomagnetic coefficient and (b) dynamic Young's modulus of the solid and laminated  $\text{Fe}_{81.6}\text{Ga}_{18.4}$  rods measured at constant current ( $T_{\text{bias}} = -9.93$  MPa,  $I_{\text{bias}} = 0.3$  A) and constant field ( $T_{\text{bias}} = -7.96$  MPa,  $H_{\text{bias}} = 2.46$  kA/m), (top) lossless component and (bottom) loss factor; dashed line denotes the expected trend (not measured data); dotted line denotes the linear fit:  $\eta_E = 0.6262 \times 10^{-3}f + 0.0398$ .

The dynamic sensing properties of the laminated rod display a weak dependence on frequency up to 1 kHz. In particular, the experimental cut-off is about 1 kHz and the theoretical cut-off is about 7 kHz when an effective conductivity ( $\sigma/(8+1)^2$ ) is used to approximate the laminated rod as a solid rod [59]. It is emphasized that  $E^I$  of the laminated rod decreases appreciably between 100 and 300 Hz. Over this frequency range,  $d_{33}^{*I}$  is nearly constant, which suggests that the magnetomechanical

behavior is not the cause. It is hypothesized that a softening of the adhesive occurs over this frequency range.

Energy dissipation in the Galfenol rods was also investigated from the minor hysteresis loops measured under constant current. The energy dissipated per cycle is highly dependent on stress amplitude; thus, it is useful to consider a normalized energy loss, such as the mechanical loss factor, which is equal to  $\eta_E$  in Fig. 3.41(b) as mentioned above. The dotted line in Fig. 3.41(b) denotes a linear fit of the measured  $\eta_E$  of the solid rod. Below the cut-off frequency, the solid rod exhibits a nearly linear increase in loss factor with frequency, suggesting that excess eddy current losses are low and there is a high density of magnetic domain walls [25]. This is supported by magnetic domain observations in single crystals of similar Galfenol alloys [110], which show that magnetic domains are about 100  $\mu\text{m}$  wide (about  $10^2$  times smaller than the specimen's diameter). As frequency increases above the cut-off, domain wall motion is significantly suppressed and the loss factor of the solid rod levels off. At high frequency, the loss factor slowly increases due to conventional viscoelastic damping. The loss factor of the laminated rod displays a moderately flat response up to 800 Hz, after which it increases nearly linearly as a result of the finite laminate thickness (i.e., eddy currents) and viscoelastic damping.

To further investigate the magnetomechanical energy loss under constant current, Fig. 3.42 presents the frequency dependence of the energy density components during steady-state oscillation: (1) supplied mechanical,  $\oint T dS$ , (2) dissipated magnetic (based on the surface field),  $\oint H dB$ , (3) dissipated magnetic (based on an approximate average internal field),  $\oint H_{\text{avg}} dB$ , and (4) supplied minus dissipated,

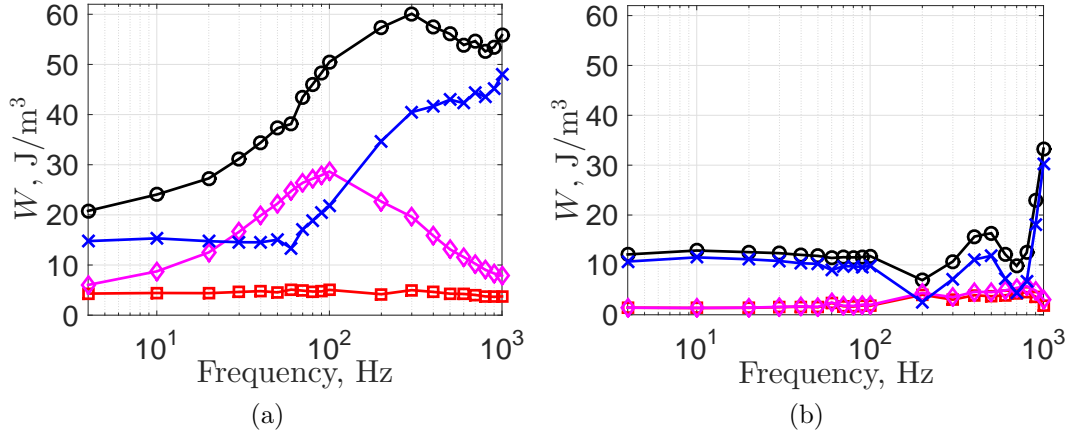


Figure 3.42: Supplied mechanical ( $\circ$ ), dissipated magnetic ( $\square$ ), dissipated magnetic (with correction) ( $\diamond$ ), and supplied minus dissipated (corrected) ( $\times$ ) energy densities per cycle associated with the minor hysteresis loops of the (a) solid and (b) laminated  $\text{Fe}_{81.6}\text{Ga}_{18.4}$  rods under constant current.

$\oint T dS - \oint H_{\text{avg}} dB$ . The energy densities per cycle were calculated from the fundamental component of each signal as explained in ASTM D5992 [7].  $H_{\text{avg}}$  is calculated from the measured  $T$  and  $H$  using the aforementioned magnetic permeabilities and conductivities as discussed by Scheidler and Dapino [134]. As expected for a mechanical-to-magnetic energy conversion,  $\oint T dS > 0$  (mechanical energy is supplied) and  $\oint H dB < 0$  (magnetic energy is dissipated) [158]. As frequency increases in the solid rod,  $H_{\text{avg}}$  quickly deviates from  $H$  due to magnetic diffusion; consequently,  $\oint H dB$  under-predicts the true magnetic energy loss, even at low frequencies. Conversely, in the laminated rod, the dissipated magnetic energy can be accurately calculated using a surface field measurement, because  $H_{\text{avg}} \approx H$  below 1 kHz. Although they should be equal if no other loss mechanisms exist, the mechanical energy supplied to the rods per cycle is considerably larger than the magnetic energy dissipated in them. This can be accounted for only in part by dissipation to the amplifier,



which was approximately  $< 10\%$  of the supplied mechanical energy, and viscoelastic damping, which is expected to be small like in other metallic materials. Similar results were found by Yoo et al. [158] for quasi-static loading, but the primary cause is currently unknown. Separation of the energy loss can be more carefully investigated using a revised experimental setup that establishes the magnetic bias condition using permanent magnets rather than an electromagnet.

### 3.2.6 Concluding remarks

This section presented a precise and complete dynamic characterization of the most widely used Galfenol alloy,  $\text{Fe}_{81.6}\text{Ga}_{18.4}$ . The objective was to measure the 1D, dynamic sensing response of the material and to quantify from the response, the frequency dependence of the material properties for 1D sensing. This was accomplished by controlling the axial, dynamic stress and static magnetic field over a specific region of a Galfenol rod, and measuring the axial strain and magnetic flux density. Auxiliary variables – drive voltage, drive current, and temperature – were also measured for reference. At each forcing frequency, sensing-based material properties were calculated using a frequency domain method adapted from an ASTM standard.

Design of the experiment was separated into six sections: (a) specimen design, (b) sensor selection and uncertainty analysis, (c) calibration methods, (d) experimental setup and methods, (e) data processing methods, and (f) procedure. The specimens were designed by considering recommendations from ASTM standards, the magnetic circuit constraints, and guidelines to avoid buckling. Solid and laminated cylindrical rod specimens of nominal dimension  $7.62 \times 0.627$  cm (L x D) were used. Mechanical, magnetic, and thermal sensors were selected based on a trade study of the available

technologies. For each sensor, calibration methods were developed and explained. In addition, the uncertainty for each measurement was calculated at the system level using error propagation equations. In most cases, the estimated uncertainty met ASTM standards. However, the magnetic flux density signal is expected to have 0.4 % to 0.9 % more error than the recommended  $\pm 1$  %.

The experimental setup and methods were explained in detail using photographs and schematic drawings. The system was refined to minimize the three key sources of error: (a) electromagnetic noise in strain signals due to Galfenol's magnetic response, (b) error in load signals due to the inertial force of fixturing, and (c) phase misalignment between signals due to conditioning electronics. For dynamic characterization, strain error was kept below 1.2 % of full scale by wiring two collocated gauges in series (noise cancellation) and through leadwire weaving. Inertial force error was kept below 0.41 % by measuring the dynamic force in the specimen using a nearly collocated piezoelectric load washer. The phase response of all conditioning electronics was explicitly measured and corrected for in post processing. Control of the magnetic field was briefly discussed; PI control was used for constant field testing.

The sensing response of the solid and laminated rods was measured for dynamic stresses up to 31 MPa and 1 kHz. For the solid rod, both constant current and constant field biases were investigated. Current control performed well, but the performance of the field controller significantly degraded above 100 to 200 Hz. In general, as frequency is increased, the sensing response becomes more linear due to an increase in eddy currents, which tend to suppress the active behavior of the material. As frequency increases above about 100 Hz, the elbow in the strain versus stress response

disappears and the region of softened behavior stiffens until it coincides with the saturated, purely-elastic regime. These trends imply that at high frequency, magnetic moment rotation is severely inhibited in the solid Galfenol rod. Compared to the solid rod, the laminated rod exhibits much slower increases in hysteresis with frequency, and its quasi-static behavior extends to higher frequencies. Both trends suggest an appreciable reduction in eddy currents.

The frequency dependence of the dynamic sensing properties of solid and laminated Galfenol ( $\text{Fe}_{81.6}\text{Ga}_{18.4}$ ) rods was explicitly measured under constant current and constant field for 2.88 MPa compressive stresses up to 1 kHz at the bias states for which the quasi-static magnetomechanical coupling of the solid rod was maximized: -9.93 MPa, 0.3 A and -7.96 MPa, 2.46 kA/m, respectively. Due to mechanically-induced magnetic diffusion cut-off frequencies of only about 44 Hz (constant field) and 105 Hz (constant current), the dynamic sensing properties of the solid rod at the given bias points vary significantly with frequency, monotonically decaying toward their saturated (passive) values. This result illustrates the inaccuracy of frequency-independent dynamic properties calculated via linear piezomagnetic models from experimental responses to electrical excitation. It also motivates the use of complex, frequency-dependent properties for modeling and design. Conversely, the sensing properties of the laminated rod exhibit a weak dependence on frequency over the measurement range (i.e., a cut-off of about 1 kHz). The loss factor of the solid rod under constant current initially increases almost linearly (suggesting that excess eddy current losses are low) from a quasi-static value of about 0.040, then, at a value of 0.120, becomes nearly frequency independent from about 300 to 900 Hz. The laminated rod displays a loss factor of about 0.015 up to 800 Hz, after which it increases

nearly linearly due to eddy currents and viscous loss. The frequency dependence of magnetic and mechanical energy densities were also presented and discussed in terms of magnetic diffusion and thermodynamic considerations.

This novel dynamic characterization provides a detailed set of data that allows for the validation of recently-developed Galfenol constitutive models that incorporate rate-dependent effects. The presented frequency-dependent material properties also permit accurate modeling of Galfenol-based systems that experience time-varying forces.

## Chapter 4: Dynamic Stiffness Change

In this chapter, the dynamic changes in the elastic modulus of magnetostrictive materials that result from real-time magnetic field changes are studied in two stages. First, a magnetostrictive transducer that can electrically tune its stiffness at high speeds is modeled, designed, and tested. Second, high-speed switching of the transducer's stiffness is applied in a computational study of switched stiffness vibration control of a simple mechanical system.

### 4.1 Magnetostrictive Variable-Stiffness Spring

In this section, a magnetostrictive transducer is designed to operate as a spring element that has a dynamically-tunable and electrically-controllable stiffness. This device is referred to as a magnetostrictive Varispring. The Varispring is designed by modeling (a) the electromechanical response of the device, (b) mechanically-induced magnetic diffusion, and (c) the effect of internal mass on the dynamic stiffness of the active element. First, experimental and practical design considerations are discussed. Then, the theoretical performance of Galfenol- and Terfenol-D-based Varisprings are calculated and compared, after which the Varispring's design is introduced. Dynamic tuning of a prototype Varispring's elastic response is then measured, including the first measurement of the dynamic  $\Delta E$  effect.

### 4.1.1 Modeling and design

#### Experimental and practical considerations

Future performance testing of the magnetostrictive Varispring will involve using the device in an experiment to simulate the variable stiffness of certain machine components. To facilitate this future experiment, the following design constraints were imposed on the prototype Varispring: (a) an axial stiffness of about  $500 \text{ N}/\mu\text{m}$  ( $2.86 \times 10^6 \text{ lbf/in}$ ), (b) a maximum applied dynamic force of  $1000 \text{ N}$  ( $224.8 \text{ lbf}$ ), and (c) a maximum diameter and height of  $50 \text{ mm}$  ( $1.97 \text{ in}$ ) and  $105 \text{ mm}$  ( $4.13 \text{ in}$ ), respectively. For precise stiffness tuning, it is desirable to operate the magnetostrictive material under small amplitude dynamic stresses, such that the material's response is approximately linear for a fixed magnetic input. Also, since the performance of Terfenol-D is slightly degraded above room temperature [95], air cooling of the magnetostrictive rod is beneficial; this necessitates an air gap between the electromagnet and magnetostrictive rod. Consequently, the length of the magnetostrictive rod was used as an independent design variable, while the rod's diameter and the electromagnet's maximum dimensions were defined by the aforementioned criteria.

As detailed in the **Inertial force error reduction** subsection of Section 3.2.3, the vibration of any mass located in-between the specimen (i.e., the magnetostrictive rod) and force transducer introduces errors in the measurement of the dynamic force in the specimen; this inertial force error is reduced by minimizing the mass in-between the specimen and force transducer. To meet the ASTM-recommended inertial force error tolerance of  $0.5 \%$  [15], the dynamic, axial force applied to the specimen was measured by a piezoelectric load washer that was located inside the Varispring and nearly adjacent to the specimen.

To increase the changes in stiffness and operate in quasi-linear regimes, a mechanical preload was applied to the magnetostrictive rod. Typically, the preload is applied by a softening Belleville spring operated near its maximum deflection to prevent excessive preload variation during loading of the device [95]. Thus, the stiffness of the Varispring's central load path relative to that of its magnetic flux return path was considered to ensure that the Belleville spring compresses during assembly of the device.

### Electrical response

The electromechanical response of a magnetostrictive transducer operated sufficiently below its first mechanical resonance frequency can be modeled as

$$F(s) = k^H s^{-1} \Delta v(s) - GI(s), \quad (4.1)$$

$$V(s) = G\Delta v(s) + (L^S s + R_{\text{coil}}) I(s), \quad (4.2)$$

where  $s$  is the Laplace parameter,  $F$  represents the force in the magnetostrictive rod (tension positive),  $\Delta v$  denotes the relative velocity of the ends of the rod,  $I$  and  $V$  are the current in and voltage applied to the electromagnet, respectively, and  $R_{\text{coil}}$  is the electromagnet's resistance [84, 58]. To incorporate constitutive nonlinearities, the magnetic field  $H$  and stress  $T$  dependence of the rod's axial stiffness at constant magnetic field  $k^H$ , inductance at constant strain  $L^S$ , and electromechanical coupling coefficient  $G$  are retained,

$$k^H(H, T) = E^H(H, T) A_{\text{rod}} l_{\text{rod}}^{-1}, \quad (4.3)$$

$$L^S(H, T) = N^2 A_{\text{coil}} (\mu^T(H, T) - d(H, T)^2 E^H(H, T)) l_{\text{coil}}^{-1}, \quad (4.4)$$

$$G(H, T) = d(H, T) E^H(H, T) N A_{\text{rod}} l_{\text{coil}}^{-1}. \quad (4.5)$$

In Eqs. (4.3)–(4.5),  $\mu^T$ ,  $d$ ,  $E^H$ ,  $l_{\text{rod}}$ , and  $A_{\text{rod}}$  denote the magnetic permeability at constant stress, piezomagnetic coefficient, Young’s modulus at constant field, length, and cross-sectional area of the magnetostrictive rod, respectively, and  $N$ ,  $l_{\text{coil}}$ , and  $A_{\text{coil}}$  are the number of windings in, axial length of, and cross-sectional area enclosed by the electromagnet, respectively. The stress- and field-dependent material properties were calculated using 1D, anhysteretic formulations of the DEA models of Galfenol and Terfenol-D discussed in the **Discrete energy-averaged constitutive models** subsection of Section 1.2.2. The models were optimized to existing measurements [96, 55]. To improve computational efficiency, these models were implemented as interpolation functions with very fine input grids.

If the magnetic flux leakage and the magnetic reluctance of the Varispring’s flux return path are assumed negligible, the magnetic field in the magnetostrictive rod is

$$H(s) = NI(s)/l_{\text{coil}}. \quad (4.6)$$

For a mechanical load of mass  $m$ , Eqs. (4.1) and (4.2) can be combined with Eq. (4.6) to quantify the field generated in the magnetostrictive rod by an applied voltage,

$$H(s) = \frac{N}{l_{\text{coil}}} \frac{ms^2 + K^H}{L^S ms^3 + R_{\text{coil}} ms^2 + (G^2 + L^S K^H) s + R_{\text{coil}} K^H} V(s), \quad (4.7)$$

where the dependence of  $K^H$ ,  $L^S$ , and  $G$  on  $H$  and  $T$  was dropped from the notation for compactness. This model does not incorporate eddy current effects and is thus more accurate for magnetostrictive rods operating below their magnetic diffusion cut-off frequency.

To maintain compressive loading of the magnetostrictive rod during dynamic operation, the Varispring is operated at a moderate compressive mechanical bias for which the rod’s zero-field Young’s modulus is nearly saturated (i.e., the stiff state).



From this bias, the Varispring's stiffness is decreased by increasing the field from zero to a tuning field  $H_{\text{soft}}$ . To approximate the Varispring's response time to a step change in the command stiffness, the rise time to reach  $H_{\text{soft}}$  from zero in response to a voltage step was calculated as a function of the magnetostrictive rod's length for  $m = 2$  kg and  $l_{\text{coil}} = l_{\text{rod}}$ . Rise times were calculated using the minimum number of windings  $N_{\text{min}}$  needed to generate the tuning field with 95 % of the maximum current  $I_{\text{max}}$  for a given wire gauge, i.e.,  $N_{\text{min}} = H_{\text{soft}} l_{\text{coil}} / (0.95 I_{\text{max}})$ . In this way, the effective electrical inductance was minimized for each design case.

The rise times for Galfenol- and Terfenol-D-based Varisprings are depicted in Fig. 4.1. Three cases are considered: (a) Galfenol, maximum Young's modulus change ( $\Delta E_{\text{max}} \approx 30$  GPa,  $H_{\text{soft, max}} = 11$  kA/m) [129, 55], (b) Terfenol-D, near maximum Young's modulus change ( $\Delta E_{\text{max}} \approx 90$  GPa,  $H_{\text{soft, max}} = 80$  kA/m) [96], and (c) Terfenol-D, equivalent Young's modulus change ( $\Delta E \approx 30$  GPa,  $H_{\text{soft}} = 35$  kA/m) [96]. The bias stress  $T_{\text{bias}}$  for all three cases is -42 MPa.

In general, the rise time decreases with the magnetostrictive rod's length, because  $A_{\text{rod}}$  decreases with its length to maintain a given nominal stiffness, which reduces  $A_{\text{coil}}$  and thus the blocked inductance. The rise time also decreases with the wire gauge, because electromagnets wound using larger wire diameters can generate  $H_{\text{soft}}$  with fewer windings due to their larger  $I_{\text{max}}$ . This reduces the coil's inductance, but at the expense of higher electrical power demands [128]. Maximal stiffness tuning of a Terfenol-D-based Varispring is appreciably slower than that of a Galfenol-based Varispring despite Galfenol's significantly higher magnetic permeability (and thus blocked inductance) due to the larger tuning field that must be generated. However, for the same change in elastic modulus, Terfenol-D provides a slightly faster response.

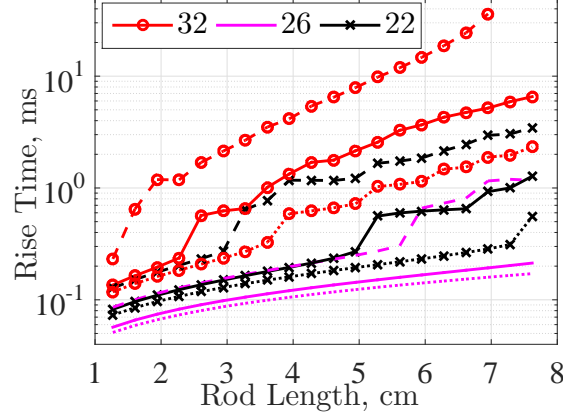


Figure 4.1: Rise time to reach  $H_{\text{soft}}$  from  $H = 0$  in response to a 250 V step voltage input to electromagnets wound with 32, 26, and 22 AWG wire; Galfenol,  $\Delta E_{\text{max}} \approx 30$  GPa (solid), Terfenol-D,  $\Delta E_{\text{max}} \approx 90$  GPa (dashed), and Terfenol-D,  $\Delta E \approx 30$  GPa (dotted).

### Effect of dynamic stress on bias magnetic fields

As detailed in Section 3.1.1, when magnetostrictive rods are subjected to constant surface magnetic fields and dynamic axial stresses, internal eddy currents are generated, which, if the forcing frequency exceeds a diffusion cut-off frequency  $\omega_c$ , significantly suppress the material's active response. The analytical cut-off frequency for linear constitutive regimes is given by Eq. (3.40). Since the Varispring is designed to operate under small amplitude dynamic stresses to maximize the stiffness variation between two bias field states, the linearity assumption is valid for dynamic loading about each bias field.

Fig. 4.2 depicts the diffusion cut-off frequency of 6.3 mm diameter Galfenol and Terfenol-D rods operating about a moderate compressive bias stress (about -25 to -50 MPa) and the worst case bias field (that which maximizes  $\mu$  and nearly minimizes

$E$ ). The magnetic permeability of each rod was analytically calculated using the DEA models.

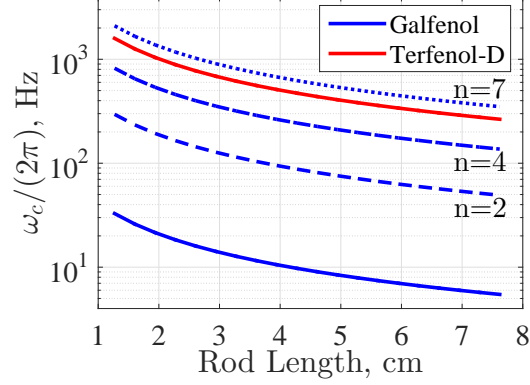


Figure 4.2: Mechanically-induced magnetic diffusion cut-off frequency of 6.3 mm diameter solid Terfenol-D, solid Galfenol, and laminated (with  $n$  laminates) Galfenol rods operating about a moderate compressive bias stress and the worst case bias field; Terfenol-D:  $\sigma = 1.72 \text{ S}/\mu\text{m}$  [85],  $\mu^T/\mu_0 = 9.4$ ; Galfenol:  $\sigma = 2.15 \text{ S}/\mu\text{m}$  [160, 131],  $\mu^T/\mu_0 = 240$ .

In general, the cut-off frequencies decrease with increases in the rod's length, because the rod's diameter must increase accordingly to maintain a given stiffness. The cut-off frequency of the Terfenol-D rod is nearly two orders of magnitude greater than that of the Galfenol rod. Thus, the cut-off frequency of laminated Galfenol rods were also calculated by approximating a laminated rod as a solid rod with an effective magnetic permeability,

$$\sigma_{\text{eff}} = \sigma / (n + 1)^2, \quad (4.8)$$

where  $n$  is the number of laminates [59]. For the properties considered, the Galfenol rod must be laminated with 7 or more laminates for its cut-off frequency to exceed that of the solid Terfenol-D rod.

## Effect of internal mass on dynamic stiffness

It is well known that the mass of a structure influences its dynamic stiffness and that this effect increases with frequency. The objective of the experimental testing of the Varispring was to measure the changes in the device's stiffness caused by changes in the elastic component of the magnetostrictive rod's stiffness. Changes in stiffness due to mass effects would have corrupted the experimental results. Consequently, the rod was designed to minimize these effects.

Below the first mechanical resonance, the effect of internal mass  $m = \rho A_{\text{rod}} l_{\text{rod}}$  on the dynamic stiffness  $D$  of the magnetostrictive rod can be approximated using the lumped parameter model shown in Fig. 4.3(a), where  $\rho$  is the density. For this model, the driving-point stiffnesses  $D_{11}$ ,  $D_{22}$  and cross-point stiffnesses  $D_{12}$ ,  $D_{21}$  are

$$D_{11}(\omega) = D_{22}(\omega) = \frac{2K(2K - m\omega^2)}{4K - m\omega^2}, \quad D_{12}(\omega) = D_{21}(\omega) = \frac{-4K^2}{4K - m\omega^2}, \quad (4.9)$$

where  $\omega$  is the forcing frequency. Fig. 4.3(b) depicts the absolute value of the percent change in the driving-point and cross-point stiffnesses of the Galfenol and Terfenol-D rods for worst case conditions (i.e., the maximum frequency, 1000 Hz, and minimum expected Young's modulus of Galfenol, 33 GPa, and Terfenol-D, 18 GPa) using the density of Galfenol and Terfenol-D, 7870 kg/m<sup>3</sup> and 9250 kg/m<sup>3</sup>, respectively. The effect of mass on the dynamic stiffness of the Terfenol-D rod is nearly double that of the Galfenol rod; however, the effect is small in both rods for the parameters considered.

## Varispring design

A prototype Varispring utilizing Terfenol-D was manufactured, because the use of Terfenol-D provides a significantly higher diffusion cut-off frequency and quasi-static

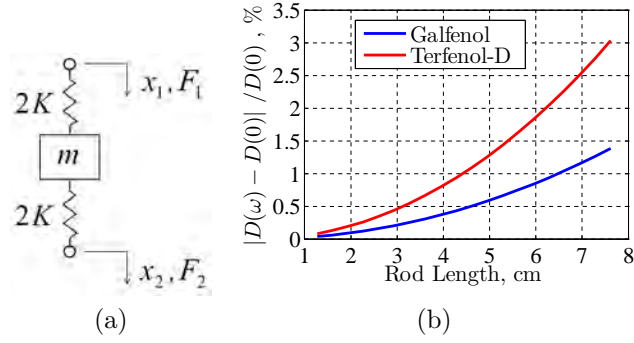


Figure 4.3: Effect of internal mass on the dynamic stiffness of the magnetostrictive rod, (a) lumped parameter model of the rod and (b) absolute value of the percent change in the driving-point and cross-point dynamic stiffnesses from their static values for worst case conditions ( $E^H = E_{\min}^H$  and  $\omega = 2\pi 1000$  rad/s), driving-point and cross-point stiffnesses overlap.

Young's modulus variation [96, 129] for rise times comparable to those of Galfenol-based Varisprings. The Terfenol-D ( $\text{Tb}_{0.3}\text{Dy}_{0.7}\text{Fe}_{1.92}$ ) rod was purchased from Etrema Products, Inc. and laminated with 0.762 mm (0.030 in) laminations and adhesive layers of about 0.048 mm (0.0019 in) to further improve its dynamic performance. The elastic modulus of the adhesive is 862 MPa. A length of 2.401 cm (0.9453 in) was selected to balance the improved performance of shorter rods with the need to attach sensors. A diameter of 1.271 cm (0.5005 in) provided the desired maximum axial stiffness of the rod. For the chosen geometry of the Terfenol-D rod, the effect of its internal mass on its dynamic stiffness is negligible.

The inertial force error was kept below the ASTM-recommended tolerance of 0.5 % [15] by measuring this dynamic force using a piezoelectric load washer nearly co-located with the rod. During experimental testing of the Varispring, the mechanical preload was applied by a load frame. When the device is used in a vibration

control application, the preload can be generated by a softening Belleville spring operated near its maximum deflection to minimize variations in the preload during operation [95].

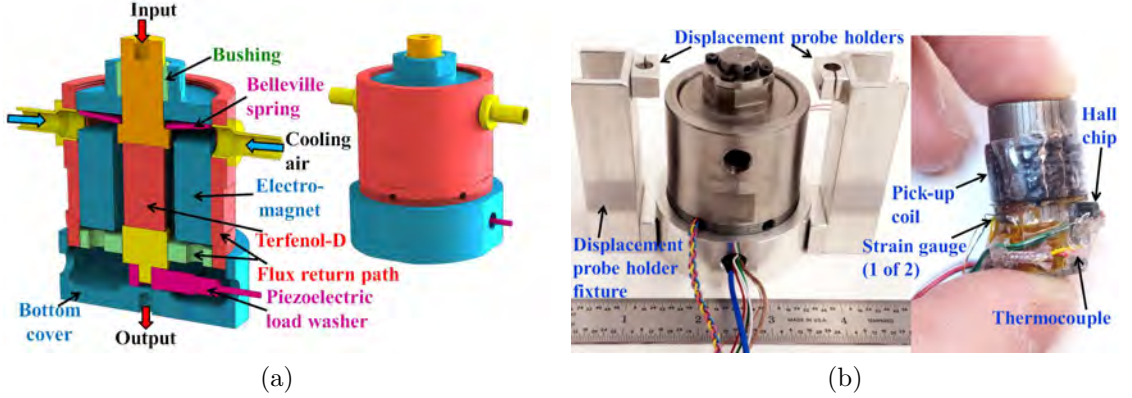


Figure 4.4: (a) CAD model of the prototype Varispring and (b) manufactured Varispring (air hose fittings removed) with capacitive displacement probe holder fixture attached (left) and Terfenol-D rod with sensors installed (right); passive structural components are 1018 steel, except for the Belleville spring (high carbon steel), bushing (Rulon J), air hose fittings (brass), and bottom cover (Al 7075).

Fig. 4.4(a) depicts a CAD model of the prototype Varispring. The central load path – from the input through the Terfenol-D rod and along the device’s cylindrical axis to the output – acts as an elastic member (i.e., a spring) with a variable stiffness. In this work, stiffness was modulated via controlled changes in the electromagnet’s current, which almost proportionally altered the axial magnetic field applied to the Terfenol-D. The magnetic flux return path was designed using magnetostatic finite element simulations to ensure that Terfenol-D’s magnetic state is nearly uniform when magnetic diffusion and internal mechanical dynamics are negligible. A sleeve bushing isolates the flux return path from forces applied to the central load path. The

dynamic, axial force was measured using a Kistler 9001A piezoelectric load washer. Using Eq. (3.88), the inertial force error at 1000 Hz for this design is about 0.2 %. The electromagnet was wound using 519 turns of 22 AWG wire and was held together by Duralco 4525 epoxy having a thermal conductivity of  $1.875 \text{ W}/(\text{m}^\circ\text{K})$ . During testing, the Varispring was aligned to the load frame using the blind holes on its ends.

The manufactured prototype and instrumented Terfenol-D rod are depicted in Fig. 4.4(b). The total displacement of the Varispring, i.e., the relative displacement between the bottom of the Varispring and a cylindrical target (shown in Fig. 4.5) that mounted to the top of the device, was measured using MicroSense 8810 capacitive displacement probes. These probes were held by aluminum fixtures that have a first natural frequency of 1492 Hz (calculated in COMSOL Multiphysics), which is sufficiently above the 1000 Hz limit considered herein.

## 4.1.2 Experimental setup

Mechanical testing of the prototype Varispring was conducted using an MTS 831.50 high frequency load frame. The axial strain at the surface of the Terfenol-D rod was measured using a pair of Vishay Micro-Measurements EA-06-250BF-350/L strain gauges, which were bonded on opposite sides of the rod and wired in series to cancel bending strains and the electromagnetic noise induced in the gauges due to the time-varying magnetic flux density in the rod, as discussed in the **Strain gauge noise reduction** subsection of Section 3.2.3. A Lake Shore Model 480 fluxmeter and custom pick-up coil were utilized to measure the magnetic flux density in the rod. An Allegro A1302ELH Hall chip was used to measure the axial magnetic field at the surface of the Terfenol-D rod. The rod's temperature was monitored with a Type K

thermocouple to ensure that temperature increases above the 25 °C ambient were  $< 3$  °C.

The electromagnet was excited by a Techron LVC 5050 linear amplifier operated in current control mode. The amplifier’s voltage monitor measured the supply voltage. However, the supply current was calculated from the voltage drop across a  $0.1 \pm 0.001$  Ohm, 15 W Leeds & Northrup Co. resistor connected in series with the Varispring, because the current monitor exhibited an erroneous offset that changed throughout the experiment. The sensors were calibrated as explained in Section C.2, except for the pick-up coil, which was calibrated by measuring the static magnetic field generated in air between the poles of a large electromagnet using the pick-up coil and calibrated Hall sensor. The calibration factor of the pick-up coil ( $NA$ ) was then scaled to correct for the presence of glue layers in the laminated Terfenol-D rod,

$$(NA)_{\text{cor}} = (NA) A_{\text{solid}}/A_{\text{lam}}, \quad (4.10)$$

where  $A_{\text{lam}}$  and  $A_{\text{solid}}$  respectively are the cross-sectional areas of Terfenol-D in the laminated rod and a solid rod of the same diameter. Measurement signals were phase aligned in post processing by correcting for the phase response of the conditioning electronics, as detailed in the **Phase calibration** subsection of Section 3.2.4.

The experimental setup is shown in Fig. 4.5. When dynamic forces were directly applied to the displacement probe target by the steel platen, the load frame’s force control performed poorly due to the Varispring’s large, high-speed stiffness changes (a disturbance to the force control system). Consequently, during dynamic stiffness tuning experiments, a soft compression spring was inserted between the platen and target to act as a mechanical low-pass filter and attenuate the disturbance; the improved force control, depicted in Fig. 4.6, performed very well up to 1 kHz. However,



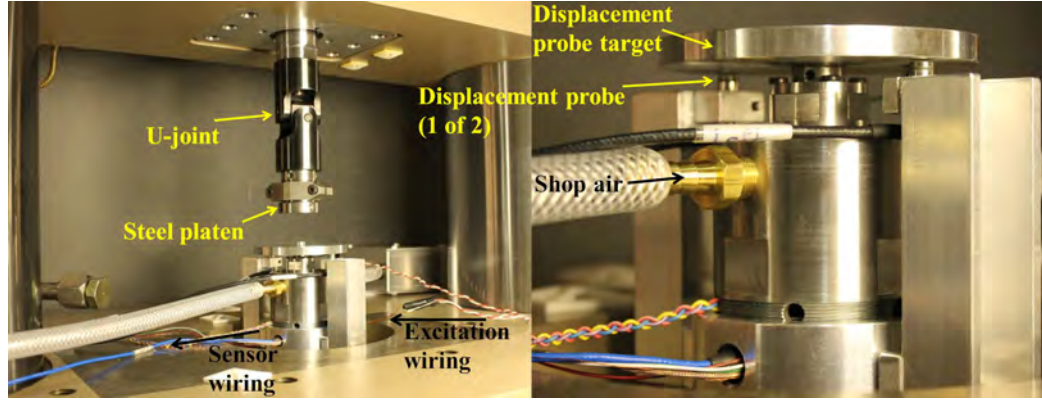


Figure 4.5: Experimental setup (the compression spring used to improve the force control during dynamic stiffness tuning tests is not shown).

due to the large motion of the steel platen that resulted, the displacement probes were removed from the experimental setup during dynamic stiffness tuning tests to prevent the possibility of damaging the probes. Thus, the Varispring's stiffness could not be calculated; instead, the strain response and Young's modulus of the Terfenol-D rod are used to study the Varispring's time-varying elastic state.

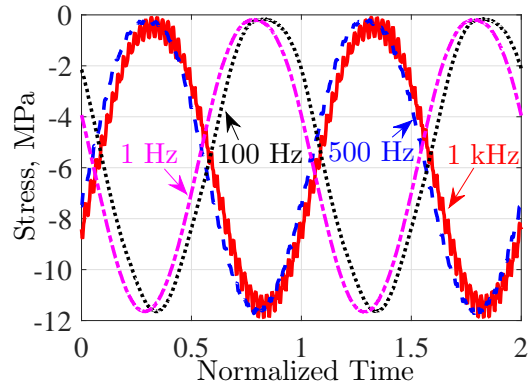


Figure 4.6: Force control performance during dynamic stiffness tuning tests when using the soft compression spring; 5.80 MPa amplitude, 25 Hz sinusoidal forcing and 1.5 A amplitude sinusoidal current at different frequencies.

### 4.1.3 Dynamic tuning

First, the quasi-static sensing response of the Terfenol-D rod was measured under constant current over the stress range of interest. The Young's modulus of the rod, shown in Fig. 4.7, was calculated by differentiating 4th order polynomials that were fit to 0.75 MPa wide sections of each half of the hysteretic responses. When the maximum current, and thus magnetic field, is limited (e.g., to prevent excessive rise times), the  $\Delta E$  effect improves as the compressive bias is increased. At the bias stress for which the Varispring was designed (-25 MPa), the maximum change in the minor loop Young's modulus (51 GPa) occurred when the current was increased from 0 A to 3.08 A. However, to prevent full compression of the required isolation spring, the bias was constrained to  $> -6$  MPa. This reduced the achievable Young's modulus variation during dynamic tuning experiments, because the current was limited.

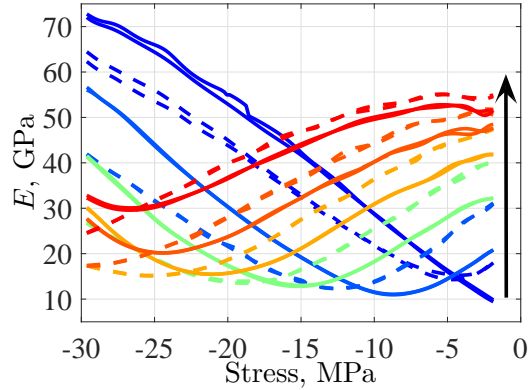


Figure 4.7: Quasi-static Young's modulus of the laminated Terfenol-D rod at constant currents of 0, 0.909, 1.72, 2.59, 3.52, and 4.82 A ( $\pm 0.2$  mA); bias current increases from blue to red (direction shown by the arrow); stress increasing (solid), stress decreasing (dashed).

Dynamic tuning of the Varispring's elastic state was conducted in two stages. First, the stiffness was continuously varied by applying a 1 to 1000 Hz sinusoidal current having a nominal amplitude of 1.50 A and bias of 1.56 A. Second, high-speed switching of the stiffness was realized via a 1 to 500 Hz square wave current having a bias of 1.56 A. To prevent instability of the amplifier's current control system, the nominal amplitude of the square wave current was reduced to 0.50 A. In each case, the Varispring was excited with a 2.00 to 5.80 MPa amplitude, 25 Hz sinusoidal stress.

The strain response of the Terfenol-D rod to 100 Hz and 500 Hz sinusoidal currents is depicted in Fig. 4.8. Since the current actuates the rod while varying its elastic state, the strain response has harmonic content at 25 Hz and the frequency of the current. The blue and red annotations respectively indicate the approximate Young's modulus at the maximum and minimum current ( $E_{I_{\max}}$  and  $E_{I_{\min}}$ ), which, at the intended operating bias, would correspond to the low and high modulus, respectively. However, Fig. 4.7 illustrates that at a -5.90 MPa bias, the minimum modulus occurs for a small, but nonzero current. Consequently,  $\Delta = E_{I_{\max}} - E_{I_{\min}}$  increases when the current amplitude is slightly reduced; this is shown in Table 4.1, which gives the current amplitude and approximate moduli for each testing condition. The amplifier did not maintain a consistent current amplitude, despite using the same current control voltage for each case; with this caveat, the Terfenol-D rod is stiffer for a smaller stress amplitude, as also observed by Kellogg and Flatau [96]. The rod's modulus tunability is roughly maintained through 500 Hz, but is degraded at 1 kHz. Magnetic diffusion in the flux return path may contribute to this reduction, although this was not investigated.

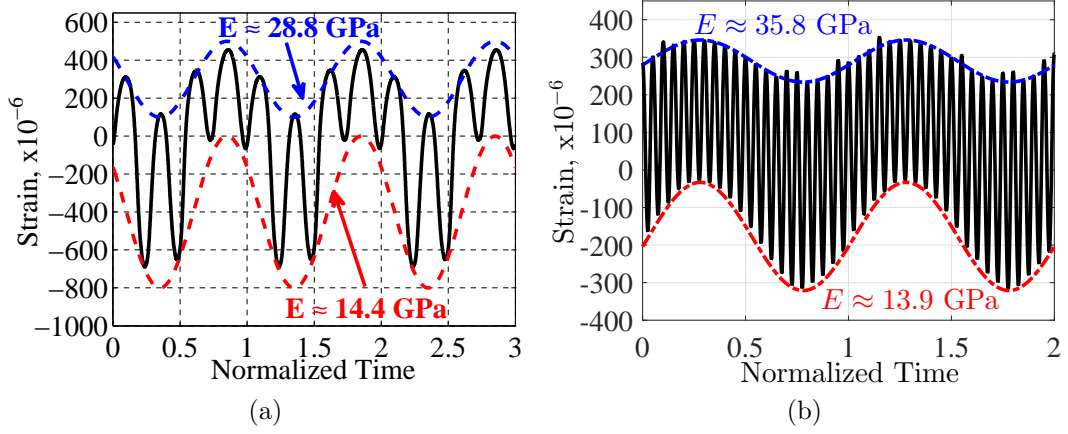


Figure 4.8: Strain response of the Terfenol-D rod inside the prototype Varispring to a (a) 100 Hz and (b) 500 Hz sinusoidal current and a 25 Hz, 2.00 MPa amplitude stress with -5.90 MPa bias.

The current control performance during testing of the dynamic  $\Delta E$  effect (i.e., square wave elastic modulus tuning) is depicted in Fig. 4.9. Even though the amplifier's current control system was tuned according to the manufacturer's suggestions, a significant amount of overshoot is observed. The settling time of this overshoot is about 2 ms; thus, a 500 Hz square wave current could not be produced and the 500 Hz strain response is not shown.

The strain response of the Terfenol-D rod to 1 Hz and 100 Hz square wave currents is illustrated in Fig. 4.10. As seen in the inset of Fig. 4.10(b), the strain response exhibits an overshoot that mirrors the current overshoot. This implies that the Varispring's rise time is  $< 1$  ms, as predicted by the nonlinear electromechanical model in the **Electrical response** subsection of Section 4.1.1. The approximate Young's moduli of the rod at the high and low current states are tabulated in Table 4.2 for each testing condition. The dynamic  $\Delta E$  effect is fairly consistent from

Table 4.1: Approximate Young’s moduli (in units of GPa) of the Terfenol-D rod inside the prototype Varispring at the maximum and minimum current for a bias stress of -5.90 MPa and different sinusoidal current frequencies and stress amplitudes.

Frequency, Hz	2.00 MPa				5.80 MPa			
	$ I $ , A	$E_{I\min}$	$E_{I\max}$	$\Delta$	$ I $ , A	$E_{I\min}$	$E_{I\max}$	$\Delta$
1	1.50	25.5	42.1	16.6	1.29	17.8	37.8	20.0
100	1.50	15.0	34.5	19.5	1.57	14.4	28.8	14.4
500	1.21	13.9	35.8	21.9	1.28	15.3	29.8	14.5
1000	1.07	22.0	26.8	4.80	1.07	19.9	22.8	2.90

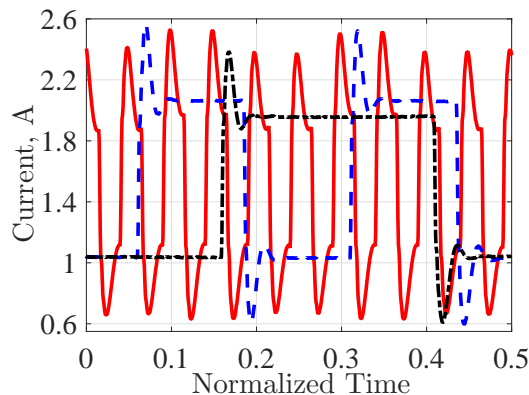


Figure 4.9: Current control performance during testing of the dynamic  $\Delta E$  effect; 25 Hz, 4.00 MPa amplitude sinusoidal forcing and current frequencies of 50 Hz (dash-dot), 100 Hz (dashed), and 500 Hz (solid).

1 Hz through 100 Hz and for the two stress amplitudes. An increase in the  $\Delta E$  effect with a decrease in the stress amplitude would be expected if the rod’s magnetomechanical behavior was nearly saturated at one of the two current states [96].

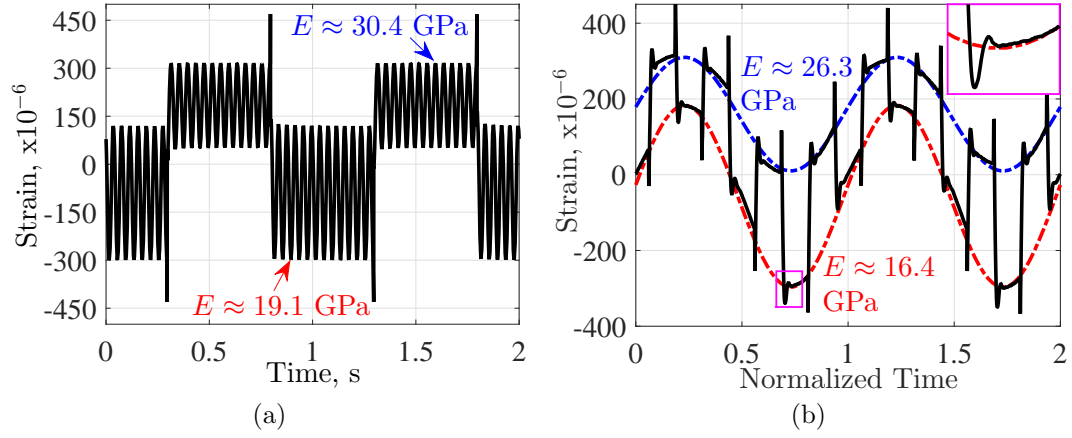


Figure 4.10: Strain response of the Terfenol-D rod inside the prototype Varispring to a (a) 1 Hz and (b) 100 Hz square wave current and a 25 Hz, 4.00 MPa amplitude stress with -5.90 MPa bias.

#### 4.1.4 Concluding remarks

In this section, an electrically-controllable magnetostrictive spring capable of dynamically tuning its stiffness (i.e., a magnetostrictive Varispring) was designed, manufactured, and tested. This Varispring has broad application to vibration control and enables in situ stiffness tuning and stiffness switching. The design was based on (a) a nonlinear electromechanical transducer model, (b) an analytical solution of linear, mechanically-induced magnetic diffusion, and (c) the effect of internal mass on the magnetostrictive material's dynamic stiffness. Terfenol-D has a much larger potential for Young's modulus tuning than Galfenol. The modeling results show that for an equal modulus change, Terfenol-D provides a slightly faster rise time to control inputs. A laminated Terfenol-D rod was selected as the active material for this reason and for its significantly higher magnetic diffusion cut-off frequency. To decrease the

Table 4.2: Approximate Young’s moduli (in units of GPa) of the Terfenol-D rod inside the prototype Varispring at the high and low current states for a bias stress of -5.90 MPa and different square wave current frequencies and stress amplitudes.

Frequency, Hz	2.00 MPa				4.00 MPa			
	$ I $ , A	$E_{I\min}$	$E_{I\max}$	$\Delta$	$ I $ , A	$E_{I\min}$	$E_{I\max}$	$\Delta$
1	0.55	22.9	32.8	9.90	0.55	19.1	30.4	11.3
10	0.57	22.3	31.2	8.90	0.51	19.3	30.0	10.7
50	0.50	21.4	30.2	8.80	0.49	17.0	29.3	12.3
100	0.49	16.8	29.1	12.3	0.49	16.4	26.3	9.90

rise time, the electromagnet in the Varispring was wound with relatively large wire (22 AWG) and the rod’s length (and thus its diameter) was minimized.

Dynamic tuning of the Varispring’s stiffness was investigated by measuring the Terfenol-D rod’s strain response to dynamic, compressive, axial forces in the presence of time-varying current inputs. Continuous and discrete Young’s modulus tuning were realized via sinusoidal and square wave currents, respectively. To achieve an acceptable level of force control, a soft compression spring was added to the load path. This prevented the measurement of the Varispring’s stiffness and constrained the bias compression to a small value, which reduced the attainable Young’s modulus variation. Nevertheless, continuous modulus changes up to 21.9 GPa and 500 Hz are observed for current amplitudes up to 1.5 A. Square wave modulus changes (dynamic  $\Delta E$  effect) up to 12.3 GPa and 100 Hz are observed for current amplitudes up to 0.5 A. Instability and overshoot in the controlled square wave current prevented measurement at higher current frequencies and amplitudes. The rise time of the Varispring is  $< 1$  ms.

To improve the Varispring's stiffness tunability, the device can be operated about a more optimal bias stress, which can be realized by using a compression spring with greater travel or by generating some of the bias with an internal Belleville spring. During stiffness switching, stiffness tunability and tuning bandwidth can be increased by also optimizing the current control, using voltage control, or by low-pass filtering the square wave current to reduce its harmonic content.

## 4.2 Case Study: Switched Stiffness Vibration Control

This section illustrates the usefulness of a magnetostrictive Varispring by applying it to switched stiffness vibration control of a single-degree-of-freedom mechanical system. Switched stiffness vibration control is a simple form of stiffness control in which vibration is attenuated via coordinated switching between high and low stiffness states [40, 117]. A computational study is presented to investigate the uncontrolled and controlled free vibration responses of the mass. First, a model is introduced that quantifies the electromechanical behavior of the magnetostrictive Varispring and its effect on the vibration of the mechanical system. Then, a discussion of the control algorithm is presented, in which modifications to the algorithm are proposed to account for the magnetostrictive force generated by the Varispring. After, vibration control results are presented.

### 4.2.1 Model development

Switched stiffness vibration control using a magnetostrictive Varispring is investigated for the mechanical system shown in Fig. 4.11, where the Varispring is used as a spring mount. Electrical excitation of the Varispring generates an axial magnetic field  $H$  in the magnetostrictive material, which is used to control the Varispring's



stiffness. Due to magnetostriction, the field also produces an uncontrolled magnetostrictive force  $F_{\text{mag}}$  that excites the mass; the presence of  $F_{\text{mag}}$  complicates the vibration control strategy, as discussed below.

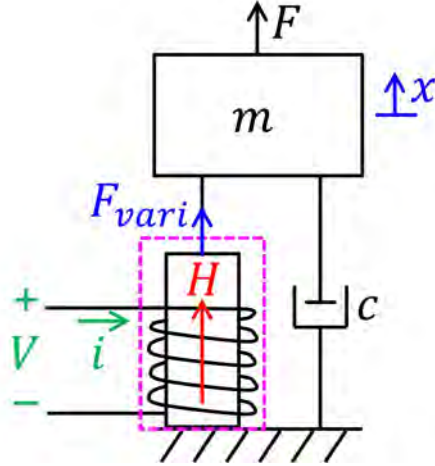


Figure 4.11: Mechanical system used to investigate switched stiffness vibration control; the magnetostrictive Varispring (dotted magenta box) has electrical inputs (green), magnetic states (red), and mechanical outputs (blue); magnetic flux density  $B$  (not shown) is positive along the direction of  $H$ .

The equation of motion for the mechanical system is

$$m\Delta\ddot{x} + c\Delta\dot{x} + \Delta F_{\text{vari}}(H, T) = F, \quad (4.11)$$

where  $\Delta x$  is the incremental displacement of mass  $m$ ,  $c$  is the viscous damping coefficient,  $\Delta F_{\text{vari}}$  is the total force imposed by the Varispring, and  $F$  is the applied force. The equation is formulated in incremental form to be consistent with the piezomagnetic equations that govern the Varispring's magnetomechanical behavior,

$$\Delta B = \mu^S(H, T)\Delta H + d(H, T)E^H(H, T)\Delta S, \quad (4.12)$$

$$\Delta T = -d(H, T)E^H(H, T)\Delta H + E^H(H, T)\Delta S. \quad (4.13)$$

$\Delta B$ ,  $\Delta T$ , and  $\Delta S$  respectively denote the incremental magnetic flux density, stress, and strain along the axis of the magnetostrictive rod, which is described by its magnetic permeability at constant strain  $\mu^S$ , Young's modulus at constant field  $E^H$ , and piezomagnetic coefficient  $d$ .  $\mu^S$  is related to the permeability at constant stress through  $\mu^S = \mu^T - d^2 E^H$ . The material properties are functions of the total field and stress, which depend on the bias field  $H_{\text{bias}}$  and bias stress  $T_{\text{bias}}$  according to

$$T = \Delta T + T_{\text{bias}}, \quad (4.14)$$

$$H = \Delta H + H_{\text{bias}}. \quad (4.15)$$

The voltage across the Varispring's electromagnet is governed by Faraday's law. As such, the incremental applied voltage  $\Delta V$  is related to the incremental current  $\Delta i$  according to

$$\Delta V = N A_{\text{coil}} \frac{d\Delta B}{dt} + R_{\text{coil}} \Delta i, \quad (4.16)$$

where  $R_{\text{coil}}$ ,  $N$ , and  $A_{\text{coil}}$  are the resistance, number of windings, and cross-sectional area of the electromagnet, respectively.

If the magnetic flux leakage and the magnetic reluctance of the Varispring's flux return path are assumed to be negligible, the magnetic field in the magnetostrictive rod is  $\Delta H = N \Delta i / l_{\text{coil}}$ , where  $l_{\text{coil}}$  is the electromagnet's axial length. When the mass vibrates at frequencies sufficiently below the Varispring's 1st resonant frequency,  $\Delta T$  and  $\Delta S$  are uniform and can be calculated as  $\Delta F_{\text{vari}} / A_{\text{rod}}$  and  $\Delta x / l_{\text{rod}}$ , respectively, where  $A_{\text{rod}}$  and  $l_{\text{rod}}$  are the cross-sectional area and length of the magnetostrictive

rod, respectively. Insertion of these expressions into Eq. (4.13) gives

$$\begin{aligned}
\Delta F_{\text{vari}} &= \frac{A_{\text{rod}} E^H(H, T)}{l_{\text{rod}}} \Delta x - A_{\text{rod}} d(H, T) E^H(H, T) \Delta H, \\
&= k^H(H, T) \Delta x - A_{\text{rod}} d(H, T) E^H(H, T) \Delta H, \\
&= k^H(H, T) \Delta x - \frac{N A_{\text{rod}} d(H, T) E^H(H, T)}{l_{\text{coil}}} \Delta i, \\
&= k^H(H, T) \Delta x - \Theta(H, T) \Delta i,
\end{aligned} \tag{4.17}$$

where  $k^H$  is the Varispring's stiffness and  $\Theta$  is an electromechanical coupling coefficient. From Eq. (4.17), the magnetostrictive force can be identified as

$$F_{\text{mag}} = -\Theta(H, T) \Delta i. \tag{4.18}$$

Inserting Eq. (4.12) and the expressions for  $\Delta H$ ,  $\Delta T$ , and  $\Delta S$  into Eq. (4.16) one gets

$$\begin{aligned}
\Delta V &= \frac{d}{dt} \left( \frac{N A_{\text{coil}} d(H, T) E^H(H, T)}{l_{\text{rod}}} \Delta x + \frac{N A_{\text{coil}} \mu^S(H, T)}{l_{\text{coil}}} \Delta i \right) + R_{\text{coil}} \Delta i, \\
&= \frac{d}{dt} (\Theta(H, T) \Delta x) + \frac{d}{dt} (L^S(H, T) \Delta i) + R_{\text{coil}} \Delta i,
\end{aligned} \tag{4.19}$$

where  $L^S$  is the blocked inductance of the Varispring<sup>10</sup> and it was assumed that  $l_{\text{coil}} = l_{\text{rod}}$  and  $A_{\text{coil}} = A_{\text{rod}}$ . The ODEs governing the electrical and mechanical responses of the system in Fig. 4.11 are found by simplifying Eq. (4.19) and inserting Eq. (4.17) into Eq. (4.11),

$$m \Delta \ddot{x} + c \Delta \dot{x} + K^H(H, T) \Delta x - \Theta(H, T) \Delta i = F, \tag{4.20}$$

$$\Theta(H, T) \Delta \dot{x} + \frac{d\Theta(H, T)}{dt} \Delta x + L^S(H, T) \Delta \dot{i} + \left( \frac{dL^S(H, T)}{dt} + R_{\text{coil}} \right) \Delta i = \Delta V. \tag{4.21}$$

Eqs. (4.20) and (4.21) are simultaneously solved using MATLAB's *ode45* function after approximating the time derivatives of  $\Theta$  and  $L^S$  using the 2nd order, backward

<sup>10</sup>This quantity has also been referred to as the self inductance of a magnetostrictive transducer [71].

finite difference method. The solution procedure is iterative and piece-wise linear (i.e., the material properties are updated at the end of each time step). Accordingly, a very small time span is used for each call of the *ode45* function to maintain accuracy.

This model incorporates the mechanical vibration of the mass, the electrical dynamics associated with voltage control of the Varispring, the magnetostrictive force, and constitutive nonlinearities. However, the model does not incorporate mechanically-induced or field-induced eddy current effects. To incorporate these effects, the nonlinear PDE governing magnetic diffusion (see Section 3.1.2) would need to be solved concurrently with Eqs. (4.20) and (4.21). This would add a considerable amount of complexity to the model. Hence, the proposed model is accurate when the mass vibrates at a frequency that is below the Varispring's magnetic diffusion cut-off frequency. Considering the results of Section 4.1, a Terfenol-D-based Varispring is considered in this section to improve the accuracy of this assumption.

### 4.2.2 Results and discussion

The control law for switched stiffness vibration control is simple. When the mass is moving toward static equilibrium, switch the stiffness to the soft state. When the mass is moving away from static equilibrium, switch to the stiff state. In terms of energy, if the stiffness is instantaneously decreased by  $\Delta k$  at the  $i^{\text{th}}$  displacement maximum  $x_{\text{max},i}$ , the potential energy in the system decreases by  $0.5\Delta k x_{\text{max},i}^2$ . Then, if the stiffness is instantaneously increased by  $\Delta k$  at static equilibrium, the potential energy does not increase. Thus, energy in the amount of  $0.5\Delta k x_{\text{max},i}^2$  is dissipated every half cycle.

In the absence of a magnetostrictive force, the performance of this control method tends to improve as the amplitude and speed of stiffness switching increases. However, the magnetostrictive force can have a significant magnitude; thus, it complicates the control method and can produce unexpected motion of the mass. In particular, resonance of the mass can be induced by the control during damped, free vibration, as shown in Fig. 4.12. In this case, the magnetostrictive force overcomes the existing damping and the energy lost due to stiffness switching. This can result when the magnetostrictive force acts in only one direction, which occurs for operation about a variety of bias conditions. Hence, the control law for switched stiffness vibration control must be modified to that illustrated in Fig. 4.13 when a magnetostrictive material is used to realize the stiffness changes. Ideally, the magnetostrictive force is as small as possible and always pushes or pulls the mass toward the static equilibrium position. However, it does not seem possible to satisfy the stiffness and force criteria for every motion condition. As such, for half of the vibration cycle, the field is set to the bias value and stiffness switching is inactive; during this time, the magnetostrictive force is approximately zero.

To determine a magnetomechanical bias condition for which the tuning conditions shown in Fig. 4.13 will be satisfied, it is beneficial to reference the Young's modulus of the magnetostrictive material and the electromechanical coupling coefficient of the Varispring, which are depicted in Fig. 4.14. For a given magnetic field change in Terfenol-D, a larger change in Young's modulus is obtained at a moderate to high bias compression than at a small compression. Larger bias compressions also help to prevent unloading of the brittle Terfenol-D rod during dynamic operation. Thus, a moderate to high bias compressive stress is considered herein. Fig. 4.14(b)

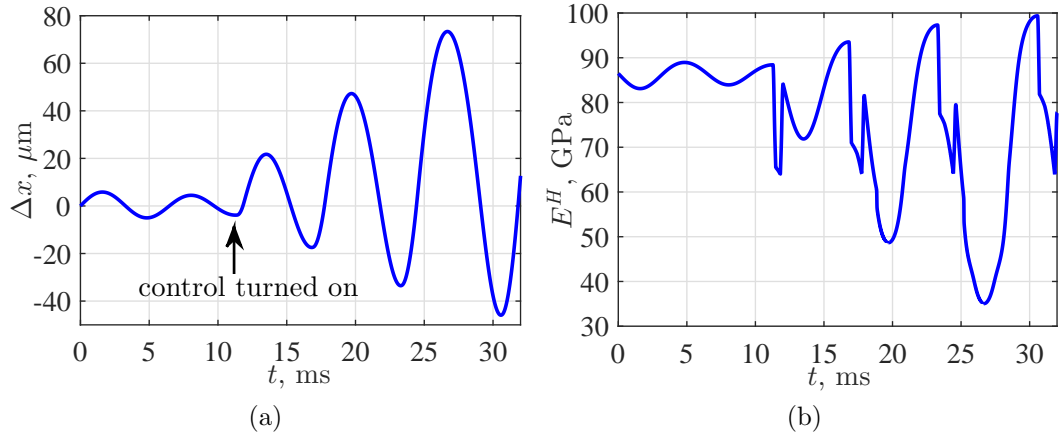


Figure 4.12: Mechanical resonance induced by switched stiffness vibration control due to the uncontrolled magnetostrictive force; model parameters given in Table 4.3,  $H = 0_{-0}^{+35}$  kA/m.

shows that the electromechanical coupling coefficient is always positive for positive magnetic fields.<sup>11</sup> According to Eq. (4.18), the magnetostrictive force can therefore only change sign if  $\Delta i$  changes polarity during stiffness switching; this implies that the bias magnetic field should be between the maximum and minimum tuning fields. At moderate to high bias compressive stress,  $\Theta$  decreases rapidly with field at low bias fields; this suggests that the bias field should be closer to the maximum tuning field than to the minimum tuning field, in order for the magnetostrictive force to have comparable positive and negative peak values.

The modified control method was applied to the damped, free vibration of the mass. The results are shown in Fig. 4.15, where the uncontrolled response is compared to two controlled responses. The model parameters common to all three cases are given in Table 4.3. The uncontrolled response is damped due to the resistive

<sup>11</sup>For negative magnetic fields (not shown in Fig. 4.14(b)), the electromechanical coupling coefficient is always negative.

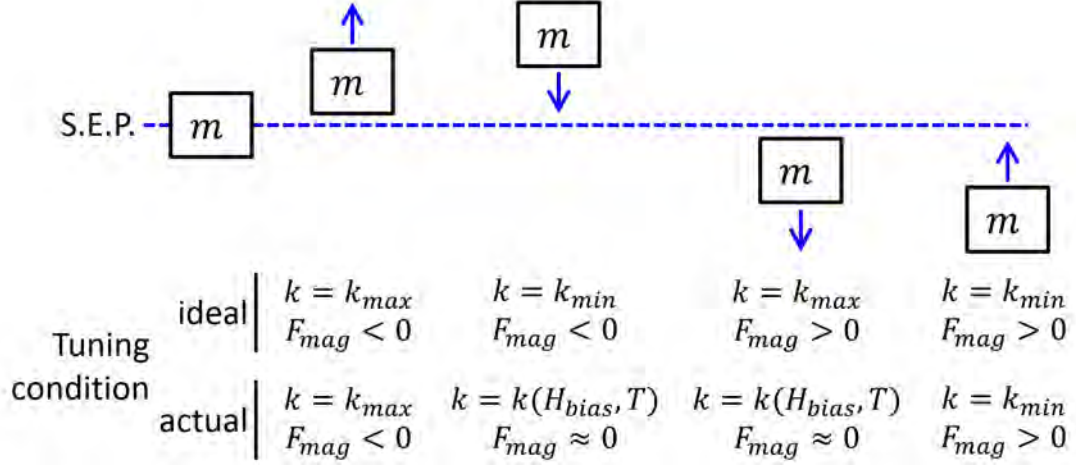


Figure 4.13: Tuning conditions of the magnetostrictive Varispring needed to realize switched stiffness vibration control in the presence of a magnetostrictive force; S.E.P. denotes the static equilibrium position.

losses associated with the current that is induced in the electromagnet according to Faraday's law. In both of the controlled responses, switched stiffness vibration control introduces a significant amount of damping; in particular, controlled response 2 (solid line) exhibits a level of damping that is equivalent to a viscous damping ratio of approximately 0.15. On close inspection, controlled response 1 initially decays faster than controlled response 2, but it converges to a steady oscillation having a small amplitude. This is caused by a small imbalance between the positive and negative peak values of the magnetostrictive force, as seen in Fig. 4.15(d).

Table 4.3: Model parameters for switched stiffness vibration control modeling.

$dt, \mu s$	$m, kg$	$c, Ns/m$	$R_{coil}, \Omega$	$N$	$A_{rod}, cm^2$	$l_{rod}, m$	$T_{bias}, MPa$
2	80	0	2.5	1840	1.27	0.144	-70

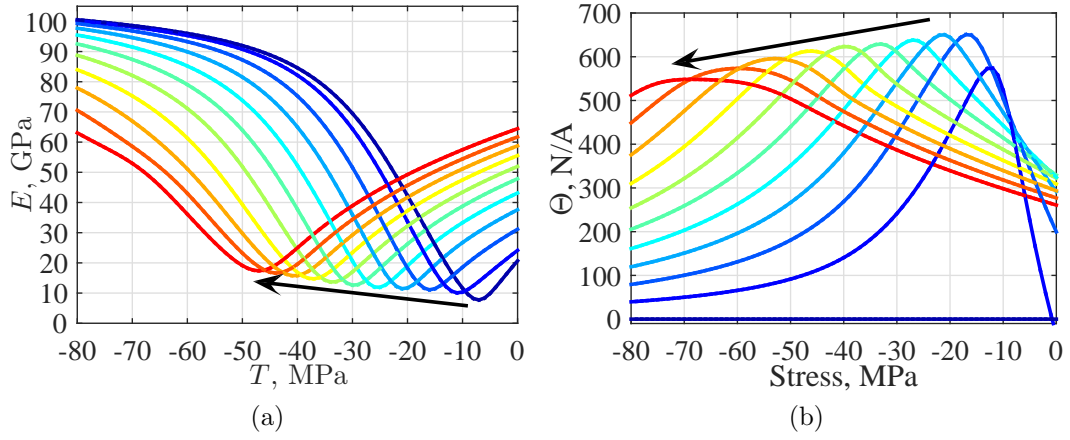


Figure 4.14: Stress and magnetic field dependence of the (a) Young's modulus of a Terfenol-D rod and (b) electromechanical coupling coefficient of a Terfenol-D-based Varispring calculated using the DEA model in [34]; from blue to red (the direction of the arrow),  $H$  increases from 0 to 100 kA/m in increments of 10 kA/m;  $A_{\text{coil}} = 1.27 \times 10^{-4} \text{ m}^2$ ,  $l_{\text{rod}} = 0.144 \text{ m}$ , and  $N = 1840$  turns (the minimum number needed to generate 85 kA/m at steady state with 22 AWG wire).

As with the conventional control method, the performance of the modified control method improves with increases in the stiffness change magnitude. However, the magnetostrictive force can play a more important role than the stiffness change. In general, the performance of the modified method improves as the amplitude of the magnetostrictive force is decreased by a change in the bias conditions or the bounds of the tuning field. Optimizing the performance requires trial and error.

### 4.2.3 Concluding remarks

In this section, a computational study of switched stiffness vibration control using a magnetostrictive Varispring was conducted. The Varispring was implemented as a tunable spring mount to dampen the vibration of a single-degree-of-freedom mechanical system. A model was presented that incorporates constitutive nonlinearities,



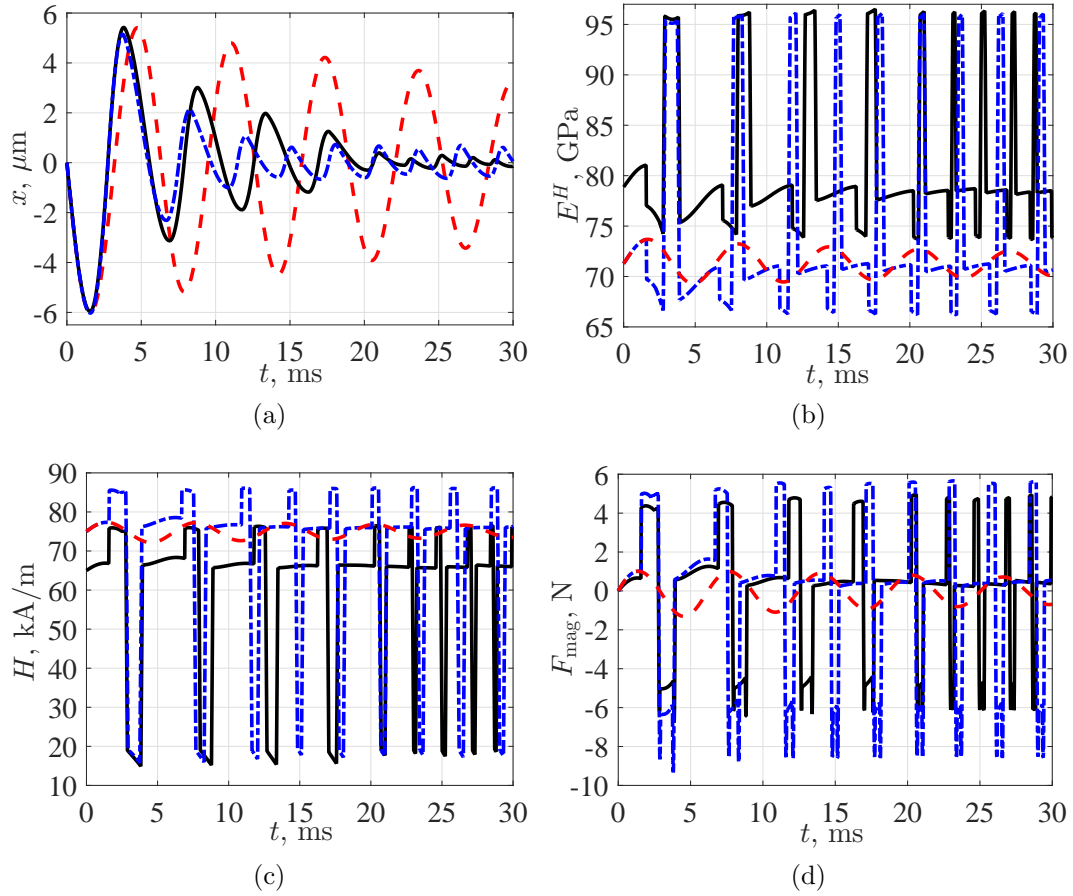


Figure 4.15: Enhanced decay of damped, free vibration using switched stiffness vibration control: no control (dashed,  $H_{\text{bias}} = 75$  kA/m), controlled response 1 (dashed-dotted,  $H = 75^{+10}_{-55}$  kA/m), and controlled response 2 (solid,  $H = 65^{+10}_{-45}$  kA/m).

mechanical vibrations, the electrical dynamics associated with voltage control of the Varispring, and the magnetostrictive force generated by the Varispring. To greatly simplify the model and numerical method, mechanically-induced and field-induced eddy current effects were neglected. As evidenced by Section 4.1, this is a valid assumption for Terfenol-D-based Varisprings operated at forcing frequencies up to about 1 kHz.

Free vibration of the mass under passive damping and switched stiffness vibration control was calculated. The magnetostrictive force, which is uncontrolled, was shown to play a significant role in the performance of the control. If the net magnetostrictive force over one vibration cycle is not small, the force can resonate the mass by overcoming the energy lost due to passive damping and stiffness switching. Thus, a modified control law was proposed to minimize the influence of the magnetostrictive force. Stiffness switching according to the modified law was found to introduce a level of damping that is equivalent to a viscous damping ratio of approximately 0.15. In general, the performance of the control improved as the stiffness change magnitude increased and the amplitude of the magnetostrictive force decreased.

## Chapter 5: Conclusions and Future Work

Although the dependence of the elastic moduli of magnetostrictive materials on bias stress and bias magnetic field is extensively reported in the literature, this behavior has been seldom applied to the development of vibration control devices. These devices, along with many other magnetostrictive systems, are subjected to dynamic stress, for which the constitutive behavior of magnetostrictive materials has rarely been studied or applied. The objectives of this dissertation were to understand the effects of dynamic stress on magnetostrictive materials and to utilize both static and dynamic stiffness changes in the development of novel vibration control devices. The research was organized into three chapters: (1) static stiffness change and its implementation in adaptive vibration absorbers, (2) dynamic stress effects in magnetostrictive materials, and (3) dynamic stiffness change and its application to switched stiffness vibration control. A detailed discussion of results and conclusions is included in these chapters. This chapter summarizes the entire research, lists its key contributions, and suggests future work in this field.

## 5.1 Research Summary

### Static stiffness change

In this chapter, the dependence of Galfenol's minor loop elastic modulus on bias stress and bias magnetic field was measured. This understanding was then applied to the modeling of adaptive vibration absorbers composed of Galfenol-based metal-matrix composite beams.

Major and minor strain versus stress responses of solid and laminated rods of research grade,  $\langle 100 \rangle$ -oriented, textured polycrystalline  $\text{Fe}_{81.6}\text{Ga}_{18.4}$  were measured under constant magnetic fields from 0.73 kA/m to 13.76 kA/m (solid rod) and under constant currents from 0 A to 1 A (solid and laminated rods). The mechanical loading consisted of 1 Hz or 4 Hz compressive stress ranging from -63.3 MPa to -0.5 MPa. The maximum major loop and minor loop  $\Delta E$  effects of the solid rod are 54.84 % / 39.01 % (constant field/current) and 37.90 % / 27.46 % (constant field/current), respectively. Despite having a 17 % lower saturation modulus than the solid rod due to soft adhesive layers, the maximum major loop  $\Delta E$  effect of the laminated rod under constant current (39.02 %) is essentially equal to that of the solid rod. In all cases, the minimum modulus occurs at larger compressive stress as the bias field or current increases. The  $\Delta E$  effect of minor loops is consistently lower than that of major loops, regardless of the magnetic bias condition. The hysteresis of constant field responses is smaller than that of constant current responses.

Semi-active control of the resonant frequency of Galfenol-based metal-matrix composite beams via changes in the bias magnetic field was studied using nonlinear, dynamic lumped parameter and distributed parameter models of the beams. Both models consider the variation in the Galfenol element's elastic modulus along its length

and thickness. The lumped parameter model was used to calculate the resonant frequency of clamped-clamped (C-C) and cantilevered absorbers from displacement transmissibility frequency responses as a function of input power amplitude, Galfenol volume fraction, and Galfenol's offset from the neutral bending axis. An input power threshold was observed, below which the resonant frequency is controllable and above which controllability decreases to zero. The boundary condition has a minimal effect on the maximum resonant frequency tunability, but the C-C beam's resonance can be controlled over a slightly larger operating space. The maximum tunability varies between 2.5 and 49 % as Galfenol volume fraction increases from 10 to 100 % (Galfenol located at the neutral axis) and between 2.5 and 5.5 % as Galfenol is offset from the composite's midplane (10 % Galfenol volume fraction).

The distributed parameter model of a C-C absorber incorporates Euler-Bernoulli beam theory, an axial force, and viscoelastic material damping. The 1st and 3rd resonant frequencies of the beam were efficiently calculated using autoresonant feedback control as a function of base acceleration and Galfenol volume fraction. An extensive validation of the model was conducted using analytical responses and measurements. The performance of the autoresonant control improved through careful selection of the vibration observation point(s) and careful tuning of the mode selector (bandpass filter). The axial force has a minimal effect on the maximum resonant frequency tunability, but an appreciable effect on the operating space over which tuning can occur. The maximum tunability does not usually degrade when the absorber is operated at higher modes. The effect of modulus changes on the composite's resonant frequency will be larger for composites having softer matrices.

## Dynamic stress effects in magnetostrictive materials

This chapter investigated the effects of dynamic stress on the constitutive behavior of magnetostrictive materials. First, the effect of mechanically-induced eddy currents on the internal magnetic field and magnetic flux density of cylindrical ferromagnets was studied. Then, precise measurements of Galfenol's strain and magnetic flux density responses to dynamic, compressive stress were presented along with a novel experimental design.

The radial dependence of magnetic diffusion in cylindrical ferromagnets that results from the application of a constant surface magnetic field with dynamic mechanical inputs was investigated analytically (for linear constitutive regimes) and numerically (for nonlinear constitutive regimes). For linear constitutive behavior, analytical time and frequency domain solutions were derived using the method of eigenfunction expansions. The solutions were non-dimensionalized after deriving a penetration (skin) depth and cut-off frequency, which were respectively found to be about 2.08 and 4.34 times those of field-induced magnetic diffusion. Mechanically-induced magnetic diffusion was shown to cause the material's effective magnetoelastic coupling coefficient and elastic modulus to be complex and frequency dependent. Up to about the cut-off frequency, the magnitude of the steady-state, dynamic field increases in proportion to  $f$ . As forcing frequency increases above that range, the magnitude overshoots its high frequency limit, peaks, then decreases to its high frequency limit, at which point the dynamic magnetic flux becomes zero and further increases in forcing frequency have no effect. Use of the analytical solutions for design purposes was also discussed.

For nonlinear constitutive regimes, magnetic diffusion was studied by solving the governing PDE using the finite difference method. The radial non-uniformity of the applied stress was also considered. A detailed model validation was presented. When the response exhibits significant nonlinearity, MATLAB's *fminunc* and the proposed numerical method do not converge; thus, the analysis was limited to small to moderate stress amplitudes and forcing frequencies. The effect of time-varying material properties on the nonlinear diffusion response was first studied by prescribing a sinusoidal variation of the properties. Then, nonlinear diffusion in a Galfenol rod at a near worst-case bias condition was investigated by calculating the material properties using the DEA model. At this bias, the results suggest that nonlinearity becomes appreciable at a stress amplitude of about 1.5 MPa and the cut-off frequency for nonlinear diffusion is about 1.4 times that of linear diffusion.

A precise dynamic characterization of solid and laminated rods of the most widely used Galfenol alloy ( $\text{Fe}_{81.6}\text{Ga}_{18.4}$ ) to dynamic, compressive stress up to 31 MPa and 1 kHz was conducted. A novel experimental design was reported, wherein a detailed discussion of specimen design, sensor selection, uncertainty analysis, calibration, error sources, and data processing methods was included. From these measurements, the frequency dependence of dynamic material properties and energy loss components is presented. The estimated uncertainties met ASTM standards in most cases. The experimental setup was refined to minimize the three key sources of error: (a) electromagnetic noise in strain signals due to Galfenol's magnetic response, (b) error in load signals due to the inertial force of fixturing, and (c) phase misalignment between signals due to conditioning electronics. For dynamic characterization, strain error was

kept below 1.2 % of full scale by wiring two collocated gauges in series (noise cancellation) and through leadwire weaving. Inertial force error was kept below 0.41 % by measuring the dynamic force in the specimen using a nearly collocated piezoelectric load washer. The phase response of all conditioning electronics was explicitly measured and corrected for in post processing.

Constant current and constant field bias conditions were investigated. In the solid rod, as frequency is increased above about 100 Hz, the sensing response becomes more linear due to an increase in eddy currents, which suppress magnetic moment rotation. Compared to the solid rod, the laminated rod exhibits much slower increases in hysteresis with frequency, and its quasi-static behavior extends to higher frequencies, suggesting an appreciable reduction in eddy currents. The frequency dependence of the dynamic sensing properties were calculated from the measurements. Due to experimental magnetic diffusion cut-off frequencies of only about 44 Hz (constant field) and 105 Hz (constant current), the dynamic sensing properties of the solid rod vary significantly with frequency, monotonically decaying toward their saturated (passive) values. This illustrates the inaccuracy of frequency-independent dynamic properties calculated via linear piezomagnetic models from experimental responses to electrical excitation. It also motivates the use of complex, frequency-dependent properties for modeling and design. The laminated rod exhibits a cut-off of about 1 kHz. The loss factor of the solid rod under constant current initially increases almost linearly (suggesting that excess eddy current losses are low), then, at a value of 0.13, becomes nearly frequency independent above 300 Hz. These measurements allow for the validation of rate-dependent Galfenol constitutive models and permit the accurate modeling of Galfenol-based systems that experience time-varying forces.



## Dynamic stiffness change

In this chapter, the dynamic changes in the elastic modulus of magnetostrictive materials that result from real-time magnetic field changes are studied in two stages. First, a magnetostrictive transducer that can electrically tune its stiffness at high speeds (a magnetostrictive Varispring) is modeled, designed, and tested. Second, high-speed switching of the transducer's stiffness is applied in a computational study of switched stiffness vibration control of a simple mechanical system.

The Varispring was designed based on (a) a nonlinear electromechanical transducer model, (b) the aforementioned analytical solution of magnetic diffusion, and (c) the effect of internal mass on the magnetostrictive material's dynamic stiffness. A laminated Terfenol-D rod (instead of a laminated Galfenol rod) was selected as the active material due to its larger modulus tunability, slightly faster rise time to control inputs, and significantly higher magnetic diffusion cut-off frequency. The rise time was further decreased by winding the contained electromagnet with relatively large wire (22 AWG) and by minimizing the rod's length (and thus its diameter). The Terfenol-D rod's strain response to dynamic, compressive forces in the presence of sinusoidal and square wave current inputs was measured to quantify continuous and discrete modulus changes, respectively. To improve the force control, the Varispring had to be operated about a small bias compression, which reduced the attainable Young's modulus variation. Continuous and square wave modulus changes up to 21.9 GPa / 500 Hz and 12.3 GPa / 100 Hz, respectively, are observed for current amplitudes up to 1.5 A and 0.5 A, respectively. Instability and overshoot in the controlled square wave current prevented measurement at higher current frequencies and amplitudes. The rise time of the Varispring was  $< 1$  ms.

In the computational study of switched stiffness vibration control, the Varispring was implemented as a tunable spring mount to dampen the vibration of a single-degree-of-freedom mechanical system. The free vibration response of the mass under passive damping and vibration control was calculated using a model that incorporates constitutive nonlinearities, mechanical vibrations, the electrical dynamics associated with voltage control of the Varispring, and the magnetostrictive force generated by the Varispring. To greatly simplify the numerical solution procedure, eddy current effects were not considered. The (uncontrolled) magnetostrictive force plays a significant role in the performance of the control, particularly when the net magnetostrictive force over one vibration cycle is not small. Hence, a modified control law was proposed to minimize the influence of the magnetostrictive force. Stiffness switching according to the modified law was found to introduce a level of damping that is equivalent to a viscous damping ratio of about 0.15. In general, the performance of the control improved as the stiffness change magnitude increased and the amplitude of the magnetostrictive force decreased.

## 5.2 Contributions and Findings

### Static stiffness change

- Experimental characterization of the major loop and minor loop strain responses of solid and laminated Galfenol ( $\text{Fe}_{81.6}\text{Ga}_{18.4}$ ) to quasi-static compressive stress under constant magnetic field and constant current bias conditions (paper [55])
  - Minor loop Young's moduli and  $\Delta E$  effects of the solid rod are stiffer and smaller, respectively, than their major loop counterparts

- The saturation modulus of the laminated rod is smaller than that of the solid rod due to soft adhesive layers, but the  $\Delta E$  effect is approximately equal
- Hysteresis is smaller for constant field bias conditions
- Validated, nonlinear, dynamic model and quantified performance of adaptive vibration absorbers composed of Galfenol-based composite beams (papers [125, 126, 133])
  - An input power threshold exists, below which the absorber’s resonant frequency is controllable and above which the controllability decreases to zero due to high stress
  - Resonant frequency tunability increases as the Galfenol element’s volume fraction and offset from the neutral bending axis increase
  - Autoresonant feedback control is a very efficient numerical technique for tracking the resonant frequency of complex nonlinear systems undergoing changes in system parameters
  - Magnetic field-induced axial forces in clamped-clamped composites appreciably affect the tuning parameters, but they have a minimal effect on the maximum resonant frequency tunability

### **Dynamic stress effects in magnetostrictive materials**

- First ever analysis and solutions of linear and nonlinear mechanically-induced magnetic diffusion in cylindrical ferromagnets (paper [134])

- Analytical, non-dimensionalized time and frequency domain solutions for the radial dependence and spatial average of the internal magnetic field
  - Analytical expressions for skin depth and cut-off frequency
  - Mechanically-induced magnetic diffusion causes the material's effective magnetoelastic coupling coefficient and elastic modulus to be complex and frequency dependent
  - Up to about the cut-off frequency, the magnitude of the steady-state, internal field increases in proportion to forcing frequency
  - Parametric excitations caused by material property variations add to the stress excitation when they are 180 degrees out-of-phase with the dynamic stress and counteract the stress excitation when they are in-phase with the dynamic stress
  - At a near worst-case bias condition, nonlinearity in Galfenol's magnetic diffusion response becomes appreciable at a stress amplitude of 1.5 MPa; the cut-off frequency for nonlinear diffusion is about 1.4 times that of linear diffusion
- Novel characterization of the mechanical and magnetic responses of solid and laminated Galfenol to small amplitude and large amplitude dynamic forces up to 1 kHz (papers [132, 131])
    - Experimental methodology for the precise measurement of the dynamic stiffness and sensitivity of magnetostrictive materials (paper [129])

- As forcing frequency increases above about 50 Hz, the solid rod’s response becomes more passive and linear due to the suppression of magnetic domain rotation by eddy currents
- The dynamic sensing properties of the solid rod vary significantly with frequency, monotonically decaying toward their saturated (passive) values above cut-off frequencies of about 44 Hz (constant field) and 105 Hz (constant current); properties of the laminated rod exhibit a weak dependence on frequency up to 1 kHz
- The mechanical loss factor of the solid rod reaches 0.13 due to eddy current-induced damping

### **Dynamic stiffness change**

- Modeling, design, and testing of a magnetostrictive Varispring – a magnetostrictive transducer that can change its axial stiffness at high speeds (papers [128, 130])
  - When magnetic diffusion is negligible, the rise time of Terfenol-D- and Galfenol-based transducers to stiffness control inputs can be on the order of 0.1 ms, suggesting that stiffness tuning bandwidths on the order of 1 kHz are feasible
  - Terfenol-D performs better than Galfenol for dynamic tuning of axial stiffness due its slightly faster rise time, significantly higher magnetic diffusion cut-off frequency, and larger elastic modulus tunability

- Continuous Young’s modulus changes up to 21.9 GPa and 500 Hz, modulus switching up to 12.3 GPa and 100 Hz, and a rise time below 1 ms are measured using a demonstration transducer
- Computational study of switched stiffness vibration control of a lumped mechanical system using a magnetostrictive Varispring (paper [127])
  - Modified control law that accounts for the effect of a magnetostrictive force
  - Control-induced damping equivalent to a viscous damping ratio of about 0.15

### **Constitutive modeling**

- Framework of an improved discrete energy-averaged model for Terfenol-D (Appendix A)
  - The unphysical kinks and slow approach to saturation previously observed in simulations can be corrected with a coordinate transformation that does not compromise computational speed or the explicitness of the model

## **5.3 Future Work**

This research has provided a greater understanding of the  $\Delta E$  effect and its application to adaptive vibration absorbers. This research also unveiled the effects of dynamic stress on magnetostrictive materials and opened a new field of research on real-time stiffness tuning and stiffness control of magnetostrictive materials. These contributions bring to light the following opportunities for future work:

- Measurements in this research suggest that giant magnetostrictive materials have the potential to simultaneously provide high stiffness and high energy

dissipation in a compact, solid-state package. Using the reported experimental methodology and analytical magnetic diffusion solutions as a platform, an in-depth study of shunt damping and mechanically-induced eddy current damping can be undertaken.

- Nonlinear mechanically-induced magnetic diffusion was studied using a solution procedure that exhibited numerical instability in highly nonlinear regimes. The development of a more robust numerical method can reveal the diffusion behavior for large amplitude, high frequency stress excitations.
- The possibility of mitigating mechanically-induced diffusion effects using a dynamic, surface magnetic field (i.e., using field-induced magnetic diffusion) can be numerically explored.
- Switched stiffness vibration control of forced vibrations using a magnetostrictive Varispring can be investigated using the model presented herein. An important extension to this model would be the inclusion of mechanically-induced and field-induced magnetic diffusion; due to constitutive nonlinearities, this will require a numerical solution of the nonlinear PDE that governs diffusion.
- Experimental testing of the magnetostrictive Varispring was limited by overshoot in the controlled current and an imperfect bias stress. A revised experiment can uncover the maximum capabilities of the Varispring, including stiffness tunability and tuning bandwidth, by increasing the bias compression (e.g., with an internal Belleville spring) and improving the electrical excitation (e.g., by optimizing the current control, using voltage control, or by low-pass filtering the square wave signal). The refined Varispring and control system can

then be used to demonstrate switched stiffness vibration control of a mechanical system; this demonstration would highlight the strengths and weaknesses of the Varispring while collecting data for model validation.

- The concept of real-time stiffness tuning and stiffness control can be extensively studied. It may be possible to actively control moderate to high frequency vibrations via small amplitude, high frequency magnetostrictive forces while modulating the nominal stiffness via the conventional  $\Delta E$  effect (i.e., a large amplitude, low frequency magnetic field).



## Appendix A: Improved Discrete Energy-Averaged Model for Terfenol-D

As explained in the *Application of the DEA model to Terfenol-D* subsection of Section 1.2.2, the current DEA model for accurately modeling the constitutive response of Terfenol-D is implicit, which increases computation time and prevents the derivation of a material Jacobian. In this appendix, a simple modification to Evans and Dapino’s original DEA model [61] is proposed that eliminates the unphysical kinks in the responses (see Fig. A.1) and provides a slow approach to saturation while also retaining the explicit nature of the original DEA model.

The DEA model is applicable to cubic magnetostrictive materials (e.g., Galfenol and Terfenol-D) that are excited by a 3D magnetic field and stress. In Evans and Dapino’s original formulation, these inputs are defined relative to the coordinate system of the material’s cubic crystal structure, rather than the coordinate system of the specimen. In a typical Galfenol specimen, this distinction is not important, because the material is manufactured such that the  $\langle 100 \rangle$  direction of its crystals is nominally aligned with the specimen’s primary axis (i.e., the symmetry axis of a cylindrical rod or the length direction of a sheet). However, Terfenol-D rods are grown along a  $\langle 112 \rangle$  crystal direction, as shown in Fig. A.2; consequently, the field and stress applied to the rod during a characterization experiment differ from those

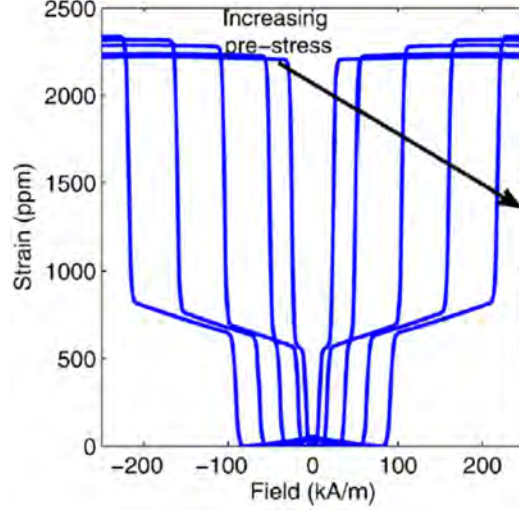


Figure A.1: Unphysical kinks in the magnetostriction response of Terfenol-D calculated using Evans and Dapino’s original DEA model [61]; plot reproduced from [34].

which are applied to the material in the original DEA model. This discrepancy can be easily accounted for using an appropriate coordinate transformation. It will be shown that the accurate implementation of this coordinate transformation eliminates the unphysical kinks and provides a smooth approach to saturation without the need for introducing a field- and stress-dependent smoothing factor (as was done in [34].

First order tensors (e.g., magnetic field and magnetization) are transformed using a transformation matrix  $\mathbf{U}$  according to

$$\mathbf{X}_G = \mathbf{U}^T \mathbf{X}_M, \quad (\text{A.1})$$

$$\mathbf{X}_M = \mathbf{U} \mathbf{X}_G, \quad (\text{A.2})$$

where  $\mathbf{X}_G$  and  $\mathbf{X}_M$  represent the tensor relative to the global and material coordinate system, respectively. Second order tensors (e.g., strain and stress) transform

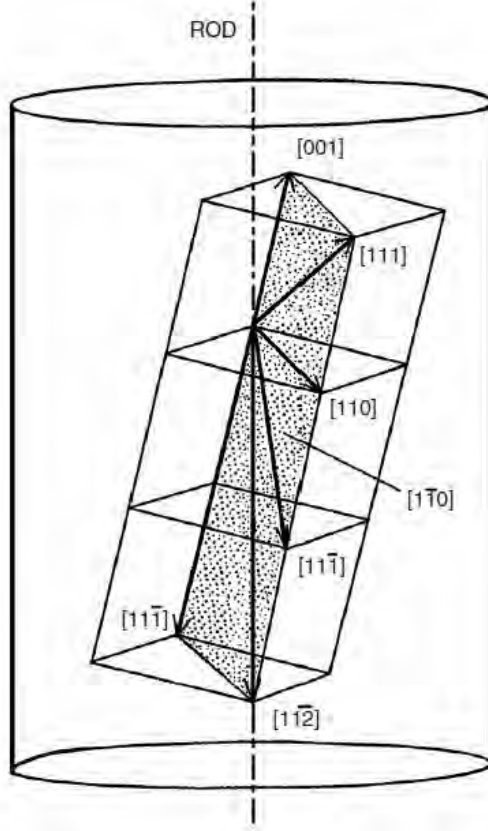


Figure A.2: Crystal structure of a Terfenol-D rod; adapted from [31] and reproduced from [96].

according to

$$\mathbf{X}_G = \mathbf{U} \mathbf{X}_M \mathbf{U}^T, \quad (\text{A.3})$$

$$\mathbf{X}_M = \mathbf{U}^T \mathbf{X}_G \mathbf{U}. \quad (\text{A.4})$$

As detailed by Chakrabarti [32],  $\mathbf{U}$  contains the normalized direction vectors (defined in the material coordinate system) that point along the global coordinate axes,

$$\mathbf{U} = \left[ \frac{\mathbf{u}_x}{\|\mathbf{u}_x\|}, \frac{\mathbf{u}_y}{\|\mathbf{u}_y\|}, \frac{\mathbf{u}_z}{\|\mathbf{u}_z\|} \right]. \quad (\text{A.5})$$

It is convenient to take the rod's axis as the global  $z$ -direction; hence,  $\mathbf{u}_z = [112]$ . For axisymmetric models,  $\mathbf{u}_x$  and  $\mathbf{u}_y$  are taken as the radial and circumferential directions,  $\mathbf{u}_r$  and  $\mathbf{u}_\theta$ , which depend upon the circumferential angle  $\theta$ . If a Cartesian global coordinate system is used,  $\mathbf{u}_x$  and  $\mathbf{u}_y$  can be any vectors that are mutually orthogonal and orthogonal to  $\mathbf{u}_z$ . Herein,  $\mathbf{u}_x = [\bar{1}\bar{1}1]$  and  $\mathbf{u}_y = [1\bar{1}0]$ .

The DEA model for Terfenol-D is improved as follows. First, the stress and magnetic field applied to the rod (defined relative to the global, i.e., the rod's, coordinate system),  $\mathbf{T}_G$  and  $\mathbf{H}_G$ , respectively, are transformed into the stress and field applied to the cubic crystal structure (defined relative to the material, i.e., the crystal's, coordinate system) using

$$\mathbf{T}_M = \mathbf{U}^T \mathbf{T}_G \mathbf{U}, \quad (\text{A.6})$$

and

$$\mathbf{H}_M = \mathbf{U} \mathbf{H}_G, \quad (\text{A.7})$$

Evans and Dapino's original DEA model [61] is then followed using  $\mathbf{T}_M$  and  $\mathbf{H}_M$  as inputs. It is emphasized that the 3D formulation of the DEA model is required even for 1D inputs, because a uniaxial stress and field applied to the rod are a 3D input from the material's perspective. Once the solution is obtained in the material coordinate system, the magnetostriction and magnetization of the rod in the global coordinate system are respectively calculated as

$$\boldsymbol{\lambda}_G = \mathbf{U} \boldsymbol{\lambda}_M \mathbf{U}^T, \quad (\text{A.8})$$

and

$$\mathbf{M}_M = \mathbf{U} \mathbf{M}_G. \quad (\text{A.9})$$

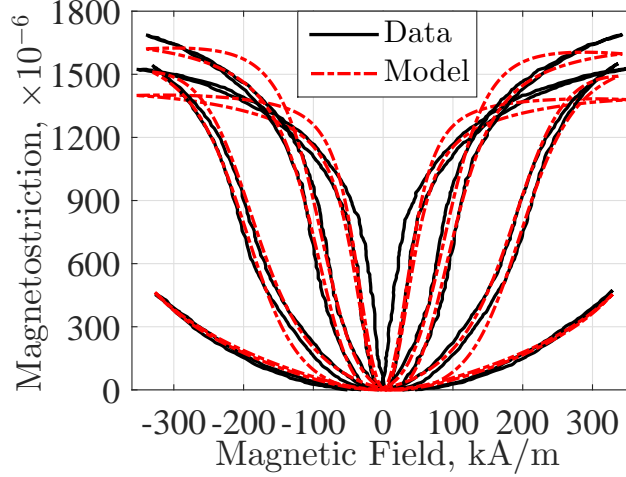


Figure A.3: Comparison of the improved DEA model for Terfenol-D with magnetostriction measurements from Etrema Products, Inc. [85] for compressive bias stresses of 6.9, 27.6, 55.2, and 110.4 MPa.

To validate the proposed DEA model for Terfenol-D, computational and measured actuation responses are compared in Fig. A.3, where the experimental data was provided by Etrema Products, Inc. [85]. The model parameters, which are summarized in Table A.1, were obtained using a coarse, preliminary optimization of the form detailed in [34]. A modeling error of about 18 % is found; although this error is considerably larger than that achieved by Chakrabarti and Dapino’s model [34], a refined optimization procedure was not developed or conducted, because it is outside the scope of this dissertation. Also, it is stressed that the proposed model does not exhibit kinks or a sharp approach to saturation; further, the proposed model is explicit, thereby permitting an analytical material Jacobian,<sup>12</sup> and is approximately 20 % faster than the current art ([34]).

<sup>12</sup>See Section 5.2.1 of [32] for a discussion of how to calculate the material Jacobian defined relative to the global and material coordinate systems.

Table A.1: Model parameters for the improved DEA model for Terfenol-D, obtained using a coarse optimization of the form detailed in [34].

$K, \text{ J} \times 10^5 / \text{m}^3$	$K_0^{1,2}, \text{ J} \times 10^5 / \text{m}^3$	$K_0^{3,4}, \text{ J} \times 10^5 / \text{m}^3$	$K_0^{5,6,7,8}, \text{ J} \times 10^5 / \text{m}^3$	$\mu_0 M_s, \text{ T}$
2.739	0.8007	0.8565	0.8620	0.6000
$\lambda_{100}, \times 10^{-3}$	$\lambda_{111}, \times 10^{-3}$	$\Omega, \text{ kJ} / \text{m}^3$	$c$	$k_p, \text{ MJ}$
0.4999	0.9905	6.600	0.8019	0.1649

## Appendix B: Galfenol Vibration Absorbers: Distributed Parameter Modeling

### B.1 Stiffness and damping matrices

For the 2nd order central difference approximation of the damping and flexural forces (Eqs. (2.30) and (2.31)), the global damping and stiffness matrices are, respectively,

$$[C] = a(\Delta x)^{-4} \begin{bmatrix} C_2 + G_2 & B_2 & A_2 & 0 & \cdots & \cdots & 0 \\ D_3 & C_3 & B_3 & A_3 & 0 & \cdots & \\ G_4 & D_4 & C_4 & B_4 & A_4 & 0 & \vdots \\ 0 & \ddots & \ddots & \ddots & \ddots & \ddots & 0 \\ \vdots & 0 & G_{N-3} & D_{N-3} & C_{N-3} & B_{N-3} & A_{N-3} \\ & \cdots & 0 & G_{N-2} & D_{N-2} & C_{N-2} & B_{N-2} \\ 0 & & \cdots & 0 & G_{N-1} & D_{N-1} & C_{N-1} + A_{N-1} \end{bmatrix}, \quad (\text{B.1})$$

and

$$[K] = (\Delta x)^{-4} \begin{bmatrix} \bar{C}_2 + G_2 & \bar{B}_2 & A_2 & 0 & \cdots & \cdots & 0 \\ \bar{D}_3 & \bar{C}_3 & \bar{B}_3 & A_3 & 0 & \cdots & \\ G_4 & \bar{D}_4 & \bar{C}_4 & \bar{B}_4 & A_4 & 0 & \vdots \\ 0 & \ddots & \ddots & \ddots & \ddots & \ddots & 0 \\ \vdots & 0 & G_{N-3} & \bar{D}_{N-3} & \bar{C}_{N-3} & \bar{B}_{N-3} & A_{N-3} \\ & \cdots & 0 & G_{N-2} & \bar{D}_{N-2} & \bar{C}_{N-2} & \bar{B}_{N-2} \\ 0 & & \cdots & 0 & G_{N-1} & \bar{D}_{N-1} & \bar{C}_{N-1} + A_{N-1} \end{bmatrix}, \quad (\text{B.2})$$

where the elements are evaluated using Eq. (2.32).

For increased accuracy, the 4th order central difference method can be used to approximate the damping and flexural forces as

$$F_i^C(t) \approx a(144\Delta x)^{-4}(H_i\dot{w}_{i+3} + J_i\dot{w}_{i+2} + L_i\dot{w}_{i+1} + N_i\dot{w}_i + O_i\dot{w}_{i-1} + Q_i\dot{w}_{i-2} + R_i\dot{w}_{i-3}), \quad (\text{B.3})$$

and

$$\begin{aligned} F_i^K(t) &\approx (144\Delta x)^{-4} (H_i\dot{w}_{i+3} + (J_i + 12\bar{P})\dot{w}_{i+2} + (L_i - 192\bar{P})\dot{w}_{i+1} \\ &\quad + (N_i + 360\bar{P})\dot{w}_i + (O_i - 192\bar{P})\dot{w}_{i-1} + (Q_i + 12\bar{P})\dot{w}_{i-2} + R_i\dot{w}_{i-3}) \\ &= (144\Delta x)^{-4} (H_i\dot{w}_{i+3} + \bar{J}_i\dot{w}_{i+2} + \bar{L}_i\dot{w}_{i+1} + \bar{N}_i\dot{w}_i \\ &\quad + \bar{O}_i\dot{w}_{i-1} + \bar{Q}_i\dot{w}_{i-2} + R_i\dot{w}_{i-3}), \end{aligned} \quad (\text{B.4})$$

where

$$\begin{aligned} H_i &= 3EI_{i+2} - 24EI_{i+1} - 24EI_i + 24EI_{i-1} - 3EI_{i-2}, \\ J_i &= -23EI_{i+2} + 176EI_{i+1} + 318EI_i - 208EI_{i-1} + 25EI_{i-2}, \\ L_i &= 23EI_{i+2} - 56EI_{i+1} - 1416EI_i + 568EI_{i-1} - 55EI_{i-2}, \\ N_i &= 30EI_{i+2} - 480EI_{i+1} + 2244EI_i - 480EI_{i-1} + 30EI_{i-2}, \\ O_i &= -55EI_{i+2} + 568EI_{i+1} - 1416EI_i - 56EI_{i-1} + 23EI_{i-2}, \\ Q_i &= 25EI_{i+2} - 208EI_{i+1} + 318EI_i + 176EI_{i-1} - 23EI_{i-2}, \\ R_i &= -3EI_{i+2} + 24EI_{i+1} - 24EI_i - 24EI_{i-1} + 3EI_{i-2}. \end{aligned} \quad (\text{B.5})$$



Using Eqs. (B.3) – (B.5), the 4th order accurate damping and stiffness matrices can be written as

$$[C] = a(144\Delta x)^{-4} \begin{bmatrix} \tau(C_2 + G_2) & \tau B_2 & \tau A_2 & 0 & \cdots & & & & 0 \\ O_3 + R_3 & N_3 & L_3 & J_3 & H_3 & 0 & \cdots & & \\ Q_4 & O_4 & N_4 & L_4 & J_4 & H_4 & 0 & \cdots & \\ R_5 & Q_5 & O_5 & N_5 & L_5 & J_5 & H_5 & 0 & \vdots \\ 0 & \ddots & \ddots & \ddots & \ddots & \ddots & \ddots & \ddots & 0 \\ \vdots & 0 & R_{N-4} & Q_{N-4} & O_{N-4} & N_{N-4} & L_{N-4} & J_{N-4} & H_{N-4} \\ & \cdots & 0 & R_{N-3} & Q_{N-3} & O_{N-3} & N_{N-3} & L_{N-3} & J_{N-3} \\ & & \cdots & 0 & R_{N-2} & Q_{N-2} & O_{N-2} & N_{N-2} & L_{N-2} + H_{N-2} \\ 0 & & & \cdots & 0 & \tau G_{N-1} & \tau D_{N-1} & \tau(C_{N-1} + A_{N-1}) & \end{bmatrix}, \quad (\text{B.6})$$

and

$$[K] = (144\Delta x)^{-4} \begin{bmatrix} \tau(\bar{C}_2 + \bar{G}_2) & \tau \bar{B}_2 & \tau A_2 & 0 & \cdots & & & & 0 \\ \bar{O}_3 + R_3 & \bar{N}_3 & \bar{L}_3 & \bar{J}_3 & H_3 & 0 & \cdots & & \\ \bar{Q}_4 & \bar{O}_4 & \bar{N}_4 & \bar{L}_4 & \bar{J}_4 & H_4 & 0 & \cdots & \\ R_5 & \bar{Q}_5 & \bar{O}_5 & \bar{N}_5 & \bar{L}_5 & \bar{J}_5 & H_5 & 0 & \vdots \\ 0 & \ddots & \ddots & \ddots & \ddots & \ddots & \ddots & \ddots & 0 \\ \vdots & 0 & R_{N-4} & \bar{Q}_{N-4} & \bar{O}_{N-4} & \bar{N}_{N-4} & \bar{L}_{N-4} & \bar{J}_{N-4} & H_{N-4} \\ & \cdots & 0 & R_{N-3} & \bar{Q}_{N-3} & \bar{O}_{N-3} & \bar{N}_{N-3} & \bar{L}_{N-3} & \bar{J}_{N-3} \\ & & \cdots & 0 & R_{N-2} & \bar{Q}_{N-2} & \bar{O}_{N-2} & \bar{N}_{N-2} & \bar{L}_{N-2} + H_{N-2} \\ 0 & & & \cdots & 0 & \tau G_{N-1} & \tau \bar{D}_{N-1} & \tau(\bar{C}_{N-1} + A_{N-1}) & \end{bmatrix}, \quad (\text{B.7})$$

where  $\tau = 144$ . Since the 4th order approximations of the damping and flexural forces at node  $i$  depend upon nodes  $i - 3$  and  $i + 3$ , the 2nd order central difference method must be used at nodes  $i = 2, N - 1$  to avoid the inclusion of fictitious nodal displacements in the 4th order damping and stiffness matrices. The 4th order method can be used at the remaining interior nodes after considering Eq. (2.33).

## B.2 Analytical response of the passive beam

The analytical free and forced vibration of the passive beam (i.e., uniform flexural rigidity and no axial force) are derived as follows. By the method of modal analysis, the solution for the beam vibration can be written as

$$\bar{w}(x, t) = \sum_{r=1}^{\infty} W_r(x) \eta_r(t), \quad (\text{B.8})$$

where  $\eta_r(t)$  are the modal coordinates and  $W_r(x)$  are the eigenfunctions of the undamped clamped-clamped beam, which are provided by Rao [118],

$$W_r(x) = C_n \left[ \sinh(\beta_r x) - \sin(\beta_r x) + \left( \frac{\sinh(\beta_r L) - \sin(\beta_r L)}{\cos(\beta_r L) - \cosh(\beta_r L)} \right) (\cosh(\beta_r x) - \cos(\beta_r x)) \right], \quad (\text{B.9})$$

$$\cos(\beta_r L) \cosh(\beta_r L) = 1. \quad (\text{B.10})$$

Inserting Eq. (B.8) into the governing PDE Eq. (2.25), neglecting the beam's non-uniformity and axial force, premultiplying by  $W_s(x)$ , and integrating over the length of the beam yields

$$\begin{aligned} \sum_{r=1}^{\infty} \left( \left( \int_0^L \rho A W_s W_r dx \right) \ddot{\eta}_r + a \left( \int_0^L EI W_s W_r^{(4)} dx \right) \dot{\eta}_r \right. \\ \left. + \left( \int_0^L EI W_s W_r^{(4)} dx \right) \eta_r \right) = \int_0^L W_r f_{\text{eq}} dx. \end{aligned} \quad (\text{B.11})$$

Using the orthonormality conditions [106] derived from the eigenvalue problem, only the  $s^{\text{th}}$  terms in Eq. (B.11) survive, giving the modal equations,

$$\ddot{\eta}_s + 2\zeta_s \omega_s \dot{\eta}_s + \omega_s^2 \eta_s = \Phi_s \sin(\omega_u t), \quad s = 1, 2, \dots, \quad (\text{B.12})$$

where the modal damping ratio  $\zeta_s$  is

$$\zeta_s = \frac{a \omega_s}{2}. \quad (\text{B.13})$$

Assuming harmonic base excitation with frequency  $\omega_u$  and magnitude  $B(\omega_u)$ , the forcing magnitude  $\Phi_s$  is

$$\Phi_s = \rho A B(\omega_u) \omega_u^2 \int_0^L W_s dx. \quad (\text{B.14})$$

For underdamped modes, the solution of Eq. (B.12) can be written as

$$\eta_s = \exp(-\zeta_s \omega_s t) (A \sin(\omega_{ds} t) + B \cos(\omega_{ds} t)) + \Phi_s \left| \tilde{G}_s(i\omega_u) \right| \sin(\omega_u t + \phi_s), \quad (\text{B.15})$$

where  $\omega_{ds}$  is the damped natural frequency of the  $s^{th}$  mode, the magnitude and phase of the modal frequency response, respectively, are

$$\left| \tilde{G}_s(i\omega_u) \right| = \frac{1}{\omega_s^2} \left( \left( 1 - \left( \frac{\omega_u}{\omega_s} \right)^2 \right)^2 + \left( 2\zeta_s \frac{\omega_u}{\omega_s} \right)^2 \right)^{-1/2}, \quad (\text{B.16})$$

$$\phi_s = -\tan^{-1} \left( 2\zeta_s \frac{\omega_u}{\omega_s} \left( 1 - \left( \frac{\omega_u}{\omega_s} \right)^2 \right)^{-1} \right), \quad (\text{B.17})$$

and the undetermined coefficients  $A$  and  $B$  are

$$\begin{aligned} A &= \eta_s(0) - \sin(\phi_s) \Phi_s \left| \tilde{G}_s(i\omega_u) \right|, \\ B &= \frac{\dot{\eta}_s(0) + \zeta_s \omega_s \eta_s(0)}{\omega_{ds}} - \frac{\zeta_s \omega_s \sin(\phi_s) + \omega_u \cos(\phi_s)}{\omega_{ds}} \Phi_s \left| \tilde{G}_s(i\omega_u) \right|. \end{aligned} \quad (\text{B.18})$$

Insertion of Eqs. (B.15) and (B.9) into Eq. (B.8) gives the time domain response of the passive beam to initial conditions and base excitation. The frequency response of the displacement transmissibility can be written as

$$\begin{aligned} G(x, i\omega_u) &= \frac{\bar{w}}{u} = \rho A \omega_u^2 \sum_{s=1}^{\infty} W_r(x) \left( \int_0^L W_s dx \right) \left| \tilde{G}_s(i\omega_u) \right| \exp(i\phi_s) \\ &= \sum_{s=1}^{\infty} \Omega_s(x, i\omega_u) \exp(i\phi_s). \end{aligned} \quad (\text{B.19})$$

The magnitude and phase of  $G(x, i\omega_u)$  are

$$\begin{aligned} |G(x, i\omega_u)| &= \left( \left( \sum_{s=1}^{\infty} \Omega_s(x, i\omega_u) \cos(\phi_s) \right)^2 + \left( \sum_{s=1}^{\infty} \Omega_s(x, i\omega_u) \sin(\phi_s) \right)^2 \right)^{1/2}, \\ \angle G(x, i\omega_u) &= \tan^{-1} \left( \frac{\sum_{s=1}^{\infty} \Omega_s(x, i\omega_u) \sin(\phi_s)}{\sum_{s=1}^{\infty} \Omega_s(x, i\omega_u) \cos(\phi_s)} \right). \end{aligned} \quad (\text{B.20})$$

## **Appendix C: Dynamic Characterization of Galfenol: Uncertainty and Calibration**

### **C.1 Uncertainty Analysis**

This section details the selection of sensors and an uncertainty analysis for each measured quantity.

#### **Distance and area**

Area was measured to calculate the axial stress in the rod. Table C.1 summarizes the recommended accuracy of distance measurements from ASTM and JIS standards. As recommended by ASTM E9, distances were measured using micrometers [17]. The micrometers had 0.001 in gradations and 0.0001 in accuracy (interpolation and instrument uncertainties of 0.0005 in and 0.0001 in, respectively). For the 0.25 in diameter specimen, these resulted in diameter and area uncertainties of  $5.1 \times 10^{-4}$  in (0.2 %) and  $2.0 \times 10^{-4}$  in<sup>2</sup> (0.4 %), respectively.

#### **Force and stress**

The force applied to the ends of the specimen was measured to calculate the axial stress in the rod according to Eq. (C.2). Applied forces were in the range -1.96 to 0 kN (-441 to 0 lbf), where a negative force indicates compression. For quasi-static and

Table C.1: ASTM and JIS recommendations for distance measurements.

Parameter	Measurement Accuracy	ASTM/JIS Standard
diameter	0.001 in (dimensions $> 0.1$ in), use avg.	E9 [17], E209 [12], E466 [10]
	$\leq 0.1$ % at 3 locations, use avg.	E1875 [8], E1876 [9]
	$\leq 0.5$ % at 2 orthogonal locations, use avg.	JIS Z 2273 [91]
area	$\leq 1$ %	E111 [11]

dynamic experiments, small amplitude (89 N / 20 lbf) and large amplitude (980 N / 220 lbf) forces were applied to the specimen. Table C.2 summarizes the recommended accuracy of force measurements from ASTM standards. Quasi-static forces were measured using an Interface 1010ACK-500-B fatigue rated load cell (2224 N / 500 lbf range) and MTS 493.21 signal conditioner. This load cell is very stiff and accurate, and is rated for  $10^8$  fully reversed loading cycles.

Table C.2: ASTM recommendations for force sensors.

Parameter	Measurement Accuracy	ASTM Standard
force (static)	$\pm 1$ % error, $\leq 1$ % repeatability	E4 [14]
force (dynamic)	$\pm 1$ % error	E467 [15]

As discussed in the *Inertial force error reduction* subsection of Section 3.2.3, dynamic forces vibrate the specimen and fixtures, resulting in inertial forces that cause error in measurements of the force applied to the specimen. This error was reduced by

minimizing the mass of fixturing located between the specimen and force sensor. The large masses of the platen and magnetic circuit prevented the accurate measurement of dynamic forces by the load cell. Inertial force errors below 0.41 % were possible by using a piezoelectric load washer. The load washer could be located almost directly below the specimen, such that the inertial forces of the platen and magnetic circuit did not influence the measurement. Specifically, dynamic forces ( $> 100$  Hz) were measured using a Kistler 9001A piezoelectric load washer (7.5 kN / 1686 lbf range) and Kistler 5010 charge amplifier. This frequency cut-off was selected, because the load washer's phase response is nonlinear below this cut-off (see the *Phase calibration* subsection of Section 3.2.4).

The interface load cell was used for force control of the dynamic load frame. To compensate for inertial force errors during dynamic testing, the force command signal was increased until the load washer readout indicated the desired dynamic force amplitude.

Table C.3 gives the uncertainty for the load cell and load washer. The uncertainties of the MTS conditioner were not specified. However, as detailed in Section C.2, the entire static force measurement system was calibrated to the accuracy specified in ASTM E4 ( $\leq \pm 1$  % of the reading) [14]. The uncertainty in the calculation of dynamic force was determined from the load washer's uncertainty, Eq. (3.84), the charge amplifier's sensitivity ( $\text{Sens}_{\text{ChargeAmp}}$  in V/pC) and uncertainty ( $\pm 0.5$  %), and the expression for the dynamic force ,

$$F_{\text{Dynamic}} = q_{\text{LoadWasher}} \text{Sens}_{\text{ChargeAmp}} X, \quad (\text{C.1})$$

where  $q_{\text{LoadWasher}}$  is the charge generated by the load washer in pC and  $X$  is the range setting in N/V. The uncertainty in the static and dynamic stress measurements was

estimated using the force uncertainties, Eq. (3.84), and the equation for axial stress,

$$T = \frac{F}{A}. \quad (\text{C.2})$$

The force and stress uncertainties are plotted as a function of the measured force in Fig. C.1.

Table C.3: Uncertainties of the force sensors.

	Device	Interpolation Uncertainty, N (lbf)	Instrument Uncertainty, N (lbf)	Device Uncertainty, N (lbf)
static force	Interface 1010ACK-500- B <sup>13</sup>	$\approx 0$	$\pm 1.3$ (0.29)	$\pm 1.3$ (0.29)
dynamic force	Kistler 9001A <sup>14</sup>	$\pm 0.005$ (0.001)	$\pm 23$ (5.1)	$\pm 23$ (5.1)

## Temperature

The temperature of the specimen was monitored to prevent excessive temperature variation during repeated testing. If the temperature increase from room temperature exceeded 7 °C, tests were paused and the specimen was allowed to return to room temperature. Table C.4 outlines the recommended uncertainty of temperature measurements and the allowable temperature variation. Temperature was measured using a Type K thermocouple and an Omega DRG-SC-TC signal conditioner, which has an uncertainty of  $\pm 2$  °C. The Omega conditioner also has a very low bandwidth (about 4 Hz). However, for the specified purpose, this bandwidth and uncertainty

<sup>13</sup>assuming isothermal conditions and neglecting load eccentricity and creep

<sup>14</sup>assuming isothermal conditions and optimal installation

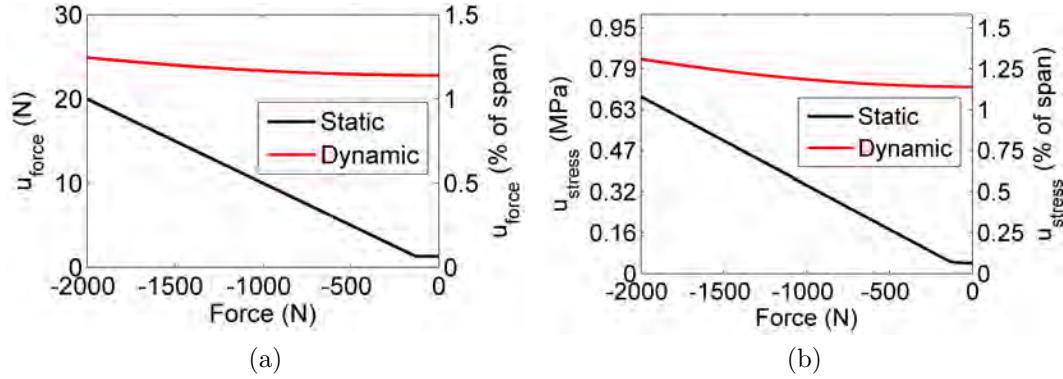


Figure C.1: Uncertainty in the (a) force and (b) stress calculations; the force and stress spans (maximum value minus minimum value), 2000 N and 63 MPa, respectively, are the same for static and dynamic measurements.

was sufficient, although the uncertainty did not meet the recommendations shown in Table C.4.

Table C.4: ASTM and ISO recommendations for temperature sensors and constant temperature testing.

Parameter	Specification	ASTM/ISO Standard
temperature	$\pm 1\text{ }^{\circ}\text{C}$	ISO 4664-1 [87]
allowable temperature variation during	$\pm 5.5\text{ }^{\circ}\text{C}$	E1875 [8]
constant temperature testing	$\pm 3\text{ }^{\circ}\text{C}$	E209 [12]

## Displacement and strain

A strain (or displacement) sensor was intended to measure (or calculate) the average, axial surface strain in the gauge region of the rod. Galfenol's elastic modulus is a function of magnetic field and stress. The magnetic circuit only controlled the magnetic state over a gauge region (Fig. 3.17b). Consequently, the elastic modulus



varied along the specimen's length; thus, displacement or strain measurements had to be confined to the gauge region. This precluded the use of many sensors, including capacitive displacement probes, laser displacement sensors, and potentiometers. Extensometers and strain gauges were suitable. However, laser extensometers have an insufficient resolution, while extensometers have a lower bandwidth relative to strain gauges and add an eccentric mass to the specimen. Semiconductor and piezoelectric strain gauges have multiple advantages, but could not conform to the small curvature of the specimen. Therefore, metal foil strain gauges were selected. Recommended specifications of strain sensors from ASTM and ISO standards are summarized in Table C.5.

Table C.5: ASTM and ISO recommendations for strain sensors.

Parameter	Measurement Accuracy	ASTM/ISO Standard
strain	$\pm 1 \%$	ISO 4664-1 [87]
	$\pm 0.1 \%$ to $\pm 1 \%$	E9 [17], E83 [16]
strain gauge resistance	$\pm 0.1 \%$ , repeatability $\leq 0.04 \%$	E251 [13]
strain resolution	$\leq 0.05 \%$ to $\leq 0.5 \%$	E9 [17], E83 [16]

Selection of a metal foil strain gauge was guided by the discussions in [75]. Constantan sensing alloy was chosen for its minimal magnetic effects. A long, but narrow gauge pattern was selected to average the strain over multiple material grains, allow for easy alignment, and reduce the magnitude of electromagnetic noise. A self-temperature-compensation number of 6 (i.e.,  $6 \mu\text{m}/\text{m}/^\circ\text{F}$  correction) provided compensation for the thermal expansion of Galfenol, which is  $6.4 \mu\text{m}/\text{m}/^\circ\text{F}$  [48]. The largest available gauge resistance was selected to reduce leadwire effects and

heat generation, which allowed for larger excitation voltages and thus a larger signal-to-noise ratio [75, 74]. Considering these factors and availability, the Vishay Micro-Measurements EA-06-250BF-350/L strain gauges were selected. Vishay's magnetic field strain gauge (H06A-AC1-125-700) could not be used due to its 17 week lead time. However, electromagnetic noise was quantified and minimized as detailed in the *Strain gauge noise reduction* subsection of Section 3.2.3.

To minimize the electromagnetic noise, axial strain was measured using two identical strain gauges (resistance  $R_G = 350 \, \Omega$ , gauge factor  $F_G = 2.155$ ) wired in series and located on opposite sides of the rod. These gauges together formed the active arm of a Wheatstone quarter bridge circuit. It can be shown that this circuit can be analyzed as a quarter bridge containing a single, effective strain gauge having a resistance of  $R_1 = 2R_G$  and gauge factor of  $F_G$ . This analogy holds if the strain gauges are identical and experience the same axial strain, but opposite bending strain. The uncorrected strain  $\epsilon'$  for this circuit was calculated as

$$\epsilon' = \frac{4}{F_G} \frac{\Delta E_0}{E}, \quad (\text{C.3})$$

where  $E$  is the excitation voltage and  $\Delta E_0$  is the bridge output voltage relative to the zero strain state. The uncorrected strain can be corrected for the quarter bridge nonlinearity and the resistance imbalance  $\delta R$  between the active bridge arm  $R_1$  and its adjacent arm  $R_2$  using

$$\epsilon'' = \frac{\epsilon' \left(2 + \frac{\delta R}{R_2}\right)^2}{4 \left[ \left(1 + \frac{\delta R}{R_2}\right) - \frac{F_G \epsilon'}{4} \left(2 + \frac{\delta R}{R_2}\right) \left(1 + \frac{\delta R}{R_2}\right) \right]}. \quad (\text{C.4})$$

The effect of leadwire resistance on the bridge nonlinearity can be neglected, because the leadwire resistance was only 0.07 % of the gauge resistance [78]. A correction for

the strain output due to thermal effects can then be applied as follows [76],

$$\epsilon''' = \left[ \epsilon'' - (\epsilon_{T/0} + \Delta\epsilon_{T/0}) \frac{2}{F_G} \right] \frac{1}{1 + \frac{\Delta F_G}{100} \Delta T_{\text{room}}}, \quad (\text{C.5})$$

where  $\Delta F_G$  is the variation in gauge factor with temperature (specified as a percentage per 100 °C by the manufacturer),  $\Delta T_{\text{room}}$  is the difference between the testing temperature and room temperature (75 °F / 24 °C),  $\epsilon_{T/0}$  is the thermal output of the gauge relative to the thermal output at the temperature for which the strain indicator is zeroed, and  $\Delta\epsilon_{T/0}$  is a correction to the thermal output due to the surface curvature of the installation location [67],

$$\Delta\epsilon_{T/0} = \frac{1}{r} [(1 + 2v_{A-B}) (h_A\alpha_A + h_B\alpha_B) - 2v_{A-B}\alpha_S (h_A + h_B)] \Delta T_{\text{ref}}, \quad (\text{C.6})$$

where  $r$  is the radius of curvature,  $\alpha_S$ ,  $\alpha_A$ , and  $\alpha_B$  are the coefficient of thermal expansion of the specimen, adhesive, and backing, respectively,  $h_A$  and  $h_B$  are the thickness of the adhesive and backing, respectively,  $v_{A-B}$  is the average Poisson's ratio of the adhesive and backing, and  $\Delta T_{\text{ref}}$  is the difference between the testing temperature and the temperature at which the strain indicator is zeroed. The uncertainty of the measured variables is summarized in Table C.6. The uncertainty in the corrected strains  $\epsilon''$  and  $\epsilon'''$  was calculated using Eq. (3.84) and is shown in Fig. C.2 as a function of the strain level. The required partial derivatives were determined using the commercial symbolic software Maple (<http://www.maplesoft.com/products/Maple/>).

<sup>15</sup>from the multimeter data sheet (Agilent 34410A) and Eqs. (3.85)–(3.87)

<sup>16</sup>from Section C.1 and Eq. (3.84)

<sup>17</sup>from [48]

<sup>18</sup>from the manufacturer

<sup>19</sup>from Section C.1

<sup>20</sup>from the strain conditioner data sheet (Vishay 2310) and Eqs. (3.85)–(3.87)

Table C.6: Uncertainty of measured variables used to calculate the strain uncertainty.

$u_{\delta R}$ $\pm 0.11 \, \Omega$ <sup>15</sup>	$u_{R_2}$ $\pm 0.08 \, \Omega$ <sup>15</sup>	$u_r$ $\pm 6.5 \times 10^{-6} \, \text{m}$ <sup>16</sup>	$u_{\alpha_S}$ $\pm 0.4 \times 10^{-6} \, 1/^{\circ}\text{C}$ <sup>17</sup>
$u_{F_G}$ $\pm 0.5 \, \% \, (0.0108)$ <sup>18</sup>	$u_{\Delta F_G}$ $\pm 0.2 \, \%$ <sup>18</sup>	$u_T$ $\pm 2 \, ^{\circ}\text{C}$ <sup>19</sup>	$u_{\Delta T}$ $\pm 2.8 \, ^{\circ}\text{C}$ <sup>19</sup>
$u_{\Delta E_0}$ $\pm 1.06 \times 10^{-5} \, \text{V}$ <sup>20</sup>	$u_E$ $\pm 0.0034 \, \text{V}$ <sup>20</sup>		

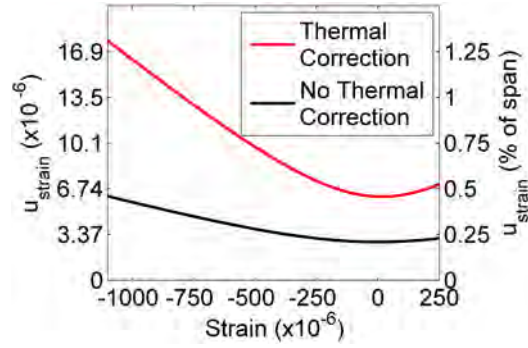


Figure C.2: Uncertainty in the strain calculation.

During repeated testing, temperature increases above the  $25 \, ^{\circ}\text{C}$  ambient were typically 3 to  $4 \, ^{\circ}\text{C}$ , and no more than  $7 \, ^{\circ}\text{C}$ . Using Eqs. (C.5) and (C.6) and specifications for the strain gauge, these 4 and  $7 \, ^{\circ}\text{C}$  changes caused a thermal strain output of  $7.31 \times 10^{-6}$  and  $10.4 \times 10^{-6}$  (0.54 and 0.77 % of the span), respectively. The thermal strain can be corrected for, but at the expense of an appreciable increase in uncertainty. Since the strain uncertainty is exacerbated in the calculation of elastic properties, the thermal strain was not corrected for in the reported data.

## Magnetic field

A magnetic field sensor was needed to measure the axial, surface magnetic field in the gauge region of the rod. The applied magnetic field was in the range -18 to 18 kA/m (-226 to 226 Oe). The recommended accuracy of magnetic field sensors is  $\pm 1\%$  [6]. Magnetic fields can be measured with H coils, Flip H coils, Rogowski coils, giant magnetoresistive (GMR) sensors, and Hall effect sensors. The pick-up coils can only estimate the field at the surface of the specimen based on multiple measurements away from the surface. GMR sensors have an insufficient range ( $\leq 8$  kA/m) and about 5 % uncertainty. Hall probes provide the best accuracy, but must be located using a fixture and have a sensing region about 1.5 to 4 mm (0.059 to 0.160 in) from their tip. Hall chips are less accurate than Hall probes, but can be directly mounted to the specimen's surface, and have a sensing region only 0.3 to 1.5 mm (0.012 to 0.059 in) from their surface. Consequently, an Allegro A1321LUA Hall chip was selected, which could measure  $\pm 35$  kA/m over the temperature range -40 to 150 °C.

The selected Hall chip has an interpolation uncertainty of 0.0208 V and an instrument uncertainty (in units of V) of

$$u_{c\text{Hall}} = \pm 9.425 (10^{-4}) H, \quad (\text{C.7})$$

where the magnetic field  $H$  is in units of kA/m (assuming isothermal conditions and a constant supply voltage). The uncertainty in the magnetic field was calculated using these uncertainties, Eqs. (3.84) and (3.85), the Hall chip's sensitivity ( $\text{Sens}_{\text{Hall}}$ , V-m/kA) and uncertainty ( $\pm 5\%$ ), and the expression for the magnetic field,

$$H = \frac{V_{\text{Hall}}}{\text{Sens}_{\text{Hall}}}. \quad (\text{C.8})$$

The primary source of uncertainty in the calculated field was the uncertainty in the sensitivity. Through calibration (see Section C.2), the uncertainty in the sensitivity could be reduced below  $\pm 1\%$  (Fig. C.3a). The magnetic field uncertainty with and without an point calibration is shown in Fig. C.3b.

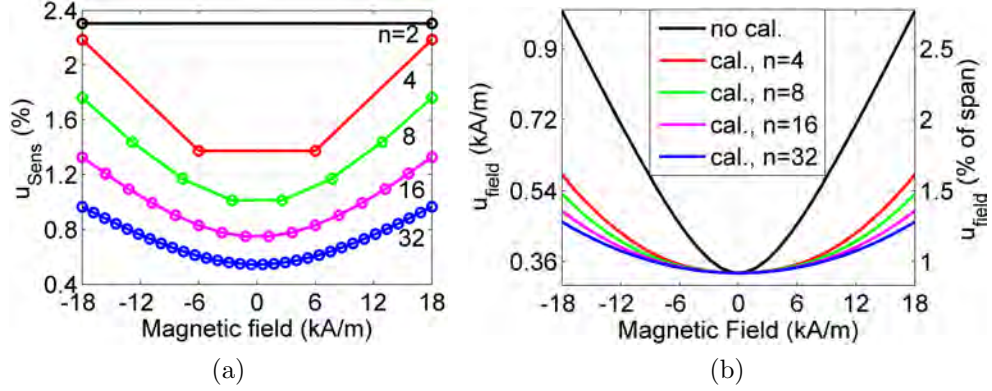


Figure C.3: Uncertainty in (a) the Hall chip's sensitivity and (b) the magnetic field calculation after an  $n$  point calibration of the sensitivity; see [129] for the calculation of the uncertainty in the sensitivity.

## Magnetic flux density

The intent of this sensor was to measure the average magnetic flux density within the gauge region of the rod. The range of magnetic flux density was -1.65 to 1.65 T. For magnetic flux density measurements, it is recommended that (a) sensors have  $\leq 1\%$  of span accuracy, (b) sensing/pick-up coil voltage integrators have drift adjust circuitry with drift  $\leq 100$  Mx-turns/min ( $1 \mu\text{Wb}$ -turns/min), and (c) the cross-sectional area enclosed by the pick-up coil and its number of turns be known to  $\leq 0.5\%$  accuracy [6]. As detailed earlier in Section C.1, the uncertainty in the area was  $0.4\%$ .

Integration of the pick-up coil voltage is the preferred method of measuring magnetic flux (over ballistic galvanometers and moving coil fluxmeters), because of the integrator's superior accuracy, stability, and ease of operation [6]. Consequently, a Lake Shore Model 480 integrating fluxmeter was used with a custom pick-up coil. The integrator drift of this fluxmeter is  $\pm 1 \mu\text{Vs}/\text{min}$  ( $\pm 1 \mu\text{Wb-turns}/\text{min}$ ), while its accuracy is  $\pm (1 \% \text{ of the reading} + 0.33 \% \text{ of the range})$ . Using a calibrated pick-up coil (see Section C.2), the uncertainty in the magnetic flux density is shown in Fig. C.4. Due to the sensitivity of the pick-up coil and the magnitude of the signal, the signal was only about 15 % of the optimal fluxmeter range; thus, the range-dependent uncertainty was about 1.4 % of the signal's span.

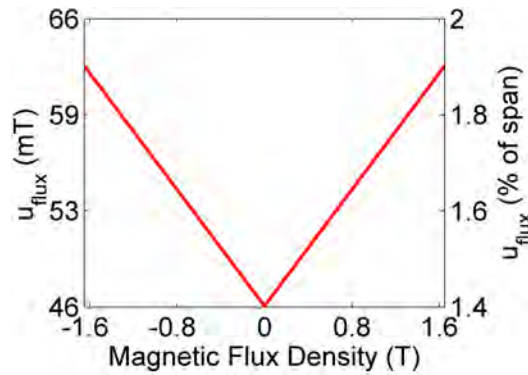


Figure C.4: Uncertainty in the magnetic flux density.

## C.2 Calibration Methods

This section describes the methods and experimental setups used to calibrate each of the sensors and the linear power amplifier used to drive the excitation coils.

## Linear power amplifier

A power amplifier was used to drive the excitation coils of the magnetic circuit and produce a magnetic field. For this experiment, a Kepco BOP 72-6M linear amplifier was selected based on its availability. The amplifier was operated in current control mode, so that the excitation coils produced magnetic fields proportional to the amplifier's input signal, where the proportionality factor is a function of the stress- and field-dependent magnetic permeability of the Galfenol rod.

The experimental setup for the calibration of the Kepco amplifier is shown in Fig. C.5. Static control voltages were used to generate static currents in the load. The current output was calculated by measuring the voltage across a purely resistive load using an Agilent 34410A precision multimeter, which was calibrated by the NASA GRC Metrology and Calibration Lab within the previous year. The load resistance was measured at room temperature by the 4-wire method using the Agilent 34410A multimeter. The load was formed by 4 high power resistors placed on a thick aluminum plate to minimize temperature changes, which cause resistance changes. The current and voltage monitors were calibrated using a linear, least-squares regression as shown in Fig. C.6.

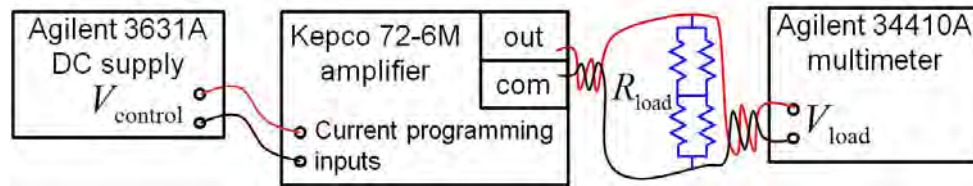


Figure C.5: Experimental setup for the calibration of the linear power amplifier.



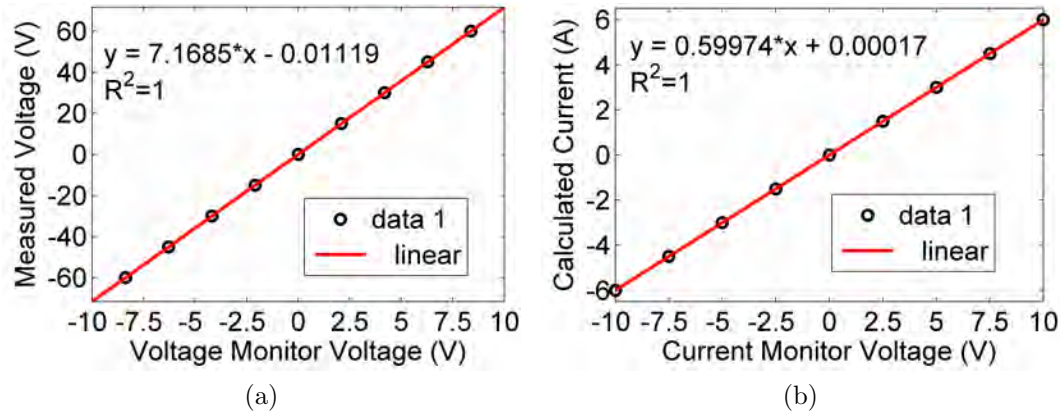


Figure C.6: Calibration of the linear power amplifier: (a) voltage monitor, (b) current monitor.

## Load cell

The Interface load cell, its conditioning electronics, and its data acquisition channel were calibrated according to ASTM E4 [14] by Absolute Calibration & Consulting Services, LLC within the previous year.

## Load washer

The Kistler load washer and charge amplifier were calibrated together using the setup shown in Fig. C.7. Since the load washer cannot measure static forces, calibration was conducted quasi-statically at 10 Hz. To verify that 10 Hz was within the passband of the load washer system, the calibration was repeated for a 40 Hz force; results were within 0.2 % of the 10 Hz calibration. The calibration factor was determined by comparing the magnitude of the primary harmonic (located at 10 Hz) of the load washer and load cell signals (Fig. C.8). The signals were measured at the same time with the same sampling rate and duration.

This calibration assumed that (a) the inertial force error in the Interface load cell measurement was negligible at the calibration frequency of 10 Hz and (b) the resulting load washer calibration factors were constant throughout the operating frequency range (up to 1 kHz). Using Eq. (3.88), the stiffness of the Interface load cell (1 GN/m), and the mass of the steel platen, the inertial force error at 40 Hz was 0.0067 %. The unloaded 1st natural frequency  $\omega_1^1$  of the load washer is 65 kHz ( $m_1 = 0.003$  kg). The decrease in the 1st natural frequency due to added mass was approximated using

$$\omega_1^2 = \omega_1^1 \sqrt{\frac{m_1}{m_2}}, \quad (\text{C.9})$$

where  $m_2 > m_1$ . Using a conservative estimate for the effective mass during calibration,  $m_2 = 2$  kg, the natural frequency reduced to 2.5 kHz, which was well above the frequency range of interest. This suggested that the calibration factor measured at 10 Hz should be valid up to 1 kHz.

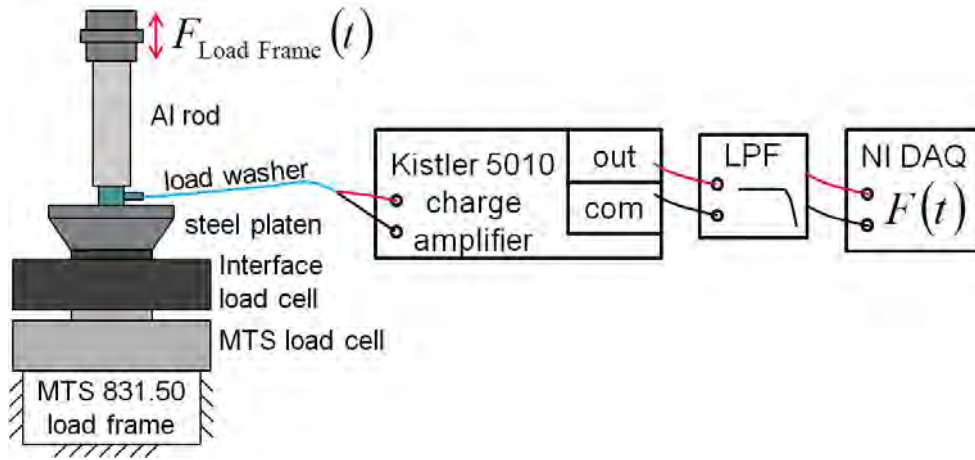


Figure C.7: Experimental setup for the calibration of the Kistler load washer and charge amplifier (schematic not to scale).

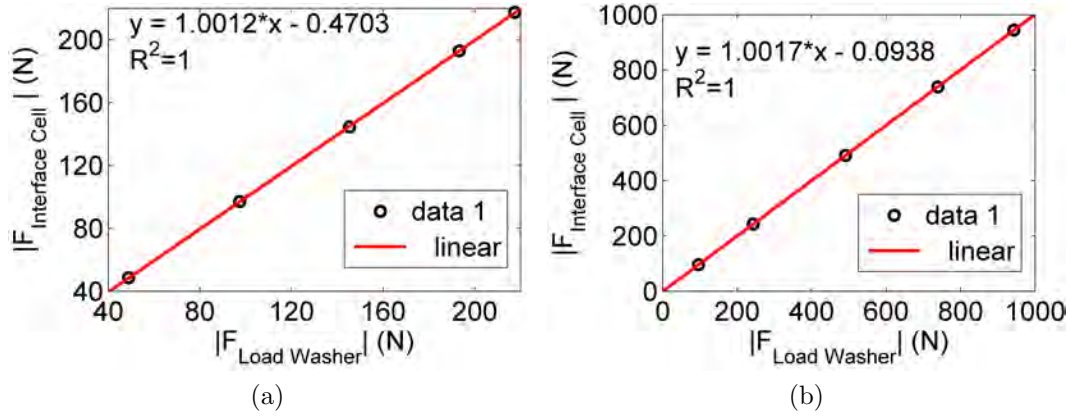


Figure C.8: Calibration of the Kistler load washer and charge amplifier for a 10 Hz force: (a) 0 to 500 N range (250 N offset, 3.72 pC/N load washer sensitivity), (b) 0 to 2000 N range (1000 N offset, 3.87 pC/N load washer sensitivity); each data point is the average of the results from six time captures.

## Thermocouple

The thermocouple signal conditioner was calibrated from 0 to 100 °C using a Wahl C-65 thermocouple calibration standard, which can output the precise voltage that would be generated by a Type K thermocouple at a specified temperature. During calibration, this voltage was the source for the thermocouple measurement system (Fig. C.9). The calibration is shown in Fig. C.10. The calibration was validated by measuring the temperature of boiling water and ice water baths using the Wahl calibration standard and the thermocouple measurement system (Table C.7).

## Strain gauge

The strain measurement system was shunt calibrated using the experimental setup depicted in Fig. C.11, where the pair of strain gauges is represented by a single, effective gauge of double the resistance (see Section C.1). The axial strain  $\epsilon_{\text{axial, simulated}}$

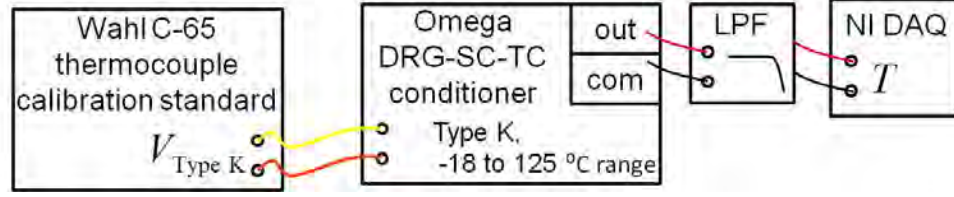


Figure C.9: Experimental setup for the thermocouple calibration.

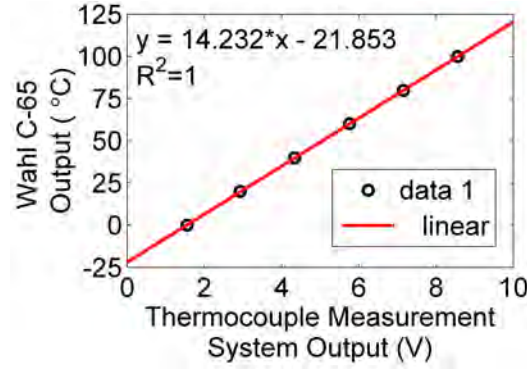


Figure C.10: Calibration of the thermocouple.

simulated by shunting the effective gauge with a shunt resistor  $R_C$  at its terminals was found by calculating the change in resistance of the shunted arm of the Wheatstone bridge and using the definition of the gauge factor,

$$\epsilon_{\text{axial, simulated}} = \frac{-2R_G}{F_G (2R_G + R_C)}. \quad (\text{C.10})$$

For a Wheatstone quarter bridge, Eq. (C.10) is exact for any strain level [78]. For the circuit in Fig. C.11, the simulated strain was  $-1952.5 \times 10^{-6}$ . The shunt calibration is given in Fig. C.12. This 2-point calibration accurately scaled the strain measurement system. Instrument verification using a strain calibrator was not performed.

Table C.7: Temperature measurement of boiling water and ice water baths after calibration; tabulated values are an average of measurements obtained on two days.

	Wahl calibration standard, °C	Thermocouple measurement system, °C
ice water bath	0.2	0.7
boiling water bath	99.7	99.8

The strain gauges on the laminated rod were found to have a calibration factor of  $-214.47 \mu\text{m}/\text{m}/\text{V}$ .

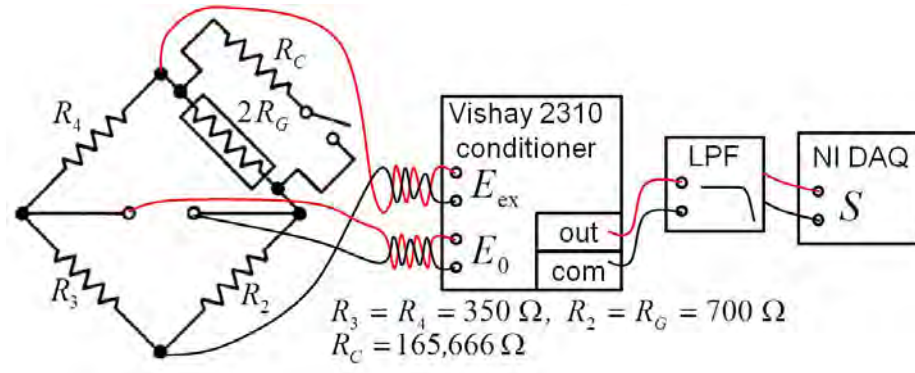


Figure C.11: Experimental setup for the strain calibration.

### Hall effect sensor

The Hall effect sensor was calibrated by relating the Hall chip's output voltage to the magnetic field measured by a F.W. Bell 4048 gaussmeter and F.W. Bell 1435 Hall probe, which were calibrated by the manufacturer. The sensors were placed in the center of a uniform magnetic field that was generated by a Harvey-Wells Corporation electromagnet (Fig. C.13). The electromagnet's poles have a diameter of 12 in (about

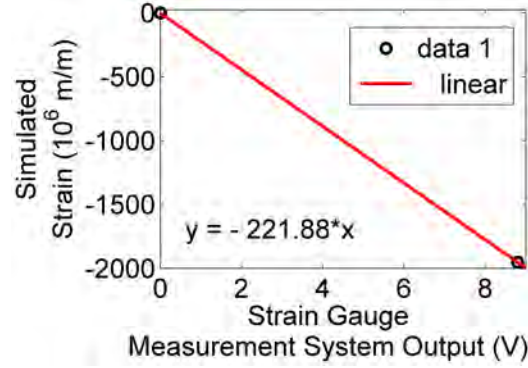


Figure C.12: Calibration of the strain measurement system.

2 orders of magnitude larger than each sensor's active area); thus, fringing of the magnetic field was negligible. Each sensor was independently rotated in the field until a maximum output was reached. Maximum outputs were recorded for 30 different static magnetic fields. The calibration results are shown in Fig. C.14.

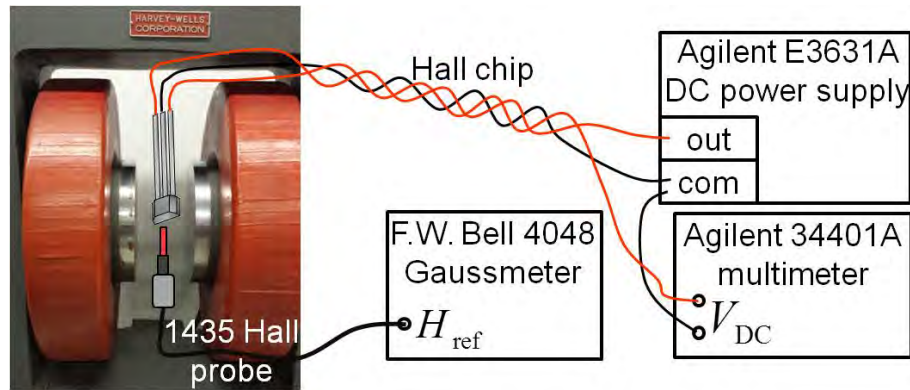


Figure C.13: Experimental setup for the Hall effect sensor calibration (sensors not to scale); the Hall chip supply voltage was 5.000 V.

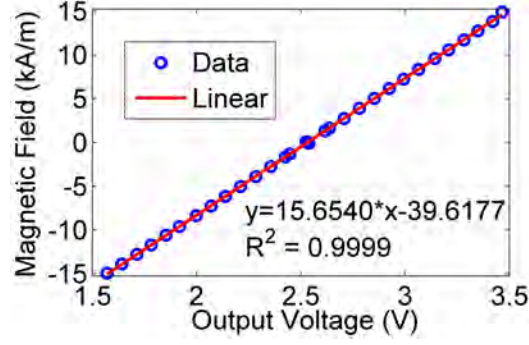


Figure C.14: 30 point calibration of the Hall effect sensor.

### Magnetic flux density sensing coil

Magnetic flux density sensing coils can be calibrated using a reference magnet or known magnetic field (e.g., a field produced by a calibrated Helmholtz coil). In the absence of these instruments, calibration can be performed by measuring the magnetic response of a specimen for which an accurate measurement is available. In this experiment, calibration was conducted by measuring the magnetic response of a commercially-pure nickel (Ni 200) rod having the same dimensions as the Galfenol specimen (Fig. C.15). The previously calibrated Hall chip was used to measure the applied magnetic field. The measured response was then compared to accurate measurements published by [139], as shown in Fig. C.16. The calibration factor was determined as the factor that provided the closest fit (in a least-squares sense) of the measured response to the reference response.

In the laminated rod, the presence of adhesive layers reduces the cross-sectional area of Galfenol and thus the total flux linked by the sensing coil, which decreases the induced voltage in the coil. Consequently, if the calibration factor for the solid rod,  $C_{\text{solid}}^B$ , was used with the laminated rod, magnetic flux density measurements would



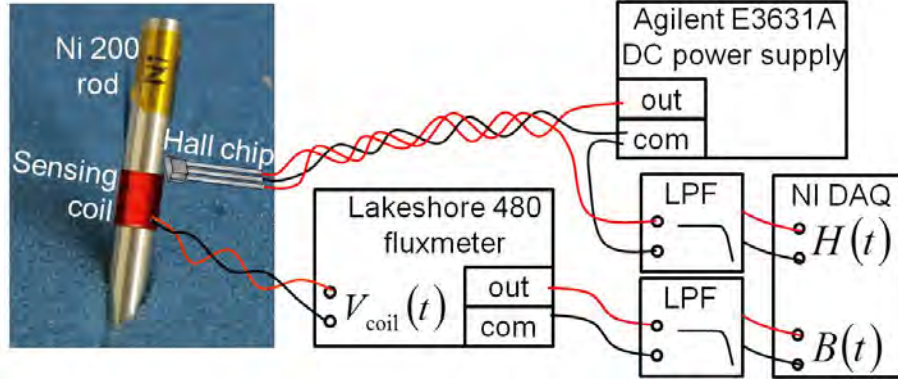


Figure C.15: Experimental setup for the calibration of the magnetic flux density sensing coil and fluxmeter; the magnetic circuit shown in Figs. 3.16 and 3.17 was used to magnetize the Ni 200 rod.

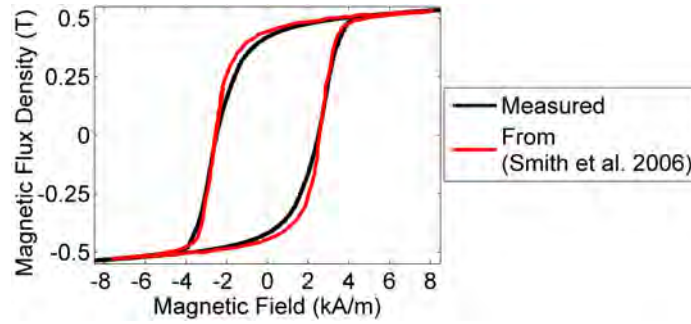


Figure C.16: Calibration of the magnetic flux density measurement system, 4.673 T/V calibration factor (30 mVs fluxmeter range).

be artificially low. A corrected calibration factor,  $C_{\text{laminated}}^B$ , was calculated as

$$C_{\text{laminated}}^B = C_{\text{solid}}^B A_{\text{solid}}^{\text{FeGa}} (A_{\text{laminated}}^{\text{FeGa}})^{-1}, \quad (\text{C.11})$$

where  $A_{\text{solid}}^{\text{FeGa}}$  and  $A_{\text{laminated}}^{\text{FeGa}}$  are the cross-sectional areas of Galfenol in the solid and laminated rods, respectively. The thickness of the adhesive layers was given by the manufacturer as 0.0018 to 0.002 in. Using an adhesive thickness of 0.0019 in, the



lamination thickness (0.033 in), and the rod's diameter (0.247 in), the corrected calibration factor for the laminated rod was calculated as 4.936 T/V.

## **C.3 Experimental Setup and Methods**

### **C.3.1 Wiring**

Fig. C.17 is a schematic representing the wiring for all of the measurement channels. This includes the interconnection between the sensors, signal conditioning, and data acquisition electronics, as well as grounding information. Noise was minimized by eliminating ground loops, through the use of shielded wire, and by separating the power and signal wires.

### **C.3.2 Magnetic field control**

When the current in the electromagnet is held constant while the magnetostrictive sample is stressed, the magnetic field in the sample changes due to its stress-dependent magnetic permeability [22]. In Galfenol, this effect is significant, because its magnetic permeability is a strongly nonlinear function of stress; Galfenol's magnetic permeability can vary by almost three orders of magnitude [53]. The variation in magnetic field with the applied stress confounds the measured results, and so a feedback control system was used to adjust the current to achieve a more constant field. Magnetic field control was implemented in addition to constant current control, rather than as a replacement for it, because constant current control could be realized over a greater bandwidth.

The control system is schematically illustrated in Fig. C.18, for the case of a PID-type control law. A dSPACE DS1103 board was used to implement real-time control. Feedback was provided by the hall sensor, and the controller's output drove



specimen. Initially, the D gain was set to zero due to the relatively noisy magnetic field signal. To reduce the noise, an analog low-pass filter was inserted in the feedback loop. This allowed for the derivative term to be used, but that provided a negligible improvement in the control performance. Therefore, the D term was set to zero (effectively PI control) and the filter was removed to reduce the time delay of the control system. For dynamic sensing experiments, one set of gains ( $P=2$ ,  $I=100$ ) was used for frequencies  $\leq 600$  Hz and another set ( $P=0.5$ ,  $I=100$ ) for frequencies  $> 600$  Hz in order to provide adequate control over the range of forcing frequencies. To improve control performance, the sampling rate of the dSPACE system was maximized. The maximum rate was 150 kHz. The control system performed well up to 100 Hz, but the performance considerably degraded above 200 Hz.

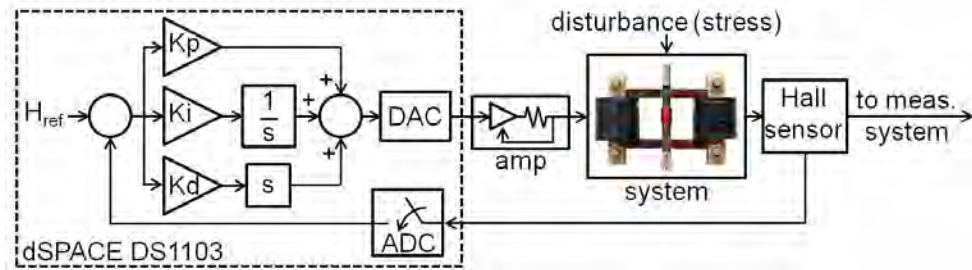


Figure C.18: Schematic of the magnetic field control system, which was independent of the measurement system and thus only included the signal conditioning depicted here.

Sliding mode and lookup table methods of control were briefly evaluated as alternatives to PID. It was found that the sliding mode control performed comparably; however, sliding mode control required larger voltages than for PID control. As frequency was increased, the required switching voltages exceeded the capabilities of

the amplifier. To implement lookup table control, the relationship between current, stress, and magnetic field was measured. For each operating frequency, the data was catalogued in a table through a series of measurements with constant applied current and varying stress. The appropriate control output was then based on referencing the table to find the required output current to achieve a constant field for the given operating frequency and the measured stress level. This control method was not successfully implemented, because it required too many measurements to produce a lookup table of sufficient resolution. In addition, the control processor could not access the table values fast enough to implement this method in real time at high frequency. Given the limitations of sliding mode and lookup table control, PI control was used for all characterization tests where constant field was desired.

### **C.3.3 Sensor reset**

The zero offset of the magnetic field, temperature, voltage, and current sensors was quantified during sensor calibration. However, the output of magnetic flux density and strain sensors had to be periodically reset during testing due to thermally-induced drift. The reference state at which these sensors were zeroed was well defined and consistent throughout testing, as detailed below.

Drift in the magnetic flux density measurement was minimized through manual and automatic adjustment of the fluxmeter's drift correction circuitry. Additionally, the fluxmeter integrator was manually reset about every minute to avoid appreciable drift error. Typically, the integrator is reset when the magnetostrictive material is in a zero flux state. In this work, a faster, alternative method was used due to the extensive testing matrix. First, the fluxmeter was reset using the conventional

method. Then, the quasi-static sensing response of the Galfenol rod was measured for a single constant current (or magnetic field) level. Next, a point in the saturated region of the response was selected and the corresponding flux density, stress, and current (or field) was recorded. Finally, when a reset was needed, the stress and current (or field) were held constant at the recorded values while the integrator was reset. The fluxmeter then output the flux density relative to the recorded value. Since the recorded point was in the saturation region and Galfenol exhibits a high degree of kinematic reversibility (see the *Solid rod: major stress-strain loops under constant field* subsection of Section 2.1.2), the loading history used to reach the recorded stress and current (or field) had a negligible influence. The integrator was reset at  $-50 \pm 1$  N and 1 A (or 15 kA/m), for which the flux density was 1.599 T (or 1.601 T) for the solid Galfenol rod and 1.474 T for the laminated rod. The true flux density was calculated in post processing by adding the recorded value to the measured flux.

To minimize the drift in the strain signal while maintaining an appropriate signal-to-noise ratio, a Wheatstone bridge excitation of 7 V was used. This excitation was only about 40 % of the estimated maximum excitation voltage, which was calculated according to [74]. First, a saturating magnetic field was established, then the field was reduced to zero. The strain signal was then zeroed at zero applied current (or magnetic field) after disengaging the load frame piston from the specimen. Due to hysteresis, the strain in Galfenol at this state was not zero, but rather  $0.6 \times 10^{-6}$  (determined from actuation measurements). Thus, all strain signals were reduced by this value in post processing.

## **C.4 Data Processing Methods**

### **C.4.1 Amplitude calibration**

Figs. C.19 and C.20 show the so-called signal flow diagram, which represents how each sensor signal was scaled during acquisition. The green section of the diagram shows how the signals were modified by the sensors and electronics, while the blue section shows the calibration factors applied to restore the physical meaning of the signals. Phase correction of the signals was handled in post-processing, as explained in the following section.

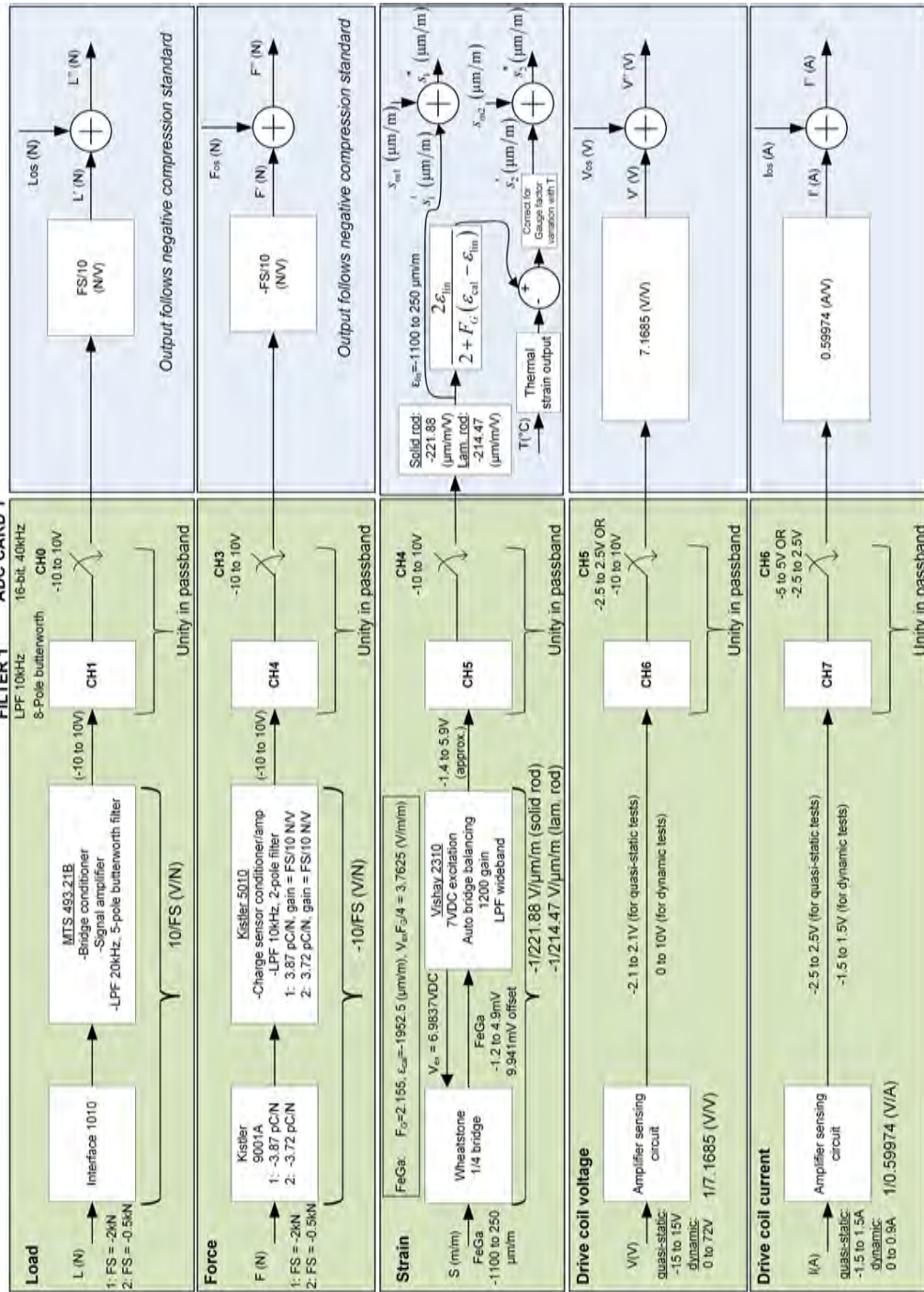


Figure C.19: Signal flow diagram 1 of 2.

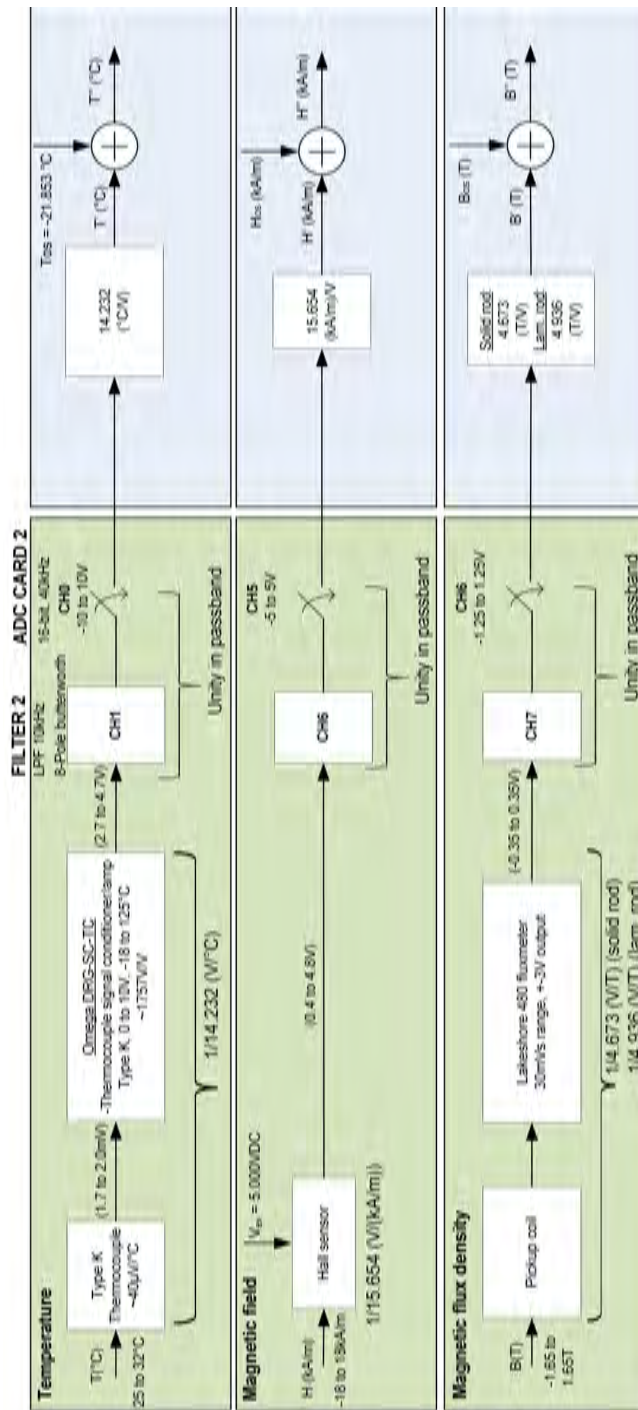


Figure C.20: Signal flow diagram 2 of 2.



### C.4.2 Filtering

Filtering was performed during post-processing to reduce noise. Filtering was implemented using MATLAB's *filtfilt* function combined with a digital Butterworth low-pass filter having a passband ripple of 0.0043 dB (0.1 % after forwards and reverse filtering). This filtering introduced zero phase distortion. Selection of the passband cutoff frequency was guided by DFTs of the response variables (strain and magnetic flux density). The forcing frequency and the level of nonlinearity in the response were different for each group of measurements; thus, a different cutoff frequency was used for each group, as discussed below.

A DFT of the magnetic flux density and strain actuation responses is shown in Fig. C.21a for a representative bias stress (-10.23 MPa). The fundamental frequency is 0.1 Hz. For the measured actuation responses, a 10 Hz cutoff was chosen to preserve the appreciable harmonics and attenuate 60 Hz noise, which was present, but small in magnitude. The actuation strain responses exhibit more nonlinearity than the actuation flux density responses. Thus, to illustrate the effect of the filter, the filtered and unfiltered actuation strain (magnetostriction) responses are compared in Fig. C.21b; the filtered magnetostriction response for the representative case retains the full nonlinearity of the unfiltered response.

Fig. C.22a presents a DFT of the quasi-static (1 Hz), major loop sensing response measured at a constant current of 0.60 A. For quasi-static constant current responses, a 25 Hz low-pass cutoff frequency was selected, because it attenuated noise while preserving the integrity of the signals, as evidenced by the comparison of filtered and unfiltered flux density responses in Fig. C.22b. Flux density responses are shown

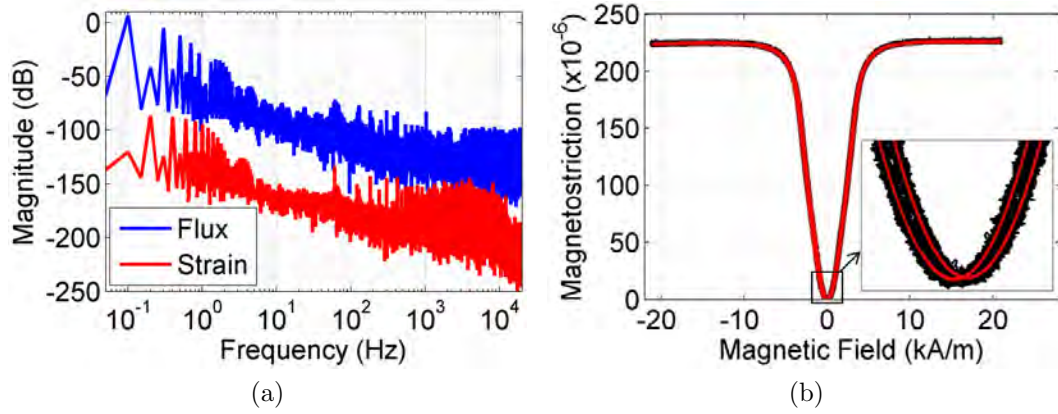


Figure C.21: (a) DFT of the unfiltered actuation response of the solid Galfenol rod for a mean bias stress of -10.23 MPa, (b) comparison of the filtered (red) and unfiltered (black) magnetostriction responses at -10.23 MPa.

rather than strain responses, because for sensing, the flux density responses are more nonlinear.

Since the quasi-static (1 Hz) sensing response for constant magnetic field is steeper and more nonlinear than for constant current, a larger number of harmonics are appreciable for constant field responses. Thus, a higher low-pass cutoff frequency was required. A 40 Hz cutoff was found to be sufficient, as illustrated by the DFT and comparison of filtered and unfiltered flux density responses in Fig. C.23.

For dynamic sensing measurements, the forcing frequency was varied between 4 and 1000 Hz. In general, as frequency is increased, the sensing response becomes more linear due to an increase in eddy currents, which tend to suppress the active behavior of the material. DFTs of the dynamic major loop responses indicate that low-pass filtering must preserve about 20 harmonics for forcing frequencies up to about 100 Hz, but only 5 to 10 harmonics for frequencies above that. Considering

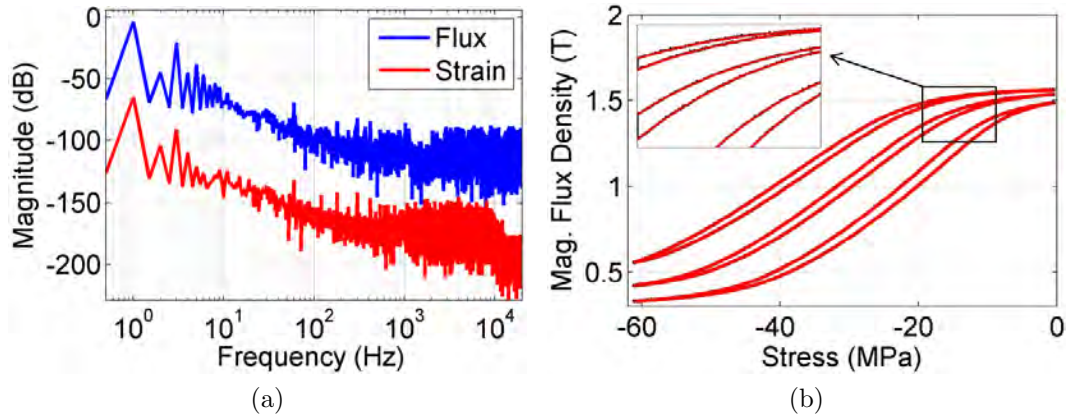


Figure C.22: (a) DFT of the unfiltered sensing response of the solid Galfenol rod for a mean bias current of 0.60 A, (b) comparison of the filtered (red) and unfiltered (black) flux density responses at 0.50, 0.60, and 0.70 A.

this result and the fact that a 10 kHz analog low-pass filter had already been used (see Figs. C.19 and C.20), only measurements for forcing frequencies up to 50 Hz were digitally filtered (using a cutoff at the 20th harmonic). Despite this, the signal-to-noise ratio of the unfiltered, high frequency signals is sufficient, and the majority of the perceived variation in the responses is due to small variations in the force and current (or field) resulting from imperfect control of these variables.

### C.4.3 Evaluation of reversibility in the constitutive response

According to prior measurements of Galfenol, the material shows a very high degree of kinematic reversibility (i.e., the order of application of stress and magnetic field does not matter) [65, 154]. To provide confidence in the experimental setup and reported measurements, kinematic reversibility of the solid Galfenol rod was investigated. To enable this investigation, the actuation response of the solid rod was measured in addition to the sensing response. Reversibility was evaluated by

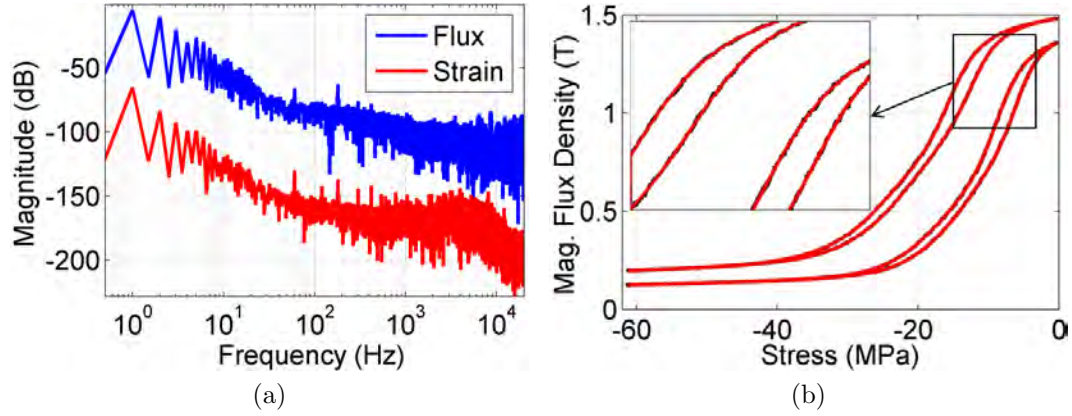


Figure C.23: (a) DFT of the unfiltered sensing response of the solid Galfenol rod for a mean bias field of 3.88 kA/m, (b) comparison of the filtered (red) and unfiltered (black) flux density responses at 2.41 and 3.88 kA/m.

comparing each actuation curve measured at a constant stress to discrete points obtained from all of the sensing curves measured at constant field. Actuation points were separately obtained from the upper and lower branches of the sensing curves, thereby generating a hysteretic set of actuation points to compare with each hysteretic actuation curve. For more details, see [65].

## C.5 Procedure

Prior to each set of experiments, all electronics were allowed to warm up for at least 1 hour. For all experiments, the applied load was controlled using PI control. Below, the procedure used to obtain the reported measurements is listed separately for each testing group.

### Quasi-static Actuation:

1. Set up the experiment as shown in Fig. 3.22a

2. Tune the load control gains while magnetically actuating the specimen and attempting to hold the load constant
3. Zero the strain signal according to Section C.3.3, if needed
4. Reset the fluxmeter integrator as discussed in Section C.3.3, if needed
5. Apply a 0 A current
6. Apply the bias force
7. Apply the low frequency, AC current
8. Record the amplitude-scaled signals (Section C.4.1) for 20 s
9. Stop the AC current
10. Repeat steps 3 to 9 for the remaining bias forces
11. Shift the strain and flux density signals as discussed in Section C.3.3 to yield the true strain and flux density
12. Digitally filter the measured signals according to Section C.4.2
13. Calculate the stress in the rod from the force using Eq. (C.2)
14. Calculate the actuation-based material properties as discussed in the *Calculation of material properties* subsection of Section 3.2.4
15. Save the manipulated signals and plot the results

Quasi-static Sensing:

1. Set up the experiment as shown in Fig. 3.22a

2. Tune the load control gains to achieve a slightly overdamped response to a 1 Hz square wave command signal
3. Zero the strain signal according to Section C.3.3, if needed
4. Reset the fluxmeter integrator as discussed in Section C.3.3, if needed
5. Apply the bias current (or field)
6. Apply the bias force
  - (a) for a given bias current (or field), start with the major loop then proceed to its corresponding minor loops
7. Apply the low frequency, dynamic force
8. Record the amplitude-scaled signals (Section C.4.1) for 2 s (major loop responses) or 1 s minor loop responses)
9. Stop the dynamic force
10. Repeat steps 3 to 9 for the next bias force
11. Repeat steps 3 to 10 for the remaining bias currents (or fields)
12. Shift the strain and flux density signals as discussed in Section C.3.3 to yield the true strain and flux density
13. Digitally filter the measured signals according to Section C.4.2
14. Calculate the stress in the rod from the force using Eq. (C.2)

15. Calculate the sensing-based material properties as discussed in the *Calculation of material properties* subsection of Section 3.2.4
16. Save the manipulated signals and plot the results

Dynamic Sensing:

1. Set up the experiment as shown in Fig. 3.22b
2. Tune the load control gains to achieve a fully overdamped response to a 1 Hz square wave command signal
3. Zero the strain signal according to Section C.3.3, if needed
4. Reset the fluxmeter integrator as discussed in Section C.3.3, if needed
5. Apply the bias current (or field)
6. Apply the bias force
7. Apply the high frequency, dynamic force
8. Activate an amplitude-phase compensator (APC) for the load control, allow it to stabilize, then pause the APC
9. Record the amplitude-scaled signals (Section C.4.1) for 2 s
10. Stop the dynamic force
11. Repeat steps 3 to 10 for the next forcing frequency or loading type
12. Shift the strain and flux density signals as discussed in Section C.3.3 to yield the true strain and flux density

13. Phase align the signals as discussed in the *Phase calibration* subsection of Section 3.2.4
14. Digitally filter the measured signals according to Section C.4.2
15. Calculate the stress in the rod from the force using Eq. (C.2)
16. Calculate the sensing-based material properties as discussed in the *Calculation of material properties* subsection of Section 3.2.4
17. Save the manipulated signals and plot the results

Table C.8 is a matrix of the nominal testing conditions for each measurement. Exact bias conditions are stated in Sections 2.1.2 and 3.2.5. The stress range in this experiment was approximately -63 MPa to 0 MPa. For major loops, it was desired to excite the Galfenol specimen over this entire range while ensuring that compression of the specimen was maintained. Consequently, a stress bias of -31.9 MPa and amplitude of 31.4 MPa were chosen for major loops. For the dynamic minor loops, the bias conditions were those for which the quasi-static magnetomechanical coupling of the solid rod was maximized (i.e., maximum sensitivity and minimum elastic modulus). To allow for a comparison of dynamic major and minor loops, dynamic major loops were measured at the same bias current and field used for dynamic minor loops. An extra group of dynamic major loops was measured at a high constant current to compare with dynamic major loops at a low current; this allowed for the effect of forcing frequency on positive and negative saturation to be determined.



Table C.8: Matrix of testing conditions for actuation, quasi-static sensing, and dynamic sensing experiments.

Testing group	Rod type	Magnetic	Loading type Mechanical	Load / stress, N Static	Dynamic	Frequency, Hz	Current, A	Field, kA/m
actuation	solid	major loop	const. force	Note 1	—	0.1	1.5 A amplitude	—
quasi-static	solid	const. current	major loop	-985 (-31.9)	970 (31.4)	1	Note 2	—
		const. current	minor loop	Note 3	89 (2.88)	4	—	—
		const. field	major loop	-985 (-31.9)	970 (31.4)	1	—	Note 4
		const. field	minor loop	Note 3	89 (2.88)	4	—	—
dynamic	laminated	const. current	major loop	-985 (-31.9)	970 (31.4)	1	Note 2	—
	solid	const. current	major loop	-985 (-31.9)	970 (31.4)	4, 10, 20, 30, 40, 50, 60,	0.3	—
		const. current	minor loop	-307 (-9.93)	89 (2.88)	70, 80, 90,	0.8	—
		const. field	major loop	-985 (-31.9)	970 (31.4)	100, 200, 300,	—	2.5
		const. field	minor loop	-246 (-7.96)	89 (2.88)	400, 500, 600,	—	—
	laminated	const. current	major loop	-985 (-31.9)	970 (31.4)	700, 800, 900,	0.3	—
		const. current	minor loop	-307 (-9.93)	89 (2.88)	and 1000	—	—

### Notes for Table C.8

1. 0, -50, -317, -633, -950, -1267, -1584, and -1900 N (0, -1.62, -10.3, -20.5, -30.7, -40.9, -51.2, and -61.5 MPa)
2. 0, 0.1, 0.2, 0.3, 0.4, 0.5, 0.6, 0.7, 0.8, 0.9, and 1 A
3. -177, -399, -621, -842, -1064, and -1286 N (-5.73, -12.9, -20.1, -27.2, -34.4, and -41.6 MPa)
4. 0, 0.8, 1.5, 2.5, 4, 5.6, 7.3, 9, 10.7, 12.4, and 14 kA/m (the approximate fields at zero stress for each of the constant current levels)

## Bibliography

- [1] B.D. Agarwal, L.J. Broutman, and K. Chandrashekhara. *Analysis and performance of fiber composites*. John Wiley & Sons, Inc., Hoboken, NJ, 3 edition, 2006.
- [2] P.M. Anderson. Magnetomechanical coupling,  $\Delta E$  effect, and permeability in FeSiB and FeNiMoB alloys. *Journal of Applied Physics*, 53:8101, 1982.
- [3] William D. Armstrong. An incremental theory of magneto-elastic hysteresis in pseudo-cubic ferro-magnetostrictive alloys. *Journal of Magnetism and Magnetic Materials*, 263:208–218, 2003.
- [4] O.N. Ashour and A.H. Nayfeh. Adaptive control of flexible structures using a nonlinear vibration absorber. *Nonlinear Dynamics*, 28(3):309–322, 2002.
- [5] Nakhlé H. Asmar. *Partial differential equations and boundary value problems with Fourier series and boundary value problems*. Pearson Prentice Hall, Upper Saddle River, NJ, 2nd edition, 2000.
- [6] ASTM Standard A 314/A314M, 2005. Standard test method for direct current magnetic properties of materials using D-C permeameters and the ballistic test methods. ASTM International, West Conshohocken, PA, 2005.
- [7] ASTM Standard D5992, 2011. Standard guide for dynamic testing of vulcanized rubber and rubber-like materials using vibratory methods. ASTM International, West Conshohocken, PA, 2011.
- [8] ASTM Standard E 1875, 2009. Standard test method for dynamic Young's modulus, shear modulus, and Poisson's ratio by sonic resonance. ASTM International, West Conshohocken, PA, 2009.
- [9] ASTM Standard E 1876, 2009. Standard test method for dynamic Young's modulus, shear modulus, and Poisson's ratio by impulse excitation of vibration. ASTM International, West Conshohocken, PA, 2009.

- [10] ASTM Standard E 466, 2007. Standard practice for conducting force controlled constant amplitude axial fatigue tests of metallic materials. ASTM International, West Conshohocken, PA, 2007.
- [11] ASTM Standard E111, 2010. Standard test method for Young's modulus, tangent modulus, and chord modulus. ASTM International, West Conshohocken, PA, 2010.
- [12] ASTM Standard E209, 2010. Standard practice for compression tests of metallic materials at elevated temperatures with conventional or rapid heating rates and strain rates. ASTM International, West Conshohocken, PA, 2010.
- [13] ASTM Standard E251, 2009. Standard test methods for performance characteristics of metallic bonded resistance strain gauges. ASTM International, West Conshohocken, PA, 2009.
- [14] ASTM Standard E4, 2014. Standard practices for force verification of testing machines. ASTM International, West Conshohocken, PA, 2014.
- [15] ASTM Standard E467, 2009. Standard practice for verification of constant amplitude dynamic forces in an axial fatigue testing system. ASTM International, West Conshohocken, PA, 2009.
- [16] ASTM Standard E83, 2010. Standard practice for verification and classification of extensometer systems. ASTM International, West Conshohocken, PA, 2010.
- [17] ASTM Standard E9, 2009. Standard test methods of compression testing of metallic materials at room temperature. ASTM International, West Conshohocken, PA, 2009.
- [18] J. Atulasimha and A.B. Flatau. A review of magnetostrictive iron–gallium alloys. *Smart Materials and Structures*, 20(4):043001, 2011.
- [19] J. Atulasimha, A.B. Flatau, and E. Summers. Characterization and energy-based model of the magnetomechanical behavior of polycrystalline iron–gallium alloys. *Smart Materials and Structures*, 16(4):1265, 2007.
- [20] Jayasimha Atulasimha, George Akhras, and Alison B. Flatau. Comprehensive three dimensional hysteretic magnetomechanical model and its validation with experimental  $\{110\}$  single-crystal iron-gallium behavior. *Journal of Applied Physics*, 103(7):07B336, 2008.
- [21] Jayasimha Atulasimha and Alison B Flatau. Experimental actuation and sensing behavior of single-crystal iron-gallium alloys. *Journal of Intelligent Material Systems and Structures*, 2008.

- [22] Jayasimha Atulasimha, Alison B Flatau, and Rick A Kellogg. Sensing behavior of varied stoichiometry single crystal Fe-Ga. *Journal of Intelligent Material Systems and Structures*, 17(2):97–105, 2006.
- [23] V.I. Babitsky. Autoresonant mechatronic systems. *Mechatronics*, 5(5):483–495, 1995.
- [24] Richard Becker and Werner Döring. *Ferromagnetismus*, volume 1. J. Springer, Berlin, 1939.
- [25] Giorgio Bertotti and Isaak D Mayergoyz, editors. *The Science of Hysteresis: Hysteresis in Materials*, volume 3. Academic Press, Oxford, UK, 2006.
- [26] R.M. Bozorth. *Ferromagnetism*. D. Van Nostrand Co. Inc., Princeton, NJ, 1951.
- [27] F. Braghin, S. Cinquemani, and F. Resta. A model of magnetostrictive actuators for active vibration control. *Sensors and Actuators A: Physical*, 165(2):342–350, 2011.
- [28] Michael D Bryant, Benito Fernandez, Ning Wang, Venkatesh V Murty, Viswanath Vadlamani, and Timothy Scott West. Active vibration control in structures using magnetostrictive Terfenol with feedback and/or neural network controllers. *Journal of Intelligent Material Systems and Structures*, 4(4):484–489, 1993.
- [29] Frederick T Calkins, Marcelo J Dapino, and Alison B Flatau. Effect of prestress on the dynamic performace of a Terfenol-D transducer. In *Proceedings of SPIE 3041*, pages 293–304. International Society for Optics and Photonics, 1997.
- [30] Frederick T Calkins and Alison B Flatau. Transducer-based measurements of Terfenol-D material properties. In *Proceedings of SPIE 2717*, pages 709–719. International Society for Optics and Photonics, 1996.
- [31] T.L. Cedell. *Magnetostrictive Materials and Selected Applications, Magnetically Induced Vibrations in Manufacturing Processes*. PhD thesis, Lund University, Lund, Sweden, 1995.
- [32] S. Chakrabarti. *Modeling of 3D magnetostrictive systems with application to Galfenol and Terfenol-D transducers*. PhD thesis, The Ohio State University, 2011.
- [33] S. Chakrabarti and M.J. Dapino. Nonlinear finite element model for 3D Galfenol systems. *Smart Materials and Structures*, 20(10):105034, 2011.

- [34] S. Chakrabarti and M.J. Dapino. Fully coupled discrete energy-averaged model for Terfenol-D. *Journal of Applied Physics*, 111(5):054505–054505, 2012.
- [35] Suryarghya Chakrabarti and Marcelo J Dapino. A dynamic model for a displacement amplified magnetostrictive driver for active mounts. *Smart Materials and Structures*, 19(5):055009, 2010.
- [36] A.E. Clark, H.S. Belson, and R.E. Strakna. Elastic properties of rare-earth-iron compounds. *Journal of Applied Physics*, 44(6):2913–2914, 1973.
- [37] AE Clark, KB Hathaway, M Wun-Fogle, JB Restorff, Thomas A Lograsso, VM Keppens, G Petculescu, and RA Taylor. Extraordinary magnetoelasticity and lattice softening in bcc Fe-Ga alloys. *Journal of Applied Physics*, 93(10):8621–8623, 2003.
- [38] A.E. Clark, J.B. Restorff, M. Wun-Fogle, and J.F. Lindberg. Magnetoelastic coupling and  $\delta E$  effect in  $Tb_xDy_{1-x}$  single crystals. *Journal of Applied Physics*, 73(10):6150–6152, 1993.
- [39] A.E. Clark and H.T. Savage. Giant magnetically induced changes in the elastic moduli in  $Tb_{0.3}Dy_{0.7}Fe_2$ . *IEEE Transactions on Sonics and Ultrasonics*, 22(50), 1975.
- [40] W.W. Clark. Vibration control with state-switched piezoelectric materials. *Journal of Intelligent Material Systems and Structures*, 11(4):263–271, 2000.
- [41] Marcelo J Dapino, Frederick T Calkins, and Alison B Flatau. Measured Terfenol-D material properties under varied applied magnetic field levels. In *Proceedings of SPIE 2717*, pages 697–708. International Society for Optics and Photonics, 1996.
- [42] Marcelo J. Dapino and Phillip G. Evans. Constitutive modeling for design and control of magnetostrictive Galfenol devices. *Advances in Science and Technology*, 54:13–18, 2009.
- [43] Marcelo J Dapino, Alison B Flatau, and Frederick T Calkins. Statistical analysis of Terfenol-D material properties. *Journal of Intelligent Material Systems and Structures*, 17(7):587–599, 2006.
- [44] Marcelo J Dapino, Ralph C Smith, Frederick T Calkins, and Alison B Flatau. A coupled magnetomechanical model for magnetostrictive transducers and its application to Villari-effect sensors. *Journal of Intelligent Material Systems and Structures*, 13(11):737–747, 2002.

- [45] Marcelo J Dapino, Ralph C Smith, and Alison B Flatau. A model for the  $\delta e$  effect in magnetostrictive transducers. In *Proceedings of SPIE 3985*, pages 174–185, 2000.
- [46] Marcelo J Dapino, Ralph C Smith, and Alison B Flatau. Structural magnetic strain model for magnetostrictive transducers. *IEEE Transactions on Magnetics*, 36(3):545–556, 2000.
- [47] S. Datta, J. Atulasimha, C. Mudivartha, and A.B. Flatau. Stress and magnetic field-dependent Young’s modulus in single crystal iron–gallium alloys. *Journal of Magnetism and Magnetic Materials*, 322(15):2135–2144, 2010.
- [48] S Datta, M Huang, J Raim, T.A. Lograsso, and A.B. Flatau. Effect of thermal history and gallium content on magneto-mechanical properties of iron gallium alloys. *Materials Science and Engineering: A*, 435:221–227, 2006.
- [49] D. Davino, A. Giustiniani, and C. Visone. Effects of hysteresis and eddy currents in magnetostrictive harvesting devices. *Physica B: Condensed Matter*, 407(9):1433–1437, 2012.
- [50] D. Davino, A. Giustiniani, C. Visone, and W. Zamboni. Stress-induced eddy currents in magnetostrictive energy harvesting devices. *IEEE Transactions on Magnetics*, 48(1):18–25, 2012.
- [51] R. De Batist. *Internal friction of structural defects in crystalline solids*. North-Holland Publishing, Amsterdam, Netherlands, 1972.
- [52] C.W. De Silva. *Vibration: Fundamentals and Practice*. CRC Press, Boca Raton, FL, 2nd edition, 2006.
- [53] Zhangxian Deng and Marcelo J Dapino. Characterization and finite element modeling of Galfenol minor flux density loops. *Journal of Intelligent Material Systems and Structures*, 2014.
- [54] Zhangxian Deng and Marcelo J. Dapino. Modeling and design of Galfenol unimorph energy harvester. In *Proceedings of SPIE 9057*, page 90572A. International Society for Optics and Photonics, 2014.
- [55] Zhangxian Deng, Justin J. Scheidler, Vivake M. Asnani, and Marcelo J. Dapino. Major and minor stress-strain loops in textured polycrystalline  $\text{Fe}_{81.6}\text{Ga}_{18.4}$  Galfenol. *Journal of Applied Physics*, (in review), .
- [56] P.R. Downey and A.B. Flatau. Magnetoelastic bending of Galfenol for sensor applications. *Journal of Applied Physics*, 97(10):10R505, 2005.

- [57] Y.F. Duan and S.W. Or. Self-sensing tunable vibration absorber incorporating piezoelectric ceramic–magnetostrictive composite sensor/actuator. *Smart Materials and Structures*, 20(8):085007, 2011.
- [58] Göran Engdahl, editor. *Handbook of Giant Magnetostrictive Materials*. Academic Press, San Diego, CA, 2000.
- [59] Göran Engdahl and Anders Bergqvist. Loss simulations in magnetostrictive actuators. *Journal of Applied Physics*, 79(8):4689–4691, 1996.
- [60] P.G. Evans and M.J. Dapino. Efficient model for field-induced magnetization and magnetostriction of Galfenol. *Journal of Applied Physics*, 105(11):113901, 2009.
- [61] P.G. Evans and M.J. Dapino. Efficient magnetic hysteresis model for field and stress application in magnetostrictive Galfenol. *Journal of Applied Physics*, 107(6):063906, 2010.
- [62] P.G. Evans and M.J. Dapino. Dynamic model for 3-D magnetostrictive transducers. *Magnetics, IEEE Transactions on*, 47(1):221–230, 2011.
- [63] Phillip G. Evans. *Nonlinear Magnetomechanical Modeling and Characterization of Galfenol and System-Level Modeling of Galfenol-Based Transducers*. PhD thesis, The Ohio State University, 2009.
- [64] Phillip G. Evans and Marcelo J. Dapino. Fully-coupled magnetoelastic model for galfenol alloys incorporating eddy current losses and thermal relaxation. In *Proceedings of SPIE*, volume 6929, pages 69291W–1–69291W–12. International Society for Optics and Photonics, 2008.
- [65] Phillip G Evans and Marcelo J Dapino. Measurement and modeling of magnetic hysteresis under field and stress application in iron–gallium alloys. *Journal of Magnetism and Magnetic Materials*, 330:37–48, 2013.
- [66] Wolfgang Exner. Nvh phenomena in light truck drivelines. Technical report, SAE Technical Paper 952641, 1995.
- [67] F.F. Hines. *Proceedings of the Western Regional Strain Gage Committee*, Nov. 9th, pp. 39-44.
- [68] D.E. Figliola and R.S. Beasley. *Theory and design for mechanical measurements*. John Wiley & Sons, Inc., Hoboken, NJ, 4th edition, 2006.
- [69] A.B. Flatau, M.J. Dapino, and F.T. Calkins. High bandwidth tunability in a smart vibration absorber. *Journal of Intelligent Material Systems and Structures*, 11(12):923–929, 2000.



- [70] Daniel Fleisch. *A Student's Guide to Maxwell's Equations*. Cambridge University Press, Cambridge, UK, 2008.
- [71] Eiichi Fukada, Munehiro Date, and Kosei Sekigawa. Vibration control by magnetostrictive actuator coupled with negative inductance circuits. *Japanese Journal of Applied Physics*, 42(11R):7124, 2003.
- [72] A. Globus. Universal hysteresis loop for soft ferrimagnetic material. *Proc. Europ. Physical Society, Conference on Soft Magnetic Material*, 2:233, 1975.
- [73] C.D. Graham Jr. Physical origin of losses in conducting ferromagnetic materials. *Journal of Applied Physics*, 53(11):8276–8280, 1982.
- [74] Vishay Precision Group. Optimizing strain gage excitation levels. Technical Note TN-502, 2010.
- [75] Vishay Precision Group. Strain gage selection: Criteria, procedures, recommendations. Technical Note TN-505-4, 2010.
- [76] Vishay Precision Group. Strain gage thermal output and gage factor variation with temperature. Technical Note TN-504-1, 2012.
- [77] Vishay Precision Group. Noise control in strain gage measurements. Technical Note TN-501-2, 2013.
- [78] Vishay Precision Group. Shunt calibration of strain gage instrumentation. Technical Note TN-514, 2013.
- [79] K.B. Hathaway, A.E. Clark, and J.P. Teter. Magnetomechanical damping in giant magnetostriction alloys. *Metallurgical and Materials Transactions A*, 26(11):2797–2801, 1995.
- [80] Tom Hilgert, Lieven Vandeveld, and Jan Melkebeek. Neural-network-based model for dynamic hysteresis in the magnetostriction of electrical steel under sinusoidal induction. *IEEE Transactions on Magnetics*, 43(8):3462–3466, 2007.
- [81] M.W. Hiller, M.D. Bryant, and J Umegaki. Attenuation and transformation of vibration through active control of magnetostrictive Terfenol. *Journal of Sound and Vibration*, 134(3):507–519, 1989.
- [82] K. A. Hoffmann and S. T. Chiang. *Computational fluid dynamics*. Engineering Education System, Wichita, KS, 2000.
- [83] K Honda and T Terada. On the change of elastic constants of ferromagnetic substances by magnetization. *The London, Edinburgh, and Dublin Philosophical Magazine and Journal of Science*, 13(73):36–83, 1907.

- [84] Frederick V. Hunt. *Electroacoustics: the analysis of transduction, and its historical background*. Acoustical Society of America, 1954.
- [85] Etrema Products, Inc. Terfenol-D data sheet, [Online] 2013. Available from: <http://www.etrema-usa.com/documents/Terfenol.pdf>. [Accessed: 2nd May 2013].
- [86] M Ishimoto, H Numakura, and M Wuttig. Magnetoelastic damping in Fe–Ga solid-solution alloys. *Materials Science and Engineering: A*, 442(1):195–198, 2006.
- [87] ISO Standard 4664-1:2011(E). Rubber, vulcanized or thermoplastic Determination of dynamic properties part 1: General guidance. The International Organization for Standardization, Geneva, Switzerland, 2011.
- [88] D. C. Jiles and D. L. Atherton. Theory of ferromagnetic hysteresis. *Journal of Magnetism and Magnetic Materials*, 61:48–60, 1986.
- [89] David C Jiles. *Introduction to magnetism and magnetic materials*. CRC Press, 1998.
- [90] Ke Jin, Yong Kou, and Xiaojing Zheng. The resonance frequency shift characteristic of Terfenol-D rods for magnetostrictive actuators. *Smart Materials and Structures*, 21(4):045020, 2012.
- [91] JIS Standard Z 2273-1978. General Rules for Fatigue Testing of Metals. Japanese Standards Association, Tokyo, Japan, 1978.
- [92] Carl T. A. Johnk. *Engineering Electromagnetic Fields and Waves*. John Wiley & Sons, Inc., 1988.
- [93] N.J. Jones, J.B. Restorff, M. Wun-Fogle, and A.E. Clark. Magnetostriction and magnetization of tension annealed rods of Fe<sub>82</sub>Ga<sub>18</sub>. *Journal of Applied Physics*, 107(9):09A915, 2010.
- [94] R.A. Kellogg. *Development and modeling of iron–gallium alloys*. PhD thesis, Iowa State University, Ames, Iowa, 2003.
- [95] Rick Kellogg and Alison Flatau. Wide band tunable mechanical resonator employing the  $\delta E$  effect of Terfenol-D. *Journal of Intelligent Material Systems and Structures*, 15(5):355–368, 2004.
- [96] Rick Kellogg and Alison Flatau. Experimental investigation of Terfenol-D’s elastic modulus. *Journal of Intelligent Material Systems and Structures*, 19(5):583–595, 2008.

- [97] Rick A. Kellogg, Alison B. Flatau, Arthur E. Clark, Marilyn Wun-Fogle, and Thomas A. Lograsso. Quasi-static transduction characterization of Galfenol. *Journal of Intelligent Material Systems and Structures*, 16:471, 2005.
- [98] D. Kendall and A. R. Piercy. Comparison of the dynamic magnetomechanical properties of  $\text{Tb}_{0.27}\text{Dy}_{0.73}\text{Fe}_2$  and  $\text{Tb}_{0.30}\text{Dy}_{0.70}\text{Fe}_2$ . *Journal of Applied Physics*, 76(10):7148–7150, 1994.
- [99] C. Kittel. Physical theory of ferromagnetic domains. *Rev. Mod. Phys.*, 21:541–583, 1949.
- [100] L. Kvarnsjö and G. Engdahl. Examination of the interaction between eddy currents and magnetoelasticity in Terfenol-D. *Journal of Applied Physics*, 69(8):5783–5785, 1991.
- [101] Eric W Lee. Magnetostriction and magnetomechanical effects. *Reports on progress in physics*, 18(1):184, 1955.
- [102] L.P. Lefebvre, S. Pelletier, and C. Gelinas. Effect of electrical resistivity on core losses in soft magnetic iron powder materials. *Journal of Magnetism and Magnetic Materials*, 176(2):L93–L96, 1997.
- [103] G.J. Liao, X.L. Gong, S.H. Xuan, C.J. Kang, and L.H. Zong. Development of a real-time tunable stiffness and damping vibration isolator based on magnetorheological elastomer. *Journal of Intelligent Material Systems and Structures*, 23(1):25–33, 2012.
- [104] F. Liorzou, B. Phelps, and D. L. Atherton. Macroscopic models of magnetization. *IEEE Transactions on Magnetics*, 36(2):418–428, 2000.
- [105] Warren P Mason. *Physical Acoustics and the Properties of Solids*. D. Van Nostrand Co., Inc., Princeton, N.J., 1958.
- [106] L. Meirovitch. *Fundamentals of vibrations*. Waveland Press, Inc., Long Grove, IL, 1 edition, 2010.
- [107] J Mendoza, K Chevva, F Sun, A Blanc, and S.B. Kim. Active vibration control for helicopter interior noise reduction using power minimization. NASA/CR-2014-218147, 2014.
- [108] Mark B. Moffett, Arthur E. Clark, Marilyn Wun-Fogle, Jan Linberg, Joseph P. Teter, and Elizabeth A. McLaughlin. Characterization of Terfenol-D for magnetostrictive transducers. *The Journal of the Acoustical Society of America*, 89(3):1448–1455, 1991.

- [109] Chaitanya Mudivartha, Supratik Datta, Jayasimha Atulasimha, Alison B Flatau, Phillip G Evans, and Marcelo J Dapino. Equivalence of magnetoelastic, elastic, and mechanical work energies with stress-induced anisotropy. In *Proceedings of SPIE 6929*, page 69291X. International Society for Optics and Photonics, 2008.
- [110] Chaitanya Mudivartha, Suok-Min Na, Rudolf Schaefer, Mark Laver, Manfred Wuttig, and Alison B Flatau. Magnetic domain observations in Fe–Ga alloys. *Journal of Magnetism and Magnetic Materials*, 322(14):2023–2026, 2010.
- [111] Marcus Neubauer, Robert Oleskiewicz, Karl Popp, and Tomasz Krzyzynski. Optimization of damping and absorbing performance of shunted piezo elements utilizing negative capacitance. *Journal of Sound and Vibration*, 298(1):84–107, 2006.
- [112] P Pagliarulo, K Kuhnen, C May, and H Janocha. Tunable magnetostrictive dynamic vibration absorber. In *Proceedings of the 9th International Conference on New Actuators*, pages 367–370, 2004.
- [113] G. Petculescu, K.B. Hathaway, Thomas A. Lograsso, M. Wun-Fogle, and A.E. Clark. Magnetic field dependence of Galfenol elastic properties. *Journal of Applied Physics*, 97(10):10M315–10M315, 2005.
- [114] K Prajapati, R.D. Greenough, and A Wharton. Magnetic and magnetoelastic response of stress cycled Terfenol-D. *Journal of Applied Physics*, 81(8):5719–5721, 1997.
- [115] K Prajapati, R.D. Greenough, A Wharton, M Stewart, and M.G. Gee. Effect of cyclic stress on Terfenol-D. *IEEE Transactions on Magnetics*, 32(5):4761–4763, 1996.
- [116] F. Preisach. Über die magnetische Nachwirkung. *Zeitschrift für Physik*, 94(5–6):277–302, 1935.
- [117] Arun Ramaratnam and Nader Jalili. A switched stiffness approach for structural vibration control: theory and real-time implementation. *Journal of Sound and Vibration*, 291(1):258–274, 2006.
- [118] S.S. Rao. *Mechanical Vibrations*. Pearson Prentice Hall, Upper Saddle River, NJ, 4 edition, 2003.
- [119] Paavo Rasilo, Deepak Singh, Anouar Belahcen, and Antero Arkkio. Iron losses, magnetoelasticity and magnetostriction in ferromagnetic steel laminations. *IEEE Transactions on Magnetics*, 49(5):2041–2044, 2013.

- [120] J.B. Restorff, M Wun-Fogle, and Eric Summers. Hysteresis,  $d_{33}^*$  and  $d_{33}$  of  $\text{Fe}_{81.6}\text{Ga}_{18.4}$  textured polycrystals. *Journal of Applied Physics*, 109(7):07A922, 2011.
- [121] N. N. Sarawate and M. J. Dapino. Dynamic sensing behavior of ferromagnetic shape memory Ni–Mn–Ga. *Smart Materials and Structures*, 18(10):104014, 2009.
- [122] N.N. Sarawate and M.J. Dapino. Stiffness tuning with bias magnetic fields in ferromagnetic shape memory Ni–Mn–Ga. *Journal of Intelligent Material Systems and Structures*, 20(13):1625–1634, 2009.
- [123] H.T. Savage, A.E. Clark, and J. Powers. Magnetomechanical coupling and  $\delta E$  effect in highly magnetostrictive rare earth–Fe 2 compounds. *IEEE Transactions on Magnetics*, 11(5):1355–1357, 1975.
- [124] Marcelo A Savi, Aline S De Paula, and Dimitris C Lagoudas. Numerical investigation of an adaptive vibration absorber using shape memory alloys. *Journal of Intelligent Material Systems and Structures*, 22, 2010.
- [125] J.J. Scheidler and M.J. Dapino. Nonlinear dynamic model for magnetically-tunable Galfenol vibration absorbers. In *Proceedings of SPIE 8690*, page 869002, 2013.
- [126] J.J. Scheidler and M.J. Dapino. Nonlinear dynamic modeling and resonance tuning of Galfenol vibration absorbers. *Smart Materials and Structures*, 22(8):085015, 2013.
- [127] J.J. Scheidler and M.J. Dapino. Switched stiffness vibration control via electrically-controlled stiffness tuning of a magnetostrictive spring. *Journal of Sound and Vibration*, in preparation.
- [128] Justin J. Scheidler, Vivake M. Asnani, and Marcelo J. Dapino. Design and testing of a dynamically-tuned magnetostrictive spring with electrically-controlled stiffness. In *Proc. SPIE 9433, Industrial and Commercial Applications of Smart Structures Technologies*, pages 94330F–1–94330F–10, 2015.
- [129] Justin J. Scheidler, Vivake M. Asnani, and Marcelo J. Dapino. Dynamic characterization of Galfenol ( $\text{Fe}_{81.6}\text{Ga}_{18.4}$ ). NASA/TP-2015-218754, 2015.
- [130] Justin J. Scheidler, Vivake M. Asnani, and Marcelo J. Dapino. Design and testing of a dynamically-tuned magnetostrictive spring with electrically-controlled stiffness. *Smart Materials and Structures*, manuscript completed.

- [131] Justin J. Scheidler, Vivake M. Asnani, and Marcelo J. Dapino. Frequency-dependent, dynamic sensing properties of polycrystalline Galfenol ( $\text{Fe}_{81.6}\text{Ga}_{18.4}$ ). *Applied Physics Letters*, (in review).
- [132] Justin J. Scheidler, Vivake M. Asnani, Zhangxian Deng, and Marcelo J. Dapino. Dynamic characterization of Galfenol. In *Proc. SPIE 9432, Behavior and Mechanics of Multifunctional Materials and Composites*, pages 94320J–1–94320J–9, 2015.
- [133] Justin J. Scheidler and Marcelo J. Dapino. Stiffness tuning of FeGa structures manufactured by ultrasonic additive manufacturing. In *Proc. of SPIE 9059*, page 905907, 2014.
- [134] Justin J. Scheidler and Marcelo J. Dapino. Mechanically-induced magnetic diffusion in cylindrical ferromagnets. *Journal of Magnetism and Magnetic Materials*, (in review).
- [135] D. Schick, S.S. Babu, D.R. Foster, M. Dapino, M. Short, and J.C. Lippold. Transient thermal response in ultrasonic additive manufacturing of aluminum 3003. *Rapid Prototyping Journal*, 17(5):369–379, 2011.
- [136] L. Shu, M.J. Dapino, P.G. Evans, D. Chen, and Q. Lu. Optimization and dynamic modeling of Galfenol unimorphs. *Journal of Intelligent Material Systems and Structures*, 22(8):781–793, 2011.
- [137] L. Shu, L.M. Headings, M.J. Dapino, D. Chen, and Q. Lu. Nonlinear model for Galfenol cantilevered unimorphs considering full magnetoelastic coupling. *Journal of Intelligent Material Systems and Structures*, 25(2):187–203, 2013.
- [138] Julie C Slaughter, Marcelo J Dapino, Ralph C Smith, and Alison B Flatau. Modeling of a Terfenol-D ultrasonic transducer. In *Proc. of SPIE 3985*, pages 366–377, 2000.
- [139] Ralph C Smith and Marcelo J Dapino. A homogenized energy framework for ferromagnetic hysteresis. *IEEE Transactions on Magnetics*, 42(7):1747–1769, 2006.
- [140] I.J. Sokolov and V.I. Babitsky. Phase control of self-sustained vibration. *Journal of sound and vibration*, 248(4):725–744, 2001.
- [141] G.H. Staab. *Laminar composites*. Butterworth-Heinemann, Boston, MA, 1999.
- [142] E. C. Stoner and E. P. Wohlfarth. A mechanism of magnetic hysteresis in heterogeneous alloys. *IEEE Transactions on Magnetics*, 27(4):3475–3518, 1991.

- [143] Eric M Summers, Thomas A Lograsso, Jonathan D Snodgrass, and Julie C Slaughter. Magnetic and mechanical properties of polycrystalline Galfenol. In *Proceedings of SPIE*, volume 5387, pages 448–459, 2004.
- [144] Jan Szczygłowski. Influence of eddy currents on magnetic hysteresis loops in soft magnetic materials. *Journal of Magnetism and Magnetic Materials*, 223(1):97–102, 2001.
- [145] Hafez Tari, J.J. Scheidler, and M.J. Dapino. Robust solution procedure for the discrete energy-averaged model on the calculation of 3D hysteretic magnetization and magnetostriction of iron–gallium alloys. *Journal of Magnetism and Magnetic Materials*, 384:266–275, 2015.
- [146] Stephen C Thompson, Julie Slaughter, Eric Summers, Charles Allen, and Richard J Meyer. Variable compliance split-cylinder transducer using Galfenol for frequency control. *The Journal of the Acoustical Society of America*, 126(4):2276–2276, 2009.
- [147] Luke M Twarek and Alison B Flatau. Dynamic property determination of magnetostrictive iron-gallium alloys. In *Proc. of SPIE 5761, Smart Structures and Materials*, pages 209–220, 2005.
- [148] J. Twiefel. Vibration shape effects on the power output in piezoelectric vibro-impact energy harvesters. In *Proceedings of SPIE*, volume 8688, 86880K, 2013.
- [149] Toshiyuki Ueno and Sotoshi Yamada. Performance of energy harvester using iron–gallium alloy in free vibration. *IEEE Transactions on Magnetics*, 47(10):2407–2409, 2011.
- [150] Eric E Ungar and Edward M Kerwin Jr. Loss factors of viscoelastic systems in terms of energy concepts. *The Journal of the Acoustical Society of America*, 34(7):954–957, 1962.
- [151] S. Voronina and V. Babitsky. Autoresonant control strategies of loaded ultrasonic transducer for machining applications. *Journal of Sound and Vibration*, 313(3-5):395–417, 2008.
- [152] T. Walker. Experimental characterization and modeling of Galfenol (FeGa) alloys for sensing. Master’s thesis, The Ohio State University, 2012.
- [153] Philip Weetman and George Akhras. Modelling the quasistatic and dynamical sensing response of Galfenol-based magnetostrictive devices. *Applied Physics Letters*, 95(7):072504, 2009.

- [154] L. Weng, T. Walker, Z. Deng, M.J. Dapino, and B. Wang. Major and minor stress-magnetization loops in textured polycrystalline  $\text{Fe}_{81.6}\text{Ga}_{18.4}$  Galfenol. *Journal of Applied Physics*, 113(2):024508, 2013.
- [155] Ling Weng, Bowen Wang, M. J. Dapino, Ying Sun, Li Wang, and Baozhi Cui. Relationships between magnetization and dynamic stress for galfenol rod alloy and its application in force sensor. *Journal of Applied Physics*, 113(17):17A917, 2013.
- [156] M. Wun-Fogle, J.B. Restorff, and A.E. Clark. Soft and hard elastic moduli of Galfenol transduction elements. *Journal of Applied Physics*, 105(07A923), 2009.
- [157] Jin-Hyeong Yoo and Alison B Flatau. Measurement of field-dependence elastic modulus of iron–gallium alloy using tensile test. *Journal of Applied Physics*, 97(10):10M318–10M318, 2005.
- [158] Jin-Hyeong Yoo, Gerry Pelligrini, Supratik Datta, and Alison B Flatau. An examination of Galfenol mechanical–magnetic coupling coefficients. *Smart Materials and Structures*, 20(7):075008, 2011.
- [159] JinHyeong Yoo, Andrew Murray, and Alison B Flatau. Evaluation of magnetostrictive shunt damper performance using iron (Fe)-gallium (Ga) alloy. In *Proceedings of SPIE*, volume 90573, 90573I, 2014.
- [160] X. Zhao and D.G. Lord. Application of the Villari effect to electric power harvesting. *Journal of Applied Physics*, 99(8):08M703, 2006.
- [161] H.M. Zhou and Y.H. Zhou. Vibration suppression of laminated composite beams using actuators of giant magnetostrictive materials. *Smart Materials and Structures*, 16(1):198, 2007.